Cosmology and the galaxy-matter connection using weak gravitational lensing cross-correlations in the Dark Energy Survey

Judit Prat Martí

Cosmology and the galaxy-matter connection using weak gravitational lensing cross-correlations in the Dark Energy Survey

Judit Prat Martí

Tesi Doctoral
Programa de Doctorat en Física
Director: Dr. Ramon Miquel Pascual

Departament de Física
Facultat de Ciències
Universitat Autònoma de Barcelona
2019

Contents

Introduction and Motivation

Cosmology is the study of the origin, evolution and fate of the Universe. The Universe is not static and in 1929 Edwin Hubble discovered it is expanding, which is understood as a natural consequence of the Big Bang. Also, since Albert Einstein developed his theory of General Relativity in 1915, we know that the geometry and the dynamics of the Universe are governed by its content. In particular, the total energy density of the Universe dictates its geometry, whether it is flat, open or closed, while its dynamics is determined by the fractional densities of the different forms of energy present in it. If we are able to know the evolution of the energy density of each component of the Universe from the Big Bang until today, we will be able to predict how the Universe will evolve in the future and its ultimate fate. That is why measuring the content of the Universe and its evolution with high precision has become one of the major goals of modern cosmology and in particular one of the motivations for this thesis.

Observations made during the previous century have enabled major advancements in the field. They indicated that the components of the Universe that have dominated its energy density are radiation at early times and matter after that (mostly dark matter), clustered forming structures in the late Universe such as galaxies living in dark matter halos. However, this picture became incomplete when, only two decades ago, it was found that the expansion of the Universe was accelerating, against everyone's intuition. Neither the presence of radiation nor the one of matter could explain the positive acceleration of the expansion of the Universe. Before that, it had always been assumed that the expansion of the Universe had been decelerating because of the presence of matter in the Universe, which acts as a binding force due to gravity. At that moment, the concept of dark energy emerged: a special kind of energy density that would be capable of causing a positive acceleration in the expansion of the Universe. If dark energy has to explain the accelerated expansion, it has to dominate the energy density of today's Universe, being higher than the one of matter. However, even though it has been possible to measure the amount of dark matter and dark energy present in the Universe, their intrinsic natures remain unknown. Understanding the nature of these mysterious entities, which represent the majority of the energy in today's Universe, has become another major goal of modern cosmology. Particularly, it is specially important

to learn how dark energy evolves with time, since the fate of the Universe depends in great measure on it.

The other option still on the table to explain the observed acceleration is that General Relativity is not valid at the largest scales. This could make us think that the expansion of the Universe is accelerating when it is actually not. However, many modified gravity theories have already been ruled out by observations and therefore, as time passes, the hypothesis of the existence of dark energy gains strength and is currently considered as the most likely one. Throughout this thesis, we work under the assumption that dark energy exists and that General Relativity is valid at all scales, but also present some tests of this theory, which is still under examination.

To try to answer the big current questions of cosmology presented above, one of the approaches we are taking as a scientific community is to build instruments that are able to map the observable Universe, every time faster and deeper. We are creating maps of the Universe, called galaxy surveys, that allow us to probe the geometry and the growth of structure of the Universe as a function of time. These quantities are affected by the relative amount of dark energy and dark matter in the Universe and their evolution, and therefore we can measure it with such surveys. The first galaxy survey, CfA Redshift Survey (Huchra et al., 1983), was completed in 1982 after mapping around two thousand galaxies. Today we are in the era of big data, and over 500 million galaxies have been observed since then. Sloan Digital Sky Survey(SDSS) pioneered this explosion building both a spectroscopic and an imaging survey and was a turning point in the field. Other past and current imaging surveys include the Canada-France Hawaii Telescope Legacy Survey (CFHTLens), the Kilo-Degree Survey(KiDS), the Physics of the Accelerating Universe Survey (PAUS), the Hyper Suprime-Cam Subaru Strategic Program (HSC) and the Dark Energy Survey (DES). DES is the primary survey used in this thesis. It has covered 5000 square degrees taken during six years of observations that finished in January 2019, detecting over 300 million galaxies. Also, there are already a few planned future generation imaging surveys, such as the Large Synoptic Survey Telescope (LSST), the Euclid Survey and the Wide Field Infrared Survey Telescope (WFIRST), which will start observations soon and together will map all the sky which is not obscured by our galaxy during the next decade.

One of the reasons imaging galaxy surveys have recently become so popular is that they allow us to measure the shapes of galaxies. Galaxy shapes are one of the indispensable elements to measure gravitational lensing effects. Gravitational lensing is produced when light from background objects is deflected due to some foreground mass distribution that curves the space-time canvas. In particular, weak gravitational lensing, which can only be measured in a statistical manner, has emerged as one of the most powerful probes of cosmology, being sensitive to both the geometry of the Universe and the history of structure growth, and is one of the main techniques used in this thesis.

Besides weak lensing, imaging galaxy surveys can measure other probes of cosmol-

ogy at low redshift which in combination break degeneracies between parameters and, with the rise of large and deep galaxy surveys, are becoming competitive with high redshift probes such as the Cosmic Microwave Background, which used to be more constraining in relative terms. The comparison between cosmological results from these two epochs is a required test for the current Standard Cosmological Model, that for the first time we will be able to perform with comparable constraining power. The main topic of this thesis is studying weak gravitational lensing measurements from the Dark Energy Survey, which are one of the key ingredients for performing this comparison. In particular, this thesis is focused on measuring weak lensing cross-correlations between foreground galaxy positions and background galaxy shapes and orientations, known as galaxy-shear cross-correlations or galaxy-galaxy lensing.

In addition, galaxy surveys are not only suited to measure the composition of the Universe or the expansion rate as a function of time but are incredibly useful to learn about the formation and evolution of galaxies, about the relation between galaxies and dark matter, and many other subjects. Actually, these topics, besides already being interesting on their own, are key to properly model all scales in cosmological analyses that use weak gravitational lensing and the spatial distribution of galaxies in the Universe, since galaxies are biased tracers of the underlying dark matter field. Therefore, to fully exploit all the constraining power available in galaxy surveys, it is crucial to understand the relationship between galaxies and dark matter, the so-called galaxy bias. In this thesis, besides using galaxy-galaxy lensing to obtain cosmological information, we also use it to study the galaxy bias using early DES data.

An alternative way of performing weak lensing measurements without relying on (usually quite noisy) galaxy shape estimates from galaxy surveys is to use the light from the Cosmic Microwave Background (CMB). The CMB light is a relic from the very early Universe, which was emitted when the Universe became transparent, before structures were formed, and has been traveling since then filling all space. This light, in the same way as the light of background galaxies, is deflected by the curvature in the space-time produced by foreground structures. Therefore, the CMB provides an independent way of performing weak lensing studies which is sensitive to higher redshift information. Carrying so much information, there exist many experiments dedicated to observing this microwave light. In this thesis we have used data from the South Pole Telescope (SPT) and Planck satellite, which are current state-of-the art CMB surveys, to measure CMB lensing cross-correlations with foreground structure detected by the Dark Energy Survey. Specifically, we have obtained cosmological constraints just from geometrical information, taking appropriately defined ratios of CMB lensing and galaxy-galaxy lensing measurements.

This thesis is structured in the following way. In Part I, we introduce the cosmological background necessary to understand the rest of the thesis, and present in more detail the Dark Energy Survey. In Part II, we use galaxy-galaxy lensing measurements

to study the galaxy bias using early DES data. This project was published in Prat et al. (2018b). In Part III, galaxy-galaxy lensing measurements are used to probe cosmology (Prat et al., 2018a), and in combination with other probes, cosmological constraints are obtained and discussed. In Part IV, we use CMB lensing and galaxy-galaxy lensing to obtain constraints on the geometry of the Universe, published in Prat et al. (2019). We finally conclude in the end.

Part I

Preliminars

This first part contains the theoretical background needed to understand the rest of the thesis, including first a general cosmological framework, followed by a description of weak gravitational lensing. Then we proceed to introduce the Dark Energy Survey and some of the main techniques used to measure galaxy shapes and redshifts in such a survey.

Chapter 1

Cosmological background

This chapter is intended to provide a comprehensive introduction to the standard cosmological model that will be used throughout this thesis and other crucial cosmological concepts.

1.1 The cosmological principle and the expanding universe

The *cosmological principle* states that at large scales the Universe is homogeneous, i.e. there is no preferred observing position, and isotropic, i.e. it looks the same in every direction. In 1929 Hubble measured the distances and the velocities of several galaxies and found most of them were moving away from us, moving faster the further they were from us. In combination with the cosmological principle, this led to the development of the Big Bang theory, which describes the Universe as expanding from an initial very high density and high temperature state. As the Universe is expanding, distances change over time. Hence, it is useful to define a *scale factor* $a(t)$ to describe this expansion. The *physical* or *proper distance* $\vec{r}$ between two simultaneous events $(\vec{\chi}, t)$ and $(\vec{\chi} + d\vec{\chi}, t)$ is

$$\vec{r} = a(t) d\vec{\chi}, \tag{1.1}$$

where $\vec{\chi}$ is called *comoving distance*. It is usual to take $a_0 \equiv a(t_0) = 1$, so at the present time the proper and comoving distances are equal. If we could place a ruler and measure the distance between any two objects today, that distance would be the comoving distance. The physical distance between two objects in the past, again measured with this hypothetical ruler, would have been smaller than today by a factor of $a(t)$. All the changes due to expansion are therefore captured by the scale factor; the comoving distance remains constant throughout, exceptuating changes due to peculiar velocities coming from local interactions.

1.2 The metric of the Universe

In the case of a smooth expanding universe, the scale factor connects the comoving distance with the physical distance. Generally, the *metric* is used to perform this conversion and is therefore an essential tool to make quantitative predictions in an expanding universe. The only metric that can describe a universe that is expanding, homogenous and isotropic is the *Friedmann–Lemaître–Robertson–Walker* (FLRW) metric. It is an exact solution of Einstein's field equations of general relativity, although Einstein's equations are not needed in deriving the general form for the metric: it follows directly from the geometric properties of homogeneity and isotropy. In this metric, the space-time separation between two events $(\vec{\chi}, t)$ and $(\vec{\chi} + d\vec{\chi}, t + dt)$ in spherical coordinates is:

$$ds^2 = -c^2 dt^2 + a^2(t) \left[d\chi^2 + S_k^2(\chi) d\Omega^2 \right], \tag{1.2}$$

where Ω is the solid angle, χ is the radial comoving distance and S_k depends on the curvature k of the Universe:

$$S_k(\chi) = \begin{cases} \sin\chi & (k = 1, \text{ closed Universe}) \\ \chi & (k = 0, \text{ flat Universe}) \\ \sinh\chi & (k = -1, \text{ open Universe}) \end{cases} \tag{1.3}$$

A big advantage of the metric is that it can incorporate gravity. Instead of thinking of gravity as an external force and considering particles moving in a gravitational field, we can include gravity in the metric and consider particles moving freely in a curved space-time. For instance, to quantify gravitational lensing later in this thesis, we need to consider light propagation in an inhomogeneous Universe, discussed in detail later in Chapter 2.

The line element for a general metric that describes an expanding Universe with first-order perturbations to its homogeneity is given by

$$ds^2 = -\left(1 + \frac{2\Psi}{c^2}\right) c^2 dt^2 + a^2(t) \left(1 - \frac{2\Phi}{c^2}\right) dl^2, \tag{1.4}$$

where $dl^2 = d\chi^2 + S_k^2(\chi) d\Omega^2$. The two potentials Ψ and Φ describe weak gravitational fields with $\Psi, \Phi \ll c^2$. This condition is fulfilled for all masses M and potentials $\Psi, \Phi \sim GM/R = (c^2/2)(R_s/R)$ whose extents R are much larger than their Schwarzschild radius R_s, where G is Newton's gravitational constant. In general relativity the two potentials are equal, $\Psi = \Phi$. Also, if there are no perturbations, the metric reduces to the FLRW metric.

1.3 Redshift and the Hubble Law

As we anticipated at the beginning of this chapter, Hubble found evidence for the expansion of the Universe by discovering that most of the galaxies were receding from us. However, the velocity of a galaxy is not an observable quantity and he instead measured the relative shift between the observed spectrum of a galaxy and the one we would expect if it was at rest. This is known as the *redshift* since the Universe is expanding and therefore the emitted wavelength λ_e is typically stretched and observed redder, as λ_0. Using the Doppler effect, the redshift z can be converted to the radial velocity v:

$$z \equiv \frac{\lambda_0 - \lambda_e}{\lambda_e} = \sqrt{\frac{1+v/c}{1-v/c}} - 1 \simeq \frac{v}{c}, \tag{1.5}$$

where the last approximation holds for low velocities. Then, Hubble related the redshift, or velocity, of several galaxies to their distances, finding there was a linear relation between these two quantities, which is exactly what one would expect in an expanding universe. This relation is known as the Hubble Law:

$$v \simeq zc = H_0 r, \qquad (z \ll 1) \tag{1.6}$$

only valid at low redshifts. H_0 is the Hubble constant today, which according to the latest *Planck* results is 67.4 ± 0.5 km s^{-1} Mpc^{-1} (Planck Collaboration 2018) and is usually expressed as $H_0 = 100\,h$ km s^{-1} Mpc^{-1}. The value of H, called the *Hubble rate*, changes over time and quantifies the rate of expansion of the Universe. Since $r = a\chi$ and $v = \dot{r} = \dot{a}\chi$ in the absence of peculiar velocities ($\dot{\chi} = 0$), the Hubble rate can be written as

$$H(a) = \frac{\dot{a}}{a}, \tag{1.7}$$

where the derivatives are with respect to time.

The redshift is a very useful quantity, because besides being observable it can be related to the scale factor a. The relation is only exact in the absence of peculiar velocities, that is to say, the scale factor can only be related to the *cosmological redshift*, the one that is due to the expansion of the Universe. In order to derive this relationship, consider light that was emitted at a time t_e and is observed by us at a later time t_0. Since light travels along null geodesics ($ds = 0$), then $cdt = a(t)d\chi$ for light in a FLRW metric. Thus, the comoving distance traveled by light is

$$\chi = c\int_{t_e}^{t_0} \frac{dt}{a(t)}. \tag{1.8}$$

Now, suppose the light is emitted with a wavelength λ_e. Then, consider two successive

wave crests emitted at times t_e and $t_e + \lambda_e/c$ and observed at times t_0 and $t_0 + \lambda_0/c$, respectively. For the second wave crest, the traveled comoving distance is

$$\chi = c \int_{t_e+\lambda_e/c}^{t_0+\lambda_0/c} \frac{dt}{a(t)}. \tag{1.9}$$

Comparing (1.8) and (1.9) yields

$$\int_{t_e}^{t_0} \frac{dt}{a(t)} = \int_{t_e+\lambda_e/c}^{t_0+\lambda_0/c} \frac{dt}{a(t)}. \tag{1.10}$$

If we subtract the integral

$$\int_{t_e+\lambda_e/c}^{t_0} \frac{dt}{a(t)} \tag{1.11}$$

from each side of equation (1.10), we obtain

$$\int_{t_e}^{t_e+\lambda_e/c} \frac{dt}{a(t)} = \int_{t_0}^{t_0+\lambda_0/c} \frac{dt}{a(t)}, \tag{1.12}$$

which means that the integral of the inverse of the scale factor between the emission of successive wave crests is equal to the same integral between the observation of successive wave crests. Also, since the Universe does not have time to expand a significant amount between the emission or observation of two successive wave crests, $a(t)$ is effectively constant in the integrals of (1.12). Therefore,

$$\frac{\lambda_e}{a(t_e)} = \frac{\lambda_0}{a(t_0)}. \tag{1.13}$$

Finally, using the definition of redshift (1.5), we can relate it to the scale factor:

$$1 + z = \frac{a(t_0)}{a(t_e)} = \frac{1}{a}. \tag{1.14}$$

The redshift cannot only be related to the scale factor as we have seen above, but it can also be related to the cosmological time through the Hubble rate, using the equation we have just derived:

$$H(t) = \frac{1}{a}\frac{da}{dt} = -\frac{1}{1+z}\frac{dz}{dt} \qquad \Longrightarrow \qquad dt = -\frac{1}{H(z)(1+z)}dz. \tag{1.15}$$

Together with the Friedman equation (1.26), which we will introduce later, this expression is useful to compute the age of the Universe at a certain redshift. Also, combining Eq. (1.15) with (1.8) we can obtain the last relation we will derive in this section,

which is the one between redshift and comoving distance:

$$\chi(z) = c \int_0^{z_e} \frac{dz}{H(z)}. \tag{1.16}$$

This relation is illustrated in Fig. 1.4, for different expansion histories $H(z)$.

1.4 The Cosmic Microwave Background

Besides the discovery that most objects are getting away from us displayed in Hubble's diagram, there is another crucial piece of observational evidence for the expansion of the Universe and the Big Bang theory: the Cosmic Microwave Background (CMB).

After the observation of an expanding Universe, cosmologists could conclude that the Universe was smaller in the past. As a result, the radiation filling the Universe was more energetic (or hotter) than it is today. This is because the energy of radiation is inversely proportional to its wavelength, and the wavelength is proportional to the scale factor, which was smaller in the past for an expanding universe. Applying the first law of thermodynamics to an expanding universe, it can be derived that the temperature of radiation is also related to the scale factor, as $T(t) = T_0/a(t)$, where T_0 is the temperature of the radiation today. Therefore, the temperature of the Universe must have been very high at early times, possibly high enough to be able to ionize atoms such as hydrogen and helium. If the baryonic matter was completely ionized, the free electrons were coupled with the photons via Thomson scattering, and therefore the mean free path of the photons was very short, effectively making the Universe opaque. Also, any hydrogen atoms being formed in that period were quickly ionized by ambient photons. Because of these constant interactions, photons were in equilibrium during that time, and therefore they should have had a blackbody spectrum. As the Universe cooled and expanded, the energy of ambient photons was no longer high enough to ionize hydrogen, and the mean free path of photons grew drastically, effectively making the Universe transparent and in principle able to transmit that light until us today.

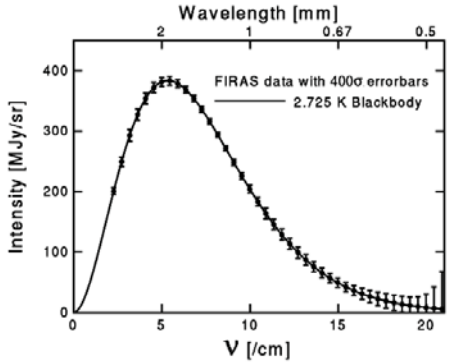

Figure 1.1: Intensity of CMB radiation as a function of frequency (and wavelength) for the COBE FIRAS experiment (Mather et al., 1994), showing impressive agreement with a blackbody sepctrum (note that errorbars are magnified by a factor of 400 in the plot!).

In the mid twentieth century, cosmologists started looking for the remnants of this radiation coming from the very early Universe, as a proof of the Big Bang theory. The Cosmic Microwave Background (CMB) was first detected serendipitously by Penzias & Wilson (1965), in a single wavelength. This first detection was further confirmed by other experiments, but it was the COsmic Background Explorer (COBE) satellite, launched in 1989, that impressively extended it to a broad range of wavelengths (Mather et al., 1994), confirming its agreement with a blackbody spectrum as seen in Fig. 1.1, and hence providing direct observational evidence for the Big Bang. Also, the CMB is called like this for its higher intensity in the microwave part of the radio spectrum today.

After COBE, many experiments like the satellites WMAP and more recently *Planck* have characterized the CMB properties. Nowadays we know that CMB radiation arises from the Universe when it was about 400,000 years old (redshift $z \simeq 1100$), and its frequency spectrum today corresponds to a blackbody at an equivalent temperature of $T_0 = 2.72548 \pm 0.00057K$ (Fixsen, 2009), ~ 1100 times lower than the temperature of the Universe when it became transparent of $\sim 3000K$, as a result of the expansion of the Universe.

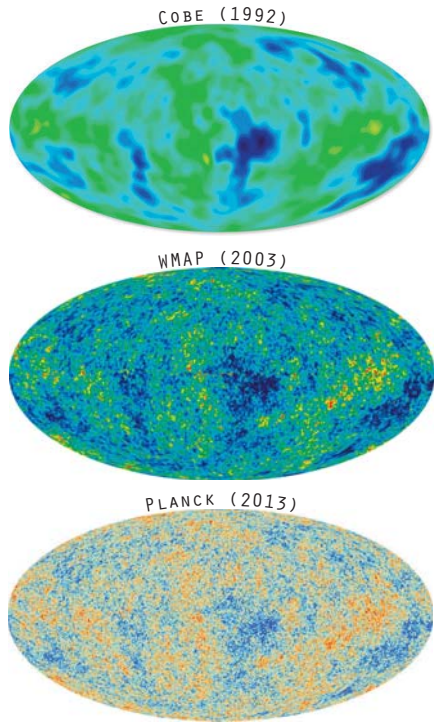

Figure 1.2: Anisotropies in the CMB (color scales show differences of the order of 10^5) as shown by three different satellites: COBE, WMAP and *Planck*, which are the three existing CMB full-sky surveys up to this date.

Even though the CMB represents the most precise blackbody spectrum in nature, and it looks the same in all directions without variations at the percent level (what is known as the CMB monopole), it is not perfectly isotropic. First, there exists an anisotropy of the order of 1 part in 10^3 which corresponds to the Doppler effect caused by the movement of the Earth with respect to the CMB reference rest frame; this is known as the CMB dipole anisotropy, since one half of the sky is slightly blueshifted to higher temperatures, and in the other half the spectrum is slightly redshifted to lower temperatures. More interestingly, after the dipole distortion is subtracted away, there are temperature fluctuations at the level of 1 part in 10^5. These temperature fluctuations, first detected by COBE (Smoot et al., 1992) but later confirmed with higher accuracy by the following experiments WMAP (Ben-

nett et al., 2013) and *Planck* (Planck Collaboration, 2018), can be seen in Fig. 1.2. They carry a huge amount of information since they are caused by the density fluctuations in the early Universe, which eventually led to the structures we see today (galaxies, clusters of galaxies, filaments...). One of the main effects imprinted in the CMB anisotropies comes from the oscillations of the coupled baryon-photon plasma in the early Universe. Gravity tries to compress the photon-baryon fluid sitting on primordial gravitational potential wells, while radiation pressure acts in the opposite way, resulting in acoustic (pressure) oscillations. In general these anisotropies provide an enormous insight on the composition of the Universe and hence can be used to measure the cosmological parameters, introduced in the following section. In fact, some of the current tightest constraints on cosmological parameters come from the analysis of the latest full-sky CMB experiment, the *Planck* satellite. These constraints, which are coming from the early universe, can then be compared with results from late-type probes, obtained with surveys such as the Dark Energy Survey. Only if the two agree the current cosmological model will be sufficient.

1.5 The Standard Cosmological Model

In this section we will derive the equations for the current standard cosmological model. Inserting the FLRW metric, described in Sec. 1.2, into Einstein's field equations of general relativity, we obtain the *Friedmann-Lemaître equations*:

$$\begin{aligned} \left(\frac{\dot{a}}{a}\right)^2 &= \frac{8\pi G\rho}{3} - \frac{k}{a^2} \\ \frac{\ddot{a}}{a} &= -\frac{4\pi G}{3}\left(\rho + 3p\right), \end{aligned} \tag{1.17}$$

where ρ is the energy density and p is the pressure. The above equations highlight the idea of general relativity that the metric is determined by the matter and energy in the region of interest. Looking at the first equation, it reveals that the rate of expansion of the Universe $H = \dot{a}/a$ depends on its geometry and total energy density. The second equation is telling us that the acceleration of this expansion (and its sign) depends both on the energy density and the pressure associated with the material filling the Universe — if the energy density and pressure are both positive, then it provides a negative acceleration. Therefore, these equations emphasize that it is crucial to determine the geometry, pressure and energy density of the components of the Universe as a function of time and its relative abundance to learn about the dynamics of the Universe. In order to do that, following from these equations we can derive the *continuity equation* for a perfect fluid:

$$\frac{\partial\rho}{\partial t} + 3\frac{\dot{a}}{a}\left(\rho + p\right) = 0, \tag{1.18}$$

which does not provide independent information but it is useful to derive the evolution of the energy density with time. However, we still need an extra piece of information, which is the relation between the pressure and energy density, also called equation of state. In general, equations of state can have complicated nonlinear expressions. Fortunately, cosmology usually deals with dilute gases, for which the equation of state is simple and can be written as:

$$p = w\rho, \tag{1.19}$$

where w is a dimensionless number. Using the equation of state, we can rearrange the continuity equation to yield

$$\frac{d\rho}{\rho} = -3(1+w)\frac{da}{a}. \tag{1.20}$$

Then, integrating each side and assuming w is constant we obtain

$$\rho = \rho_0 a^{-3(1+w)} = \rho_0(1+z)^{3(1+w)}. \tag{1.21}$$

Thus, we can already predict how each component of the Universe evolves with time. Let's go through the list of known components of the Universe. There is nonrelativist matter, which has effectively zero pressure (and hence has $w \approx 0$). Then, its density falls as $\rho_m \propto a^{-3}$. This is expected since the density of particles is inversely proportional to the volume as the Universe expands. For simplicity, in general we will refer to the component of the Universe that consists of nonrelativistic particles as "matter". For instance, this includes baryonic matter and also dark matter, which actually represents most of the matter in the Universe.

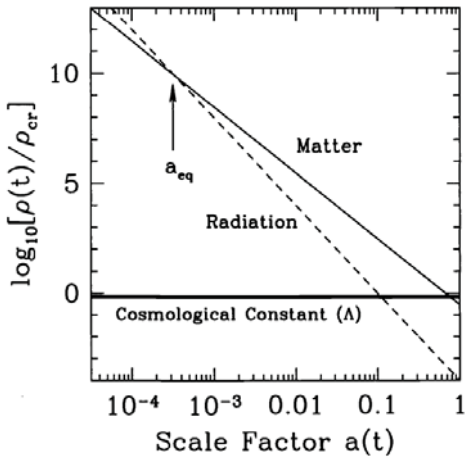

Figure 1.3: Energy density as a function of the scale factor for different components of the Universe, following Eq. (1.21). All energy densities are normalized by the critical density today. It shows that dark energy, in this case a cosmological constant, and matter dominate the density of the Universe today, while in the early Universe radiation used to dominate. The time at which matter and radiation are equal is $a_{\rm eq}$. Figure from Dodelson (2003).

The Universe also contains photons and other relativistic particles, which we will refer to as "radiation". Radiation has pressure $p_r = \rho/3$, resulting in $\rho_r \propto a^{-4}$. This also agrees with intuition, since in the case of radiation its energy density decreases with the expansion of the

Universe because of the same reason as matter but also because the wavelength of the light increases by a factor of a, decreasing its energy by the same factor. Figure 1.3 illustrates the evolution of matter and radiation with time, where we can see that because of the different dependency, radiation dominated the total energy density in the very early Universe until matter took over.

If the Universe would only contain matter and radiation, its expansion would be slowing down, as given by the second Friedmann-Lemaître equation. This is what everyone was expecting when in 1998 there was a big surprise. Two independent experiments found observational evidence that the expansion was accelerating, instead of decelerating. From Friedmann-Lemaître second equation, we deduce that if the acceleration of the expansion is positive, there must be something in the Universe with $w < -1/3$. This hypothetical substance is generically referred to as "dark energy". A particular case is $w = -1$, which is referred to as a cosmological constant because its energy density does not evolve with time, as can be seen from Eq. (1.21). The cosmological constant has $p = -\rho$ and is designated by the letter Λ. The famous model that includes dark energy in the form of a cosmological constant and Cold (which basically means non-relativistic) Dark Matter is called ΛCDM, and is considered the Standard Cosmological model so far. The model comprising general dark energy instead of a cosmological constant is referred to as wCDM. Summarizing, for each component:

$$p = w\rho \begin{cases} \text{Matter} & w_m = 0 & \rho_m \propto a^{-3} \\ \text{Radiation} & w_r = \frac{1}{3} & \rho_r \propto a^{-4} \\ \text{Cosmological constant} & w_\Lambda = -1 & \rho_\Lambda = \rho_0 \\ \text{Dark energy} & w_{de} = w(a) < -\frac{1}{3} & \rho_{de} \propto a^{-3\,[1+w(a)]} \end{cases} \tag{1.22}$$

where in its most general form, dark energy's equation of state can evolve with time and is usually parametrized as

$$w(a) = w_0 + (1-a)w_a + O(1-a)^2. \tag{1.23}$$

In order to measure the expansion and acceleration of the Universe, besides having to know how each component evolves with time, we are left to figure out their relative abundances. For this purpose, it is useful to define the following dimensionless parameters, also simply called *cosmological parameters*:

$$\Omega_{i,0} \equiv \frac{\rho_{i,0}}{\rho_{cr}}, \tag{1.24}$$

where $\rho_{i,0}$ is the density of the component i today, normalized by the *critical density*:

$$\rho_{cr} = \frac{3H_0^2}{8\pi G}, \tag{1.25}$$

which is the particular value of density obtained when setting the curvature $k = 0$ in the first Friedmann equation, given some value of H_0. If the total energy density is greater than this value, the Universe will be closed, and if it is less than this value, it will be open. Combining the previous equations, we can express the first Friedmann equation as

$$H^2(z) = H_0^2 \left[\Omega_m(1+z)^3 + \Omega_r(1+z)^4 + \Omega_k(1+z)^2 + \Omega_{de}(1+z)^{3(1+w)}\right], \tag{1.26}$$

where $\Omega_k = -\frac{k}{H_0^2}$. Hereafter we use Ω_i to refer to $\Omega_{i,0}$ for simplicity and w for the parameter describing dark energy equation of state, since for the rest of the components it is a known parameter. The equation above implies the following consistency relation:

$$\sum_i \Omega_i + \Omega_k = 1, \tag{1.27}$$

where i refers to every component besides curvature.

At this point we have defined all cosmological parameters necessary to describe the dynamics of the expansion of the Universe. A minimal set is: $\{\Omega_i\}, \Omega_k, H_0, w$. One of the goals of modern cosmology is to measure these parameters to sufficient accuracy to understand the history and fate of the Universe we are living in. Using data from the Cosmic Microwave Background (CMB), it has already been possible to place tight constraints on some of them. Nowadays, we know that our Universe is nearly flat, with $\Omega_k = 0.001 \pm 0.002$ from combined *Planck* + BAO constraints from Planck Collaboration 2018. Also, we know that radiation is a really small component of our Universe now, as opposed to the early Universe, which was radiation dominated (see Fig. 1.3). Quantitatively, $\Omega_r \sim 10^{-5}$ today. Then, the current Universe is dominated by matter, $\Omega_m = 0.315 \pm 0.007$ (Planck Collaboration, 2018), and dark energy. The matter component is further divided between cold dark matter (CDM) and baryonic matter, $\Omega_b h^2 = 0.0224 \pm 0.0001$ also from the latest *Planck* results. Then, CMB measurements indicate that dark matter is far more abundant than baryonic matter.

Eventhough we have been able to measure each of these parameters with high accuracy, the nature of dark matter and dark energy is still unknown, which means that we do not understand yet the nature of most of the content of our Universe today. On top of that (or because of that), one of the other main questions that remain to answer is whether the dark energy density evolves with time or whether it is a cosmological constant. This translates on measuring w for dark energy, and checking whether it is compatible with -1. Measuring w and providing independent measurements from the CMB on the other cosmological parameters is the main reason for the existence of galaxy surveys such as the Dark Energy Survey and of studies such as this thesis. In Chapter 6, we will present the results obtained for this parameter and for the other

components described above using data from the first year of observations of the Dark Energy Survey.

1.6 Distances

As we have seen in Section 1.3, we can relate the redshift, which is observable, to the comoving distance via Eq. (1.16) if we know the history of expansion of the Universe, given by $H(z)$. Alternatively, if we are able to measure the distance to an object independently from its redshift, we can measure the cosmological parameters that appear in Eq. (1.26) using the distance-redshift relationship. This relation is illustrated in Fig. 1.4 for different values of Ω_m for a flat Universe with matter and a cosmological constant. Actually, this distance-redshift relation is what was used to discover the positive acceleration of the expansion of the Universe, using Type Ia Supernovae to extend Hubble's diagram to higher redshift. However, neither the comoving distance, which remains fixed as the Universe expands, nor the physical (or proper) distance, which grows because of the expansion, are directly related to observations. Instead, we introduce here two alternative distance estimators which are more easily related to observable quantities.

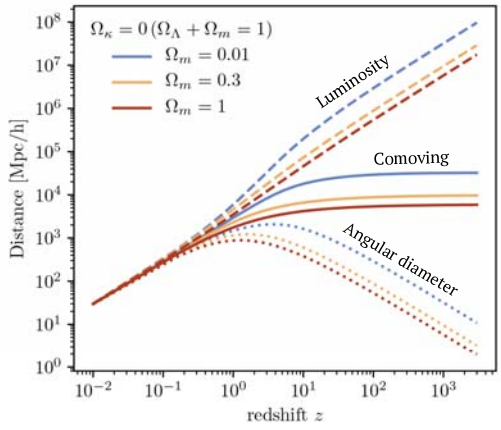

Figure 1.4: Relation between distance and redshift for different universes and distance estimators. Distances are larger in universes where there is more dark energy and less matter.

1.6.1 Angular diameter distance

One is the angular diameter distance, which can be obtained if we know the physical size of an object, l, and we can measure the angle it subtends, θ. For small angles:

$$D_A = \frac{l}{\theta}. \tag{1.28}$$

Also, the comoving size of the object will be l/a. Then, since the angle subtended is also $\theta = (l/a)/\chi$, we can relate the angular diameter distance to the comoving distance as:

$$D_A^{\text{flat}} = a\chi = \frac{\chi}{1+z}, \tag{1.29}$$

for a flat Universe. Therefore, the angular diameter distance is very similar to the comoving distance at low redshift, but it decreases at large redshift as seen in Fig. 1.4, counterintuitively making objects which are at very high redshifts appear larger than objects at intermediate redshift, at least in a flat universe. For open or closed universes, the angular diameter distance generalizes to:

$$D_A = \frac{a}{H_0\sqrt{|\Omega_k|}} \begin{cases} \sinh\left(\sqrt{\Omega_k} H_0 \chi\right) & \Omega_k > 0 \\ \sin\left(\sqrt{-\Omega_k} H_0 \chi\right) & \Omega_k < 0 \end{cases} \tag{1.30}$$

Both of these expressions reduce to the flat case in the limit that curvature goes to zero.

1.6.2 Luminosity distance

Another way of inferring distances in astronomy is to measure the flux from an object with known luminosity, such as Type Ia Supernovae. The flux F we observe from an object at a distance d with luminosity L without taking into account the expansion of the Universe is

$$F = \frac{L}{4\pi d^2}, \tag{1.31}$$

since the total luminosity is shared between a spherical shell with area $4\pi d^2$. In an expanding universe, the distance between the observer and the source evolves with time, as well as the luminosity, and thus we need to write each quantity as a function of the scale factor:

$$F(a) = \frac{L(a)}{4\pi\chi^2(a)}. \tag{1.32}$$

$L(a)$ is the luminosity that goes through a comoving spherical shell with radius $\chi(a)$ and it changes because of expansion due to two reasons. First, the energy of the photons will be smaller today by a factor of a than at emission, because of the expansion. If we assume all photons were emitted with the same energy to simplify, then $L(a)$ is this energy multiplied by the number of photons passing through a (comoving) spherical shell per unit of time, and therefore is reduced by a factor of a. Secondly, the number of photons crossing a shell in a fixed time interval will be smaller today than at emission also by a factor of a, reducing the observed luminosity by the same factor since they are directly proportional. This is because photons travel farther on the comoving grid at early times than at late times since the associated physical distance at early times is smaller.

Then, the luminosity being transmitted at the time the observer receives the light will be reduced by a factor a^2 with respect to the luminosity at the source:

$$L(a) = L_{\text{source}} a^2. \tag{1.33}$$

Then, the flux we observe will be:

$$F = \frac{L_{\text{source}} a^2}{4\pi\chi^2(a)}, \tag{1.34}$$

and if we define the luminosity distance as:

$$D_L \equiv \frac{\chi}{a}, \tag{1.35}$$

we can write the observed flux in an expanding universe as:

$$F = \frac{L_{\text{source}}}{4\pi D_L^2(a)}. \tag{1.36}$$

The relation between the different distance definitions is represented in Fig. 1.4 for different values of Ω_m in a flat Universe with matter and a cosmological constant.

1.7 The Inhomogeneous Universe

The Universe can be approximated as being homogeneous and isotropic only on very large scales. On smaller scales, it is clear that this is not the case, as on some spots there are super-clusters of galaxies while on other places empty space dominates. This is evidenced by galaxy surveys such as the one shown in Fig. 1.5, or in the anisotropies from the CMB, shown in Fig. 1.2. Actually, a completely homogeneous density field cannot exist: quantum fluctuations must occur on microscopic scales. However, the observed fluctuations are way too large compared to those expected from evolving fluctuations with gravity originated from a pure quantum process in an expanding universe. Then the following question arises: how did the structures we observe today form?

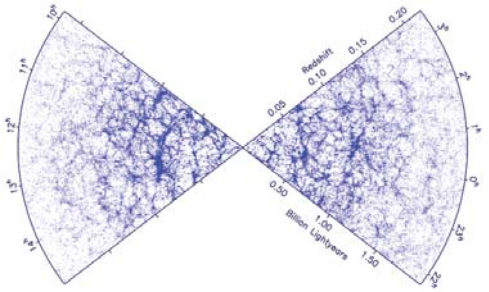

Figure 1.5: Redshift cones from the 2dF Galaxy Redshift Survey, evidencing the existence of large-scale structures in the Universe (Colless et al., 2001).

1.7.1 Structure Formation

The *inflationary* theory (Guth, 1981), which describes a period of exponential expansion of space in the early Universe, was initially proposed as a way to solve the flatness and the horizon problems. These refer, respectively, to the fact that the Universe

appears to be flat (too flat to be a coincidence), and also homogeneous and isotropic on scales much larger than the distance light had time to travel since the Big Bang, called cosmological horizon, and that therefore had never been in causal contact (again too homogeneous and too isotropic to be a coincidence). Besides solving these two problems, inflation also provides an explanation for the observed structures in the Universe: quantum fluctuations in the very early Universe were magnified to cosmic size due to the exponential expansion, becoming the seeds of the anisotropies observed in the CMB and, at later times, the Large-Scale Structure (LSS) of the Universe.

After inflation, structure formation started with small density fluctuations that grew in time and became the known structures of the Universe today, such as galaxies, galaxy clusters and voids. The basic mechanism for growing large structures is called *gravitational instability*. A slightly overdense region has a somewhat higher self-gravity than the average region of the Universe, so its expansion rate will be slightly lower than that of the Universe as a whole. As a result of slower expansion, the density contrast of this region increases further, retarding expansion more, and so on. In order to statistically describe the inhomogeneous Universe, let's define the dimensionless *overdensity field* δ, also called density contrast, which describes the energy density fluctuations at any 3D position $\vec{x}$ and time t with respect to the mean energy density $\bar{\rho}$:

$$\delta(\vec{x},t) \equiv \frac{\rho(\vec{x},t) - \bar{\rho}(t)}{\bar{\rho}(t)}. \tag{1.37}$$

$\delta < 0$ corresponds to underdense regions while $\delta > 0$ corresponds to overdense regions. Note that $-1 \leq \delta < \infty$, as $\delta = -1$ corresponds to $\rho(\vec{x}) = 0$, while there is no upper bound for δ.

1.7.2 Statistics of the matter density field

Even though above we have defined the density contrast as a function of position and time, no theory predicts that a galaxy will form in a given position in the Universe or if a particular region will be overdense or underdense. Instead, in order to compare observations to theoretical predictions, we need to measure how matter is distributed on average, for which we can make theoretical predictions. The simplest statistic we can obtain is the mean of $\delta(\vec{x})$, which by its definition in Eq. (1.37) vanishes:

$$\langle \delta(\vec{x}) \rangle = 0, \tag{1.38}$$

where the angular brackets refer to taking the average over all the space. The next simplest statistic we could take is the variance of fluctuations: $\sigma^2 \equiv \langle \delta^2(\vec{x}) \rangle$. However, there is a more sophisticated two-point statistic called *two-point correlation function*, that encodes information about the typical lengths over which matter is clustered, and

how clustered a distribution is — the higher the value of the correlation function, the more clustered matter is. It is defined as

$$\xi(\vec{x},\vec{y}) \equiv \langle \delta(\vec{x})\,\delta(\vec{y})\rangle = \xi(|\vec{x}-\vec{y}|), \tag{1.39}$$

and since the Universe is homogeneous and isotropic, the correlation function ξ cannot depend on the exact position or direction and therefore it only depends on the magnitude of the distance difference $|\vec{x}-\vec{y}|$.

The two-point correlation function is the most straightforward quantity that can be computed from the data, but in order to compare to theoretical predictions there is a more useful statistic called *power spectrum*, which is just the Fourier transform of the two-point correlation function. In order to define the power spectrum, let's first express the matter density fluctuations in Fourier Space. Also, since δ is defined in a three-dimensional space (rather than on the surface of a sphere) we expand $\delta(\vec{x})$ in terms of its 3D Fourier components:

$$\delta(\vec{x}) = \frac{1}{(2\pi)^3}\int d^3k\,\tilde{\delta}(\vec{k})\,e^{i\vec{k}\cdot\vec{x}} \tag{1.40}$$

which can be inverted to yield:

$$\tilde{\delta}(\vec{k}) = \int d^3x\,\delta(\vec{x})e^{-i\vec{k}\cdot\vec{x}}. \tag{1.41}$$

Then, the Fourier transform of the two-point correlation function $\xi(\vec{x}-\vec{y})$ is

$$\begin{aligned}\left\langle \tilde{\delta}(\vec{k})\,\tilde{\delta}^*(\vec{k}')\right\rangle &= \int d^3x\,e^{-i\vec{k}\cdot\vec{x}}\int d^3y\,e^{i\vec{k}'\cdot\vec{y}}\,\xi(\vec{x}-\vec{y}) = \\ &= \int d^3x\,e^{-i(\vec{k}-\vec{k}')\cdot\vec{x}}\int d^3\alpha\,e^{-i\vec{k}'\cdot\vec{\alpha}}\,\xi(\vec{\alpha})\end{aligned} \tag{1.42}$$

where we have defined the variable $\vec{\alpha} = \vec{x}-\vec{y}$. Then, switching the order of integration:

$$\begin{aligned}\left\langle \tilde{\delta}(\vec{k})\,\tilde{\delta}^*(\vec{k}')\right\rangle &= (2\pi)^3\,\delta_D^3(\vec{k}-\vec{k}')\int d^3\alpha\,e^{-i\vec{k}'\cdot\vec{\alpha}}\,\xi(\vec{\alpha}) = \\ &= (2\pi)^3\,\delta_D^3(\vec{k}-\vec{k}')\,P(k),\end{aligned} \tag{1.43}$$

where to avoid confusion with the density contrast, δ_D^3 is the Dirac Delta. $P(k)$ is the matter power spectrum, which only depends on the magnitude of its argument k, since the Universe is isotropic. The equation above indicates that the power spectrum is related to the variance of the distribution, that is to say, if there are lots of very under- and overdense regions, the power spectrum will be large, while if it is small, the distribution

is smooth. Also, notice that the different Fourier modes are uncorrelated. An example of a predicted dark matter power spectrum in shown in the left panel of Fig. 1.6.

In Eq. (1.43) and in (1.39) so far we have interpreted the angular brackets as averaging over all space, but it actually also means that we are averaging over all realizations of the density field. This is understood in the following way. The cosmic density field is one realization of a random process, in which, early on, every Fourier mode $\tilde{\delta}(\vec{k})$ was drawn randomly accordingly to some distribution. This distribution is usually assumed to be a *Gaussian random field*, which means that it will be proportional to $\exp\{-|\tilde{\delta}(\vec{k})|^2/(2P(k))\}$.

Assuming it was a Gaussian distribution is justified because most inflationary scenarios predict that the density fluctuations created by inflation were an isotropic and homogeneous Gaussian field, and besides that, there is no observation contradicting this so far. For instance, the cosmic microwave background probes fluctuations from the very early Universe, mostly in the linear regime, and they have been measured to be very Gaussian (seen in Fig. 1.2). However, non-linear structure formation at late times destroys Gaussianity and generates the filamentary cosmic web (seen in Fig. 1.5). Searching for primordial non-Gaussianities to probe departures from simple inflation is a very hot topic but no convincing evidence for primordial non-Gaussianities has yet been found. Also, if a Gaussian field is homogeneous and isotropic, then all its statistical properties are summed up in the power spectrum $P(k)$. For instance its variance in real space can be obtained from integrating it over all the Fourier modes, as seen below:

$$\begin{aligned}\sigma^2 \equiv \left\langle \delta^2(\vec{x}) \right\rangle &= \int \frac{d^3k}{(2\pi)^3} \int \frac{d^3k'}{(2\pi)^3} e^{i\,\vec{x}(\vec{k}-\vec{k}')} \left\langle \tilde{\delta}(\vec{k})\, \tilde{\delta}^*(\vec{k}') \right\rangle = \\ &= \int \frac{d^3k}{(2\pi)^3} P(k) = \int_0^\infty \frac{dk}{k} \frac{k^3 P(k)}{2\pi^2},\end{aligned} \tag{1.44}$$

where we have initially transformed both $\delta(\vec{x})$ and then used Eq. (1.43) to simplify. Thinking of the above integral as the sum over logarithmic bins in k: $d\ln(k) = dk/k$, in each bin, the contribution to the variance is given by the dimensionless combination $k^3P(k)/2\pi^2$. When this number is small, the fluctuations on the scale k are small, and since it is dimensionless, in particular it means that if it is approximately smaller than one, the fluctuations are linear, while if it is larger than one, the fluctuations have gone nonlinear. This is illustrated in the right panel of Fig. 1.6, where we compare the linear and nonlinear matter power spectrum, the later having been obtained with numerical simulations, as we will detail in the next section when we discuss non-linear evolution of the matter density field.

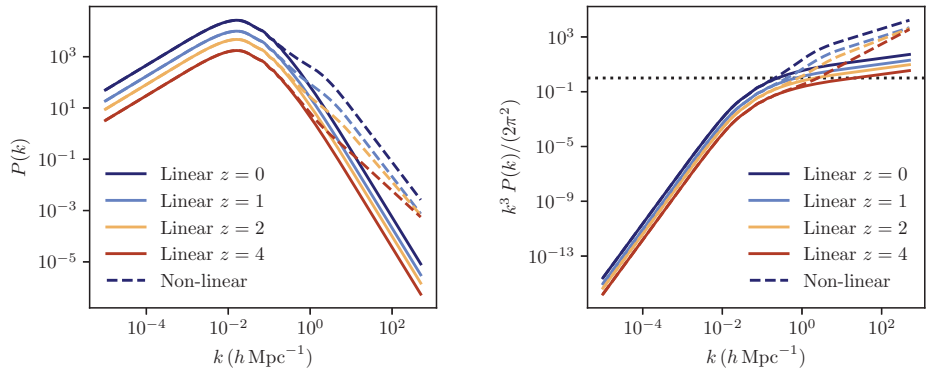

Figure 1.6: **Left:** The dark matter power spectrum, assuming DES Y1 best fit cosmological parameters (DES Collaboration, 2018b). Solid lines show the linear power spectrum while dashed lines show the non-linear power spectrum obtained with `Halofit` (Takahashi et al., 2012) . **Right:** Dimensionless parameter which is less than one where the Universe is smooth and more than one where the density has gone non-linear, at small scales. The dotted line indicates unity to make this comparison, which is the point at which the linear and non-linear power spectrum start to differ.

Smoothed density fields

The power spectrum is theoretically determined when knowing the composition and expansion of the Universe except for an overall normalization. One way to measure the normalization of the power spectrum is by considering density fluctuations on a given sphere, since in practice it is impossible to measure the density perturbation $\delta(\vec{x})$ at a particular point. Thus, we replace the density field $\delta(\vec{x})$ by a smoothed field,

$$\delta(\vec{x}) = \int d^3\vec{x}'\, W(\vec{x}')\delta(\vec{x}+\vec{x}'), \tag{1.45}$$

where $W(\vec{x}')$ is a window function. The most common window function is a spherical top-hat of radius R: $W_R(r) = 3/(4\pi R^3)$ for $r < R$ and $W_R(r) = 0$ for $r > R$. The Fourier transform of this particular window function is $\tilde{W}_R(kR) = 3j_1(kR)/(kR)$, where $j_1(kR)$ is the spherical Bessel function of the first kind of order one. As we did before, the dispersion of a smoothed density with this window function W_R field is then

$$\sigma_R^2 \equiv \left\langle \delta_R^2(x) \right\rangle = \frac{1}{2\pi^2} \int k^2 P(k)\, |\tilde{W}(kR)|^2 dk. \tag{1.46}$$

The case $R = 8$ Mpc/h, using the Fourier transform of the top-hat as the window function, defines the cosmological parameter σ_8:

$$\sigma_8^2 = \frac{1}{2\pi^2} \int k^2 P(k) \left[\frac{3j_1(kR)}{kR}\right]^2 dk, \tag{1.47}$$

which is used to provide the normalization of the power spectrum. The relative fluctuations of the galaxy number density in the local Universe are of order unity if one considers spheres of radius $R = 8$ Mpc/h, which is the typical scale of massive galaxy clusters. If one assumes that galaxies accurately trace the underlying dark matter field, this observation would imply that the fluctuation $\delta(\vec{x})$, averaged over a scale of $R = 8$ Mpc/h, has a dispersion ~ 1. However, there is no guarantee that the galaxy number density field closely follows the dark matter distribution. One often summarizes our ignorance about the relative distribution of galaxies and dark matter in what we call the galaxy bias, which we describe in detail in Sec. 1.7.4. Therefore, the galaxy bias and σ_8 are highly degenerate parameters when we obtain cosmological parameters from the distribution of a sample of galaxies. From the latest Planck results, $\sigma_8 = 0.811 \pm 0.006$ (Planck Collaboration, 2018).

1.7.3 Evolution of the density field

The inflationary theory predicts the initial power spectrum of density fluctuations, referred to as the primordial power spectrum, to be

$$P_0(k) = A_s k^{n_s}, \tag{1.48}$$

which has a scale-invariant, power-law form, where A_s is the amplitude of the primordial power spectrum and n_s is called the *spectral index*, and has a favored value of close to one from observations and theory. From the latest Planck measurements, $n_s = 0.965 \pm 0.004$ (Planck Collaboration, 2018). Also, inflation predicts a spectral index that is smaller but very close to unity. The preferred primordial power spectrum, $P(k) \propto k$ is called the Harrison-Zeldovich spectrum (Harrison, 1970; Zeldovich, 1972). In Fig. 1.6, we can appreciate that the fluctuations grow with time, as at lower redshift the power spectrum is higher. We can understand how this initial spectrum evolves as the Universe expands and becomes more inhomogeneous using linear perturbation theory. This evolution is often quantified in terms of the transfer function $T(k, z)$, which connects the primordial power spectrum to the linear matter power spectrum today:

$$P(k, z) = T^2(k, z)\, P_0(k). \tag{1.49}$$

The transfer function depends on the contents of the Universe and is hence a function of the particular cosmological model, and therefore the power spectrum depends on the cosmological parameters. Just as an example, the position of the peak of the power spectrum is sensitive to the time when the universe reached matter-radiation equality, and hence is a probe of Ω_γ/Ω_m.

To study how large scale structure evolves with time, we need to know how small fluctuations in density grow in amplitude in the presence of a gravitational field. New-

tonian gravity is an adequate approximation of general relativity on scales well inside the Hubble radius or horizon ($d_H = c/H_0$) and when describing non-relativistic matter (for which the pressure P is much less than the energy density ρ). In particular, we can use the Newtonian treatment to describe sub-Hubble fluctuations for cold dark matter (CDM) and baryons after decoupling. Also, if the amplitude of fluctuations remains small ($|\delta| \ll 1$) we can use Newtonian linear perturbation theory to describe the evolution of δ (Peebles 1980). In this case, the matter density contrast which, given our assumptions is essentially the total energy density contrast $\rho = \rho_m$, is related to the 3D gravitational potential Φ via the Poisson equation in comoving coordinates,

$$\nabla^2\Phi(\vec{x},t) = \frac{4\pi G}{c^2}\bar{\rho}_m(t)\, a^2(t)\, \delta(\vec{x},t) \tag{1.50}$$

where the factor c^2 accounts for the fact that the density $\bar{\rho}_m$ is the mean energy in matter density, not the mass density. This equation reflects a battle between two effects. On the one hand, in an expanding universe the gravitational potential gets diluted. On the other hand, the energy fluctuations grow with time due to gravity attracting more matter around an already overdense region. For non-relativistic matter, the two effects balance and the gravitational potential remains constant with time. As we saw previously, the matter density scales as $\sim a^{-3}$ with the expansion. Thus, if non-relativistic matter is the dominant form of energy, the overdensity δ grows as a.

In general the winning effect will depend on the dominant form of energy in the Universe, which can be derived using other expressions still in the context of Newtonian gravity, such as the Euler equation. During the radiation-dominated epoch, dark matter density fluctuations grew only at a logarithmic rate, intuitively due to the high pressure of radiation. At late times, when the Universe is dominated by dark energy, the growth is suppressed as well, due to the accelerated expansion. In particular, if it is dominated by a cosmological constant, the matter fluctuations reach a constant fractional amplitude. Therefore, studying the history of growth of structures in the Universe gives us information about its composition as a function of time. Specifically, measuring the two-point correlation function or power spectrum of galaxies, which encapsulates this information, we can infer the cosmological parameters.

Non-linear evolution

When an overdense region reaches an overdensity of $\delta \sim 1$, its evolution can no longer be treated with a simple linear perturbation approach. This happens for instance in the process needed to form a galaxy. In ΛCDM, the formation of structures is hierarchical: first small structures are formed around peaks in the initial density field, collapsing into virialized dark matter halos, and larger structures form later, either from the accretion of mass in the neighborhood or from the merging of smaller halos. Over-

densities collapse to form a gravitationally bound dark matter halo when they exceed a given value for δ, known as the critical density δ_c, under the Spherical Collapse model (Press & Schechter, 1974; Mo & White, 1996). At the time this happened, even though cold dark matter (CDM) was able to form gravitationally bound structures, the temperature of baryonic matter was still too high to form bound objects from their own gravitational field. Then, baryonic matter falls into already formed dark matter halos by feeling their gravitational attraction, allowing for galaxy formation to happen.

The non-linear gravitational collapse of dark matter halos, the possible merging between them and the successive galaxy formation processes are so complicated that most predictions of the non-linear power spectrum are the result of large N-body simulations. The matter structures generated in the simulations are used to obtain fitting formulas for the non-linear power spectrum, as in e.g. Smith et al. (2003) and more recently Takahashi et al. (2012), such as the non-linear power spectrum shown in Fig. 1.6 for a given set of cosmological parameters.

1.7.4 Galaxy bias

Structure formation is dominated by the dark matter component, but we can only observe the galaxies directly. Therefore, we are interested in knowing the exact relation between baryonic matter (or galaxies) and dark matter. Galaxies are good tracers of the dark matter distribution since they live in dark matter halos, but they are not unbiased estimators of the dark matter distribution. This is because the galaxy formation laws are highly complex and non-linear. The statistical relationship between the galaxy and matter distribution is known as *galaxy bias*. The simplest model of biasing, called linear deterministic biasing, relates the matter density fluctuations δ to the galaxy fluctuations δ_g linearly through the galaxy bias b:

$$\delta_g = b\,\delta. \tag{1.51}$$

This relation translates into a connection between the galaxy and matter two-point correlation functions, or between the power spectra of galaxies and matter:

$$\xi_{gg}(r) = b^2 \xi_{\delta\delta}(r), \qquad P_{gg}(k) = b^2 P_{\delta\delta}(k). \tag{1.52}$$

The bias is expected to be linear and scale independent at large scales, where the density field is still in its linear evolution. However, in general it will be a function of scale and redshift, $b\,(r, z)$, or $b\,(k, z)$ in Fourier Space. The galaxy bias relates the amplitude of the fluctuations, which are generally larger for galaxies than for matter, since galaxies form at the peaks of the underlying dark matter distribution. In addition, the peaks of the two distributions can be at different locations, since there is also some stochasticity involved in the galaxy formation process. This difference is encapsulated in the *cross-*

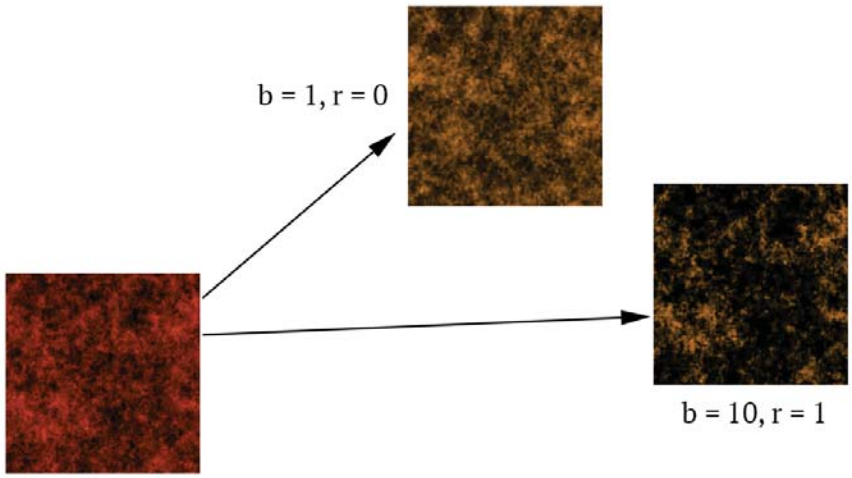

Figure 1.7: Illustration of the galaxy bias b and cross-correlation coefficient r between distributions. When $r = 0$, the peaks of the distribution are not correlated, and when the bias is large, the peaks of the distribution are much more pronounced.

correlation coefficient r, which in general will also depend on scale and redshift:

$$r = \frac{\xi_{\delta g}}{\sqrt{\xi_{\delta\delta}\,\xi_{gg}}}, \qquad r = \frac{P_{\delta g}}{\sqrt{P_{\delta\delta}\,P_{gg}}}, \tag{1.53}$$

where $\xi_{\delta g}$ is the galaxy-matter cross-correlation function, which is then related to the matter correlation function in the following way, and analogously for the power spectra:

$$\xi_{\delta g} = b \cdot r\,\xi_{\delta\delta}, \qquad P_{\delta g} = b \cdot r\,P_{\delta\delta}. \tag{1.54}$$

In Fig. 1.7 we show two distributions which are not correlated with each other ($r = 0$), and two distributions which are completely correlated ($r = 1$). In there we can also appreciate the effect of the bias between two distributions: when the bias is large, for instance in the figure $b = 10$, only the most pronounced peaks of the distribution are sampled while when $b = 1$, the amplitude of the fluctuations is the same in both distributions.

On large enough scales, we expect the galaxy and matter distributions to trace the same structures and hence the cross-correlation coefficient to approach unity. Therefore, due to the different dependencies on the galaxy bias, measuring both the galaxy and the galaxy-matter correlation functions we will be able to break degeneracies between the galaxy bias and the matter two-point correlation function, which encloses the cosmological information. In order to measure the galaxy two-point correlation function it is enough to measure the position of a large sample of galaxies. To probe

the galaxy-matter cross-correlation function though, we need to probe matter directly, which cannot be done by just measuring galaxy positions. Instead, we will need to use a technique called weak gravitational lensing, that will allow us to probe the matter distribution directly, and which we describe in detail in the following chapter.

Chapter 2

Weak Gravitational Lensing

As we saw in previous sections, from general relativity we learned that the mass content in the universe shapes its metric, with massive bodies curving the space-time canvas around them. Gravitational lensing is caused by light traveling in such a curved space time, according to some gravitational potential, as illustrated in Fig. 2.1. Light from distant galaxies is bent as it passes close to massive objects. In some cases, the bending of the light is so significant that multiple images of the galaxy are actually formed. This is referred to as strong gravitational lensing. In other cases, this bending is small, and the images of galaxies are distorted, stretched and magnified in small amounts. This is referred to as weak gravitational lensing. In this section we will develop the weak lensing formalism, deriving the equations that describe the deflection of light rays in the presence of massive bodies, introducing the concept of shear and the relevant quantities that are used throughout this thesis.

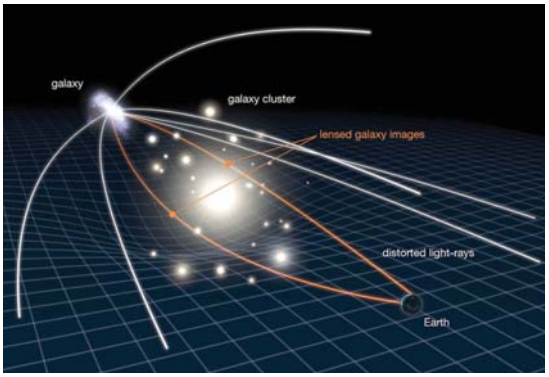

Figure 2.1: Illustration of the gravitational lensing effect: light from a background galaxy is bent when going through a foreground mass distribution, in this case a galaxy cluster.

2.1 Light propagation and the deflection angle

Photons propagate on null geodesics, $ds^2 = 0$. That means that the time of light ray travel can be obtained from the metric equation (1.4), which we described at the beginning of the previous chapter. In general relativity and for weak gravitational fields

($\Phi/c^2 \ll 1$), we obtain:

$$t = \frac{1}{c}\int \left(1 - \frac{2\Phi}{c^2}\right) dr, \tag{2.1}$$

where the integral is along the light path in physical coordinates r. Then, we can do an analogy between the gravitational potential and a medium with variable refractive index $n = 1 - 2\Phi/c^2$. Actually, this is the origin of the name of gravitational lensing. After that, we can use Fermat's principle that says that the light travels by the minimum-time path, $\delta t = 0$. Therefore, we get the Euler-Lagrange equations for the refractive index. Integrating these equations along the light path one can obtain the expression for the *deflection angle* $\hat{\alpha}$, that is the difference between the directions of the emitted and received light rays, illustrated in Fig. 2.2:

$$\hat{\alpha} = -\frac{2}{c^2}\int \nabla^p_\perp \Phi dr. \tag{2.2}$$

The gradient of the potential is taken perpendicular to the light path, with respect to physical coordinates. As it stands, this equation for the deflection angle is not very useful, as we would have to integrate over the actual light path, which is unknown. However, since $\Phi/c^2 \ll 1$, we expect the deflection angle to be small. Then, we can adopt the *Born approximation* and integrate over the unperturbed light path, as illustrated in Fig. 2.3. Considering a point-like body of mass M whose gravitational potential is $\Phi = -GM/r$, and using the Born approximation, the deflection angle reduces to:

$$\hat{\alpha} = \frac{4GM}{bc^2}, \tag{2.3}$$

where b is the distance of closest approach to the lens, called impact parameter. This result assuming general relativity gives twice the classical prediction for the deflection angle using Newtonian dynamics. This factor of two comes from the fact that the perturbed Minkowski metric has equal perturbations in both its temporal and spatial components. In 1919, a team led by Franck Watson Dyson and Arthur Eddington, proved that general relativity gave the correct factor by measuring the change in position of stars as their light passed near the sun during a solar eclipse.

We can now consider another particular case of a single lens, but extended in the transverse direction (perpendicular to the line of sight). This extension is still much simpler than a general gravitational potential but realistic enough in a wide number of cases. For instance even in the case of lensing by galaxy clusters, the physical size of the lens is generally much smaller than the distances between observer, lens and source. The deflection therefore arises along a very short section of the light path, and we can adopt the so-called *thin lens approximation*, where the distribution of matter is assumed to be in the *lens plane*. Within this approximation, the lens matter distribution is fully

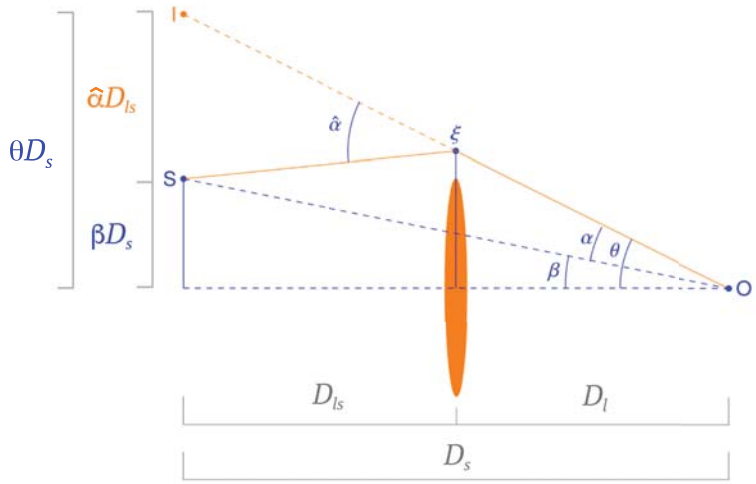

Figure 2.2: Sketch of a gravitational lens system from Bartelmann & Maturi (2017). The optical axis runs from the observer O through the center of the lens. The angle between the source S and the optical axis is β, the angle between the image I and the optical axis is θ. The light ray towards the image is bent by the deflection angle $\hat{\alpha}$, measured at the lens. The reduced deflection angle α is measured at the observer.

described by its *surface density*,

$$\Sigma(\vec{\xi}) = \int \rho(\vec{\xi}, z)\, dz, \tag{2.4}$$

where $\vec{\xi}$ is a two-dimensional vector on the lens plane, also illustrated in Fig. (2.2), and ρ is the three-dimensional density. As long as the thin lens approximation holds, the total deflection angle is obtained by summing the contribution of all the mass elements $\Sigma(\vec{\xi})d^2\vec{\xi}$:

$$\hat{\vec{\alpha}}(\vec{\xi}) = \frac{4G}{c^2} \int \frac{(\vec{\xi} - \vec{\xi}')\Sigma(\vec{\xi}')}{|\vec{\xi} - \vec{\xi}'|^2} d^2\vec{\xi}' \tag{2.5}$$

2.1.1 The lens equation

Figure 2.2 illustrates a thin-lens system. Although not obvious from the figure, the angles have both an amplitude and a direction. The amplitude describes how the incoming ray is tilted with respect to the z-axis, where the line connecting the observer to the center of the lens is chosen to be the z-axis, or optical axis. The directions of the angles specify the locations in the plane perpendicular to the line of sight, the plane of the sky. Thus, the source S tranverse position in the $z = D_s$ plane is given by $D_s\,\vec{\beta}$ and the image position is given by $D_s\,\vec{\theta}$, where D_s is the angular diameter distance to the source. Looking at the diagram and assuming the angles are small, we can relate these

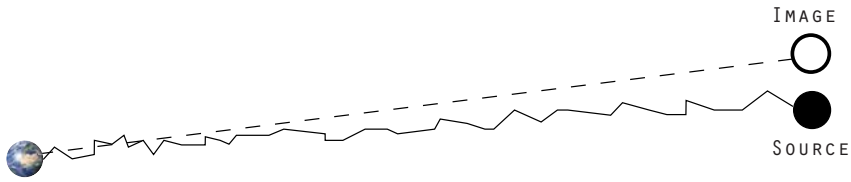

Figure 2.3: Born approximation visualization. The true path taken by the light from the source at position $\vec{\beta}$, curved because of gravitational lensing by the structure along the line of sight, compared to the line back to the image inferred from the arrival direction $\vec{\theta}$. The Born approximation is sufficient for most applications.

two positions to the deflection angle $\hat{\vec{\alpha}}$ through the so-called *lens equation*

$$D_s\,\vec{\beta} = D_s\,\vec{\theta} - D_{ls}\,\hat{\vec{\alpha}}, \tag{2.6}$$

where D_{ls} is the angular diameter distance between the lens and the source (note angular diameter distances are not additive). As Fig. 2.2 shows, the lens equation is trivial to derive and only requires that the following Euclidean relation should exist between the angle enclosed by two lines and their separation: separation = angle $\times$ distance. It is not obvious that the same relation should also hold in curved spacetimes. However, angular diameter distances are defined exactly so that this relation holds (see Sec. 1.6.1), and thus the lens equation holds. Dividing by D_s and introducing the reduced deflection angle:

$$\vec{\alpha}(\vec{\theta}) \equiv \frac{D_{ls}}{D_s}\hat{\vec{\alpha}}(\vec{\theta}) \tag{2.7}$$

leads to the lens equation in its simplest form:

$$\vec{\beta} = \vec{\theta} - \vec{\alpha}(\vec{\theta}), \tag{2.8}$$

which actually hides quite a bit of complexity: the mapping from lens coordinates $\vec{\theta}$ to source coordinates $\vec{\beta}$ may be non-linear and have multiple solutions (only in the strong lensing regime) so that a given single point source at $\vec{\beta}$ has multiple images $\vec{\theta}$.

2.1.2 Lensing potential

Still in the context of the thin-lens approximation, an extended distribution of matter is characterized by its effective lensing potential, obtained by projecting the three-dimensional potential along the $z-$axis (notice here z does *not* refer to the redshift, but to the physical coordinate z of the line of sight):

$$\psi(\vec{\theta}) = \frac{2}{c^2}\frac{D_{ls}}{D_l D_s}\int \Phi(D_l\vec{\theta}, z)\,dz. \tag{2.9}$$

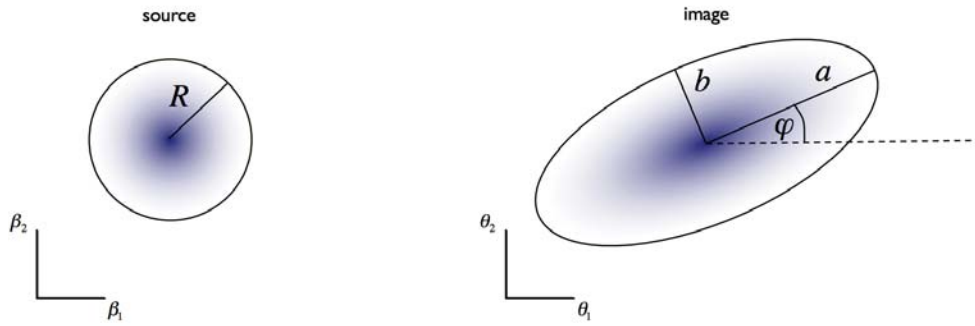

Figure 2.4: Mapping between the source coordinates $\vec{\beta}$ and the image coordinates $\vec{\theta}$ described by the Jacobian matrix A, via the convergence and the shear.

From the equation above we can learn in which cases the effect of gravitational lensing will be stronger. The contribution to Φ from inhomogeneities close to the source is suppressed by the D_{ls} factor and when the angular distance to the lens is similar to the angular distance between the lens and the source the effect will be larger. Also, in the equation above we are using again the Born approximation, since we are integrating the potential along the line of sight between the apparent position $D_l\vec{\theta}$ and us, not along the path the light actually traveled, as illustrated in Fig. 2.3. More generally, if the potential is constant across the sky, there is no deflection. Lensing emerges then from changes in the projected gravitational potential across the sky. Mathematically, this is expressed by the gradient of the lensing potential, which yields the deflection angle $\vec{\alpha}$:

$$\vec{\alpha}(\vec{\theta}) = \vec{\nabla}_{\vec{\theta}}\psi. \tag{2.10}$$

Moreover, the Laplacian of the potential is proportional to the surface-mass density at the lens plane position $D_l\vec{\theta}$ via the Poisson equation:

$$\nabla^2_{\vec{\theta}}\psi = \frac{\Sigma(D_l\vec{\theta})}{\Sigma_{\text{crit}}} \equiv 2\kappa(\vec{\theta}), \tag{2.11}$$

where we have defined the dimensionless parameter κ, called *convergence*, and the geometrical factor

$$\Sigma_{\text{crit}} = \frac{c^2}{4\pi G}\frac{D_s}{D_l D_{ls}}, \tag{2.12}$$

also called *critical surface mass density*.

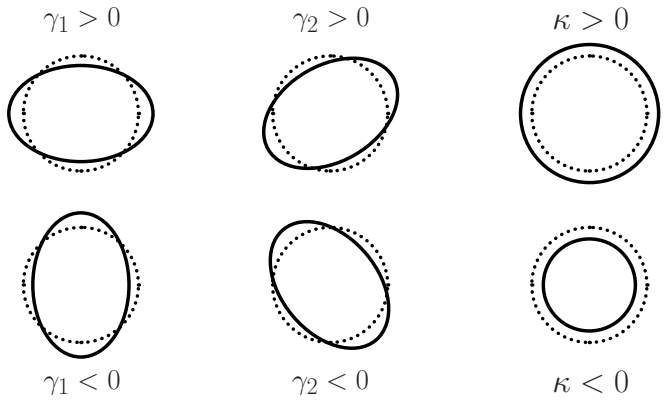

Figure 2.5: The effects of the elements of the Jacobian matrix shear $\gamma = (\gamma_1, \gamma_2)$ and convergence κ on an initially circular background object (dotted circles).

2.2 Linearised lens mapping: Shear and magnification

Using Eq. (2.10), the lens equation (2.8) can be written in terms of the lensing potential in the following way:

$$\vec{\beta} = \vec{\theta} - \vec{\nabla}\,\psi. \tag{2.13}$$

If the extent of a source is much smaller than the scale of variation in the deflection angle, we can linearise the lens equation by defining the *Jacobian matrix* A and Taylor expanding the lens equation:

$$\delta\vec{\beta} \approx A\delta\vec{\theta} \tag{2.14}$$

with A having the components

$$A_{ij} = \frac{\partial\beta_i}{\partial\theta_j} = \delta_{ij} - \frac{\partial\alpha_i}{\partial\theta_j} = \delta_{ij} - \partial_i\partial_j\psi, \tag{2.15}$$

where the partial derivatives are with respect to $\vec{\theta}$. This matrix describes the linear mapping between the lensed, $\vec{\theta}$, and the unlensed, $\vec{\beta}$, coordinates. In the absence of a lensing potential, the lens mapping is simply identity. In the presence of a lens, the local properties of the lens mapping are determined by the curvature of the lensing potential, expressed by the matrix of second derivatives of ψ. Moreover, for the physical interpretation of the Jacobian matrix, it is convenient to parametrize it in terms of the two-component shear field $\gamma \equiv \gamma_1 + i\gamma_2 = |\gamma|e^{2i\varphi}$ (see Fig. 2.4 for an illustration of

φ) and the scalar convergence κ as

$$A = \begin{pmatrix} 1-\kappa-\gamma_1 & -\gamma_2 \\ -\gamma_2 & 1-\kappa+\gamma_1 \end{pmatrix}. \tag{2.16}$$

That means that the shear and the convergence can be expressed as second derivatives of the lensing potential ψ:

$$\begin{aligned} \kappa &= \frac{1}{2}(\partial_1\partial_1 + \partial_2\partial_2)\psi = \frac{1}{2}\nabla^2\psi \\ \gamma_1 &= \frac{1}{2}(\partial_1\partial_1 - \partial_2\partial_2)\psi \\ \gamma_2 &= \partial_1\partial_2\psi, \end{aligned} \tag{2.17}$$

as we had already anticipated for the convergence in Eq. (2.11). We can also rewrite A as

$$A = (1-\kappa)\begin{pmatrix} 1 & 0 \\ 0 & 1 \end{pmatrix} - |\gamma| \begin{pmatrix} \cos(2\varphi) & \sin(2\varphi) \\ \sin(2\varphi) & -\cos(2\varphi) \end{pmatrix}, \tag{2.18}$$

where we can see that the $(1-\kappa)$ term only affects the size and not the shape of the observed image. Thus, the convergence quantifies the isotropic change in size of the source image and the shear quantifies an anisotropic stretching, that is a change in shape of the image, turning a circle into an ellipse, as illustrated in Fig. 2.5.

The Jacobian matrix actually tells us the inverse of what we typically want to know from weak gravitational lensing, that is going from source coordinates to lensed coordinates. To obtain this other mapping, if A has a non-zero determinant, we can invert it:

$$\delta\vec{\theta} \approx A^{-1}\delta\vec{\beta}. \tag{2.19}$$

The Jacobi determinant is

$$\det A = (1-\kappa)^2 - |\gamma|^2 \approx 1 - 2\kappa \tag{2.20}$$

with $|\gamma|^2 = \gamma_1^2 + \gamma_2^2$, where the last approximation is only valid in the weak lensing regime with $\gamma, \kappa \ll 1$. Thus, we can assume that in the weak lensing regime the linear lens mapping is invertible and that the inverse of the Jacobian matrix is

$$A^{-1} = \frac{1}{\det A}\begin{pmatrix} 1-\kappa+\gamma_1 & \gamma_2 \\ \gamma_2 & 1-\kappa-\gamma_1 \end{pmatrix} \tag{2.21}$$

The overall factor in this expression indicates that the solid angle spanned by the image is changed compared to the solid angle covered by the source by the *magnification* factor

μ:

$$\mu = \frac{1}{detA} = \frac{1}{(1-\kappa)^2 - |\gamma|^2} \approx 1 + 2\kappa, \tag{2.22}$$

where again the last approximation only holds in the weak lensing regime. Thus, in weak lensing, the magnification of an image is essentially determined by the convergence, not by the shear.

Regarding the shape distortions produced by the shear, a hypothetical circular source is deformed to become an ellipse whose semi-major and semi-minor axes, a and b respectively, illustrated in Fig. 2.4, are proportional to the eigenvalues $\lambda_\pm$ of the inverse Jacobi matrix A^{-1}:

$$\lambda_\pm = \frac{1 - \kappa \pm |\gamma|}{\det A} = \frac{1}{1 - \kappa \mp |\gamma|}. \tag{2.23}$$

Then, the image *ellipticity* ϵ of an originally circular source is:

$$\epsilon \equiv \frac{a-b}{a+b} = \frac{\lambda_+ - \lambda_-}{\lambda_+ + \lambda_-} = \frac{\gamma}{1-\kappa}. \tag{2.24}$$

The equation above shows that the ellipticity is determined by the *reduced shear* quantity, which involves both the shear and the convergence:

$$g \equiv \frac{\gamma}{1-\kappa}. \tag{2.25}$$

Then, since galaxy shear measurements are based on the measurement of galaxy shapes (ellipticities) because we cannot observe the source prior to lensing, the relevant quantity is the reduced shear g rather than the shear itself. Thus, from galaxy shapes measurements we can only obtain information on the reduced shear. If $\kappa \ll 1$, which is generally the case for weak lensing, then the reduced shear is a good approximation to the shear.

In the expressions above we have been considering an originally circular source to understand the effect of weak lensing in the shapes of galaxies. However, in general the source will have some intrinsic ellipticity ϵ^s. In that case, the general expression for the relation between shear and ellipticity is given by

$$\epsilon = \frac{\epsilon^s + g}{1 + g^* \epsilon^s}, \tag{2.26}$$

where the asterisk denotes complex conjugation. When $\epsilon^s = 0$, it reduces to Eq. (2.24). Also, note that this expression depends on the convention used to define the ellipticities. There are two common conventions used in weak lensing, which lead to different relations between the ellipticity and the reduced shear. The expression above corresponds to the same convention used in Eq. (2.24) and in Section 2.3 in Eqs. (2.28).

So far we have looked at the effect shear and magnification produce on the source images. Now we turn into general procedures used to estimate these quantities with photometric surveys. Magnification is in general much harder to measure than shear. In very short terms, this is because the intrinsic galaxy size cannot be averaged out as it can be done with the intrinsic ellipticities of the galaxies. The result is that to get a significant measurement of magnification, one has to beat much more noise than for shear. As a result, up until this moment most of the weak lensing studies, and in particular this thesis, use shear as the main observable. Thus, in the following sections we will focus on describing how to measure shear specifically.

2.3 Measurement of galaxy shapes and estimation of shear

The ellipticity can be quantified in terms of moments of the surface brightness. The surface brightness I is defined as the flux of energy per unit time per unit area per solid angle, so has units of Energy Time^{-1} Length^{-2} steradian^{-1} and is conserved in gravitational lensing processes. The quadrupole moments Q_{ij} of the surface brightness are

$$Q_{ij} = \int d^2\theta \, I(\vec{\theta})\theta_i\theta_j, \qquad i,j = 1,2. \tag{2.27}$$

From these moments we can measure the two components of the ellipticity:

$$\epsilon_1 = \frac{Q_{11} - Q_{22}}{2N_Q}, \qquad \epsilon_2 = \frac{Q_{12}}{N_Q}, \qquad N_Q \equiv \frac{1}{2}\mathrm{tr}Q + \sqrt{\det Q}. \tag{2.28}$$

Measuring ellipticities of distant galaxies is a highly non-trivial task. There are several algorithms dedicated to this, with very different approaches. In the following chapter we will describe some of the most commonly used techniques in surveys such as the Dark Energy Survey. But for now, assuming we have a good method to measure the ellipticities, how can we go from these observables to quantities with cosmological information such as the shear? The galaxy sources typically used in weak lensing measurements are of course not circular, but intrinsically elliptical. Taking the weak lensing limit of Eq. (2.26), the intrinsic source ellipticity ϵ^s and the ellipticity caused by gravitational lensing can be added:

$$\epsilon \approx \epsilon^s + \gamma. \tag{2.29}$$

If the intrinsic ellipticities of the galaxies are randomly aligned, the mean of the observed ellipticity is an unbiased estimator of the shear, since $\langle \epsilon^s \rangle = 0$,

$$\langle \epsilon \rangle \approx \gamma. \tag{2.30}$$

In practice, this estimator is biased by the presence of *intrinsic galaxy alignment*, which happens when the shapes of galaxies are correlated in the absence of gravitational lensing, due to gravitational interactions between galaxies. Because galaxy ellipticities are no longer randomly oriented, intrinsic alignments can add an excess of correlation between the galaxy shapes that can bias the results.

Then, in the weak lensing regime, the shear cannot be estimated for a single galaxy. This is because the typical value of the shear will usually not be larger than $\gamma \sim 0.01$, much smaller than the typical intrinsic ellipticity RMS $\sigma_{\epsilon^s} = \left\langle |\epsilon|^2 \right\rangle^{1/2} \approx 0.2$ (Bartelmann & Maturi 2017). The noise due to intrinsic ellipticities is usually referred to as *shape noise*. The S/N for a given lens would hence be:

$$\frac{S}{N} = \frac{\gamma}{\sigma_{\epsilon^s}} \sqrt{N_s}, \tag{2.31}$$

so it scales with the square root of the number of source galaxies N_s used to estimate the shear. Thus, in general weak lensing relies on shape measurements for a large number of background galaxies in order to beat down the noise.

Observationally, there are other effects different from gravitational lensing that can alter the shape of galaxies when they are detected. Effectively, galaxy images are also convolved by a kernel, known as the Point Spread Function (PSF), which describes the response of the telescope to a point-like source. If the PSF is isotropic, it will make galaxies look rounder, hence erasing the shear effect, while an ansitropic PSF will directly contaminate the shear signal by making galaxies look more elongated in the direction of the anisotropy. Therefore, we also need to deconvolve the effect of the PSF on the galaxy images to recover an unbiased estimate of the shear.

2.3.1 Spherical Distribution: Tangential and Cross Components of the Shear

The shear components γ_1 and γ_2 are defined relative to a reference Cartesian coordinate frame. However, because of the way background galaxies are distorted by a foreground mass, it is useful to consider the shear components in a rotated reference frame. For example, in the case of a *spherical distribution* of matter, the shear at any point will be oriented tangentially to the direction toward the center of symmetry as can be seen in a real image in Fig. 2.6, where a massive cluster is bending the light of galaxies behind it. The lensed images, in some cases arcs, form in this tangential way because of the spherical symmetry, and also because the light passing closer to the lens gets more deflected, as illustrated in Fig. 2.7. This *tangential* pattern expected by gravitational lensing for a circularly-symmetric matter distribution is also depicted in the left part of Fig. 2.8.

Then, for a given lens-source pair of galaxies it is useful to define the *tangential* and

Figure 2.6: The massive foreground cluster (Abell 1689) causes the images of the background galaxies to be distorted, forming arcs, due to strong gravitational lensing. The arcs are tangentially aligned, and so their ellipticity is oriented tangent to the direction of the foreground mass, in this case the cluster. Image taken with the Advanced Camera for Surveys on board the Hubble Space Telescope. Credits: NASA.

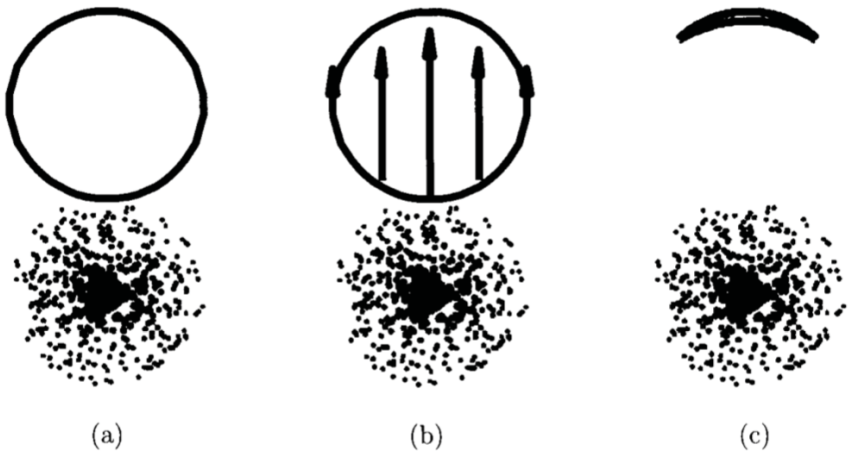

Figure 2.7: (a) The source circular galaxy is behind a foreground mass distributions (points). (b) The light from the source galaxy is bent as it goes by the mass distribution. The rays passing closer to the lens get more deflected. (c) Resulting image is an arc, similar to those observed in Fig. 2.6. From Dodelson (2003).

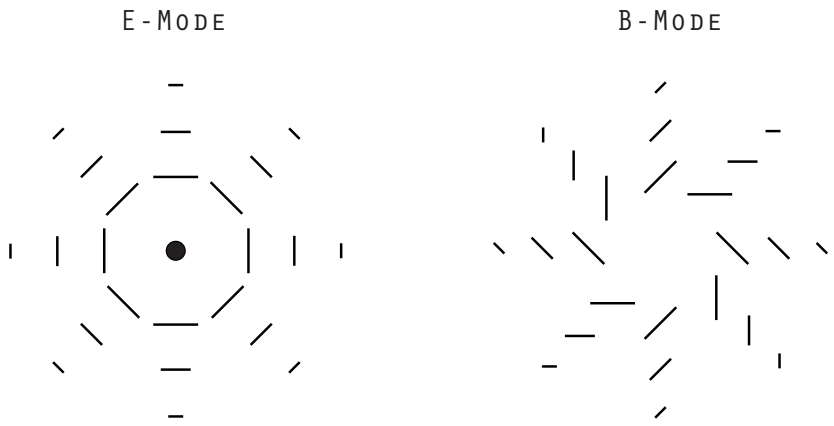

Figure 2.8: **Left panel:** The shear pattern around a point mass. All shears are oriented perpendicular to the line connecting with the center, and therefore are *tangential*. All the signal from galaxy-galaxy lensing is captured by this component, and thus is referred as E-mode. **Right panel:** Cross shear pattern that cannot be produced by gravitational lensing, neither by overdensities nor by underdensities. That is why it is also referred to as B-mode. If this pattern is detected at levels above the noise, it indicates there could be a systematic problem affecting the data. The pattern of the cross-component corresponds to rotating the shears from the left diagram by 45 degrees.

cross components of the shear

$$\gamma_t = -\mathrm{Re}\left[\gamma e^{-2i\phi}\right],\ \gamma_\times = -\mathrm{Im}\left[\gamma e^{-2i\phi}\right], \tag{2.32}$$

where ϕ is the position angle of the source galaxy with respect to the horizontal axis of the cartesian coordinate system, centered at the lens galaxy, as represented in Fig. 2.9. This can be expanded to yield

$$\begin{aligned} \gamma_t &= -\gamma_1 \cos(2\phi) - \gamma_2 \sin(2\phi) \\ \gamma_\times &= \gamma_1 \sin(2\phi) - \gamma_2 \cos(2\phi). \end{aligned} \tag{2.33}$$

The tangential component will capture all the gravitational lensing signal produced by a spherically symmetric distribution of mass, while the cross-component of the shear $\gamma_\times$ vanishes if the mass distribution is spherically symmetric. Both components are represented in Fig. 2.8. In there we can see that the cross-component has a curl pattern, something that cannot be produced by a scalar field such as the convergence κ. That is why, making an analogy with electromagnetism, where the magnetic field is the gradient of a scalar field and the magnetic field is the curl of a vector field, this cross pattern is sometimes called the B-mode, and the tangential component is usually called the E-mode. Therefore, $\gamma_\times$ can be used as a null test, a diagnostic to check the measurement is free of systematics.

It should also be noted that, like the cartesian components, the tangential and cross-components of the shear cannot be observed for a single galaxy, but they can only be measured for a large number of lens-source pairs, after averaging out the random component of the intrinsic ellipticity of the galaxies. Thus, in order to perform these measurement, we actually need to project the ellipticity for each source galaxy to the tangential or cross component for each lens-source pair, which can be defined in full analogy to the shear, and then average over all the pairs. The tangential shear measurement is one of the main observables of galaxy-galaxy lensing, described in the following section.

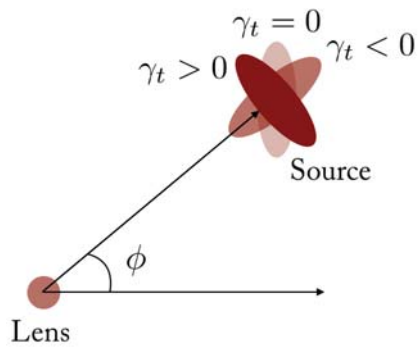

Figure 2.9: Illustration of the tangential component of the shear of a source galaxy with respect to a lens position, on the plane of the sky. If $\gamma_t > 0$ it is produced by an overdensity and if $\gamma_t < 0$, by an underdensity.

To better understand the physical interpretation of the tangential shear measurement, the deflection angle from a spherically symmetric distribution is equal to (Dodelson, 2017)

$$\vec{\alpha}(\vec{\theta}) = \frac{\vec{\theta}}{\theta^2} \frac{M(\theta)}{\pi D_l^2 \Sigma_{\rm crit}} \tag{2.34}$$

where $M(\theta)$ is the mass enclosed within a cylinder of angular radius θ. Obtaining the Cartesian shear components γ_1 and γ_2 by deriving the deflection angle with respect to the image position $\vec{\theta}$, as given in Eq. (2.15), we can then rotate them to the tangential projection:

$$\gamma_t(\theta) = -\frac{\theta}{2\pi D_L^2 \Sigma_{\rm crit}} \frac{\partial}{\partial \theta} \left[\frac{M(\theta)}{\theta^2} \right], \tag{2.35}$$

which is the tangential shear in an annulus with radius θ produced by a spherical mass distribution. Performing the derivative we obtain

$$\gamma_t(\theta) = \bar{\kappa}(\leq \theta) - \kappa(\theta), \tag{2.36}$$

where κ is the surface density divided by the critical surface mass density $\Sigma_{\rm crit}$, as given in Eq. (2.11) and $\bar{\kappa}$ is the average of the convergence within the angular radius θ. If we multiply the expression above by the critical surface mass density we obtain the definition for the *surface mass excess* $\Delta\Sigma$:

$$\Delta\Sigma \equiv \gamma_t(\theta)\Sigma_{\rm crit} = \bar{\Sigma}(< \theta) - \Sigma(\theta), \tag{2.37}$$

which is a slightly more physical quantity.

2.4 Galaxy-galaxy lensing

Galaxy-galaxy lensing (GGL) measures the effect some foreground galaxies (lenses) have on the shapes that we see of some other background galaxies (sources) due to the foreground galaxy masses, dominated by their dark matter halos. Since it is a correlation between the shear of the source galaxies and the position of the lens galaxies, it is sometimes referred as *galaxy-shear* correlation. The distortions in the shapes of the background galaxies can be plotted as a function of their projected distance from the center of a foreground galaxy. The density profile of the galaxy, including all its mass, affects the shape of this shear vs. distance curve. Therefore, galaxy-galaxy lensing is a powerful way to probe the relation between the mass and the luminosity of galaxies, i.e. between dark and baryonic matter. The tangential component of the shear, described in the previous section, measured as a function of scale is one of the main observables of galaxy-galaxy lensing. The tangential shear measurement is obtained by grouping pairs of foreground and background galaxies by the angular separation θ between them, measuring the tangential component of the ellipticity of the source galaxies for each lens-source pair and finally averaging this tangential component in each angular bin.

The first attempt to detect such a galaxy-galaxy lensing signal was reported in Tyson et al. (1984), but the observational results of their study were inconclusive. A few years later, Brainerd, Blandford & Smail (1996) presented the first detection and analysis of galaxy-galaxy lensing. Since then, several surveys have measured this effect, including the Dark Energy Survey, for instance with the tangential shear measurements presented in this thesis.

Another galaxy-galaxy lensing estimator is the surface mass excess $\Delta\Sigma$, defined in Eq. (2.37). If we wanted to estimate $\Delta\Sigma$ for large separations between the lens and the source galaxies, for instance much larger than the visible part of the foreground galaxy, which usually extend up to 5–10 kpc, we could assume the signal is produced by a point mass (if all the mass of the galaxy was contained in the visible part). For a point mass, $\Sigma(\theta)$ is zero everywhere except at the origin, thus

$$\Delta\Sigma_{\text{point mass}}(R) = \frac{M}{\pi R^2}. \tag{2.38}$$

Then for a point mass the signal falls as R^{-2}, where R is the projected distance between the lens and the source galaxy. If we consider that a dark matter halo with an isothermal profile $\rho \propto r^{-2}$ surrounds the visible part of the galaxy, the point mass approximation is no longer valid[1]. For an isothermal profile, $\Delta\Sigma$ has the following form:

[1] Usually r is used to refer to the 3D distance between galaxies and R to the projected one in the plane of the sky.

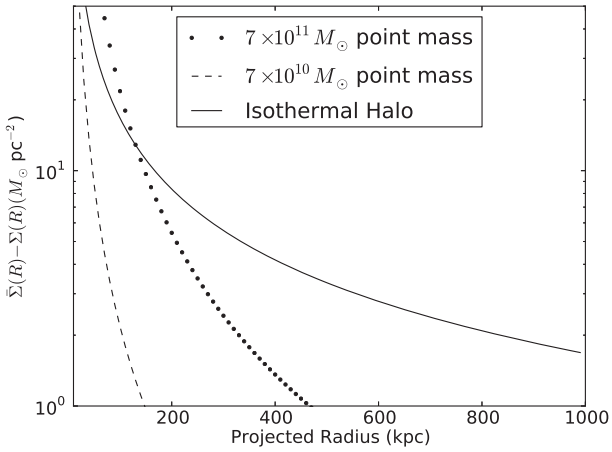

Figure 2.10: Predictions for the galaxy-galaxy lensing $\Delta\Sigma$ profile of background galaxies produced by a foreground galaxy as a function of the projected distance between the two, from Dodelson (2017). The point mass is meant to represent a galaxy with no dark matter and the isothermal halo one with a dark matter halo. The two values of the point mass correspond to the mass of the isothermal halo within 10 kpc ($7 \times 10^{10} M_\odot$) and 100 kpc ($7 \times 10^{11} M_\odot$). The two profiles are significantly different and observations only agree with the isothermal halo profile.

$$\Delta\Sigma_{\text{isothermal halo}}(R) = \frac{\sigma^2}{2GR}, \tag{2.39}$$

where σ is the velocity dispersion of the elements that comprise the distribution (stars in this case), which also serves as an indicator of the mass of the galaxy. In Fig. 2.10, we can see the difference in the two lensing signals. Current galaxy-galaxy lensing observations of galaxy profiles are not compatible with a point mass (Dodelson, 2017). Therefore, galaxy-galaxy lensing provides evidence for the existence of dark matter and can be used to test galaxy profiles.

Besides being a very sensitive probe to the relation between baryonic matter and dark matter, galaxy-galaxy lensing can also be used to constrain cosmological parameters in combination with other probes, as we describe in the following sections and put in practice in Part III of this thesis.

2.5 Cosmological weak lensing

In this section we want to relate weak lensing observables to cosmological parameters, in order to understand how we can extract cosmological information from measurements such as the tangential shear. We will also describe the relation between the tangential shear and other quantities such as the galaxy bias and show how we can model it.

2.5.1 Generalization of the lensing potential

First it is useful to generalize the lensing potential from Eq. (2.9) to extended lenses in redshift, i.e. beyond the thin-lens approximation, since this approximation is not appropriate to describe the lensing by the large-scale structures of the Universe. To achieve this, we only need to move the distance factors inside the integral and it will also be useful to convert the angular diameter distances we have been using so far to comoving distances. Doing these changes and assuming a flat universe, the lensing potential now reads as:

$$\psi(\vec{\theta}) = \frac{2}{c^2}\int_0^{\chi_s} \frac{\chi_s - \chi_l}{\chi_s \chi_l}\Phi'(\chi_l\vec{\theta}, \chi_l)\, d\chi_l, \tag{2.40}$$

where we have replaced the factor of angular diameter distances to:

$$\frac{D_{ls}}{D_l D_s} \longrightarrow (1+z_l)\frac{\chi_s - \chi_l}{\chi_s \chi_l}. \tag{2.41}$$

Notice that angular diameter distances are not additive since D_{ls} is defined as:

$$D_{ls} \equiv \frac{\chi_s - \chi_l}{(1+z_s)} \qquad \text{(Flat universe)} \tag{2.42}$$

in a flat universe. We also replaced the differential dz from Eq. (2.9), which was in proper distance, to $dz = 1/(1+z_l)d\chi$, using Eqs. (1.1) and (1.14). Also, notice the 3D Newtonian potential Φ is now a function of comoving distance and therefore has a different form than in Eq. (2.9) and is labeled as Φ'. Finally, even though here we are assuming a flat geometry for simplicity, the general reasoning of the rest of the section is still valid with non-zero curvature, replacing the above distance changes with general curvature ones and propagating them in every equation below.

2.5.2 Convergence as the projected matter density

Copying here again the 2-D Laplacian of the lensing potential (2.17) and the 3-D Poisson equation (1.50) in comoving coordinates,

$$\kappa = \frac{\nabla^2\psi}{2}, \qquad \nabla^2\Phi = \frac{4\pi G}{c^2}\bar{\rho}_m\, a^2\, \delta \tag{2.43}$$

and using the expression for the generalized lensing potential (2.40) and the one for the mean matter density

$$\bar{\rho}_m = \frac{3H_0^2}{8\pi G}\Omega_m a^{-3} \tag{2.44}$$

we can relate the convergence κ to the density contrast δ to obtain:

$$\kappa(\vec{\theta},\chi) = \frac{3H_0^2\Omega_m}{2c^2}\int_0^{\chi} d\chi' \frac{\chi'(\chi-\chi')}{\chi}\frac{\delta(\chi'\vec{\theta},\chi')}{a(\chi')}. \tag{2.45}$$

Then, we can think of the convergence κ as the 2D projected analogue of the matter overdensity δ, weighted by the lensing efficiency factor. For a redshift distribution of sources $n_z(z)dz = n_\chi(\chi)d\chi$, the convergence becomes:

$$\kappa(\vec{\theta}) = \int_0^{\chi_{\rm lim}} d\chi\, n_\chi(\chi)\,\kappa(\vec{\theta},\chi) = \frac{3H_0^2\Omega_m}{2c^2}\int_0^{\chi_{\rm lim}} d\chi\, g(\chi)\,\chi\,\frac{\delta(\chi\vec{\theta},\chi)}{a(\chi)}, \tag{2.46}$$

where $\chi_{\rm lim}$ is the limiting comoving distance of the source galaxy sample and $g(\chi)$ is the source-redshift weighted lens efficiency factor:

$$g(\chi) = \int_{\chi}^{\chi_{\rm lim}} d\chi'\, n_\chi(\chi')\,\frac{\chi'-\chi}{\chi'}, \tag{2.47}$$

which indicates the lensing strength of the combined source distribution at a distance χ.

In the equations above, it already becomes apparent that weak lensing quantities such as the convergence are directly related to the cosmological parameters which we defined in the previous chapter, and not only through the direct proportional factors from Eq. (2.45), but also through the relation between redshift and comoving distance hidden in the same equation, through the scale factor and density contrast. However, the convergence κ alone can only be measured directly through magnification, as seen in Eq. (2.22), and this is hard to accomplish. Instead, the shear is the main observable used in this thesis. However, deriving the equations for the convergence is simpler and later we will see they can be easily related to the ones of shear.

2.5.3 Projected densities for the foreground distribution

The tangential shear measurement is the cross-correlation between the positions of a foreground galaxy sample (usually projected in 2D) and the tangential component of the shear of a source galaxy sample, also projected in 2D. One of the goals of this section is to be able to relate the tangential shear measurement to cosmological parameters. To achieve that it will be useful to first consider the expressions for projected densities of the foreground galaxy sample, also simply called the *lenses*.

Consider a population of lens galaxies with a spatial number density $n(\vec{\chi})$. The number density of these galaxies on the sky at $\vec{\theta}$ is then $N(\vec{\theta}) = \int d\chi\,\nu(\chi)\,n(\chi\vec{\theta})$, where $\nu(\chi)$ is the selection function, describing which fraction of galaxies at comoving distance χ are included in the sample. In addition, $\nu(\chi)$ accounts for the fact that for

large distances, only the more luminous galaxies will be in the observed galaxy sample, among other effects (Schneider, Kochaneck & Wambsganss 2006). The mean number density of galaxies on the sky is $\bar{N} = \int d\chi\, \nu(\chi)\, \bar{n}(\chi)$ and the line of sight distribution will be $p_f(\chi) = \nu(\chi)\, \bar{n}\,(\chi)/\bar{N}$. Then, defining the 3D density contrast of galaxies analogously to the one of matter

$$\delta_g(\vec{\chi}, z) \equiv \frac{n_g(\vec{\chi}, z) - \bar{n}(z)}{\bar{n}(z)}, \tag{2.48}$$

one finds that the projected number density of galaxies $N(\vec{\theta})$ is

$$N(\vec{\theta}) = \bar{N}\left[1 + \int d\chi\, p_f(\chi)\, \delta_g\,(\chi\, \vec{\theta})\right]. \tag{2.49}$$

Then, we can define the 2D fractional number density contrast κ_g as:

$$\kappa_g(\,\vec{\theta}\,) \equiv \frac{N(\,\vec{\theta}\,) - \bar{N}}{\bar{N}} = \int d\chi\, p_f(\chi)\, \delta_g(\chi\, \vec{\theta}), \tag{2.50}$$

which is the 2D projection of the 3D galaxy density contrast δ_g.

2.5.4 Angular correlation function and angular power spectrum

As already discussed in Sec. 1.7.2, no theory is able to predict the exact positions of overdensities and underdensities in the Universe, but only the statistical properties of the density field. Thus, in the same way, we cannot predict the lensing effects produced by this density field along one particular line of sight. Moreover, the mean of the density contrast vanishes $\langle\delta\rangle = \langle\kappa\rangle = 0$, also in the 2D case with the convergence. Then, just as in the 3D case, the information resides in the statistical properties of the distributions beyond the mean. That is why in lensing we also use two-point correlation functions (described also in Sec. 1.7.2) to compare with the theory predictions. They capture the degree to which lensing quantities such as the lensing potential, the deflection angle, the convergence and the shear are correlated with each other, constituting the lensing *auto-correlations*, or how they correlate with the density field, comprising the so-called *cross-correlations*. As an example for the lensing auto-correlations, if some image distortion is measured in one direction, the image distortion measured nearby should be similar. The smaller the angle between the two directions, the more correlated they are expected to be. The same happens for cross-correlations, the lensing distortions are expected to be correlated with the density field producing them.

Here we are describing *angular two-point correlation functions*, which are the ones commonly used in photometric surveys such as the Dark Energy Survey, where the redshift is not known with enough accuracy to measure 3D correlation functions. Angular

two-point correlation functions are a 2D projection of the 3D version, integrating over all galaxies in a certain redshift range, i.e. correlating 2D quantities instead of 3D ones. In analogy to Eq. (1.39), they are defined as:

$$\xi_{\alpha\beta}(\theta) \equiv \left\langle \alpha(\vec{\theta'})\, \beta(\vec{\theta'} + \vec{\theta}) \right\rangle, \tag{2.51}$$

where α and β are the two quantities being correlated at the angular position $\vec{\theta'}$ and $\vec{\theta}$ is the angular separation between two positions. If $\alpha = \beta$ and it is a lensing quantity, then ξ is a lensing autocorrelation function, often referred to as *cosmic shear*. If one of the two quantities is the projected density field of foreground galaxies, ξ is a cross-correlation between lensing and the density field, such as the tangential shear correlation in which this thesis is particularly focused. As in the 3D case we derived in Sec. 1.7.2, the angular two-point correlation function only depends on the absolute value of θ, but not on its orientation due to the isotropy of the Universe. The corresponding Fourier-transform of the correlation function, called *angular power spectrum*, is more convenient in some occasions and is defined as

$$\mathcal{C}(\ell) = \int d^2\theta\, \xi(\theta)\, \mathrm{e}^{-i\vec{\ell}\cdot\vec{\theta}}, \tag{2.52}$$

where $\vec{\ell}$ is the two-dimensional wave vector conjugate to the angular separation $\vec{\theta}$. However, to reduce computing time, quite often the lensing power spectra are calculated using the *Limber approximation*. It states that if the quantities $\alpha(\vec{\theta})$ and $\beta(\vec{\theta})$ defined in two dimensions are a projection of the quantities $a(\vec{r})$ and $b(\vec{r})$ defined in three dimensions with a window function $W(\chi)$, as in here

$$\alpha(\vec{\theta}) = \int_0^{\chi_{\rm lim}} d\chi\, W_a(\chi)\, a(\chi\vec{\theta}, \chi), \qquad \beta(\vec{\theta}) = \int_0^{\chi_{\rm lim}} d\chi\, W_b(\chi)\, b(\chi\vec{\theta}, \chi), \tag{2.53}$$

then the angular cross-power spectrum of α and β is given by

$$\mathcal{C}_{\alpha\beta}(\ell) = \int_0^{\chi_{\rm lim}} d\chi \frac{W_\alpha(\chi) W_\beta(\chi)}{\chi^2} P_{ab}\left(\frac{\ell}{\chi}\right), \tag{2.54}$$

where $P_{ab}(k)$ is the 3D cross-power spectrum of a and b, taken at the three-dimensional wave number $k = \ell/\chi$. Limber's approximation holds if a, b vary on length scales much smaller than the typical length scale of the window functions W_a, W_b. Thus, the Limber approximation allows us to compute the statistics of any projected quantity as an integral over the statistics of the 3D quantity. The above equation also gives the relation for auto-correlations, when $a = b$, and then $\alpha = \beta$.

Lensing power spectra

Using Limber's approximation described above, we are ready to compute the convergence power spectrum and express it in terms of the 3D matter power spectrum $P_{\delta\delta}$. This is useful because there are many efforts aimed at computing the 3D matter power spectrum, using either linear theory or non-linear fitting formulas obtained from N-body simulations, for instance as in Takahashi et al. (2012), which can be used to later move to the lensing power spectra using the equations derived below. Equation (2.46) shows that the convergence is a projection of the density contrast δ with the window function

$$W_\kappa(\chi) = \frac{3H_0^2\Omega_m}{2c^2}\frac{g(\chi)\,\chi}{a(\chi)}, \tag{2.55}$$

Then, using Eq. (2.54), we obtain the *convergence power spectrum*

$$\mathcal{C}_{\kappa\kappa}(\ell) = \frac{9H_0^4\Omega_m^2}{4c^2}\int_0^{\chi_{\rm lim}} d\chi \frac{g^2(\chi)}{a^2(\chi)} P_{\delta\delta}\left(\frac{\ell}{\chi}\right), \tag{2.56}$$

which becomes a projection of the 3D matter power spectrum. In this way, we can also obtain the power spectrum of the cross-correlation between the convergence and a foreground galaxy distribution, parametrized as the projected galaxy density κ_g, defined in Eq. (2.50):

$$\left\langle \tilde{\kappa}(\vec{\ell})\,\tilde{\kappa}_g^*(\vec{\ell})\right\rangle = (2\pi)^2\,\delta_D(\vec{\ell}-\vec{\ell}')\,\mathcal{C}_{\kappa g}(\ell), \tag{2.57}$$

by using the window function from Eq. (2.50):

$$W_{\kappa_g} = p_f(\chi) \tag{2.58}$$

and the one from (2.55) again using Limber's approximation, we obtain the angular cross-power spectrum as a function of the 3D cross-power spectrum $P_{\delta g}$

$$\mathcal{C}_{\kappa g}(\ell) = \frac{3H_0^2\Omega_m}{2c^2}\int d\chi \frac{g(\chi)p_f(\chi)}{a(\chi)\chi} P_{\delta g}\left(\frac{\ell}{\chi},\chi\right), \tag{2.59}$$

where $p_f(\chi)$ is the radial distribution of the lens galaxy sample.

2.5.5 Modeling of the tangential shear

With all the above ingredients in place, now we can proceed to express the tangential shear as a function of the matter power spectrum as well. There is one subtlety that we need to address first, though, since the tangential shear is a cross-correlation between the lens galaxy positions and the source galaxy shears, not their convergence,

while in the above equations we have derived the expressions for convergence auto- and cross-power spectrum. Fortunately, a simple derivation shows that the shear and convergence have identical power spectrum. To see this, we transform into Fourier space the defining equations for κ and γ from Eq. (2.17):

$$\tilde{\kappa}(\vec{\ell}) = -\frac{\ell^2}{2}\tilde{\psi}(\vec{\ell}), \qquad \tilde{\gamma}_1(\vec{\ell}) = \frac{-(\ell_1^2 - \ell_2^2)}{2}\tilde{\psi}(\vec{\ell}), \qquad \tilde{\gamma}_2(\vec{\ell}) = -\ell_1\ell_2\tilde{\psi}(\vec{\ell}) \quad (2.60)$$

Then,

$$4|\tilde{\gamma}|^2 = \left[(\ell_1^2 - \ell_2^2)^2 + 4\ell_1^2\ell_2^2\right]|\tilde{\psi}|^2 = (\ell_1^2 + \ell_2^2)^2|\tilde{\psi}|^2 = 4|\tilde{\kappa}|^2, \quad (2.61)$$

which shows that the convergence and the shear power spectra are the same $\mathcal{C}_{\kappa\kappa} = \mathcal{C}_{\gamma\gamma}$, and equivalently for the cross-power spectrum $\mathcal{C}_{\kappa g} = \mathcal{C}_{\gamma g}$. Then, if we express the tangential shear $\gamma_t(\theta)$ as a function of the angular cross-power spectrum $\mathcal{C}_{\gamma g}$ we will be able to use expression (2.59) derived above. The tangential shear around a galaxy at the origin is

$$\begin{aligned}\gamma_t(\theta) &\equiv \left\langle \gamma_t(\vec{\theta})\,\kappa_g(\vec{0}) \right\rangle = \\ &= -\int \frac{d^2\ell}{(2\pi)^2}\int \frac{d^2\ell'}{(2\pi)^2}\, e^{-2\mathrm{i}\,\phi} e^{-\mathrm{i}\,\vec{\theta}\cdot\vec{\ell}'} \left\langle \tilde{\gamma}(\vec{\ell}')\,\tilde{\kappa}_g^*(\vec{\ell}) \right\rangle = \\ &= \int \frac{d\ell}{2\pi}\,\ell\, J_2(\theta\ell)\,\mathcal{C}_{\gamma g}(\ell),\end{aligned} \quad (2.62)$$

where in the first step we have used expression (2.32) for the rotation to the tangential component and applied the Fourier transform to the shear and galaxy convergence. In the second step we have used the equivalent of Eq. (2.57) for shear and the definition of the second order Bessel function of the first kind J_2, which involves in an integral over the variable ϕ. The expression for the tangential shear above can be reinterpreted as the average tangential shear around many lens galaxies. Then, combining Eq. (2.62) and (2.59), together with the fact that the power spectrum of shear and convergence are the same, yields:

$$\gamma_t(\theta) = \frac{3H_0^2\Omega_m}{2c^2}\int \frac{d\ell}{2\pi}\,\ell\, J_2(\theta\ell)\int d\chi \frac{g(\chi)p_f(\chi)}{a(\chi)\chi} P_{\delta g}\left(\frac{\ell}{\chi}, \chi\right). \quad (2.63)$$

Finally, using the relation between the cross power spectrum and the matter power spectrum from Eq. (1.54), the product $b \cdot r$ appears:

$$\gamma_t(\theta) = b \cdot r\,\frac{3H_0^2\Omega_m}{2c^2}\int \frac{d\ell}{2\pi}\,\ell\, J_2(\theta\ell)\int d\chi \frac{g(\chi)p_f(\chi)}{a(\chi)\chi} P_{\delta\delta}\left(\frac{\ell}{\chi}, \chi\right), \quad (2.64)$$

which can be outside of the integral only if the galaxy bias and cross-correlation coefficient are scale and redshift independent in the interval considered. Therefore, from this expression we can see that the components needed to model the tangential shear are: the matter power spectrum, the redshift distribution of the lens and source galaxy samples, the scale factor, the galaxy bias and cross-correlation coefficient and a cosmological model. Alternatively, tangential shear measurements can be used to measure cosmological parameters using this expression, in combination with other probes such as galaxy clustering to break degeneracies with the galaxy bias, as we will do in Part. III of this thesis.

2.6 CMB Lensing

Instead of using the light of galaxies to measure gravitational lensing effects produced by the large scale structure present between us and the source galaxies, we can use the photons coming from the Cosmic Microwave Background as the source of light. These photons will be deflected in the same way as the light from galaxy sources. Using the CMB as the source of light has the advantage that it allows to probe structures at higher redshift, since the CMB shell is at $z \simeq 1100$ and therefore its lensing kernel peaks around $z \sim 2$, as seen in Fig. 2.11 . Moreover, the redshift of the CMB is known with much higher accuracy than the redshifts of source galaxies from photometric surveys, which is a major asset when modeling the expected signal. On the other hand, current CMB lensing maps are usually noisier than galaxy shape measurements. Overall CMB lensing provides a complementary and independent way of probing the large scale structure of the Universe.

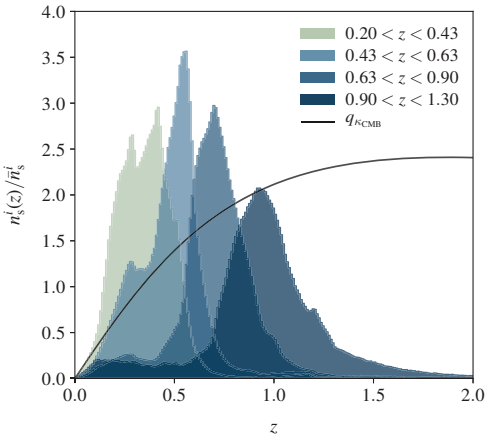

Figure 2.11: Lensing kernel of the CMB (solid line) compared with the redshift distributions of DES Y1 source galaxies, divided in four tomographic bins (shaded areas). DES source galaxies are only sensitive to LSS in front of them, with the highest sensitivity being at approximately half the distance between us and the source, while CMB lensing is able to probe structures at higher redshift. From Omori et al. (2018a).

The unlensed CMB: primordial anisotropies

Before going into the CMB lensing formalism we will discuss the unlensed CMB in more detail, following from Section 1.4, where we discussed the origin of the CMB

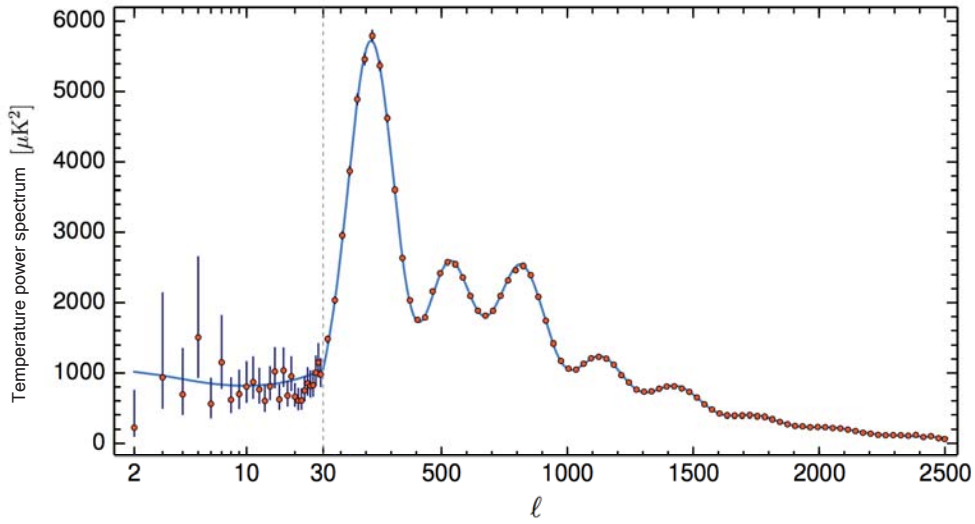

Figure 2.12: Planck 2018 temperature power spectrum (Planck Collaboration, 2018).The ΛCDM theoretical spectrum best fit to the Planck likelihoods is plotted in light blue. The dashed vertical line is used to indicate the change at $\ell = 30$ from logarithmic to linear in the horizontal.

photons and qualitatively described the anisotropies imprinted in the CMB map. These anisotropies, which are of the order of $\sim 10^{-5}$, are caused by the density fluctuations in the early Universe, arising from acoustic oscillations in the primordial photon-baryon fluid. Hence, the CMB is a snapshot of those spatially varying oscillations a the time of recombination, when photons decoupled from baryons. The small size of the perturbations means that linear perturbation theory is very accurate, and the acoustic oscillations can be modelled accurately to give robust predictions. Also, at the time of recombination, the correlations were homogeneous, which leads to the fact that Fourier modes were uncorrelated with each other. This is reflected in the temperature power spectrum:

$$\left\langle \tilde{T}(\vec{\ell})\tilde{T}^*(\vec{\ell}')\right\rangle = (2\pi)^2\,\delta_D^2(\vec{\ell}-\vec{\ell}')\,\mathcal{C}_\ell, \tag{2.65}$$

which characterizes the temperature anisotropies in the CMB. Thus, measuring temperature fluctuations we can obtain the CMB power spectrum. The perturbations on this high redshift last-scattering surface are the main contribution to the CMB anisotropy observed, with additional large-scale anisotropies from the *integrated Sachs-Wolfe* (ISW) effect from evolving potentials along the line of sight.

In Fig. 2.12 it is shown the CMB spectrum measured from *Planck* data. The hot and cold spots from the CMB have typical sizes of order a degree, and this corresponds to the first peak at multipole $\ell \sim \pi/1^\circ \sim 200$, as seen in the figure. Overall, the CMB power spectrum carries an enormous amount of information coming mostly from the

early Universe which can be used to constrain cosmological parameters. For this purpose, the lensing of the CMB is important as a contaminant. However, in Part. IV of this thesis we will use the CMB lensing map as the main signal.

The lensed CMB

The deflections of the CMB photons due to lensing are small, of order arcminutes, but the structures producing the lensing are much larger, subtending degree scales. Thus, in the context of CMB lensing, measuring the small scale anisotropies gives us information about the large-scale structure of the Universe. In other words, the types of structure that produce CMB anisotropies are long wavelength, linear density fluctuations. These fluctuations themselves are Gaussian and hence CMB lensing is lensing of a Gaussian random field by a Gaussian random field, in contrast to cosmic shear.

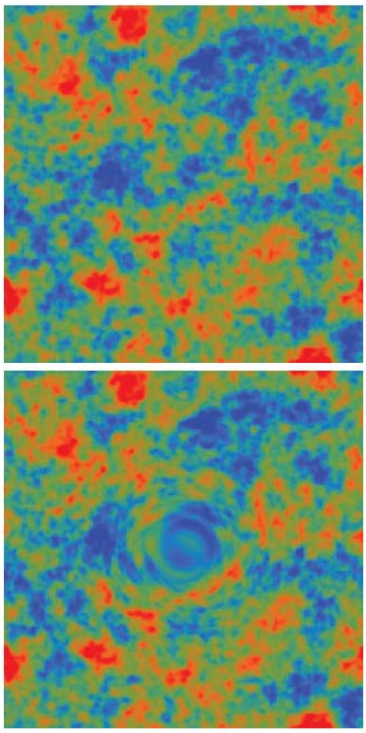

Figure 2.13: An exaggerated example of the lensing effect on a $10^o \times 10^o$ field, from Hu & Okamoto (2002a). **Top:** unlensed temperature field. **Bottom:** Lensed temperature field by a spherically symmetric deflection field.

To perform CMB lensing measurements we need to transform the CMB temperature map to a convergence map. Extracting the lensing map out of the temperature map is not an immediate process, since both effects are mixed. However we can use the fact that realizations of the temperature spectrum would be the same in every region of the sky in the absence of lensing, while lensing distorts the spectrum depending on how much mass there is along each line of sight, e.g., when the CMB photons pass by a region of nonzero convergence, they get deflected. For instance, when they pass through a hot spot, with $\kappa > 0$, the lensed image appears larger, in the same way as we illustrated in Fig. 2.5. If the hot spot can be approximated as a circle in the sky with angular radius θ, then its observed radius will be $\theta' = \theta\,(1+\kappa)$. This effect is shown in Fig. 2.13. Then, without lensing, since the correlation function does not depend on position, the Fourier modes are uncorrelated with each other, and $\left\langle \tilde{T}(\vec{\ell})\tilde{T}^*(\vec{\ell}')\right\rangle$ is proportional to a Dirac delta function with argument $\vec{\ell} - \vec{\ell}'$. The inhomogeneity induced by the convergence leads to a break down of this relation: in the presence of lensing the modes with different values of $\vec{\ell}$ will be correlated. We can use these correlations to reconstruct the lensing map

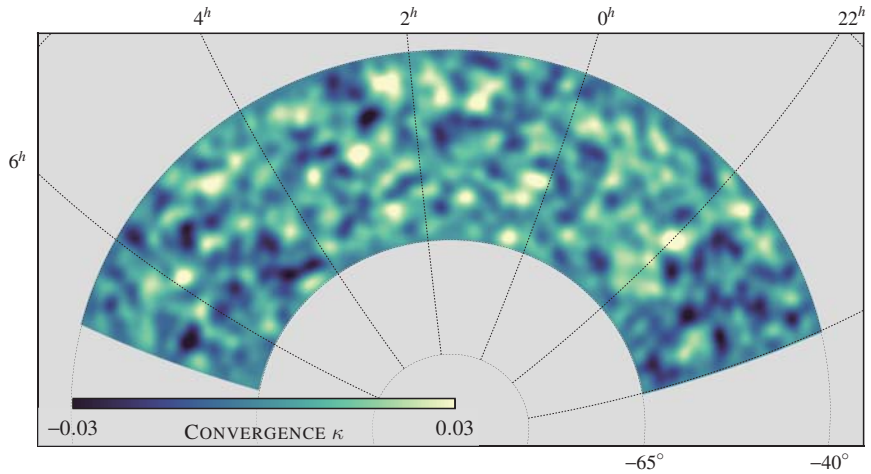

Figure 2.14: CMB lensing map from combined South Pole Telescope and *Planck* data on the SPT field in the South Hemisphere, overlapping with the Dark Energy Survey footprint The map has been smoothed with a Gaussian kernel with FWHM = 2 degrees. This map is presented in Omori et al. (2017).

in the following way. The observed lensed temperature field is equal to the unlensed temperature at position $\vec{\theta} - \vec{\alpha}$:

$$T^{\rm len}(\vec{\theta}) = T^{\rm unl}(\vec{\theta} - \vec{\alpha}). \tag{2.66}$$

Then, performing a Taylor expansion for small deflection angles $\vec{\alpha}$:

$$T^{\rm len}(\vec{\theta}) = T^{\rm unl}(\vec{\theta}) - \frac{\partial T^{\rm unl}}{\partial \theta_i}\alpha_i, \tag{2.67}$$

and, using the fact that the deflection angle is the gradient of the potential, leads to (Dodelson, 2017):

$$\left\langle \tilde{T}(\vec{\ell})\tilde{T}^*(\vec{\ell}')\right\rangle_{\vec{\ell}\neq\vec{\ell}'} \simeq \mathcal{C}_{\vec{\ell}'}\vec{\ell}' \cdot (\vec{\ell} - \vec{\ell}')\,\tilde{\Phi}(\vec{\ell} - \vec{\ell}') + \text{c.c.}, \tag{2.68}$$

in Fourier space and where c.c. stands for complex conjugate. Hence, since the convergence field κ is also related to the gravitational potential, the lensing map can be recovered using this method. In Fig. 2.14 we show a CMB lensing map obtained from a combination of South Pole Telescope (SPT) and *Planck* data. In Omori et al. (2017) more details on how to reconstruct CMB lensing maps can be found.

Chapter 3

The Dark Energy Survey

The Dark Energy Survey (DES) is designed to probe the origin of the accelerating expansion of the Universe and help understand the nature of dark energy by measuring the history of cosmic expansion with high precision, as well as the history of the growth of structure in the Universe. More than 400 scientists from 25 institutions in the United States, Spain, the United Kingdom, Brazil, Germany, Switzerland and Australia are working on the project. A map locating the institutes that are part of the DES collaboration is shown in Fig 3.1. The collaboration has built an extremely sensitive 570-Megapixel digital camera with a 3 deg^2 field-of-view, DECam (Flaugher et al. 2015; Honscheid, DePoy et al. 2008), which is shown in Fig. 3.2, mounted at the prime focus of the Blanco 4-meter telescope at Cerro Tololo Inter-American Observatory (CTIO), in northern Chile. DECam was installed in the second semester of 2012. In Fig. 3.3 we show its first image.

The Dark Energy Survey officially began taking data in August 2013 and finished in January 2019, after 758 nights of observations. The survey covers $\sim$5000 square degrees of the southern sky. After processing all images taken, DES will have measured shapes, photometric redshifts and positions for 300 million galaxies. Also, it will have detected tens of thousands of galaxy clusters and about 3000 type Ia SNe. DES represents an increase in volume over the Sloan Digital Sky Survey (SDSS) of roughly a factor of 7 (Flaugher et al. 2015). DECam observes in 5 broadband optical filters $grizY$, shown in Fig. 3.4, with a nominal limiting magnitude of $i_{AB} \simeq 24$. DES conducts two distinct multi-band imaging surveys: a $\sim$5000 deg^2 wide-area survey in the $grizY$ bands and a $\sim$27 deg^2 deep supernova survey observed in the $griz$ bands with a $\sim$7-day cadence (Diehl et al. 2014, Kessler et al. 2015). The wide-field survey uses exposure times of $90s$ for $griz$ and $45s$ for Y band.

A single raw DECam exposure is $\sim$0.5 GB in size (compressed), and DES collects $\sim$300 science exposures per night, depending on the season, survey strategy, and on the SN fields schedule. These data are transferred to NOAO for archiving and to NCSA

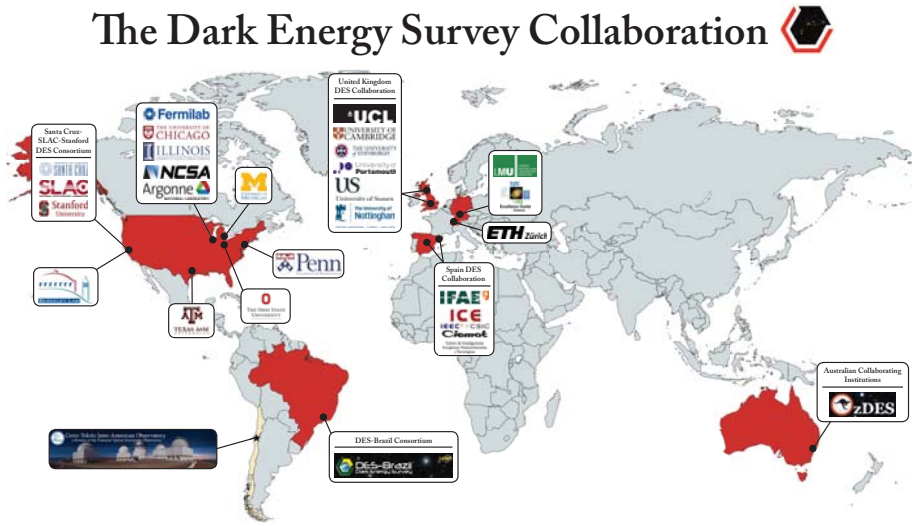

Figure 3.1: Insitutions that are part of the Dark Energy Survey Collaboration.

for further evaluation and processing by the DESDM system. Reduction consists of standard image corrections of the raw CCD information to remove instrumental signatures and artifacts and the joining of these images into 0.5 square degree combined images, called "tiles". Then, galaxies and stars in the images are identified, catalogued, and finally their properties measured and stored in a database.

The Dark Energy Survey has the potential to combine four different probes to study dark energy. The first two probes are purely geometrical and will help constrain the expansion of the Universe. On the other hand, the last two probes have information on both the geometry and the evolution of the matter distribution in the Universe. The four probes are:

1. **Type Ia Supernovae (SN)**: These objects are nearly "standard candles", which means that they almost have equal luminosity when they reach their brightest phase. Hence, we can use their apparent magnitude in order to estimate their distance. Comparing the redshift with the luminosity distance (Hubble diagram) for a large number of supernovae, we can derive the history of the expansion rate of the Universe.

2. **Baryon Acoustic Oscillations (BAO)**: The Baryon Acoustic Oscillations refer to fluctuations in the density of matter in the Universe, caused by acoustic waves in the primordial photon-baryon plasma. This early-Universe phenomenon gets imprinted in the large scale structure of the matter distribution in the Universe.

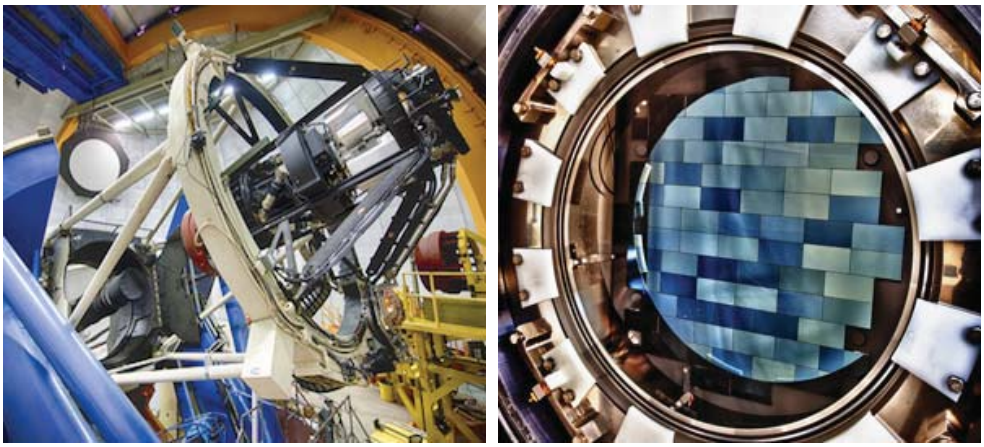

Figure 3.2: The Dark Energy Camera, mounted at the Blanco telescope at the Cerro Tololo Inter-American Observatory in Chile. The Dark Energy Camera features 62 charge-coupled devices (CCDs) for imaging and 12 CCDs for guiding and focus, which record a total of 570 megapixels per snapshot. Credit: Reidar Hahn/Fermilab.

Then, there is a slight increase in the chance of finding lumps of matter and therefore galaxies, separated by a certain distance, defined by the sound horizon distance, which provides a "standard ruler" for cosmological distance measurements at recombination.

3. **Weak Gravitational Lensing (WL)**: This is the main probe used in this thesis and described in detail in Chapter 2. The general relativistic deflection of light rays by matter allows a statistical reconstruction of the gravitational potential in the sky. It probes the distribution of not only visible matter but also dark matter. WL effects depend both on how clumped the distribution of dark matter is and on the distances to the lensing structure and the object being lensed.

4. **Galaxy Clusters (GC)**: The number of galaxy clusters of a given mass within a given volume of the Universe as a function of time carries information about the history of growth and geometry of the Universe. This is because dark energy influences how the Universe expands, so it affects how the volume grows over time, and also since the formation of a galaxy cluster depends on both matter and dark energy.

The fact that DES will be able to use all four probes is one of its big advantages, as demonstrated in DES Collaboration (2018a). This thesis is focused on the weak lensing one using data from the DES Science Verification (SV) period and from the first year of observations (Y1). SV data were taken from November 2012 to February 2013 and ~ 250 square degrees of the sky were covered to the nominal DES depth, $i_{AB} \lesssim 24$.

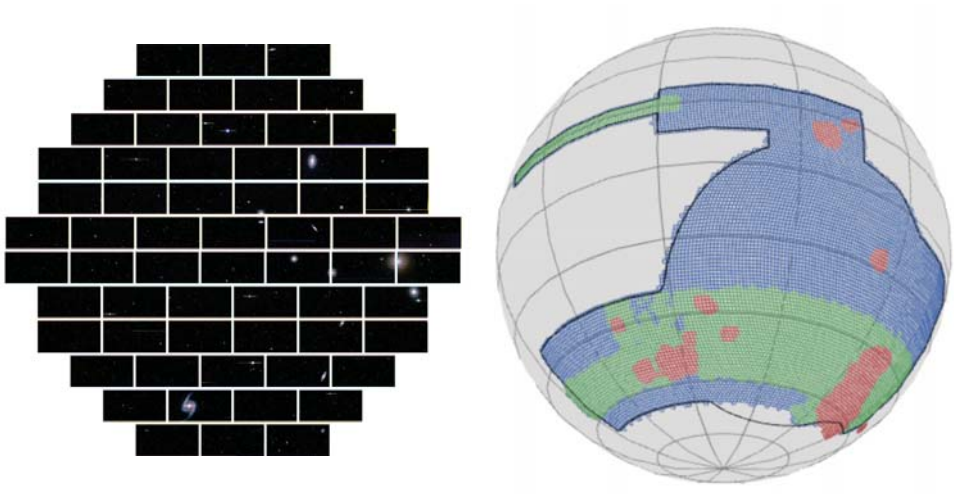

Figure 3.3: **Left:** DECam's first image in September 2012, with the Fornax Cluster. In a typical deep exposure, DECam can observe 150000 galaxies in a single shot. Credit: Dark Energy Survey Collaboration. **Right:** DES footprint. In red it is shown the Science Verification (SV) footprint, in green the footprint from the first year of observations (Y1), and in blue the final DES footprint. Credit: Nacho Sevilla.

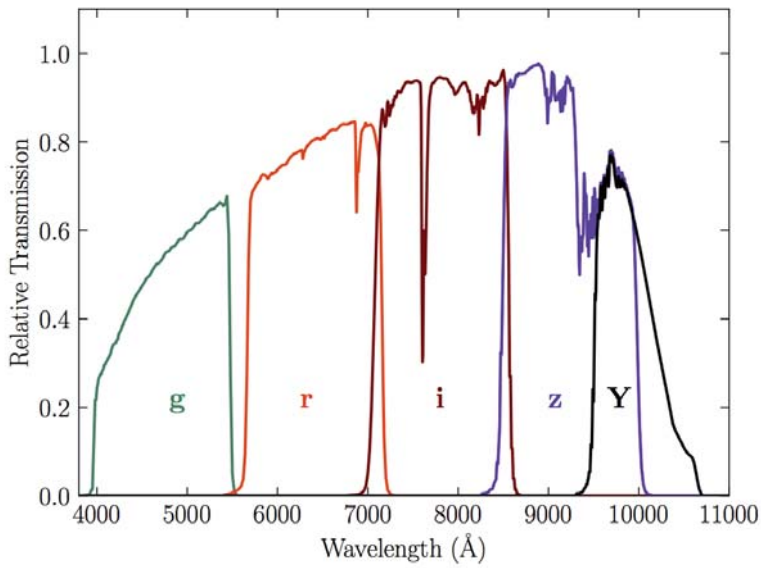

Figure 3.4: Standard Bandpasses for the DECam g, r, i, z and Y filters. The bandpasses represent the total system throughput, including atmospheric transmission (airmass = 1.2) and the average instrumental response across the science CCDs (Abbott et al., 2018b).

Y1 images were taken between August 2013 and February 2014 reaching a limiting magnitude of ≈ 22.5 in the i-band (with a mean of 3 exposures out of the planned 10 for the full survey). In Fig. 3.3 the footprints from each of these data sets are shown. In this thesis, both for SV and for Y1 data, only the largest contiguous area is used from each data set. For SV, this corresponds to the part contained in the South Pole Telescope East (SPT-E) observing region with $60^\circ < \mathrm{RA} < 95^\circ$ and $-61^\circ < \mathrm{Dec} < -40^\circ$, which covers 163 sq. deg. For Y1, this corresponds to the contiguous region of 1321 sq. deg. which also overlaps with the South Pole Telescope footprint.

In this thesis we make use of two main data products measured within the DES collaboration that are essential to perform weak lensing studies. These are the redshift and shape measurements of the galaxies, which are both obtained via complex processes. Below we aim to briefly describe the principal methods used within the field, and particularly within the DES collaboration, to compute the redshifts and the shapes of galaxies in a photometric survey.

3.1 Redshift estimation

The redshift is a very important quantity because it is the main observable which is related to the scale factor and to the comoving distance of an object. As we saw in Sec. 2.5, it is essential to characterize the redshift distribution of the samples involved in weak lensing analyses in order to model the expected signal. In this section we describe three main ways to estimate it:

- The **spectroscopic redshift** (*spec-z*) of an object can be computed using its spectrum, which is obtained with an spectrograph. Then, to determine the redshift, one searches for features in the spectrum such as absorption lines, emission lines, or other variations in light intensity. If found, these features can be compared with known features in the spectrum of local galaxies. If the same spectral line is identified in both spectra at different wavelengths, then the redshift can be calculated using Eq. (1.5).

- The **photometric redshift** (*photo-z*) of an object can be obtained using the photometry, that is, the flux of the object viewed through various standard filters, each of which lets through a relatively broad spectrum of colors. There are two main ways to estimate photometric redshifts: *template fitting* and *training* methods. In template fitting methods, the measured broadband galaxy spectral energy distribution obtained from the fluxes is compared to a set of redshifted galaxy templates until a best match is found, thereby determining both the galaxy spectral type and its redshift. On the other hand, in training methods, a set of galaxies with known spectroscopic redshifts is used to train a machine-learning algorithm

(an artificial neural network, for example), which is then applied over the galaxy set of interest.

- For a set of galaxies, there is an alternative to photometric redshifts, which has been developed recently and makes use of the clustering information. The **clustering redshift** technique (*cluster-z*) allows us to obtain the redshift distribution of a sample of galaxies by measuring the clustering between the sample of interest and another sample for which we have accurate redshift information (the *reference* sample). The reference sample is usually split in narrow redshift bins, for which the angular cross-correlation with the sample of interest is measured. The redshift distribution is then proportional to the amplitude of the clustering in each of the redshift bins. This method has proven very useful in recent cosmological analyses despite its main current limitations which are being able to model the galaxy bias of each of the samples and the scarcity of reference samples at high redshift.

In DES, even though only photometric and clustering redshifts can be obtained directly, spectroscopic redshifts coming from other surveys are used to calibrate and/or validate photometric redshift information. In particular, the Science Verification (SV) area was chosen to overlap with several deep spectroscopic surveys, such as VVDS (Le Fèvre et al., 2005), ACES (Cooper et al., 2012) and zCOSMOS (Lilly et al., 2007) to be able to calibrate the photo-z's. This is not an easy task and currently there exist several photometric redshift codes with different performances that were discussed in detail in Sánchez et al. (2014), for DES SV, and in Bonnett et al. (2016) for the shape catalogs of this initial data set. In Bonnett et al. (2016), the four best performing photo-z codes according to Sánchez et al. (2014) were studied: TPZ (Carrasco Kind & Brunner, 2013), BPZ (Benitez, 2000; Coe et al., 2006), SkyNet (Graff et al., 2014; Bonnett, 2015) and ANNz2 (Sadeh, Abdalla & Lahav, 2015). A brief description of each of these photo-z codes is given below (see Sánchez et al. (2014) for a more extended one):

- **BPZ** is a template-based method that provides the probability density distribution $p(z|m_i, \sigma_i)$ that a galaxy with magnitudes in each band $m_i \pm \sigma_i$ is at redshift z.

- **TPZ** is a training-based code based on prediction trees and random forest algorithms.

- **SkyNet** is a training-based method using a neural network algorithm to classify galaxies in classes, in this case redshift bins.

- **ANNz2** is the updated version of ANNz (Artificial Neural Network). It is a training-based method which relies on Artificial Neural Networks (ANNs), and in the up-

dated version ANNz2, also on Boosted Decision Trees (BDTs) and K-Nearest Neighbours (KNNs), as implemented in the TMVA package (Hoecker et al., 2007).

These codes became the most used for weak lensing studies in the SV period, in particular to estimate the $N(z)$ of the shape catalog. On the other hand, BPZ was the code preferentially used to estimate the redshift distribution of the source galaxy catalog in DES Y1 weak lensing studies. Details about the BPZ aplication to DES Y1 data can be found in Sec. 5.3.3 and more extensively in Hoyle et al. (2018).

3.2 Shape estimation

Galaxy shape measurements are essential to perform weak lensing studies. Actually, having a shape catalog is the main driver for the existence of photometric surveys. In Sec. 2.3 we already introduced the basic equations related to the estimation of galaxy shapes and here we focus on the application to these methods to DES data, particularly on the different codes that were applied to DES SV and DES Y1 data.

In general, one of the features that every shape catalog needs to have is a validation procedure. Typically, this is done using simulations. The basic idea is to simulate what measurements from surveys look like given a known shear and test how well the shape measurement code recovers the input shear. The quantitative metric usually employed for these tests includes the possibility that the measured shears retrieve the true shears multiplied by constant and with some offset:

$$\frac{\gamma_i^{\text{measured}}}{1-\kappa} = m_i \frac{\gamma_i^{\text{true}}}{1-\kappa} + c_i, \qquad (3.1)$$

where m_i and c_i are called multiplicative and additive shear bias, respectively. Note that we use the reduced shear for this, although the difference between the reduced and bare shears is irrelevant for most weak lensing applications.

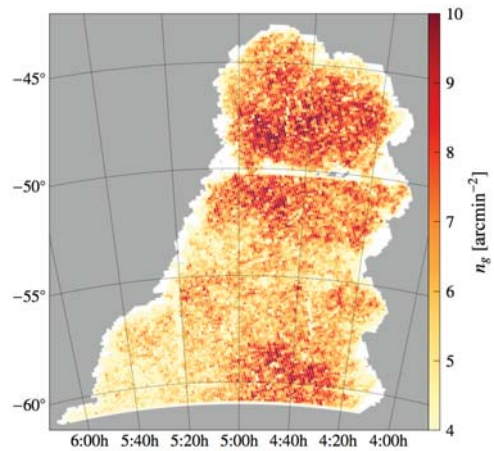

Figure 3.5: A HEALPix map of the SPT-E region, with the SV area. The white background shows the full baseline catalog, called the "Gold" catalog. The colours show the galaxy density in the NGMIX shape catalog for SV. The map for IM3SHAPE is qualitatively similar, although about 40% shallower. Figure from Jarvis et al. (2016).

In DES SV, the NGMIX and IM3SHAPE pipelines were used, which were both based on validation with simulations. They are two independent shape estimation pipelines both based on model-fitting algorithms, which are discussed in more detail in Jarvis

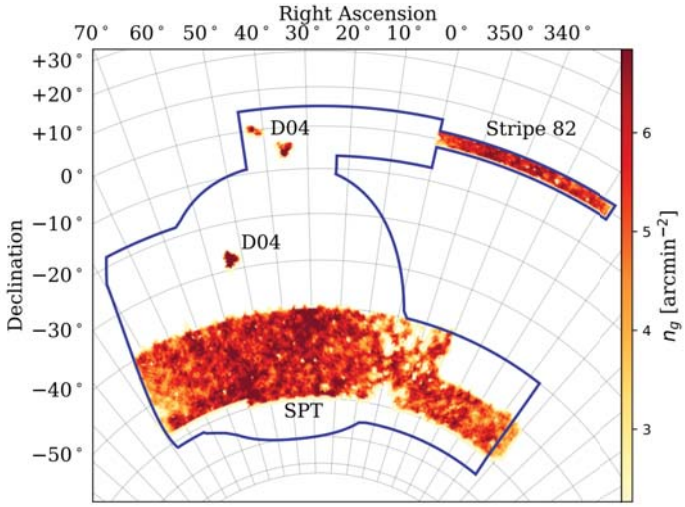

Figure 3.6: The DES Y1 shape catalog footprint with galaxy density of the METACALIBRATION catalog shown with the nominal 5-year DES footprint outline overlayed. IM3SHAPE is qualitatively similar, but slightly shallower. Figure from Zuntz et al. (2018).

et al. (2016). In Fig. 3.5 we show the DES SV NGMIX shape catalog.

For DES Y1, the NGMIX code was upgraded to become the METACALIBRATION catalog, that is based on a newly developed technique which allows to use the data itself to calibrate the shape measurements. Instead of multiplicative and additive shear biases as described above, METACALIBRATION uses the so-called *responses*, explained in more detail in Sec. 5.4.1. In Fig. 3.6 we show the METACALIBRATION number density over the DES Y1 footprint. Moreover, IM3SHAPE was also applied to DES Y1, although with some modifications with respect to the SV code. More information on the exact application of these methods to DES Y1 can be found in Zuntz et al. (2018). Here we summarize the main features of each pipeline:

- **IM3SHAPE:** It is based on the algorithm in Zuntz et al. (2013), modified according to Jarvis et al. (2016) for SV, and with the additions described in Zuntz et al. (2018) for DES Y1. It performs a maximum likelihood fit using a bulge-or-disk galaxy model to estimate the ellipticity of a galaxy, i.e. it fits de Vaucouleurs bulge and exponential disk components to galaxy images in the r band, with shear biases calibrated from realistic simulations (Zuntz et al., 2018; Samuroff et al., 2018).

- **NGMIX:** The NGMIX shape pipeline (Sheldon, 2014) for the DES SV catalogs uses an exponential disk model for the galaxy, which is fit simultaneously in the riz bands. To estimate the ellipticity, the LENSFIT algorithm (Miller et al., 2007) is used. The LENSFIT method requires a prior on the ellipticity distribution $p\,(e)$, taken from the

galaxies in the COSMOS catalog (Koekemoer et al., 2007).

- **Metacalibration**: Metacalibration (Huff & Mandelbaum, 2017; Sheldon & Huff, 2017) is a recently developed method to accurately measure weak lensing shear using only the available imaging data, without need for prior information about galaxy properties or calibration from simulations. The method involves distorting the image with a small known shear, and calculating the response of a shear estimator to that applied shear. This new technique can be applied to any shear estimation code provided it fulfills certain requirements. For DES Y1, it has been applied to the ngmix shape pipeline, which fits a Gaussian model simultaneously in the riz bands to measure the ellipticities of the galaxies. The details of this implementation can be found in Zuntz et al. (2018). In this thesis, we will refer to the ngmix shape catalog calibrated using that procedure as Metacalibration.

Part II

Galaxy bias

In this part we use early DES data to measure the galaxy bias of the benchmark Science Verification sample using galaxy-galaxy lensing and compare our results with those obtained using galaxy clustering in Crocce et al. (2016), and analogous results using CMB lensing from Giannantonio et al. (2016).

Chapter 4

Galaxy bias from galaxy-galaxy lensing in the DES Science Verification Data

4.1 Introduction

Studying the large-scale structure of the Universe provides valuable information about its composition, origin and ultimate fate. Since most of the mass in the Universe is in the form of invisible dark matter, observations of galaxies must be used as a proxy to trace the dark matter on cosmological scales. However, galaxies are not perfect tracers of the underlying mass distribution, and thus, it is important to understand the relationship between the large-scale distribution of (mostly dark) matter and that of galaxies. Most of the cosmological information in the matter distribution can be encapsulated in the power spectrum of matter density fluctuations (all in the case of a Gaussian random field), $P_{\delta\delta}(k, z)$, as a function of wavenumber k and redshift z. The power spectrum of the galaxy number density fluctuations, $P_{gg}(k, z)$, can then be related to the matter power spectrum as (Kaiser, 1984; Bardeen et al., 1986):

$$P_{gg}(k, z) = b^2(k, z)\, P_{\delta\delta}(k, z)\,, \tag{4.1}$$

where $b\,(k, z)$ is the so-called *galaxy bias* parameter, which is expected to be independent of k at large separations (small enough k). It is therefore important to learn about the properties of the galaxy bias.

One way to measure the galaxy bias is to use galaxy clustering, comparing the angular two-point correlation function of galaxies (essentially the Fourier transform of P_{gg}) with the theoretically-predicted matter two-point correlation function, to extract directly $b\,(z)$ at large-enough separation scales. Another way to probe the matter distribution is to use gravitational lensing (see Bartelmann & Schneider, 2001 for a review). A usual approach to measure gravitational lensing is to correlate some estimate of the lensing power with a tracer of the matter density field, such as galaxies. However, in

this case, in the standard parametrization given by (4.1), an additional factor appears to relate the matter power spectrum and the galaxy-matter cross-power spectrum $P_{g\delta}$ (Dekel & Lahav, 1999):

$$P_{\delta g}(k,z) = b\,(k,z)\,r\,(k,z)\,P_{\delta\delta}(k,z), \tag{4.2}$$

where the cross-correlation parameter $r\,(k,z)$ (Pen, 1998) connects not the amplitudes but the phases of the two distributions. If the distributions are completely correlated and thus the mapping between them is deterministic, then $r = 1$. On the other hand, if stochasticity and/or non-linearities are present in the relationship between the galaxy and matter distributions, then $r \neq 1$ (Simon et al., 2007). At large scales, however, r is expected to be close to 1 (Baldauf et al., 2010).

One possible way to probe the galaxy-matter cross-power spectrum is to use galaxy-CMB cross-correlations, first detected in Smith, Zahn & Doré (2007), where lensing maps of the Cosmic Microwave Background photons are cross-correlated with a density map of some foreground galaxies. Another possibility is to use galaxy-shear cross-correlations, or what is usually called galaxy-galaxy lensing (Tyson et al., 1984; Brainerd, Blandford & Smail, 1996), which is the measurement of the tangential shear of background (source) galaxies around foreground (lens) galaxies. The amount of distortion in the shape of source galaxies is correlated with the amount of mass causing the light to curve. Galaxy-galaxy lensing at large scales has been used to probe cosmology, for instance in Mandelbaum et al. (2013) and in Kwan et al. (2017), and at smaller scales to learn about the dark matter haloes, as in Sheldon et al. (2004), Velander et al. (2014) and Hudson et al. (2015).

The Dark Energy Survey (DES) Science Verification (SV) period of observations took place between November 2012 and February 2013 that provided science-quality imaging for almost 200 sq. deg. at the nominal depth of the survey. As described above, there are many ways to obtain information on $b\,(k,z)$, and several have already been attempted with this DES-SV data set. In Crocce et al. (2016) (henceforth Cr16), galaxy clustering measurements were performed to obtain the galaxy bias. The results, depicted in fig. 11 in Cr16, show a moderate increase of the galaxy bias with redshift, an increase that is expected based on numerical simulations (Gaztañaga et al., 2012), and also observed in other studies such as Coupon et al. (2012) from CFHTLS measurements. In Giannantonio et al. (2016) (henceforth G16) galaxy-CMB lensing cross-correlations of the same foreground galaxy sample as in Cr16 were presented, providing another measurement of the relationship between the mass and galaxy distributions. The results in G16, displayed in their fig. 21, show a moderate tension with those in Cr16, of $\sim 2\sigma$ using the full galaxy sample at $0.2 < z < 1.2$, and particularly at the lowest redshift, where the tension is $\sim 3\sigma$. Since the two galaxy samples are identical, the most straightforward way to reconcile the two measurements within the standard

ΛCDM cosmological model is by assuming that r differs significantly from 1 ($r \lesssim 0.6$) at redshift $z \sim 0.3$, a somewhat unexpected result.

In this work, we provide a third probe to measure the galaxy bias, using galaxy-galaxy lensing on the same foreground galaxy sample as the one used in Cr16 and G16, so that we can readily compare our results and shed light on the apparent tension mentioned above. The background set of galaxies we use is that introduced in Jarvis et al. (2016), which was used in previous DES weak lensing analyses (Baxter et al., 2016; Becker et al., 2016; Kacprzak et al., 2016; Kwan et al., 2017; Sánchez et al., 2017; DES Collaboration, 2015). Particularly, Clampitt et al. (2017) performed a series of shear tests using galaxy-galaxy lensing with the DES redMaGiC sample (Rozo et al., 2016) as lenses. Note that the background (source) galaxy sample only serves to illuminate the foreground (lens) sample, which is the one we will gain knowledge of. An advantage of this method is that, since it involves the cross-correlation between source galaxy shapes and lens galaxy density, it is, at least at first order, insensitive to those additive systematic effects that affect only one of these two galaxy samples, such as additive shear biases.

Along similar lines, Chang et al. (2016) used the ratio between the (foreground) galaxy density maps and the mass maps obtained from weak lensing in DES-SV to determine the galaxy bias parameter for the same galaxy sample as in Cr16 and G16. The approach used in Chang et al. (2016) has the advantage of being weakly dependent on the assumed cosmological parameters, such as the amplitude of the power spectrum of matter fluctuations, σ_8, but, on the other hand, in the relatively small DES-SV sample, its statistical power is somewhat limited. Chang et al. (2016) assumed $r = 1$, and, as shown in their fig. 6, their results are generally more in agreement with those in Cr16, although the errors are large. The measurements presented in this work are sensitive to the product $b \cdot r$ and therefore can help resolve the apparent discrepancy between the results in G16 (that measure $b \cdot r$ as well) and Cr16 (that measure b).

Since the main goal of the chapter is to compare with the galaxy bias results in Cr16 and G16, the same lens galaxy sample is used, despite its limited resolution. Then, our lens and source samples, defined in Sec. 4.3, significantly overlap in redshift. Other studies of galaxy-galaxy lensing (Nakajima et al., 2012; Hudson et al., 2015) have chosen to eliminate pairs of lens-source galaxies that are close in estimated redshift. We instead model the overlap in the computation of the predicted signal, which relies on the calibrated redshift distributions for lenses and sources, as described in Sánchez et al. (2014), Cr16 and Bonnett et al. (2016). In the DES-SV papers that use galaxy-galaxy lensing to obtain cosmological results (Clampitt et al., 2017; Kwan et al., 2017), an alternative lens sample composed of luminous red galaxies selected using the redMaGiC algorithm (Rozo et al., 2016) was instead used, with very precise photometric redshifts ($\sigma(z) \simeq 0.02$). A similar redMaGiC lens sample has been used for the DES Year 1 cosmological analysis, presented later in this thesis, in Part III.

The outline of this chapter is as follows. First, in Sec. 4.2 we explain the theory and the method employed to measure the galaxy bias using galaxy-galaxy lensing; next, in Sec. 4.3 we describe the data that we use; then, in Sec. 4.4, we present the methodology used to do our measurements and obtain the results, which are presented in Sec. 4.5; then in Sec. 4.6 we discuss the possible implications potential systematics might have on our measurements and finally, in Sec. 4.7 we further discuss our results comparing them to previous work and conclude.

4.2 Theory and method

Our goal is to measure the galaxy bias using galaxy-galaxy lensing, which measures the effect some foreground mass distribution traced by galaxies (lenses) has on the shapes that we observe of some other background galaxies (sources). This small distortion on the shape of the galaxy image is referred to as cosmic shear. The main observable of galaxy-galaxy lensing is the tangential shear, which can be expressed as a function of the matter power spectrum $P_{\delta\delta}$, as derived in Sec. 2.5.5 using Limber's approximation and through the galaxy bias b and the cross-correlation coefficient between matter and galaxy fluctuations r, defined in Sec. 1.7.4:

$$\gamma_t(\theta) = \frac{3H_0^2\Omega_m}{2c^2} \int \frac{d\ell}{2\pi}\, \ell\, J_2(\theta\ell) \int d\chi \left[\frac{g(\chi)\, n_l(\chi)}{a(\chi)\, \chi}\right. \\ \left. b\,(k=\frac{\ell}{\chi},\chi)\, r\,(k=\frac{\ell}{\chi},\chi)\, P_{\delta\delta}\left(k=\frac{\ell}{\chi},\,\chi\right)\right], \tag{4.3}$$

where χ is the comoving distance to a lens galaxy, $n_l(\chi)$ is the distribution along the line of sight of the lens sample, $a(\chi)$ is the scale factor and $g(\chi)$ is the lens efficiency factor:

$$g(\chi) = \int_{\chi}^{\chi_h} d\chi'\, n_s(\chi')\, \frac{\chi' - \chi}{\chi'}, \tag{4.4}$$

where $\chi_{\rm lim}$ is the limiting comoving distance of the source galaxy sample and $n_s(\chi')$ the distribution of the source sample in comoving distance. For this analysis, we measured the redshift distribution for both the lens and the source sample $n'(z)$, which we then converted to the distribution in comoving distance using the relation $n'(z)dz = n(\chi)d\chi$.

In general, both the galaxy bias and the cross-correlation coefficient depend on the scale and on the comoving distance to the lens galaxy χ, or similarly, on redshift. However, if we assume $b \cdot r$ is redshift and scale independent in the lens sample considered, the factor $b \cdot r$ can be taken out of the integrals along the line of sight and over the scales in 4.3. In this case, γ_t is directly proportional to $b \cdot r$, which in reality

is an effective average over the redshift range of the given bin and the scales considered in the measurement. This assumption is reasonable on large scales – larger than a few times the typical size of a dark matter halo (Mandelbaum et al., 2013) – where the galaxy bias tends to a constant value and we can use the linear bias approximation. The cross-correlation coefficient is also expected to be scale independent at large scales, approaching unity (Baldauf et al., 2010). The dependence on χ, or equivalently redshift, can be minimized using narrow-enough redshift bins and assuming the galaxy bias does not evolve within them. Hence, the factor $b \cdot r$ of a lens galaxy sample can be measured by comparing the predicted or modelled tangential shear using (4.3), with $b \cdot r = 1$, to the measured tangential shear around the lens galaxy sample.

To model the tangential shear, we assume a fiducial flat ΛCDM+ν (1 massive neutrino) cosmological model based on the Planck 2013 + WMAP polarization + highL (ACT/SPT) + BAO best-fit parameters (Ade et al., 2014), consistently with Cr16 and G16: $\Omega_m = 0.307$, $\Omega_\nu = 0.00139$, $\Omega_b = 0.0483$, $\sigma_8 = 0.829$, $n_s = 0.961$, $\tau = 0.0952$ and $h = 0.678$, and we compute the non-linear power spectrum with `Halofit` (Smith et al., 2003; Takahashi et al., 2012) using `CosmoSIS`[1] (Zuntz et al., 2015a).

4.3 Description of the data

In this chapter we use data from the Science Verification (SV) period from the Dark Energy Survey (DES). During the SV period, $\simeq 200$ sq. deg. of the sky were imaged to the nominal DES depth, which produced a usable catalog for early science results. The region used in this chapter is the largest contiguous area in the SV footprint, contained in the South Pole Telescope East (SPT-E) observing region with $60^\circ < \mathrm{RA} < 95^\circ$ and $-61^\circ < \mathrm{Dec} < -40^\circ$, which covers 163 sq. deg.

The most numerous catalog of reliable objects in DES-SV is the SVA1 Gold Catalog[2], which excludes objects that are known to be problematic in some way, because of, for instance, failed observations or imaging artefacts. It is generated by applying the cuts and conditions described in Jarvis et al. (2016). The SPT-E region of the Gold Catalog covers 148 sq. deg. of the sky.

4.3.1 The lenses: The Benchmark sample

The foreground catalog for the galaxy-galaxy lensing measurements in this work is the Benchmark sample, which is a subsample of the Gold Catalog. The Benchmark sample was first introduced in Cr16 to perform galaxy clustering measurements, and it

[1] `https://bitbucket.org/joezuntz/cosmosis/wiki/Home`

[2] Publicly available at `https://des.ncsa.illinois.edu/releases/sva1`

was used in G16 to perform measurements of CMB lensing around foreground galaxies. From the SPT-E region of the Gold Catalog, the Benchmark sample is selected by applying the following selection criteria:

- Dec $> -60°$: Conservative cut to remove any possible contamination from the LMC[3].
- $18 < i < 22.5$: Magnitude cut in the i-band, where i refers to SExtractor's MAG_AUTO (Bertin & Arnouts, 1996).
- $-1 < g - r < 3, -1 < r - i < 2, -1 < i - z < 2$: Color cuts to remove outliers in color space. In this case, the magnitude used is MAG_DETMODEL since it produces more accurate colors than MAG_AUTO.
- WAVG_SPREAD_MODEL > 0.003: star-galaxy separation cut. SPREAD_MODEL is a SExtractor parameter that measures the light concentration of an object (Desai et al., 2012). WAVG_SPREAD_MODEL is the weighted average of the SPREAD_MODEL values for all single epoch images used to coadd one object.
- More conservative cut to remove defective objects than the one applied in the Gold Catalog[4].

Furthermore, a mask which ensures the completeness of the sample is applied. Only regions deeper than $i = 22.5$ are included (Cr16), providing a catalog with $2,333,314$ objects remaining, covering 116.2 sq. deg.

4.3.2 The Sources: Shape Catalogs

The source catalogs for this work are the SV shape catalogs ngmix and im3shape, which have been produced for a subset of objects of the DES-SV Gold Catalog in the SPT-E region, as described in Sec. 3.2. Throughout this work, the ngmix shape catalog is used as the fiducial source catalog, since it has a larger raw galaxy number density, 6.9 arcmin^{-2}, as opposed to 4.2 arcmin^{-2} for im3shape (Jarvis et al., 2016), see Fig. 3.5 for ngmix. Also, more details on each shear pipeline are given in Sec. 3.2.

In this work, a weight factor ω related to the uncertainty in the measurement of the galaxy shape is assigned to each object in the following way:

$$\omega = \frac{1}{\sigma_{\rm SN}^2 + \sigma_e^2}, \tag{4.5}$$

[3]Note that in G16 a slightly different cut of Dec $> -61°$ was applied.
[4]Badflag ≤ 1.

	Lens redshift bins	Source redshift bins
1st	$0.2 \leq z_{\text{TPZ}} < 0.4$ $0.2 \leq z_{\text{BPZ}} < 0.4$	$0.55 < z_{\text{SkyNet}} < 1.3$
2nd	$0.4 \leq z_{\text{TPZ}} < 0.6$ $0.4 \leq z_{\text{BPZ}} < 0.6$	$0.55 < z_{\text{SkyNet}} < 1.3$
3rd	$0.6 \leq z_{\text{TPZ}} < 0.8$ $0.6 \leq z_{\text{BPZ}} < 0.8$	$0.83 < z_{\text{SkyNet}} < 1.3$

Table 4.1: Definition of the lens and source redshift bins used throughout the chapter. The lens redshift bins are identical to the ones in Cr16 and G16, defined with BPZ and TPZ as well. The source redshift bins are the same studied in Bonnett et al. (2016) and used in other DES-SV weak lensing analyses, where SkyNet is used to define the bins. z_{TPZ}, z_{BPZ} and z_{SkyNet} stand for the mean of the photo-z probability density function for each galaxy determined with each code.

where σ_{SN} represents the shape noise per component – the standard deviation of the intrinsic ellipticities – and σ_e the measurement uncertainty, estimated in different ways for both shape catalogs, see Jarvis et al. (2016). Also, both for IM3SHAPE and NGMIX, the raw values in the catalogs are intrinsically biased estimators of the shear in the presence of noise (Refregier et al. 2012; Kacprzak et al. 2012). This noise bias in the shear measurement is characterized and corrected using additive and multiplicative shear biases, as detailed in Jarvis et al. (2016).

4.3.3 Photometric redshifts

In this work, point estimates of the redshift are necessary to divide the galaxies into redshift bins and therefore allow for a tomographic study of the galaxy bias. On the other hand, the redshift distributions $n(z)_{l,s}$ of lenses and sources are also needed to model the tangential shear and consequently to measure the galaxy bias. For this reason, it is advantageous to estimate the whole redshift probability density function $P(z)$ for each galaxy, which can then be stacked for a collection of galaxies to obtain the $n(z)$. Point estimates of the redshift for each galaxy are obtained by taking the mean of each $P(z)$.

In this work we use the four best performing photo-z codes according to Sánchez et al. (2014), which were furthermore studied in Bonnett et al. (2016) for the SV shape catalogs: TPZ (Carrasco Kind & Brunner, 2013), BPZ (Benitez, 2000; Coe et al., 2006), SkyNet (Graff et al., 2014; Bonnett, 2015) and ANNz2 (Sadeh, Abdalla & Lahav, 2015). These codes are employed in this work to estimate the $n(z)$ of the shape catalog. On the other hand, in both Cr16 and G16 only two photo-z codes are used for the $n(z)$ of the Benchmark sample: TPZ and BPZ, which we will adopt in this work as well. A brief description of each of these codes is given in Sec. 3.1.

Lens redshift bin	N_{TPZ}	N_{BPZ}
$0.2 \leq z_l < 0.4$	398,658	551,257
$0.4 \leq z_l < 0.6$	617,789	647,010
$0.6 \leq z_l < 0.8$	586,298	494,469

Table 4.2: Number of galaxies in each redshift bin after the veto mask (see Sec. 4.3.4) has been applied.

Lens redshift bins

The lens sample is divided into three photo-z bins of width $\Delta z = 0.2$, from $z = 0.2$ to $z = 0.8$, as in Cr16 and G16, and as shown in Table 4.1. The objects are classified into these lens redshift bins using the mean of the photo-z probability density function determined with either BPZ or TPZ, like in Cr16 and in G16, for comparison. The photo-z precision σ_{68} (half the width of the distribution, centered at the median, where 68% of the data are enclosed) was measured to be ~ 0.1 for BPZ and ~ 0.08 for TPZ in Sánchez et al. (2014). Therefore, it is suitable to use redshift bins of width $\Delta z = 0.2$, being approximately twice the photo-z precision σ_{68}. The number of galaxies in each redshift bin is given in Table 4.2.

In Cr16 and in G16 two additional high redshift bins were used, from $z = 0.8$ to $z = 1$ and from $z = 1$ to $z = 1.2$. Both are omitted in this work, since the number of source galaxies at $z > 1$ is too low to obtain enough galaxy-galaxy lensing signal for this work.

Source redshift bins

For this work, the two high-redshift source bins studied in Bonnett et al. (2016) are adopted, to be consistent with other DES-SV analyses (Becker et al., 2016; DES Collaboration, 2015). These are defined from $z = 0.55$ to $z = 0.83$ and from $z = 0.83$ to $z = 1.3$, using the mean of the SkyNet probability density function as a point estimate of the redshift to define the bins. For the two lower redshift bins of the lenses, we use as source redshift bin the combination of both bins, from $z = 0.55$ to $z = 1.3$ to increase the number of sources and thus the signal to noise, while for the third lens bin, only the higher source redshift bin, from $z = 0.83$ to $z = 1.3$ is used, as shown in Table 4.1.

Photometric redshift distributions

We test the robustness of the galaxy bias measurement against different photo-z codes to compute the $n(z)$. For the lenses, we use BPZ to estimate the redshift distribution of the bins defined with BPZ, and analogously for TPZ, in agreement with

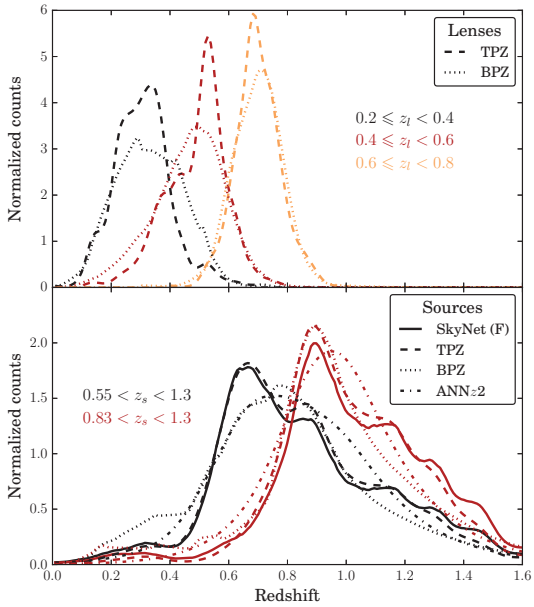

Figure 4.1: *Top panel:* Normalized counts (or normalized $n(z)$'s) of the foreground redshift distribution of lens galaxies using two photo-z codes: TPZ and BPZ, also used in each case to define the galaxies that belong to each bin (as described in Table 4.1). *Bottom panel:* Normalized counts of the background redshift distribution of source galaxies from NGMIX using the following four photo-z codes: SkyNet, TPZ, BPZ and ANNz2, for both source redshift bins. We choose SkyNet to be the fiducial photo-z code to estimate the $n(z)$ of the source galaxies.

Cr16 and G16 (top panel of Fig. 4.1). Regarding the sources, we pick all four photo-z codes described in Sec. 4.3.3 to estimate the $n(z)$ (bottom panel of Fig.4.1). We choose SkyNet to be the fiducial code for this purpose, in consistency with other DES-SV analysis (Becker et al., 2016; DES Collaboration, 2015).

4.3.4 Veto Mask

Besides the depth mask described in Sec. 4.3.1, a veto mask characterized in Cr16, removing the areas most affected by systematics, is also applied in some of the redshift bins. Using the maps of potential sources of systematics presented in Leistedt et al. (2016), Cr16 studied the relationship between the galaxy density and several potential systematics, such as seeing or airmass. In some cases, they found the galaxy density to drop from its mean value in areas with extreme systematics contamination. The regions corresponding to these systematics values are removed, which we denote as the *veto mask*. In detail, they found the seeing to be the main quantity influencing the galaxy density, differently for the various redshift bins. For the lowest redshift bin $0.2 \leq z_l < 0.4$, 19.5% and 9.7% of the galaxies are removed, for the BPZ and TPZ redshift bins, respectively. The veto mask for the $0.4 \leq z_l < 0.6$ is the same for both the BPZ and TPZ redshift bins, removing 14.8% and 14.4% of the galaxies, respectively. On the other hand, the highest redshift bin $0.6 \leq z_l < 0.8$ is found to be less affected by systematics, and thus no further masking is applied. The final number of galaxies for each redshift bin after implementing the veto mask is shown in Table 4.2. In each case, the same veto

mask used for the lenses is applied to the sources, to reduce potential geometric effects that could affect our measurements.

4.4 Measurement methodology

4.4.1 Measurement of the tangential shear and the cross-component

In this section we describe how the tangential shear is measured, as well as the cross-component of the shear, which is expected to be null in the absence of systematics. For a given lens-source pair j of galaxies we can define the tangential component of the ellipticity ϵ_t and the cross-component $\epsilon_\times$ as

$$\epsilon_{t,j} = -\mathrm{Re}\left[\epsilon_j \mathrm{e}^{-2i\phi_j}\right] \quad , \quad \epsilon_{\times,j} = -\mathrm{Im}\left[\epsilon_j \mathrm{e}^{-2i\phi_j}\right], \tag{4.6}$$

where ϕ_j is the position angle of the source galaxy with respect to the horizontal axis of the Cartesian coordinate system centered at the lens galaxy, as illustrated in Fig 2.9.

As derived in Sec. 2.3, the observed ellipticity can be approximated as the sum of the intrinsic ellipticity and the part due to shear: $\epsilon \simeq \epsilon^s + \gamma$. Assuming intrinsic ellipticities are randomly aligned, which might not always be the case (see Sec. 4.6.5), we can obtain the shear by averaging the ellipticity over a sample of galaxies $\gamma \simeq \langle\epsilon\rangle$. In our case, we grouped the galaxy pairs in 11 log-spaced angular separation bins from 4 to 100 arcminutes. Thus, including the weighting factors from Eq. (4.5) the tangential shear and cross-component are measured using `TreeCorr`[5] (Jarvis, Bernstein & Jain, 2004) in the following way:

$$\gamma_\alpha(\theta) = \frac{\sum_j \omega_j \epsilon_{\alpha,j}}{\sum_j \omega_j}, \tag{4.7}$$

where α denotes the two possible components of the shear from (4.6).

A possible sources of inaccuracy in the measurement are shear systematics. However, if the source galaxies are distributed isotropically around the lenses, additive shear systematics should average to zero. Still, due to edge and mask effects, there is a lack of symmetry on the sources distribution around the lenses. This effect can be accounted for by removing from the main galaxy-galaxy lensing measurement the signal measured around random points, which will capture the geometric effects of additive shear systematics. Thus, our final estimator for the tangential shear is:

$$\gamma_t(\theta) = \gamma_t(\theta)_{\mathrm{Lens}} - \gamma_t(\theta)_{\mathrm{Random}}. \tag{4.8}$$

Multiplicative shear bias can still be present and we assess them as explained in Sec. 4.6.4.

[5] `https://github.com/rmjarvis/TreeCorr`

4.4.2 Covariance matrix

The covariance matrix for the tangential shear is estimated using a combined approach between the jackknife method and a theory estimate, as in Cr16. In this section we describe both procedures and how we merge them.

Jackknife method

The jackknife method (see for instance Norberg et al., 2009) is a resampling technique especially useful to estimate covariances. We divide the SPT-E area into 100 spatial jackknife regions of $\sim$ 1 sq. deg., comparable to the maximum angular scales considered, of 100 arcminutes, using the `kmeans` algorithm[6]. We tested the case with $N = 50$ and obtained comparable results, with error fluctuations at the 10% level. Then, we perform the galaxy-galaxy measurement multiple times with a different region omitted each time to make $N = 100$ jackknife realizations. The covariance matrix of the tangential shear estimated with jackknife is:

$$\mathsf{Cov}_{ij}^{\mathrm{JK}}\left(\gamma_i, \gamma_j\right) = \frac{(N-1)}{N} \sum_{k=1}^{N} \left[(\gamma_i)^k - \overline{\gamma_i} \right] \left[(\gamma_j)^k - \overline{\gamma_j} \right], \tag{4.9}$$

where γ_i represents either $\gamma_t(\theta_i)$ or $\gamma_\times(\theta_i)$ and $(\gamma_i)^k$ denotes the measurement from the k^{th} realization and the i^{th} angular bin: $\gamma_t(\theta_i)^k$. Then, the mean value is

$$\overline{\gamma_i} = \frac{1}{N} \sum_{k=1}^{N} (\gamma_i)^k. \tag{4.10}$$

Clampitt et al. (2017) validated the jackknife method on simulations using 50 jackknife regions on a similar patch of the sky. In there, as well as in Shirasaki et al. (2016), it was found that the jackknife method overestimates the true covariance on large scales, where the covariance is no longer dominated by shape noise. However, recently, Singh et al. (2016) performed an extended study on galaxy-galaxy lensing covariances which concluded that subtracting the tangential shear around random points, as we do in this work, removes the overestimation of jackknife errors that was previously seen in Clampitt et al. (2017) and Shirasaki et al. (2016). A jackknife-estimated normalized covariance for a particular choice of photo-z and shear catalog is shown on the left panel of Fig. 4.2.

[6] `https://github.com/esheldon/kmeans_radec`

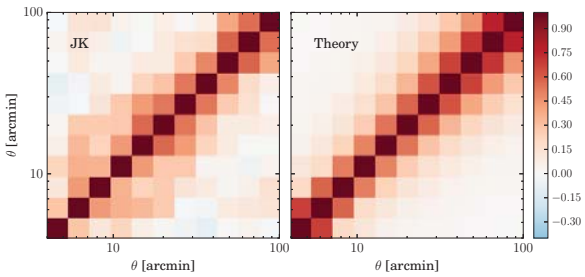

Figure 4.2: Correlation matrix (normalized covariance) for the mid-z lens bin defined with BPZ. *Left panel:* Estimated with the jackknife method (Sec. 4.4.2). *Right panel:* Estimated with a theoretical modelling (Sec. 4.4.2).

Analytic covariance

We can also model the tangential shear covariance matrix to obtain a less noisy estimate. Theoretical estimates of galaxy-galaxy lensing covariances have been studied in Jeong, Komatsu & Jain (2009) and in Marian, Smith & Angulo (2015):

$$\begin{aligned}\mathsf{Cov}_{ij}^{\mathrm{TH}}\left(\gamma_{t,i},\gamma_{t,j}\right) = \frac{1}{4\pi f_{\mathrm{sky}}}\int \frac{l\mathrm{d}l}{2\pi}\bar{J}_2(l\theta_i)\bar{J}_2(l\theta_j) \\ \times\left[\mathcal{C}_{g\kappa}^2(l)+\left(\mathcal{C}_{gg}(l)+\frac{1}{n_{\mathrm{L}}}\right)\left(\mathcal{C}_{\kappa\kappa}(l)+\frac{\sigma_{\mathrm{SN}}^2}{n_{\mathrm{S}}}\right)\right],\end{aligned} \tag{4.11}$$

where f_{sky} is the fraction of the sky covered; n_{L} and n_{S} are the effective number density of the lenses and the sources, respectively, defined in Jarvis et al. (2016); $\mathcal{C}_{g\kappa}(l)$, $\mathcal{C}_{gg}(l)$ and $\mathcal{C}_{\kappa\kappa}(l)$ are the line of sight projections of the galaxy-matter, galaxy-galaxy and matter-matter power spectrum, respectively, obtained using `Halofit` (Smith et al., 2003; Takahashi et al., 2012) with `CosmoSIS`; σ_{SN} is the shape noise per component and $\bar{J}_2$ are the bin-averaged Bessel functions of order two of the first kind, defined as:

$$\bar{J}_2(l\theta_i) \equiv \frac{2\pi}{A(\theta_i)}\int_{\theta_{i,\mathrm{min}}}^{\theta_{i,\mathrm{max}}} J_2(l\theta)\theta\mathrm{d}\theta, \tag{4.12}$$

where $A(\theta_i) = \pi\left(\theta_{i,\mathrm{max}}^2 - \theta_{i,\mathrm{min}}^2\right)$ is the area of the bin annulus. We integrate (4.11) over $1 \leq l < 4000$, which covers the range of scales used in this work. A theory estimated normalized covariance matrix is shown on the right panel of Fig. 4.2. It is much smoother than the jackknife estimation (left panel), particularly far from the diagonal.

Combined approach

As shown on the left panel of Fig. 4.2, the jackknife method gives a rather noisy estimate of the off-diagonal elements, due to the impossibility of increasing the number of realizations without being forced to use excessively small jackknife regions. However, it is relevant to obtain good estimates of the off-diagonal terms since adjacent angular

bins are highly correlated. Moreover, the inverse of a noisy, unbiased covariance is not an unbiased estimator of the inverse covariance matrix (Hartlap, Simon & Schneider, 2007), which is needed to fit the galaxy bias (see Sec. 4.4.3). We improve the estimation of the covariance by obtaining a smooth correlation matrix from theory estimation, shown on the right panel of Fig. 4.2.

On the other hand, concerning now the overall normalization of the covariance matrix, the jackknife procedure is capable of capturing effects that potentially exist in the data and cannot be derived from theory, such as shear systematics or mask effects, and can also reproduce non-linearities although we expect these to be small over the scales used. Indeed, in G16, the jackknife method was found to perform better on the diagonal elements over the theory estimates when compared to a covariance matrix derived from an N-body simulation. Also, the diagonal elements from jackknife are in principle better estimated than the off-diagonal ones, since there is more signal-to-noise in the diagonal. Then, following Cr16, we choose to combine both methods by normalizing the theory-estimated covariance with the diagonal elements of the jackknife covariance:

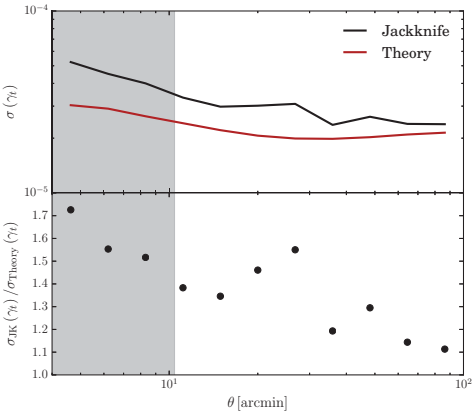

Figure 4.3: Comparison of the diagonal elements of the covariance from the jackknife method and the theory predictions for the mid-z lens bin defined with BPZ.

$$\mathsf{Cov}^{\rm COMB}_{\theta_i,\theta_j} = \mathsf{Corr}^{\rm TH}_{\theta_i,\theta_j}\sigma^{\rm JK}_{\theta_i}\sigma^{\rm JK}_{\theta_j}. \tag{4.13}$$

The comparison between the diagonal elements from the jackknife method and from theory predictions can be found in Fig. 4.3. The jackknife procedure yields larger diagonal elements for the covariance as a result of including additional sources of uncertainties as discussed above.

4.4.3 Galaxy bias estimation

We can now put together all the required ingredients to measure the product of the galaxy bias b times the cross-correlation coefficient r: the measured tangential shear (Sec. 4.4.1), the modelled tangential shear (Sec. 4.2) and the covariance matrix

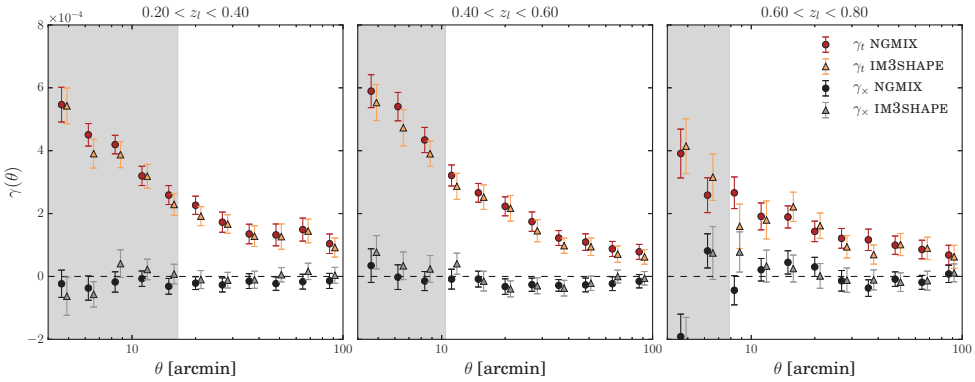

Figure 4.4: Tangential shear γ_t as a function of angular scales from NGMIX (red points) and from IM3SHAPE (orange triangles) for the three lens redshift bins defined with BPZ. Note that the measurements from NGMIX and IM3SHAPE cannot be directly compared because of the lensing efficiency being different in each case (see Sec. 4.5.1). Moreover, we show the cross-component (see Sec. 4.6.1 for discussion) for both NGMIX (black points) and IM3SHAPE (grey triangles), which is consistent with zero in all redshift bins. The null χ^2 for the cross-component are shown in Table 4.3. The shaded angular scales are not considered for the final galaxy bias measurements, which are performed over the range of scales from 4 Mpc/h to 100 arcmin.

(Sec. 4.4.2). Then, $b \cdot r$ is measured minimizing the following χ^2:

$$\chi^2\left(b\cdot r\right) = \sum_{\theta,\theta'} \left(\gamma_t(\theta) - b\cdot r\,\gamma_t^{\rm TH}(\theta)\right) \mathsf{Cov}^{-1}\left(\theta,\theta'\right) \times \left(\gamma_t(\theta') - b\cdot r\,\gamma_t^{\rm TH}(\theta')\right), \tag{4.14}$$

where $\gamma_t^{\rm TH}$ assumes $b \cdot r = 1$.

Range of selected scales

In this section we discuss the range of scales suitable to perform the fit described above. There are some limitations that we need to consider both at large and small scales. For instance, small scales are impacted by effects such as stochasticity, non-local and scale dependence bias and cross-correlation coefficient. Since this behaviour is hard to model, we need to identify the range of scales over which the product of the galaxy bias b times the correlation parameter r is scale independent, free of stochasticity and non-linear effects.

Nonetheless, it is difficult to remove all small scale information in real space, since the tangential shear at each angular scale is an integration of all multipole moments ℓ – see Eq. (4.3) –, that is to say, it contains knowledge of all scales, weighted according to the Bessel function. Then, applying a sharp cut-off in real space does not fully erase the effects present below that cut-off. Even though there exists an alternative estimator

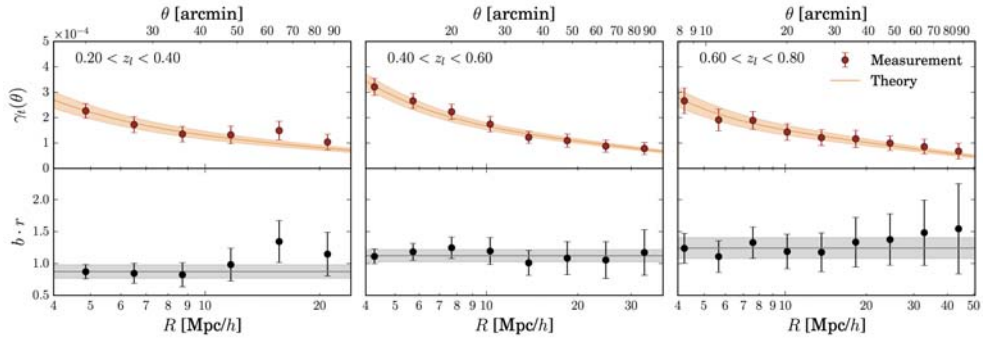

Figure 4.5: *Top panels:* Tangential shear (red points) as a function of the transverse comoving distance R (bottom axis) or the angular separation θ (top axis), together with the best-fitting theory prediction of the tangential shear modelled with `Halofit` (solid orange line) with its corresponding uncertainty band. *Bottom panels:* $b \cdot r$ as a function of scale (black points) with the best-fit (black solid line) using Eq. (4.14), with its uncertainty band. The $N(z)$ of the source galaxies is estimated with SkyNet and the source catalog is NGMIX, which are the fiducial choices.

of the tangential shear (the annular differential surface density estimator) proposed by Baldauf et al. (2010) and Mandelbaum et al. (2010) to remove all small scale information, a conservative minimum scale cut-off should be sufficient to remove enough of it for our purposes, given the current uncertainties in the measurement of the tangential shear. However, this issue might have to be addressed more carefully in future work involving larger area, which will significantly reduce the present uncertainties.

As a result of the non-linear effects at small scales, one does not expect a constant value for either b or r over this range. On the other hand, in the linear bias regime, both the galaxy bias and the cross-correlation parameter can be approximated to a constant. The transition scale from the non-linear to the linear regime should be expressed as a comoving distance R, as opposed to an angular scale θ. For galaxies acting as lenses at different redshift, the same angle θ will correspond to different distances R. Thus, it is convenient to convert the angle θ into the *transverse comoving distance* R that this angle represents. Then, for small angles, $R = \chi_{\rm lens}\,\theta$, where $\chi_{\rm lens}$ is the *radial comoving distance* to the lens galaxy, which can be related to the mean redshift of the lens redshift bin. To compute $\chi_{\rm lens}$ we assume the cosmology described in Sec. 4.2. In Fig. 4.5, both scales are displayed: the angular separation θ at the top and the transverse comoving distance R at the bottom.

In Cr16, it was studied the scale of linear growth, which is the minimum scale where the linear and the non-linear (with `Halofit`) matter power spectrum are the same. The linear growth scale for clustering was found to be ~ 4 Mpc/h, which they adopted as a minimum comoving distance for their results. Jullo et al. (2012) studied the scale of linear bias in the COSMOS field and determined $R = 2.3 \pm 1.5$ Mpc/h to be the scale beyond which bias evolves linearly.

On the other hand, the cross-correlation coefficient dependence on scale has been investigated in studies such as Baldauf et al. (2010) and Mandelbaum et al. (2013), finding $r \simeq 1$ and scale independent on scales larger than a few virial radius of galaxy halos. Jullo et al. (2012) obtained r compatible with one for $0.2 < R < 15$ Mpc/h and $0.2 < z < 1$. Hoekstra et al. (2002) measured the linear bias and cross-correlation coefficient on scales between $R = 0.2$ and 9.3 Mpc/h_{50} at $z = 0.35$. They found strong evidence that both b and r change with scale, with a minimum value of $r \sim 0.57$ at 1 Mpc/h_{50}. However, on scales larger than 4 Mpc/h_{50} they obtained r is consistent with a value of one. In App. A of Cr16 the cross-correlation coefficient r was measured in the `MICECATv2.0` simulation, which is an updated version of `MICECATv1.0` (Fosalba et al., 2015,?; Crocce et al., 2015; Carretero et al., 2014), including lower mass halos and thus more similar to the benchmark sample. They found the cross-correlation coefficient to be in the range $0.98 \leq r \leq 1$ for $z > 0.3$ in the range of scales $12 < \theta < 120$ arcmin, which approximately correspond to a comoving minimum scale of 3 Mpc/h. Even though it is worth noting that different definitions of r may yield different estimates and scale dependencies, it is relevant to this work the fact that, for the range of scales we use, various studies agree on a value of r close to unity and showing little scale dependence.

Overall, following Cr16, we choose a minimum scale cut-off of 4 Mpc/h. However, because the redshift bins have some non-negligible width, a significant fraction of lenses will be below the mean redshift of the bin. Thus, when converting from angular to physical scale, we are effectively including some galaxy pairs that are separated by less than 4 Mpc/h. We tested how important this effect is by, instead of using the mean redshift of the bin to convert from angular to physical scale, using the mean value minus one standard deviation of the redshift distribution. The variations induced by that change in the final galaxy bias measurements are at the level of 0.5-3%, thus much lower than the statistical errors.

Some limitations are present on large scales as well. The maximum valid scale is restricted by the size of the SV SPT-E patch, of 116.2 sq. deg. Moreover, we are also limited by the size of the jackknife regions used in this work to estimate covariances. We follow the approach used in Kwan et al. (2017) of using 100 jackknife regions and a maximum scale cut-off of 100 arcmin.

4.4.4 Non-linear bias model

As a further check, we have tested whether the assumption of linear bias is valid over the scales used – larger than 4 Mpc/h – by studying the robustness of the results when using a non-linear bias scheme. In order to do so, we choose the non-linear bias model adopted in Kwan et al. (2017) and originally developed in McDonald (2006), which is a reparametrization of the model described in Fry & Gaztanaga (1993). In this model, the

galaxy overdensity, δ_g, is written as:

$$\delta_g = \epsilon + b_1\,\delta_m + b_2\,\delta_m^2 + \dots\,, \tag{4.15}$$

where ϵ is the shot noise, b_1 is the linear bias and b_2 is the non-linear bias from the second order term. Then, the relationship between the galaxy-matter power spectrum and the matter power spectrum is given by

$$P_{g\delta} = b_1\,P_{\delta\delta} + b_2\,A(k), \tag{4.16}$$

since by definition ϵ is not correlated with δ_m, and where $A(k)$, defined in Kwan et al. (2017), can be calculated using standard perturbation theory. Comparing this relation to (1.54), we identify b_1 as $b \cdot r$ in the case of linear bias, corresponding to $b_2 = 0$.

Applying this non-linear bias model to the fiducial case for the three redshift bins defined with BPZ, we find that b_1 is compatible with the results coming from the linear bias model, and that b_2 is compatible with zero, for all redshift bins. The uncertainties we obtain on both b_1 and b_2 are large – in the case of b_1 between 30% and up to twice as large as for the fiducial case, depending on the redshift bin; thus, this indicates that we are lacking statistical power on these large scales to obtain competitive constrains when we introduce another parameter in the modelling. Overall, the linear bias assumption holds for scales larger than 4 Mpc/h, given the current uncertainties. Hence, all the results presented in the following sections are obtained using the linear bias model.

4.5 Results

In this section we present the main results of this work. First, we introduce the tangential shear measurements to later proceed describing the galaxy bias results.

4.5.1 Tangential shear measurements

In this subsection we present the measured tangential shear as a function of the angular separation, shown in Fig. 4.4. In that figure, BPZ is used to define the lens bins and to estimate the $n(z)$ of the lenses, and SkyNet is used to estimate the $n(z)$ of the sources. Also, the shaded angular scales from Fig. 4.4 are not considered for the final galaxy bias measurements, which are performed on the range of separations from 4 Mpc/h to 100 arcmin (see Sec. 4.4.3).

We measured the tangential shear using two different shape catalogs: ngmix and im3shape (see Sec. 4.3.2), which correspond to different galaxy samples, and thus, different redshift distributions. Then, the measurements for the tangential shear for ngmix and im3shape cannot be directly compared because of the lensing efficiency being

	Redshift bin	$\chi^2_{\rm null}$/ndf (γ_t)	$\chi^2_{\rm null}$/ndf $(\gamma_\times)$	$b \cdot r$	$\chi^2_{\rm fit}$/ndf
BPZ ngmix (F)	$0.2 \leq z_l < 0.4$	72.2/6	3.6/6	0.87 ± 0.11	3.4/5
	$0.4 \leq z_l < 0.6$	138.2/8	4.9/8	1.12 ± 0.16	2.2/7
	$0.6 \leq z_l < 0.8$	59.5/9	8.7/9	1.24 ± 0.23	1.4/8
BPZ im3shape	$0.2 \leq z_l < 0.4$	56.8/6	0.95/6	0.79 ± 0.12	3.8/5
	$0.4 \leq z_l < 0.6$	79.0/8	5.2/8	1.03 ± 0.17	3.3/7
	$0.6 \leq z_l < 0.8$	35.1/9	3.0/9	1.08 ± 0.25	7.5/8
TPZ ngmix (F)	$0.2 \leq z_l < 0.4$	61.1/6	2.3/6	0.77 ± 0.11	1.9/5
	$0.4 \leq z_l < 0.6$	124.5/8	4.6/8	1.40 ± 0.21	1.9/7
	$0.6 \leq z_l < 0.8$	93.0/9	4.1/9	1.57 ± 0.27	0.82/8
TPZ im3shape	$0.2 \leq z_l < 0.4$	48.8/6	0.98/6	0.78 ± 0.13	4.5/5
	$0.4 \leq z_l < 0.6$	93.4/8	5.9/8	1.34 ± 0.22	0.83/7
	$0.6 \leq z_l < 0.8$	53.5/9	4.5/9	1.36 ± 0.28	6.7/8

Table 4.3: Best-fitting galaxy bias results ($b \cdot r$) for the four main different combinations of photo-z codes and shape catalogs, shown also in Fig. 4.6. For instance, BPZ ngmix stands for lens redshift bins defined with BPZ and ngmix as the source catalog. $\chi^2_{\rm null}$/ndf (γ_t) is the null χ^2 of the tangential shear over the number of degrees of freedom, covering the range of scales from 4 Mpc/h to 100 arcmin (not shadowed region in Fig. 4.4), and the same for the cross-component $\gamma_\times$. $\chi^2_{\rm fit}$ corresponds to the galaxy bias fit described in Sec. 4.4.3. All combinations use SkyNet as the photo-z code for the $n(z)$ of the sources.

different in both cases. Nevertheless, we will be able to compare galaxy bias measurements (see Fig. 4.6), which are independent of the source sample redshift distribution, assuming an unbiased estimation of the $n(z)$ (see Sec. 4.6.2). We choose ngmix to be the fiducial shape catalog as it includes more galaxies, inducing less shape noise in the measurement. This effect is especially noticeable at small scales, where the shape noise contribution dominates the error budget.

In Table 4.3 we display the χ^2 of the null hypothesis and the number of degrees of freedom for the tangential shear signal over the selected range of scales, for all the different redshift bins and photo-z codes. We measure a non-zero tangential shear signal over the aforementioned scales for all different photo-z and shape catalog choices. Calculating the signal-to-noise as S/N $= \sqrt{\chi^2_{\rm null}(\gamma_t) - N_{\rm bin}}$, where $N_{\rm bin}$ is the number of angular bins considered for the galaxy bias measurements, the maximum S/N we obtain is 11.4 for the mid-z BPZ + ngmix bin, and the minimum is 5.1 for the high-z BPZ + im3shape bin.

4.5.2 Galaxy bias results

In Fig. 4.5 we present the galaxy bias fits for the fiducial photo-z codes and shape catalog, using BPZ to define the lens bins and SkyNet to estimate the $n(z)$ of the sources for the three redshift bins. On the top panels, we show the measured tangential shear together with the best-fitting theory prediction for the tangential shear over the scales

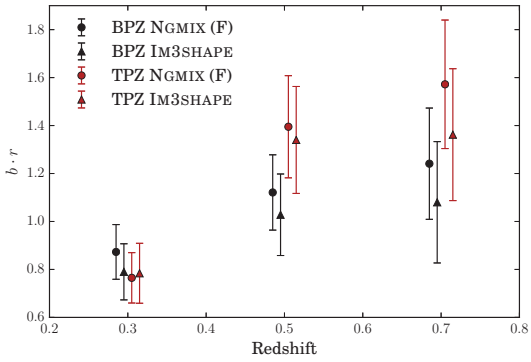

Figure 4.6: Fiducial galaxy bias results (F) along with a comparison between results obtained with different combinations of photo-z codes and shape catalogs. For instance, BPZ NGMIX stands for lens redshift bins defined with BPZ and NGMIX as the source catalog. All combinations use SkyNet as the photo-z code for the $n(z)$ of the sources. The points have been offset horizontally for clarity purposes.

of interest, which are from 4 Mpc/h to 100 arcmin. We display the comoving distance R on the bottom axis and the angular scale θ on the top axis. On the bottom panels, we show the galaxy bias as a function of separation with the best-fitting value, obtained using Eq. (4.14).

In Figs. 4.6 and 4.7 we show our fiducial galaxy bias results (BPZ + SkyNet with NGMIX and TPZ + SkyNet with NGMIX), along with the rest of combinations of photo-z codes and shape catalogs. The results from Fig. 4.6 are also presented in Table 4.3, together with the best-fit χ^2. The low χ^2 values in some of the cases might be due to an overestimation of the uncertainties given by the jackknife method, which will only lead to more conservative conclusions. In Fig. 4.6 we compare the results varying the photo-z code for the $n(z)$ of the lenses. However, this comparison is not straightforward due to the fact that galaxies in each lens sample are not the same – they have been defined using either BPZ or TPZ to directly compare with the measurements from Cr16 and G16, which use the same binning. Actually, the number of common galaxies in each redshift bin is: 273133, 406858, 348376, compared to the number of galaxies in each bin, given in Table 4.2. Hence, the galaxy bias might actually *be* different for each case. Nevertheless, even though we observe variations in the galaxy bias values, these differences are within the uncertainties. In Fig. 4.6 we also compare the galaxy bias results from using the two different shape catalogs NGMIX (fiducial) and IM3SHAPE. We obtain agreement between the results from the two shear samples.

In Fig. 4.7 we test the robustness of our results under the choice of the photo-z code used to estimate the $n(z)$ of the sources. We detect variations in the galaxy bias up to 6%, 9% and 14% for the three redshift bins, respectively. We include this source of systematic in the error budget as described in Sec. 4.6.2.

Galaxy bias evolution

In Figs. 4.6 and 4.7, we observe the evolution of the galaxy bias with redshift, in all combinations of photo-z codes and shape catalogs. There are two main reasons for this

evolution.

First, at high redshift ($z \sim 3$), galaxies form at special locations in the density field where they already trace the network of filaments emerging in the dark matter distribution. The dark matter correlation function grows in time as mass moves into this network from the surrounding regions, but the structure traced by galaxies stays relatively unchanged, and the galaxy correlation function is only weakly dependent on redshift (e.g. Weinberg et al. 2004). Then, because the dark matter correlation function does evolve in time, we expect the galaxy bias to evolve as well. More precisely, we expect the galaxy bias to be larger than one at high redshift, which means that the galaxy distribution is more clustered than the dark matter distribution.

Secondly, since we are studying a magnitude-limited sample of galaxies, in average we are naturally observing a higher luminosity sample at higher redshift. We find an increase of slightly more than a unit in absolute magnitude in the i band (corresponding to a factor of $\sim$3 in luminosity) between the low-z and the high-z lens bins. Since more luminous galaxies tend to be more biased, we would already expect the bias to increase with redshift even without intrinsic bias evolution.

4.6 Systematic effects in galaxy-galaxy lensing

In this section we explore the different systematic effects that can potentially plague our galaxy-galaxy lensing measurements. For that purpose, we perform some null tests on the data and present a series of calculations, some of them using previous analyses on the same data sample, which are all described in detail next. A summary of the significant contributions from these systematics to the total error budget is presented in Table 4.4.

4.6.1 Cross-component and tangential shear around random points

The cross-component of the shear $\gamma_\times$, which is rotated 45 degrees with respect to the tangential shear, should be compatible with zero if the shear is only produced by gravitational lensing. Hence, measuring $\gamma_\times$ provides a test of systematic errors, such as point-spread function (PSF) related errors, which can leak both into the tangential and cross-components of the galaxy shear. PSF leakage could arise from errors in the PSF model, as well as residual errors in correcting the PSF ellipticity to estimate the galaxy shear; such correction is done by analyzing the shape of stars in the field. In Sec. 4.4.1 we describe how the measurement of the cross-component of the shear is performed and in Fig. 4.4 is shown for the foreground redshift bins defined with BPZ. In order to test whether the cross-component of the shear is compatible with zero, we compute the null χ^2 statistic:

$$\chi^2_{\rm null} = \boldsymbol{\gamma}_\times^T \cdot \mathsf{Cov}^{-1} \cdot \boldsymbol{\gamma}_\times, \tag{4.17}$$

where the covariance matrix for the cross-component is estimated with the jackknife method, described in Sec. 4.4.2. Since jackknife covariance matrices comprise a non-negligible level of noise, in order to obtain an unbiased estimate of the inverse covariance a correction factor of $(N - p - 2)/(N - 1)$ has to be applied to the inverse covariance, where N is the number of JK regions and p is the number of angular bins (Hartlap, Simon & Schneider, 2007; Kaufman G.M, 1967). This factor corrects for the fact that, as mentioned in Sec. 4.2.3, the inverse of an unbiased but noisy estimate of the covariance matrix is not an unbiased estimator of the inverse of the covariance matrix. In Table 4.3 we show all the $\chi^2_{\rm null}$ values for each of the redshift bins, which are all consistent with zero.

A second test for galaxy-galaxy lensing is the measurement of the tangential shear around random points. This measurement tests the importance and possible contribution from geometrical effects in the signal. Although our estimator of galaxy-galaxy lensing in Eq. (4.8) includes the subtraction of the random points signal, it is useful to check that this correction is small. This measurement was presented in Clampitt et al. (2017) with the same sources that we use, and they found the signal to be consistent with zero.

4.6.2 Photometric redshift errors

In this section, we discuss the impact of photo-z errors on $b \cdot r$ uncertainties. Particularly, we focus on the effect caused by an overall shift on the redshift distribution of the sources. We approach this subject by following the recommendation from Bonnett et al. (2016) of adopting a Gaussian prior of width 0.05 for the shift δ_i on the mean of the distribution of the source galaxies: $n_i(z) \rightarrow n_i(z - \delta_i)$. We draw 1000 realizations of the δ_i, measuring the galaxy bias each time. Then, we add the standard deviation of the galaxy bias values in quadrature to the statistical error budget.

Including the photo-z error contribution represents a fractional increase of 7%, 38% and 42% to the galaxy bias statistical uncertainty for each redshift bin from low to high redshift (see Table 4.1), after averaging over all different photo-z choices (for ngmix only). Although almost the same source redshift distributions are used for the first ($0.2 \leq z_l < 0.4$ and $0.55 < z_s < 1.3$) and second redshift bin ($0.4 \leq z_l < 0.6$ and $0.55 < z_s < 1.3$) – not exactly the same because the veto masks are applied, which are different for each bin – the increase of the errors is significantly larger for the second redshift bin because of the geometrical factors involved. On the other hand, on average these photo-z uncertainties represent a 5%, 8% and 12% of the galaxy bias measured in each bin, similar to the 6%, 9% and 14% of maximum variation of the galaxy bias, with respect to the fiducial value, when changing the photo-z code to estimate the $n(z)$ of the source galaxies (see Sec. 4.5 and Fig. 4.7).

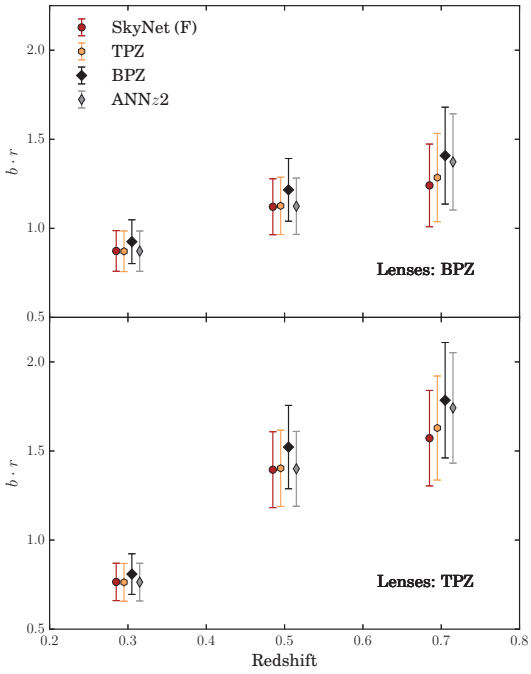

Figure 4.7: Galaxy bias results varying the photo-z code to estimate the redshift distribution of the source sample. For instance, for the red points, the $n(z)$ of the sources is estimated with SkyNet (Fiducial). We observe good agreement among the different results. *Top panel:* Lens redshift bins are defined with BPZ and the lens $n(z)$ is estimated using BPZ as well. *Bottom panel:* The same with TPZ. NGMIX is the source catalog used for these results. The points have been offset horizontally for clarity purposes.

4.6.3 Reduced shear and magnification

In all the results presented in this work, we have assumed, due to the weak lensing regime of our observations, $\kappa \ll 1$, $|\gamma| \ll 1$, that the observable reduced shear is equivalent to the shear induced by foreground mass structures, $g \approx \gamma$. Next, we provide justification for this assumption, mostly based on the work by Clampitt et al. (2017) (henceforth Cl16) presenting the galaxy-galaxy lensing measurements around Luminous Red Galaxies (LRGs) in DES-SV along with multiple systematics tests.

The observable reduced shear g is related to the shear γ according to Eq. (2.25).

Lens z-bin	$\sigma_{\rm stat}/(b\cdot r)$	$\sigma_{\text{p-}z}/(b\cdot r)$	$\sigma_{\rm m}/(b\cdot r)$	$\sigma_{\rm IA}/(b\cdot r)$
$0.2 \leq z_l < 0.4$	12%*	5%*	2%	–
$0.4 \leq z_l < 0.6$	9%*	8%*	2%	8%
$0.6 \leq z_l < 0.8$	12%*	12%*	2%	8%

* Average for the NGMIX sample.

Table 4.4: Summary of the systematic uncertainties to be added in quadrature to the statistical error budget. $\sigma_{\rm stat}$: Statistical uncertainty, as a fraction of the $b \cdot r$ values; $\sigma_{\text{p-}z}$: Photo-z uncertainty on the mean of the source redshift distribution (see Sec. 4.6.2); $\sigma_{\rm m}$: Mutiplicative shear biases (see Sec. 4.6.4); $\sigma_{\rm IA}$: Intrinsic alignments (see Sec. 4.6.5).

Since the lensing convergence κ will always be larger for a smaller distance from the halo center, the potential differences between g and γ will be largest at the lowest scales. Cl16 estimate this difference for their smallest radial scale, $R \sim 0.1$ Mpc/h, and their largest estimated halo mass, $M \sim 2 \times 10^{12} M_{\odot}/h$, and find it to be at most 0.7%. The smallest radial scale used in this work is significantly larger than that, $R \sim 4$ Mpc/h, and the mean halo mass of the benchmark galaxies is expected to be smaller than the LRG sample in Cl16, since it includes galaxies from all types and luminosities. Therefore, the error we make by ignoring non-weak shear effects will be smaller than 0.7%, and we neglect it in the analysis. Similarly, magnification can potentially affect the galaxy-galaxy lensing measurements, but it only becomes important for lenses with κ larger than the ones in the benchmark sample (see Mandelbaum et al., 2005 for a discussion of this effect).

4.6.4 Multiplicative shear biases

Jarvis et al. (2016) studied the residual multiplicative shear biases for the NGMIX and IM3SHAPE shear catalogs, for the same redshift bins that we use in this analysis. The residual multiplicative shear biases are shown in fig. 25 of that work, and for all the redshift bins that we use are less than 1%, except for the bin of NGMIX of $0.55 < z < 0.83$, where they reach 2%. We decided to add 2% of error in quadrature to the other sources of error, following the same approach as in Clampitt et al. (2017).

4.6.5 Intrinsic alignments

Intrinsic alignments (IA) in the shapes and orientations of source galaxies can be produced by gravitational tidal fields during galaxy formation and evolution. IA can induce correlations between the source ellipticity and the lens position if the two galaxies are physically close, essentially at the same redshift. We have worked under the assumption that the observed ellipticity of a galaxy is an unbiased estimation of its shear. However, a bias can arise since there is overlap in redshift between the lens and source populations used in this analysis (see Fig. 4.1), and hence we expect a contribution from IA in the observed tangential shear measurements.

At large scales, the dominant IA contribution arises from the alignment of galaxies with the tidal field, described by the "tidal/linear alignment model" (Catelan, Kamionkowski & Blandford, 2001; Hirata & Seljak, 2004; Blazek, Vlah & Seljak, 2015). On smaller scales, non-linear contributions, including angular momentum correlations from "tidal torquing," may be significant (e.g. Lee & Pen 2000). Tidal alignment is expected to be strongest for elliptical galaxies, which are pressure supported and thus have shapes and orientations that are less affected by angular momentum. Indeed, massive elliptical galaxies exhibit stronger alignments than fainter or bluer galaxies (e.g. Hirata et al.

2007; Mandelbaum et al. 2011). Including the non-linear evolution of the dark matter clustering improves the linear alignment model on smaller scales, yielding the so-called "nonlinear linear alignment model" (NLA) (Bridle & King, 2007).

We estimated the contribution of IA, assuming the NLA model, for the scenarios with the most overlap between the lenses and the sources: $0.4 \leq z_l < 0.6$ with $0.55 < z_s < 1.3$ and $0.6 \leq z_l < 0.8$ with $0.83 < z_s < 1.3$. Assuming a fiducial intrinsic alignment amplitude $A = 1$, a conventional normalization chosen by Hirata & Seljak (2004) to match ellipticity correlations in the SuperCOSMOS survey (Brown et al., 2002), a maximum fractional IA contamination on the tangential shear $|1 - \gamma_{\rm IA}/\gamma_t|$ of 4% was obtained for these samples. Also, we found the fractional IA contamination to be nearly scale-independent, since lensing and IA are sourced by the same underlying potential. DES Collaboration (2015) estimated the IA amplitude as $A = 2 \pm 1$ for the same DES-SV source sample. This result was model dependent, and A was found to be consistent with 0 for some cases. Following a conservative approach, we add an IA contamination of 8% in quadrature to the error budget, corresponding to an uncertainty at the level of $A = 2$.

4.6.6 Splitting sources in redshift

For the following test, we split the source population into two separate redshift bins. Although the tangential shear measurements from two source populations with different redshift distributions $n(z)$ will have different lensing efficiencies, we can still compare the galaxy bias, since the theory predicted tangential shear also depends on the source $n(z)$. Thus, the dependency of the galaxy bias on the source redshift distribution is cancelled in case of being able to determine it precisely. Otherwise, biases in the $n(z)$ can arise differences between the galaxy bias from the two source bins. Hence, in some sense, this is also a photo-z test.

We have separated the sources from the ngmix shear catalog with $0.55 < z_s < 1.3$ into the two higher redshift bins used in other DES-SV weak lensing analyses (e.g. DES Collaboration 2015), which are $0.55 < z_s < 0.83$, and $0.83 < z_s < 1.3$. We have performed this test on the low-z lens bin from 0.2 to 0.4, to minimize the impact intrinsic alignments effects could have on the test. For the BPZ lens bin, we obtain $b \cdot r = 0.78 \pm 0.15$ for the low-z source bin and $b \cdot r = 0.90 \pm 0.12$ for the high-z source bin. The two results are consistent, neglecting the correlation between the two measurements.

4.6.7 Observational systematic effects

DES is a photometric survey and, as such, it is subject to changing observing conditions that may affect the galaxy catalogs and the measurements performed with them.

Photo-z code	Probe	$0.2 \leq z_l < 0.4$	$0.4 \leq z_l < 0.6$	$0.6 \leq z_l < 0.8$
BPZ	g-g lensing – This work ($b \cdot r$)	0.87 ± 0.11	1.12 ± 0.16	1.24 ± 0.23
	g clustering – Crocce et al. (2016) (b)	1.05 ± 0.07	1.23 ± 0.05	1.35 ± 0.04
	g-CMB lensing – Giannantonio et al. (2016) ($b \cdot r$)	0.36 ± 0.22	0.76 ± 0.24	1.13 ± 0.25
TPZ	g-g lensing – This work ($b \cdot r$)	0.77 ± 0.11	1.40 ± 0.21	1.57 ± 0.27
	g clustering – Crocce et al. (2016) (b)	1.07 ± 0.08	1.24 ± 0.04	1.34 ± 0.05
	g-CMB lensing – Giannantonio et al. (2016) ($b \cdot r$)	0.41 ± 0.21	0.75 ± 0.25	1.25 ± 0.25
SkyNet	g-γ maps – Chang et al. (2016) (b/r)	1.12 ± 0.19	0.97 ± 0.15	1.38 ± 0.39

Table 4.5: Comparison between this work's fiducial galaxy bias measurements for BPZ and TPZ lens redshift bins, galaxy clustering measurements from Cr16, galaxy-CMB lensing real space measurements from G16 and bias measurements for SkyNet lens bins from cross-correlations between galaxy density and weak lensing maps from Chang et al. (2016).

Cr16 carried out a series of careful tests to determine and correct for any possible observational systematics in the data. In particular, they found a number of effects impacting on the detection efficiency of galaxies and hence causing density variations across the survey area. In order to study them, they used maps created from single-epoch properties potentially related to changes in the sensitivity of the survey, such as depth, seeing, airmass, etc. (see Leistedt et al., 2016 for more details on the creation of the maps). They reported significant effects of some of these quantities on the galaxy clustering observable, especially depth and seeing variations, and they corrected for them in several ways, including using cross-correlations between the galaxy and systematics maps, and the application of a veto mask avoiding the regions most affected by these systematics.

On the other hand, Kwan et al. (2017) studied the impact of the same systematics on galaxy-galaxy lensing, which being a cross-correlation is naturally more robust to systematic errors. They found that the effect in the galaxy-galaxy lensing observables is not significant given the statistical power of the observations in DES-SV. Based on these findings, we do not apply any correction from cross-correlations with systematics maps, but we do apply the veto masks in Cr16 to eliminate regions with high concentrations of these observational systematics (see Sec. 4.3.4).

4.7 Discussion and Comparison to previous work

In this work, we aim to provide another angle to the discussion of the possible tension between galaxy bias results in the DES-SV benchmark galaxy sample obtained using galaxy clustering (Cr16) and galaxy-CMB lensing correlations (G16) by adding a third probe to the discussion: galaxy-galaxy lensing.

In Cr16, galaxy bias was measured by finding the best-fit between the galaxy angular correlation function (2PCF) and a prediction of the same function using the non-linear dark matter power spectrum. The ratio of the measurement to the unbiased theory pre-

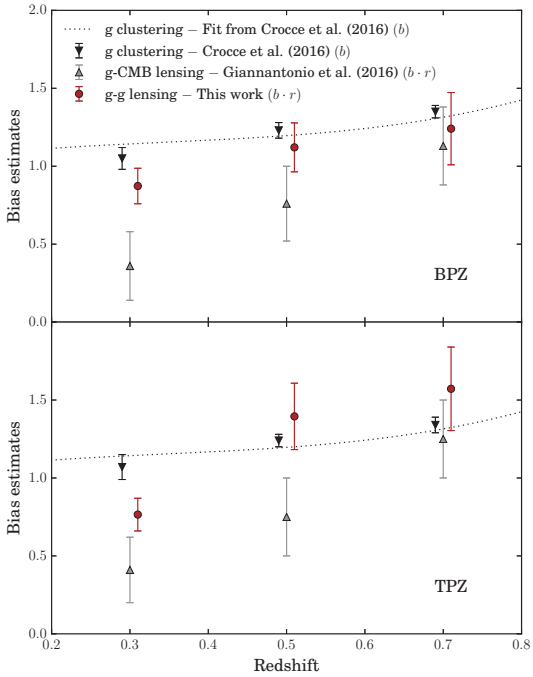

Figure 4.8: Fiducial galaxy bias results from this work using galaxy-galaxy lensing (g-g lensing, red points) as a function of redshift compared with previous measurements on the same Benchmark sample using galaxy clustering (g clustering, black down triangles) from Cr16 and the real space analysis results from CMB lensing (g-CMB lensing, gray upper triangles) from G16. *Top panel:* Lens redshift bins are defined with BPZ and the lens $N(z)$ is estimated using BPZ as well. *Bottom panel:* Lens redshift bins are defined with TPZ and the lens $N(z)$ is estimated using TPZ as well. The points have been offset horizontally for clarity purposes.

diction yields the square of the galaxy bias, b^2, from which b can be directly derived. G16 measured the cross-correlations between the galaxy density field and the lensing of the CMB, using both Planck and South Pole Telescope (SPT) maps. In that case, the comparison to theory predictions returns the galaxy bias b times a factor A_{Lens} which encapsulates different effects that can influence the amplitude of the CMB lensing signal. If the underlying true cosmology matches their fiducial ΛCDM model, A_{Lens} should be equal to one provided the scales they use are not affected by stochasticity or non-linearities. In the general case where those can be present, their estimator yields the galaxy bias times the cross-correlation coefficient, $b \cdot r$ (cf. G16 Section 7.4). The tomographic measurements of the galaxy bias were obtained using galaxy-SPT cross-correlations, due to their higher significance. Also, both real- and harmonic-space analyses were performed, yielding consistent results. All three analyses measure the galaxy bias of the same sample of galaxies, the so-called Benchmark sample. Also, aiming for consistency, the same fiducial cosmology is assumed in all three probes: a flat ΛCDM+ν (1 massive neutrino) cosmological model based on the Planck 2013 + WMAP polarization + highL (ACT/SPT) + BAO best-fit parameters from Ade et al. (2014).

In Fig. 4.8, as well as in Table 4.5, we compare our fiducial galaxy bias results with those from Cr16 and G16. In the top panel, lens redshift bins defined with BPZ are used and the $N(z)$ of the lenses is computed with BPZ for all probes, and analogously for TPZ on the bottom panel. However, different calculations of the galaxy bias cannot

be directly compared since the three probes do not measure exactly the same quantity. Instead, only the galaxy clustering measurement gives a direct estimate of the galaxy bias b. On the other hand, both galaxy-galaxy lensing and galaxy-CMB lensing are sensitive to $b \cdot r$. Nevertheless, the cross-correlation coefficient is expected to be close to unity over the scales considered in this work, $R > 4$ Mpc/h (see Sec. 4.4.3). Also, when comparing the different probes, their potential cross-covariance should be considered, since a significant covariance between them would make overall discrepancies more significant. The cross-covariance between galaxy-galaxy lensing and galaxy clustering is expected to be close to zero on small scales, where the errors are dominated by the lensing shape noise. On large scales, it is expected to be slightly higher; Mandelbaum et al. (2013) find values $\sim$ 10–15% but compatible with zero. Similarly, Baxter et al. (2016) found that CMB-lensing and galaxy-galaxy lensing measurements on the Benchmark sample are largely uncorrelated. For the following discussion, we assume there is no correlation between probes, which is reasonable given the statements above but should be noted. The different photo-z bins are also covariant to some extent, given their partial overlap in redshift due to photo-z errors and the use of shared sources in galaxy-galaxy lensing. Thus, since it is not easy to quantify the overall agreement of the results of the three probes across the three photo-z bins, we discuss the differences between probes on a bin by bin basis.

Then, as shown in Table 4.5, and neglecting the correlation between probes, our results of $b \cdot r$ are compatible within 1σ with results of Cr16 in all redshift bins, except for the low-z bin ($0.2 < z < 0.4$), with a 1.3σ difference in the BPZ case and a more significant 2.3σ tension for TPZ. Similarly, our measurements are in moderate tension with $b \cdot r$ results of G16 (1–2σ) at low and medium redshift ($0.2 < z < 0.6$), with a maximum tension of 2.1σ for the low-z BPZ bin and 2.0σ for the mid-z TPZ bin, while they are compatible within 1σ at higher redshift ($0.6 < z < 0.8$). However, note that the G16 results shown in Table 4.5 and Fig. 4.8 come from real space analysis. The galaxy bias results measured using harmonic space in G16 are closer to our measurements at low and medium redshift but further at higher redshift: 0.57 ± 0.25, 0.91 ± 0.22, 0.68 ± 0.28, from the low-z to the high-z bin, defined with TPZ.

A fourth analysis (Chang et al. 2016, hereafter Ch16) also measured the galaxy bias on DES-SV data cross-correlating weak lensing shear and galaxy density maps, using the method described first in Amara et al. (2012) and later re-examined in Pujol et al. (2016), which has the advantage that is only weakly dependent on the assumed fiducial cosmology. Ch16 measured the bias on the Benchmark sample assuming $r = 1$ over the considered range of scales, and using the same lens redshift binning as the three other analyses, but adopted SkyNet to define the lens redshift bins. Thus, the lens sample slightly differs from the one used in the other three probes. In Ch16 the galaxy bias was estimated in four tomographic bins; the results obtained for the first three redshift bins can be found in Table 4.5, which agree at the 1–2σ level with our measurements.

In Fig. 4.8 we observe that most of the differences between the results coming from auto-correlations and the ones coming from cross-correlations could be partially explained if $r < 1$. This would be the case if the galaxies are either stochastically or non-linearly biased, or a mixture of both (Pen, 1998; Simon et al., 2007). Consider a general relation between the galaxy density contrast δ_g and the dark matter density contrast δ_m:

$$\delta_g = f(\delta_m) + \epsilon\,, \tag{4.18}$$

where f is some function and ϵ a random variable (noise) that satisfy $\langle \epsilon\, f(\delta_m)\rangle = \langle \epsilon\, \delta_m\rangle = 0$, since ϵ is not correlated with either f or δ_m. If f is linear (δ_g and δ_m are Gaussian random variables) and $\epsilon = 0$, we have a linear deterministic relation between δ_g and δ_m: $\delta_g = b_1\, \delta_m$. Otherwise, f being a non-linear function leads to non-linear bias, and $\epsilon \neq 0$ introduces some dispersion in the relation, usually called stochasticity. Then, $r < 1$ can be generated by the presence of either non-linearities or stochasticity, or both, following from Eq. (1.53):

$$r = \frac{\langle \delta_m \delta_g\rangle}{\sqrt{\langle \delta_m^2\rangle \left\langle \delta_g^2\right\rangle}} = \frac{\langle \delta_m f(\delta_m)\rangle}{\sqrt{\langle \delta_m^2\rangle \left(\left\langle [f(\delta_m)]^2\right\rangle + \langle \epsilon^2\rangle\right)}}. \tag{4.19}$$

Next, we proceed to discuss the potential reasons for the possible tension between the galaxy bias estimations of the different probes, including non-linear and stochastic bias, which would both lead to $r < 1$, as well as how the choice of the fiducial cosmology can affect the bias results and what is the impact of systematics effects.

4.7.1 Non-linear bias

In Sec. 4.4.4, we have tested the impact of using a non-linear bias modelling for scales larger than 4 Mpc/h, obtaining results consistent with the linear bias values. Thus, linear bias theory is currently sufficient over this range of scales given our current uncertainties. Also, other DES-SV studies have been performed on the scale of linear bias. For instance, Kwan et al. (2017) followed a different approach to study it on the SV redMaGiC sample (Rozo et al., 2016), finding a slightly larger value of $\sim$5.5 Mpc/h, as expected for a red sample of galaxies.

In G16 smaller scales were used (down to 2.4 arcmin, which approximately corresponds to 0.6 Mpc/h at $z = 0.3$ and to 1.2 Mpc/h at $z = 0.7$), in order to extract as much signal as possible, since in their case the theoretical uncertainties due to non-linearities were much smaller than the statistical errors. Then, it is possible that non-linear bias is present over this range of scales. Refer to Sec. 4.4.3 for an extended discussion on the range of scales considered in this work.

4.7.2 Stochasticity

Assuming non-linear bias can be ignored on the scales of interest and also that the fiducial cosmology (defined in Sec. 4.2) is fixed, it is possible to attribute the differences between the results of different probes to stochasticity. In this special case, G16 measured $r = 0.73 \pm 0.16$ using a novel linear growth bias-independent estimator – denoted by D_G in G16 – which would imply a 1.7σ measurement that there is some stochasticity. In G16, the measurement was extended to lower separations, where r might deviate from one. Thus, this could partially explain the systematically lower results at low redshift of G16 compared to Cr16 and our measurements.

In our case, neglecting the correlation with Cr16, in the low-z bin we measure $r = 0.83 \pm 0.12$, that is, 1.3σ away from one, for BPZ, and $r = 0.71 \pm 0.11$, 2.6σ away from one, for TPZ, when comparing our results with those of Cr16. In the other redshift bins, the significance is much lower. Since Cr16 results and this work are potentially correlated, the given confidence levels are a lower limit.

4.7.3 Fiducial cosmology dependence

Another possibility for the differences in the galaxy bias results is that the true cosmology does not match the fiducial cosmology, since the various probes might depend differently on the cosmological parameters. Then, even if the same fiducial cosmology is assumed (defined in Sec. 4.2), which is the case for Cr16, G16 and this work, this could still produce variations in the galaxy bias results. Regarding Ch16, even though a different fiducial cosmology is assumed – the MICE cosmology (Fosalba et al., 2015,?; Crocce et al., 2015; Carretero et al., 2014) – their approach is only weakly dependent on it. On the contrary, the galaxy bias measurements in Cr16, G16 and this work are significantly dependent on cosmology.

Particularly, the three probes are especially sensitive to σ_8 and Ω_m. At large scales, if Ω_m is fixed, the galaxy bias becomes independent of scale and is hence fully degenerate with the amplitude of the matter power spectrum, σ_8. However, the dependency is different for each probe. At large scales, the galaxy clustering correlation function depends on σ_8 like $\omega^{gg}(\theta) \propto b^2\sigma_8^2$, the tangential shear as $\gamma_t \propto b \cdot r\ \sigma_8^2$ and the galaxy-CMB lensing correlation function as $\omega^{\kappa g}_{\rm CMB} \propto b \cdot r\ \sigma_8^2$. Then, the bias from the auto-correlation depends differently on σ_8 than the bias from the cross-correlations: $b \propto \sigma_8^{-1}$, $b \cdot r \propto \sigma_8^{-2}$. Hence, for instance, if the true value of σ_8 was lower than Planck's, as hinted by CFHTLenS (Heymans et al., 2013), b would increase, but $b \cdot r$ would increase even more, reducing the tension between probes in most of the cases.

As an illustration to this, also involving the other cosmological parameters, G16 studied how changing the fiducial cosmology from Planck to MICE affects the galaxy bias results. MICE simulations are based on the ΛCDM cosmological parameters: $\Omega_m = 0.25$, $\Omega_{\rm DE} = 0.75$, $\Omega_b = 0.044$, $\sigma_8 = 0.8$, $n_s = 0.95$ and $h = 0.7$. This variation

of the cosmological parameters produces an increase of the galaxy bias of $\sim 4\%$ for galaxy clustering and of $\sim 21\%$ for CMB lensing (G16), for the whole redshift range $0.2 < z_l < 1.2$. For galaxy-galaxy lensing, we obtain an increase of $\sim 22\%$, for the redshift bin whose mean value is closest to the one G16 uses. Thus, the relative increases of the galaxy bias would reduce the existing tension between probes in most of the cases.

Furthermore, we studied how the results vary performing a more plausible change in the fiducial cosmology. Using Planck 2015 + External cosmology (TT, TE, EE + lowP + Lensing + BAO + SN Ia): $\Omega_m = 0.307$, $\Omega_{\nu_{\rm mass}} = 0.00139$, $\Omega_b = 0.0486$, $\sigma_8 = 0.816$, $n_s = 0.967$ and $h = 0.677$ (Ade et al., 2016), which corresponds to a 1σ variation of σ_8 with respect to the Planck 2013 value, represents an increase of $\sim 4\%$ in the bias from galaxy-galaxy lensing, not enough to account for all the difference between probes. Further discussion on how the various cosmological parameters and models impact the bias measurements can be found in G16.

4.7.4 Photo-z errors and systematics

Another possible reason for the tension between probes are systematic errors. In Sánchez et al. (2014) it was found that the absence of u band could have led to imprecise photo-z measurements, particularly in the lowest redshift bin, which could potentially induce larger uncertainties in the redshift distribution of galaxies, which can affect differently each probe. For instance, auto-correlations are more sensitive to the width of the $N(z)$ distribution, while cross-correlations are more sensitive to its mean. Moreover, the shape of the CMB lensing kernel could increase the impact of photo-z uncertainties at low-z (see G16 for an extended discussion of how photo-z can influence each probe).

Other systematics, such as stellar contamination, can also alter the galaxy bias results in a different manner for each probe. For instance, in the case of stellar contamination, the measured galaxy clustering amplitude would be higher than otherwise, increasing the bias as well. This is already taken into account in Cr16. On the other hand, the tangential shear amplitude and the galaxy-CMB lensing cross-correlation would decrease, and so would the bias. The stellar contamination of the DES galaxy sample in the COSMOS field was found to be at most 2% in Cr16. Although this might contribute to the observed differences in the bias, such a small contamination would produce negligible variations compared to the statistical errors.

Overall, as a conclusion for the discussion presented in this section, we find no strong evidence that the cross-correlation coefficient is smaller than one, except perhaps at low redshift. In the $0.2 < z_l < 0.4$ bin, we measure $r = 0.83 \pm 0.12$ for BPZ, and $r = 0.71 \pm 0.11$ for TPZ, provided the differences between probes are attributed

only to the cross-correlation parameter being smaller than one. Both non-linear bias and stochasticity can cause $r < 1$, but, since the linear bias model is found to be a good fit for our data given the current uncertainties, our findings favor stochasticity.

Another possibility is that the differences do not have a single origin, but that they result from a combination of a few of the effects presented during this discussion. Some of these potential reasons, such as a mismatch between the fiducial cosmology and the underlying true cosmology or photo-z errors, while unlikely to account for the differences separately, might be able to explain them when combined.

The DES-SV data used in this analysis represents only about 3% of the final survey coverage. With these data, we have acquired some hints of possible causes that might have generated the differences between the results from the three probes (Cr16, G16 and this work), which will be useful for future measurements. Additional data from DES will significantly reduce the statistical uncertainties as well as allowing to probe larger scales, which will enable more precise studies of galaxy bias. In Section 5.7 of this thesis we revisit this topic, and compare galaxy bias measurements from galaxy clustering and from galaxy-galaxy lensing using DES data from the first year of observations.

Part III

Galaxy-galaxy lensing to probe cosmology

In this part we use DES data from the first year of observations to measure the galaxy-galaxy lensing data vector and test its robustness against a set of potential systematics, which we present in the first chapter of this part. These measurements are then used in the 3x2pt DES Y1 cosmological analysis, which combines weak lensing and galaxy clustering probes to obtain cosmological parameters. The cosmological results from this powerful and robust combination are shown in the second chatper of this part.

Chapter 5

Dark Energy Survey Year 1 Results: Galaxy-Galaxy Lensing

5.1 Introduction

Weak gravitational lensing refers to the small distortions in the images of distant galaxies by intervening mass along the line of sight. Galaxy-galaxy lensing refers to the cross-correlation between foreground (lens) galaxy positions and the lensing shear of background (source) galaxies at higher redshifts (Tyson et al., 1984; Brainerd, Blandford & Smail, 1996; Dell'Antonio & Tyson, 1996). The component of the shear that is tangential to the perpendicular line connecting the lens and source galaxies is a measure of the projected, excess mass distribution around the lens galaxies. Galaxy-galaxy lensing at small scales has been used to characterize the properties of dark matter halos hosting lens galaxies, while at large scales it measures the cross correlation between galaxy and matter densities. The measurements have many applications, ranging from constraining halo mass profiles (Navarro, Frenk & White, 1997) to estimating the large-scale bias of a given galaxy population to obtaining cosmological constraints (Cacciato et al., 2009; Mandelbaum et al., 2013; Cacciato et al., 2013; More et al., 2015; Kwan et al., 2017; van Uitert et al., 2017a). Recent surveys such as CFHTLenS (Heymans et al., 2012; Erben et al., 2013) have presented measurements on galaxy-galaxy lensing (Gillis et al., 2013; Velander et al., 2014; Hudson et al., 2015). Similarly, measurements from KiDS (de Jong et al., 2013; Kuijken et al., 2015) have also studied the galaxy-mass connection using galaxy-galaxy lensing (Sifon et al., 2015; Viola et al., 2015; van Uitert et al., 2016; Joudaki et al., 2017). The galaxy-mass connection has also been studied in Sheldon et al. (2004); Mandelbaum et al. (2006) and by Leauthaud et al. (2012) at high redshift.

In this thesis we present measurements and extensive tests of the tomographic galaxy-galaxy lensing signal from Year 1 data of the Dark Energy Survey (DES). Our goals are to present the measurements of galaxy-galaxy lensing with DES, carry out a series of null tests of our measurement pipeline and the data, and carry out related

analyses of the lensing and photometric redshift (photo-z) performance that are critical for the Y1 cosmological analysis (DES Collaboration, 2018b). We use five redshift bins for the lens galaxies and four bins for the source galaxies. The detailed tests presented here will serve as a foundation for future work relying on galaxy-galaxy lensing measurements, such as Halo Occupation Distribution (HOD) analyses (Berlind & Weinberg, 2002; Cooray & Sheth, 2002). The galaxy-galaxy lensing studies with the DES Science Verification (SV) data, such as the work presented in the previous chapter (Prat et al., 2018b), serve as precursors to this part of the thesis (Clampitt et al., 2017; Park et al., 2016; Kwan et al., 2017).

The lens galaxy sample used is the red-sequence Matched-filter Galaxy Catalog (redMaGiC, Rozo et al. 2016), which is a catalog of photometrically selected luminous red galaxies (LRGs). The redMaGiC algorithm uses the redMaPPer-calibrated model for the color of red-sequence galaxies as a function of magnitude and redshift (Rykoff et al., 2014, 2016). This algorithm constructs a galaxy sample with far more reliable redshift estimates than is achievable for a typical galaxy in DES.

For the source galaxy redshifts, we rely on less well-constrained photo-z estimates, calibrated in two independent ways (Hoyle et al., 2018; Gatti et al., 2018; Davis et al., 2017). In this thesis, we use the expected behavior of the galaxy-galaxy lensing signal with the distance to source galaxies (the shear-ratio test) to validate the photo-z estimates and calibration. The scaling of the galaxy-galaxy lensing signal with source redshift for a given lens bin is mostly driven by the geometry of the lens-source configuration, with cosmology dependence being subdominant to potential biases in the redshift estimation of the galaxies involved. Therefore, such measurements provide useful constraints on the redshift distribution of source galaxies, which we then compare to findings by independent studies.

The DES Y1 cosmological analysis (DES Collaboration, 2018b) relies on the assumption that the cross-correlation coefficient between galaxies and matter is unity on the scales used for this analysis. In this work we provide validation for this assumption by showing the linear galaxy bias estimates from galaxy-galaxy lensing to be consistent with those obtained from galaxy clustering using the same galaxy sample (Elvin-Poole et al., 2018).

The plan of the chapter is as follows. In Section 5.2, we present the modelling. Section 5.3 describes our data, including basic details of DES, descriptions of the lens galaxy sample, pipelines for source galaxy shape measurements, and the photometric redshift estimation of lens and source galaxies. We also describe a set of lognormal simulations used for tests of the measurement methodology. The details of the measurement and covariance estimation, together with our galaxy-galaxy lensing measurements, are presented in Section 5.4. Tests of potential systematic effects on the measurement are shown in Section 5.5. Section 5.6 presents the use of tomographic galaxy-galaxy lensing to test the photo-z's of source galaxies. Finally, in Section 5.7 we compare the galaxy

bias estimates from galaxy-galaxy lensing to those obtained using the angular clustering of galaxies (Elvin-Poole et al., 2018), and we conclude in Section 5.8.

5.2 Theory

Galaxy-galaxy lensing is the measurement of the tangential shear of background (source) galaxies around foreground (lens) galaxies (see Bartelmann & Schneider (2001) for a review). The amplitude of distortion in the shapes of source galaxies is correlated with the amount of mass that causes passing light rays to bend. Assuming that lens galaxies trace the mass distribution following a simple linear biasing model ($\delta_g = b\delta_m$), the galaxy-matter power spectrum relates to the matter power spectrum by a single multiplicative bias factor. In this case, the tangential shear of background galaxies in redshift bin j around foreground galaxy positions in redshift bin i at an angular separation θ can be written as the following integral over the matter power spectrum $P_{\delta\delta}$:

$$\gamma_t^{ij}(\theta) = b^i \, \frac{3}{2} \, \Omega_m \left(\frac{H_0}{c}\right)^2 \int \frac{d\ell}{2\pi} \, \ell \, J_2(\theta\ell) \times$$
$$\times \int dz \left[\frac{g^j(z) \, n_l^i(z)}{a(z) \, \chi(z)} \, P_{\delta\delta}\left(k = \frac{\ell}{\chi(z)}, \, \chi(z)\right)\right], \tag{5.1}$$

where we are assuming $b^i(z) = b^i$ within a lens redshift bin, J_2 is the second order Bessel function, l is the multipole moment, k is the 3D wavenumber, a is the scale factor, χ is the comoving distance to redshift z, $n_l^i(z)$ is the redshift distribution of foreground (lens) galaxies in bin i and $g^j(z)$ is the lensing efficiency for background galaxies in bin j, computed as

$$g^j(z) = \int_z^\infty dz' \, n_s^j(z') \, \frac{\chi(z') - \chi(z)}{\chi(z')}, \tag{5.2}$$

where $n_s^j(z)$ is the corresponding redshift distribution of background (source) galaxies in bin j. The tangential shear in Eq. (5.1) depends on the cosmological parameters not only through the explicit dependencies but also through the matter power spectrum $P_{\delta\delta}$. Nonetheless, the dependence on the cosmological parameters is heavily degenerate with the galaxy bias of the lens galaxy population, b^i.

It is also useful to express the tangential shear in terms of the excess surface mass density $\Delta\Sigma$. This estimator is typically used to study the properties of dark matter halos (see for instance Mandelbaum et al. (2006)). However, with the large scales used in this analysis, the lensing effect is caused by general matter overdensities which are traced by galaxies. In this work, we make use of this estimator because the geometrical

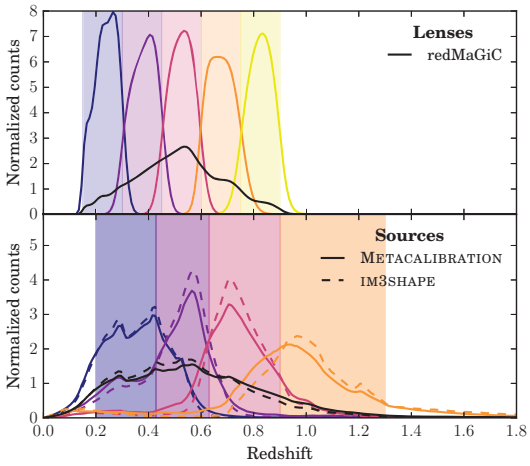

Figure 5.1: (*Top panel*): Redshift distributions of redMaGiC lens galaxies divided in tomographic bins (*colors*) and for the combination of all of them (*black*). The $n(z)$'s are obtained stacking individual Gaussian distributions for each galaxy. (*Bottom panel*): The same, but for our two weak lensing source samples, Metacalibration and im3shape, using the BPZ photometric redshift code.

dependence of the lensing signal becomes more evident. The estimator reads:

$$\gamma_t = \frac{\Delta\Sigma}{\Sigma_{\rm crit}}, \tag{5.3}$$

where the lensing strength $\Sigma_{\rm crit}^{-1}$ is a geometrical factor that depends on the angular diameter distance to the lens $D_{\rm l}$, the source $D_{\rm s}$ and the relative distance between them $D_{\rm ls}$:

$$\Sigma_{\rm crit}^{-1}(z_{\rm l}, z_{\rm s}) = \frac{4\pi G}{c^2}\frac{D_{\rm ls}\, D_{\rm l}}{D_{\rm s}}, \tag{5.4}$$

with $\Sigma_{\rm crit}^{-1}(z_l, z_s) = 0$ for $z_s < z_l$, and where z_l and z_s are the lens and source galaxy redshifts, respectively. Since the redshift distributions of our lens and source samples, $n_l(z), n_s(z)$ respectively, have a non-negligible width and even overlap, we take this into account by defining an effective $\Sigma_{\rm crit}^{-1}$ integrating over the corresponding redshift distributions. For a given lens bin i and source bin j, this has the following form:

$$\Sigma_{\rm crit,eff}^{-1\,i,j} = \int\int dz_l dz_s\, n_l^i(z_l)\, n_s^j(z_s)\, \Sigma_{\rm crit}^{-1}(z_l, z_s). \tag{5.5}$$

We need to assume a certain cosmology (flat ΛCDM with $\Omega_m = 0.3$) when calculating the angular diameter distances in $\Sigma_{\rm crit}^{-1}$. The results presented in this analysis depend only weakly on this choice of cosmology, as we will further discuss in the relevant sections (see Sec. 5.6).

5.3 Data and simulations

The Dark Energy Survey is a photometric survey that will cover about one quarter of the southern sky (5000 sq. deg.) to a depth of $r > 24$, imaging about 300 million galaxies in 5 broadband filters ($grizY$) up to redshift $z = 1.4$ (Flaugher et al., 2015; DES Collaboration, 2016). In this work we use data from a large contiguous region of 1321 sq. deg. of DES Year 1 observations which overlaps with the South Pole Telescope footprint -60 deg. < δ < -40 deg. and reaches a limiting magnitude of ≈ 23 in the r-band (with a mean of 3 exposures out of the planned 10 for the full survey). Y1 images were taken between 31 Aug 2013 and 9 Feb 2014.

5.3.1 Lens sample: redMaGiC

The lens galaxy sample used in this work is a subset of the DES Y1 Gold Catalog (Drlica-Wagner et al., 2018) selected by redMaGiC (Rozo et al., 2016), which is an algorithm designed to define a sample of luminous red galaxies (LRGs) with minimal photo-z uncertainties. It selects galaxies above some luminosity threshold based on how well they fit a red sequence template, calibrated using redMaPPer (Rykoff et al., 2014, 2016) and a subset of galaxies with spectroscopically verified redshifts. The cutoff in the goodness of fit to the red sequence is imposed as a function of redshift and adjusted such that a constant comoving number density of galaxies is maintained. The redMaGiC photo-z's show excellent performance, with a scatter of $\sigma_z/(1+z) = 0.0166$ (Elvin-Poole et al., 2018). Furthermore, their errors are very well characterized and approximately Gaussian, enabling the redshift distribution of a sample, $n(z)$, to be obtained by stacking each galaxy's Gaussian redshift probability distribution function (see Rozo et al. (2016) for more details).

The sample used in this work is a combination of three redMaGiC galaxy samples, each of them defined to be complete down to a given luminosity threshold $L_{\rm min}$. We split the lens sample into five equally-spaced tomographic redshift bins between $z = 0.15$ and $z = 0.9$, with the three lower redshift bins using the lowest luminosity threshold of $L_{\rm min} = 0.5L^\star$ (named High Density sample) and the two highest redshift bins using higher luminosity thresholds of $L_{\rm min} = 1.0L^\star$ and $L_{\rm min} = 1.5L^\star$ (named High Luminosity and Higher Luminosity samples, respectively). Using the stacking procedure mentioned above, redshift distributions are obtained and shown in Fig. 5.1. Furthermore, redMaGiC samples have been produced with two different photometric reduction techniques, `MAG_AUTO` and Multi-object fitting photometry (`MOF`), both described in Drlica-Wagner et al. (2018). We follow the analysis of Elvin-Poole et al. (2018) and we use `MAG_AUTO` photometry for the three lower redshift bins and `MOF` photometry for the rest, as it was found in Elvin-Poole et al. (2018) that this combination was optimal in minimizing systematic effects that introduce spurious angular galaxy clus-

tering.

5.3.2 Source samples: Metacalibration and im3shape

See section 3.2 for a description of the im3shape and Metacalibration algorithms. Due to conservative cuts on measured galaxy properties, e. g. signal-to-noise ratio and size, that have been applied to both Metacalibration and im3shape, the number of galaxies comprised in each shear catalog is significantly reduced compared to that of the full Y1 Gold catalog. Still, the number of source galaxies is unprecedented for an analysis of this kind. Metacalibration consists of 35 million galaxy shape estimates, of which 26 are used in the cosmological analysis due to redshift and area cuts, and im3shape is composed of 22 million galaxies, of which 18 are used for cosmology. The fiducial results in this chapter, for instance in Sec. 5.6 and Sec. 5.7, utilize Metacalibration due to the higher number of galaxies included in the catalog.

5.3.3 Photometric redshifts for the source sample

Galaxy redshifts in DES are estimated from $griz$ multiband photometry. The performance and accuracy of these estimates was extensively tested with Science Verfication (SV) data, using a variety of photometric redshift algorithms and matched spectroscopy from different surveys (Sánchez et al., 2014; Bonnett et al., 2016).

The fiducial photometric redshifts used in this work are estimated with a modified version of the Bayesian Photometric Redshifts (BPZ) code (Benitez, 2000; Hoyle et al., 2018). BPZ defines the mapping between color and redshift by drawing upon physical knowledge of stellar population models, galaxy evolution and empirical spectral energy distributions of galaxies at a range of redshifts.

Such photo-z's are used to split our source samples into four tomographic bins by the mean of the estimated individual redshift probability density functions ($p(z)$) between $z = 0.2$ and $z = 1.3$. For Metacalibration in particular, where potential selection biases need to be corrected for (cf. Equation 5.4.1), this is done using photo-z estimates based on Metacalibration measurements of multiband fluxes. For both shear catalogs, the corresponding redshift distributions come from stacking random draws from the $p(z)$ and are shown in Fig. 5.1. Details of this procedure are described in section 3.3 of Hoyle et al. (2018).

The photo-z calibration procedure we follow in Y1 is no longer based on spectroscopic data, since existing spectroscopic surveys are not sufficiently complete over the magnitude range of the DES Y1 source galaxies. Instead, we rely on complementary comparisons to 1) matched COSMOS high-precision photometric redshifts and 2) constraints on our redshift distributions from DES galaxy clustering cross-correlations. We refer the reader to the four dedicated redshift papers (Hoyle et al., 2018; Davis et al.,

2017; Gatti et al., 2018; Cawthon et al., 2018). In addition, in this work we will provide further independent validation of their calibration, using weak gravitational lensing (Sec. 5.6).

5.3.4 Lognormal simulations

Lognormal models of cosmological fields, such as matter density and cosmic shear, have been shown to accurately describe two-point statistics such as galaxy-galaxy lensing on sufficiently large scales. Furthermore, the production of lognormal mock catalogs that reproduce properties of our sample is significantly less demanding in terms of computational expenses than N-body simulations such as those detailed in DeRose et al. (2017). One of the first descriptions of lognormal fields in cosmological analyses was outlined in Coles & Jones (1991). The assumption of lognormality for these cosmological fields has shown good agreement with N-body simulations and real data up to nonlinear scales (Kayo, Taruya & Suto, 2001; Lahav & Suto, 2004; Hilbert, Hartlap & Schneider, 2011). Thus, lognormal mock simulations provide a way to assess properties of the galaxy-galaxy lensing covariance matrix that are particularly dependent on the number of simulations produced, due to their low-cost nature of production.

We use the publicly available code FLASK[1] (Xavier, Abdalla & Joachimi, 2016), to generate galaxy position and convergence fields consistent with our lens and source samples, and produce 150 full-sky shear and density mock catalogs. The maps are pixelated on a HEALPix grid with resolution set by an $N_{\rm side}$ parameter of 4096. At this $N_{\rm side}$, the typical pixel area is 0.73 arcmin^2 and the maximum multipoles resolved for clustering and shear are $\ell = 8192$ and $\ell = 4096$, respectively. We mask out regions of the grid to then produce eight DES Y1 footprints for a given full-sky mock. This produces a total of 1200 mock surveys that mimic our sample.

To correctly capture the covariance properties of this sample, such as shot noise, we match the number density of the mock tomographic bins to those of the data. We add noise properties to the shear fields according to the same procedure detailed in Troxel et al. (2018). Galaxy bias is introduced in the lens samples through the input angular auto and cross power spectra between bins, and is also chosen to approximately match the data. The tracer density fields are subsequently Poisson sampled to yield discrete galaxy positions.

[1] `http://www.astro.iag.usp.br/~flask/`

5.4 Measurement and covariance

5.4.1 Measurement methodology

Here we describe the details of the tangential shear measurement $\langle\gamma_t\rangle$. Similarly, we can measure the cross-component of the shear $\langle\gamma_\times\rangle$, which is a useful test of possible systematic errors in the measurement as it is not produced by gravitational lensing. For a given lens-source galaxy pair j we define the tangential (e_t) and cross ($e_\times$) components of the ellipticity of the source galaxy as

$$e_{t,j} = -\mathrm{Re}\left[e_j \mathrm{e}^{-2i\phi_j}\right] \quad , \quad e_{\times,j} = -\mathrm{Im}\left[e_j \mathrm{e}^{-2i\phi_j}\right], \tag{5.6}$$

where $e_j = e_{1,j} + i\, e_{2,j}$, with $e_{1,j}$ and $e_{2,j}$ being the two components of the ellipticity of the source galaxy measured with respect to a Cartesian coordinate system centered on the lens, and ϕ_j being the position angle of the source galaxy with respect to the horizontal axis of the Cartesian coordinate system. Assuming the intrinsic ellipticities of individual source galaxies are randomly aligned, we can obtain the mean weak lensing shear $\left\langle\gamma_{t/\times}\right\rangle$ averaging the ellipticity measurements for each component over many such lens-source pairs. However, note that the assumption of random galaxy orientations is broken by intrinsic galaxy alignments (IA), which lead to non-lensing shape correlations (e.g. Troxel & Ishak 2015), which are included in the modelling of the combined probes cosmology analysis (DES Collaboration, 2018b)). Then:

$$\langle\gamma_\alpha(\theta)\rangle = \frac{\sum_j \omega_j e_{\alpha,j}}{\sum_j \omega_j}, \tag{5.7}$$

where θ is the angular separation, $\alpha = t$ or $\times$ denotes the two possible components of the shear and $w_j = w_\mathrm{l}\, w_\mathrm{s}\, w_\mathrm{e}$ is a weight associated with each lens-source pair, which will depend on the lens (w_l, see 5.5.4), on the source weight assigned by the shear catalog (w_s, see 5.4.1 & 5.4.1) and on a weight assigned by the estimator (w_e, see App. A). These estimates need to be corrected for shear responsivity (in the case of Metacalibration shears, 5.4.1) or multiplicative and additive bias (in the case of im3shape, 5.4.1). Also note that in this work $w_\mathrm{e} = 1$ because we are using the γ_t estimator, which weights all sources uniformly. Another option would be to choose an optimal weighting scheme that takes into account the redshift estimate of the source galaxies to maximize the lensing efficiency, as it is the case of the $\Delta\Sigma$ estimator. In the context of a cosmological analysis combining galaxy-galaxy lensing and cosmic shear, using uniform weighting for the sources has the considerable advantage that nuisance parameters describing the systematic uncertainty of shear and redshift estimates of the sources are the same for both probes. In Appendix A, we find the increase in signal-to-noise ratio due to the optimal weighting scheme to be small given the photo-z precision of source galaxies

in DES, and hence we use the γ_t estimator in this work to minimize the number of nuisance parameters in the DES Y1 cosmological analysis (DES Collaboration, 2018b).

In all measurements in this work, we grouped the galaxy pairs in 20 log-spaced angular separation bins between 2.5 and 250 arcmin. We use `TreeCorr`[2] (Jarvis, Bernstein & Jain, 2004) to compute all galaxy-galaxy lensing measurements in this work.

One advantage of galaxy-shear cross-correlation over shear-shear correlations is that additive shear systematics (with constant γ_1 or γ_2) average to zero in the tangential coordinate system. However, this cancellation only occurs when sources are distributed isotropically around the lens and additive shear is spatially constant, two assumptions that are not accurate in practice, especially near the survey edge or in heavily masked regions, where there is a lack of symmetry on the source distribution around the lens. To remove additive systematics robustly, we also measure the tangential shear around random points: such points have no net lensing signal (see Sec. 5.5.1), yet they sample the survey edge and masked regions in the same way as the lenses. Our full estimator of tangential shear can then be written as:

$$\langle \gamma_\alpha(\theta) \rangle = \langle \gamma_\alpha(\theta)_{\rm Lens} \rangle - \langle \gamma_\alpha(\theta)_{\rm Random} \rangle \,. \tag{5.8}$$

Besides accounting for additive shear systematics, removing the measurement around random points from the measurement around the lenses has other benefits, such as leading to a significant decrease of the uncertainty on large scales, as was studied in detail in Singh et al. (2016). We further discuss the implications the random point subtraction has on our measurement and covariance in App. B.

Metacalibration responses

In the Metacalibration shear catalog (Huff & Mandelbaum, 2017; Sheldon & Huff, 2017; Zuntz et al., 2018), shears are calibrated using the measured response of the shear estimator to shear, which is usually the ellipticity $\boldsymbol{e} = (e1, e2)$. Expanding this estimator in a Taylor series about zero shear

$$\begin{aligned} \boldsymbol{e} &= \boldsymbol{e}|_{\gamma=0} + \left.\frac{\partial \boldsymbol{e}}{\partial \boldsymbol{\gamma}}\right|_{\gamma=0} \boldsymbol{\gamma} + ... \\ &\equiv \boldsymbol{e}|_{\gamma=0} + \boldsymbol{R}_\gamma \boldsymbol{\gamma} + ... \,, \end{aligned} \tag{5.9}$$

we can define the shear response $\boldsymbol{R}_\gamma$, which can be measured for each galaxy by artificially shearing the images and remeasuring the ellipticity:

$$R_{\gamma,i,j} = \frac{e_i^+ - e_i^-}{\Delta\gamma_j}, \tag{5.10}$$

[2] `https://github.com/rmjarvis/TreeCorr`

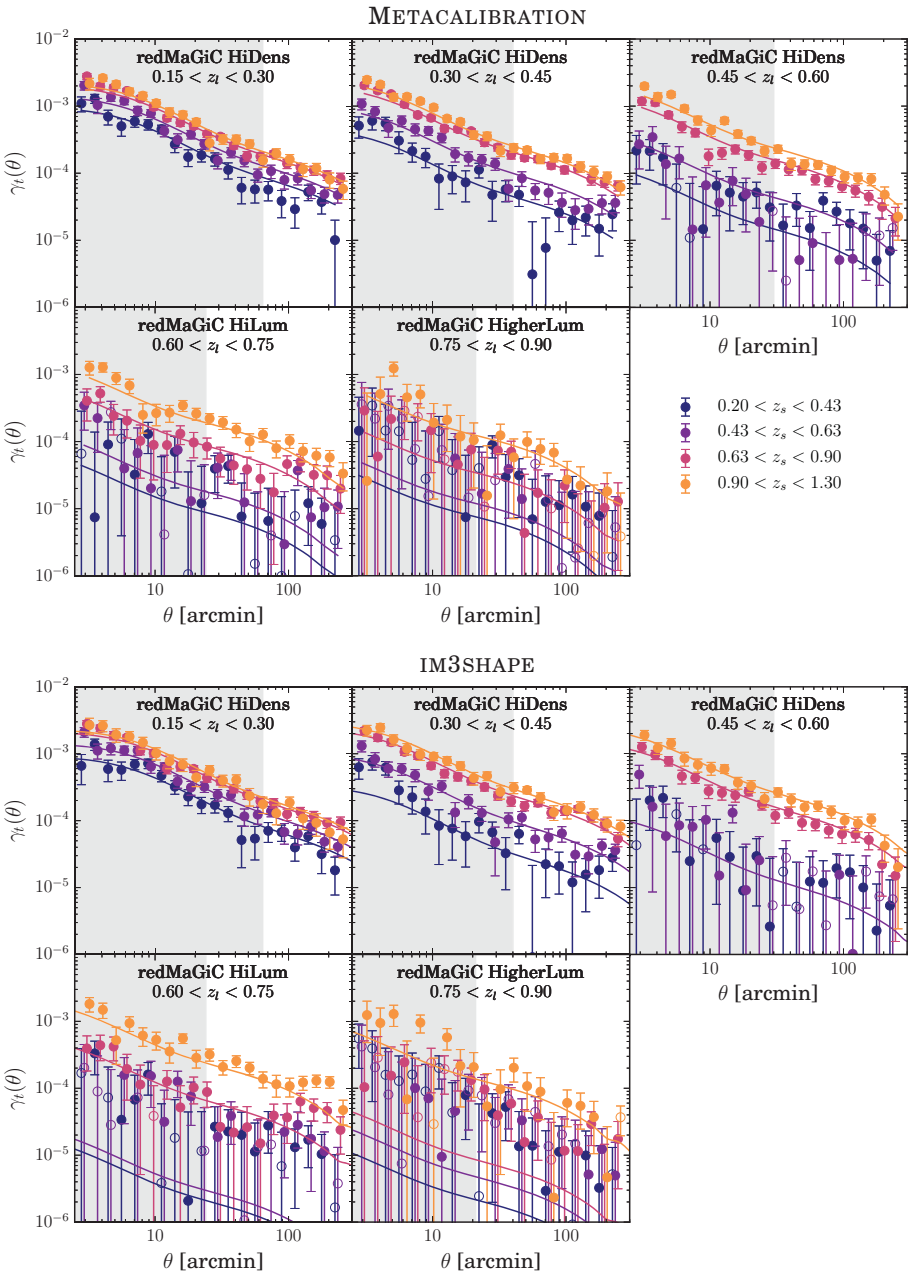

Figure 5.2: Tangential shear measurements for Metacalibration and im3shape together with the best-fit theory lines from the DES Y1 multiprobe cosmological analysis (DES Collaboration, 2018b). Scales discarded for the cosmological analysis, smaller than $12\,h^{-1}\mathrm{Mpc}$ in comoving distance, but which are used for the shear-ratio test, are shown as shaded regions. Unfilled points correspond to negative values in the tangential shear measurement, which are mostly present in the lens-source combinations with low signal-to-noise due to the lenses being at higher redshift than the majority of sources. `HiDens`, `HiLum` and `HigherLum` correspond to the three redmagic samples (High Density, High Luminosity and Higher Luminosity) described in Sec. 5.3.1.

where e_i^+, e_i^- are the measurements made on an image sheared by $+\gamma_j$ and $-\gamma_j$, respectively, and $\Delta\gamma_j = 2\gamma_j$. In the Y1 Metacalibration catalog, $\gamma_j = 0.01$. If the estimator $\boldsymbol{e}$ is unbiased, the mean response matrix $\langle R_{\gamma,i,j}\rangle$ will be equal to the identity matrix.

Then, averaging Eq. (5.9) over a sample of galaxies and assuming the intrinsic ellipticities of galaxies are randomly oriented, we can express the mean shear as:

$$\langle\gamma\rangle \approx \langle\boldsymbol{R}_\gamma\rangle^{-1}\langle\boldsymbol{e}\rangle \tag{5.11}$$

It is important to note that any shear statistic will be effectively weighted by the same responses. Therefore, such weighting needs to be included when averaging over quantities associated with the source sample, for instance when estimating redshift distributions (cf. Hoyle et al. (2018), their section 3.3). We are including these weights in all the redshift distributions measured on Metacalibration used in this work.

Besides the shear response correction described above, in the Metacalibration framework, when making a selection on the original catalog using a quantity that could modify the distribution of ellipticities, for instance a cut in S/N, it is possible to correct for selection effects. In this work, we are taking this into account when cutting on S/N and size (used in Sec. 5.5.3 to test for systematics effects) and in BPZ photo-z's (used to construct the source redshift tomographic bins). This is performed by measuring the mean response of the estimator to the selection, repeating the selections on quantities measured on sheared images. Following on the example of the mean shear, the mean selection response matrix $\langle\boldsymbol{R}_S\rangle$ is

$$\langle R_{S,i,j}\rangle = \frac{\langle e_i\rangle^{S_+} - \langle e_i\rangle^{S_-}}{\Delta\gamma_j}, \tag{5.12}$$

where $\langle e_i\rangle^{S_+}$ represents the mean of ellipticities measured on images without applied shearing in component j, but with selection based on parameters from positively sheared images. $\langle e_i\rangle^{S_-}$ is the analogue quantity for negatively sheared images. In the absence of selection biases, $\langle\boldsymbol{R}_S\rangle$ would be zero. Otherwise, the full response is given by the sum of the shear and selection response:

$$\langle\boldsymbol{R}\rangle = \langle\boldsymbol{R}_\gamma\rangle + \langle\boldsymbol{R}_S\rangle\,. \tag{5.13}$$

The application of the response corrections depends on the shear statistic that is being calibrated; a generic correction for the two point functions, including the tangential shear, which is our particular case of interest, is derived in Sheldon & Huff (2017). In this work we make use of two approximations that significantly simplify the calculation of the shear responses. First, in principle we should take the average in Eq. (5.13) over the sources used in each bin of θ, but we find no significant variation with θ and use a

constant value (see App. C). Therefore, the correction to the tangential shear becomes just the average response over the ensemble. Second, we assume the correction to be independent of the relative orientation of galaxies, so that we do not rotate the response matrix as we do with the shears in Eq. (5.6). Overall, our simplified estimator of the tangential shear for Metacalibration, which replaces the previous expression from Eq. (5.7) is:

$$\langle \gamma_{t,\mathrm{mcal}} \rangle = \frac{1}{\langle R_\gamma \rangle + \langle R_S \rangle} \frac{\sum_j \omega_{\mathrm{l},j}\, e_{t,j}}{\sum_j \omega_{\mathrm{l},j}}, \tag{5.14}$$

summing over lens-source or random-source pairs j and where $\omega_{\mathrm{l},j}$ are the weights associated with the lenses.

The measured selection effects due to sample selection and photo-z binning for each tomographic bin are 0.0072, 0.014, 0.0098 and 0.014, which represent 0.99%, 2.1%, 1.5% and 2.4% of the total response in each bin.

im3shape calibration

For the im3shape shear catalog, additive and multiplicative corrections need to be implemented in the following manner, replacing the previous expression from Eq. (5.7) (Zuntz et al., 2018):

$$\langle \gamma_{t,\mathrm{im3shape}} \rangle = \frac{\sum_j \omega_{\mathrm{l},j}\, \omega_{\mathrm{s},j}\, e_{t,j}}{\sum_j \omega_{\mathrm{l},j}\, \omega_{\mathrm{s},j}\, (1 + m_j)}, \tag{5.15}$$

summing over lens-source or random-source pairs j, where m_j is the multiplicative correction and the additive correction c_j has to be applied to the Cartesian components of the ellipticity, before the rotation to the tangential component, defined in Eq. (5.6), has been performed. $\omega_{\mathrm{l},j}$ are the weights associated with the lenses and $\omega_{\mathrm{s},j}$ the ones associated with the im3shape catalog.

From here on, we will refer to the mean tangential shear $\langle \gamma_t \rangle$ as γ_t for simplicity.

5.4.2 Measurement results

We present the DES Y1 galaxy-galaxy lensing measurements in Fig. 5.2. The total detection significance using all angular scales for the fiducial Metacalibration catalog corresponds to $S/N = 73$. Signal-to-noise is computed as in Troxel et al. (2018), $S/N = (\gamma_t^{\mathrm{data}} C^{-1} \gamma_t^{\mathrm{model}})/(\sqrt{\gamma_t^{\mathrm{data}} C^{-1} \gamma_t^{\mathrm{model}}})$, where C and $\gamma_t^{\mathrm{model}}$ are the covariance matrix and the best-fit models for galaxy-galaxy lensing measurements in the DES Y1 cosmological analysis (DES Collaboration, 2018b). A series of companion papers present other two-point functions of galaxies and shear on the same data sample, as well as the associated cosmological parameter constraints from the combination of all these

two-point function measurements (Elvin-Poole et al., 2018; Troxel et al., 2018; DES Collaboration, 2018b). The shaded regions from this figure correspond to scales that are excluded in the multiprobe cosmological analysis, i.e., scales smaller than 12 $h^{-1}\mathrm{Mpc}$ in comoving distance for the galaxy-galaxy lensing observable (Krause et al., 2017). In the top panel we present the measurements for the Metacalibration shear catalog, and for im3shape in the bottom panel. Note that the measurements from the two shear catalogs cannot be directly compared, since their populations and thus their corresponding redshift distributions differ. For each of the five lens redshift bins, we measure the tangential shear for four tomographic source bins, which result in 20 lens-source redshift bin combinations. The relative strength of the galaxy-galaxy lensing signal for a given lens bin depends on the geometry of the lens-source configuration. This feature is exploited in the shear-ratio test, presented in Sec. 5.6, where we constrain the mean of the source redshift distributions using the small scales that are not used in the cosmological analysis (shaded in Fig 5.2).

5.4.3 Covariance matrix validation

Galaxy-galaxy lensing measurements are generally correlated across angular bins. The correct estimation of the covariance matrix is crucial not only in the usage of these measurements for cosmological studies but also in the assessment of potential systematic effects that may contaminate the signal. While a validated halo-model covariance is used for the DES Y1 multiprobe cosmological analysis (Krause et al., 2017), in this work we use jackknife (JK) covariance matrices given the requirements of some systematics tests performed here, such as splits in area, size or S/N. A set of 1200 lognormal simulations, described in Section 5.3.4, is used to validate the jackknife approach in the estimation of the galaxy-galaxy lensing covariances. We estimate the JK covariance using the following expression:

$$C_{ij}^{\mathrm{JK}}\left(\gamma_i,\gamma_j\right)=\frac{N_{\mathrm{JK}}-1}{N_{\mathrm{JK}}}\sum_{k=1}^{N_{\mathrm{JK}}}\left(\gamma_i^k-\overline{\gamma_i}\right)\left(\gamma_j^k-\overline{\gamma_j}\right), \tag{5.16}$$

where the complete sample is split into a total of N_{JK} regions, γ_i represents either $\gamma_t(\theta_i)$ or $\gamma_\times(\theta_i)$, γ_i^k denotes the measurement from the k^{th} realization and the i^{th} angular bin, and $\overline{\gamma_i}$ is the mean of N_{JK} resamplings.

Jackknife regions are obtained using the `kmeans` algorithm[3] run on a homogeneous random point catalog with the same survey geometry and, then, all foreground catalogs (lenses and random points) are split in $N_{\mathrm{JK}}=100$ subsamples. Specifically, `kmeans` is a clustering algorithm that subdivides n objects into N groups (see Appendix B in Suchyta et al. (2016) for further details).

[3] `https://github.com/esheldon/kmeans_radec`

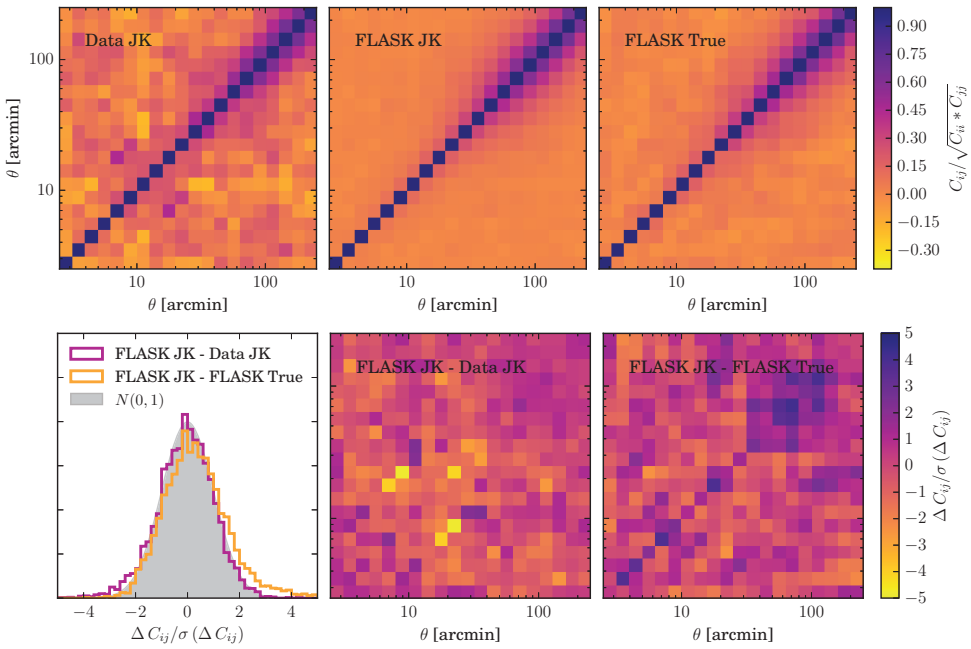

Figure 5.3: Correlation matrices obtained from the jackknife method on the data (top-left panel), from the mean of jackknife covariances using 100 FLASK realizations (top-middle panel) and from the 1200 lognormal simulations FLASK (top-right panel), for an example redshift bin ($0.3 < z_l < 0.45$ and $0.63 < z_s < 0.90$). In the bottom-middle and bottom-right panels, we show the differences between the covariance matrices shown in the upper panels normalized by the uncertainty on the difference, for the same example redshift bin. On the bottom-left panel, we display the normalized histograms of these differences (20×20 for each covariance, corresponding to 20 angular bins) for all the 5×4 lens-source redshift bin combinations, compared to a Gaussian distribution centered at zero with a width of one.

In the upper panels of Fig. 5.3 we present the different covariance estimates considered in this work, namely the jackknife covariance in the data (`Data JK`), the mean of 100 jackknife covariances measured on the lognormal simulations (`FLASK JK`) and the true covariance from 1200 lognormal simulations (`FLASK True`), for a given lens-source redshift bin combination ($0.3 < z_l < 0.45$ and $0.63 < z_s < 0.90$). On the lower panels of this figure, we show the differences between them normalized by the corresponding uncertainty. The lower left panel shows the distribution of these differences and its agreement with a normal distribution with $\mu = 0$ and $\sigma = 1$, as expected from a pure noise contribution, using all possible lens-source bin combinations, and the lower middle and right panels show the same quantity element-by-element for the redshift bin combination used in the upper panels. The uncertainty on the data jackknife covariance comes from the standard deviation of the jackknife covariances measured on 100 lognormal simulations. The uncertainties on the two other covariance estimates are significantly smaller; in the mean of 100 jackknife covariances it is $\sqrt{N}$ times smaller, where $N = 100$ in our case. On the other hand, the uncertainty on each element of the true covariance from 1200 lognormal simulations is calculated using $(\Delta C_{ij})^2 = (C_{ii}C_{jj} + C_{ij}C_{ij})/(N-1)$, where $N = 1200$ in our case. The lower left panel shows an overall good agreement between the covariance estimates, even though the larger tail of the orange histogram with respect to a normal distribution indicates a potential slight overestimation of the covariance obtained with the jackknife method.

In Fig. 5.4 we compare the diagonal elements of the covariance for the 20 lens-source redshift bin combinations, obtaining good agreement for all cases and scales. As in Fig. 5.3, the uncertainty on the data jackknife covariance comes from the standard deviation of the jackknife covariances measured on 100 lognormal simulations. The uncertainties on the two other error estimates are also shown on the plot, but are of the same order or smaller than the width of the lines.

Overall, we have validated the implementation of the jackknife method on the data by comparing this covariance to the application of the same method on 100 lognormal simulations and to the true covariance obtained from 1200 lognormal simulations, and finding good agreement among them, both for the diagonal and off-diagonal elements.

5.5 Data systematics tests

In order to fully exploit the power of weak gravitational lensing, we need to measure the shapes of millions of tiny, faint galaxies to exceptional accuracy, and possible biases may arise from observational, hardware and software systematic effects. Fortunately, weak lensing provides us with observables that are very sensitive to cosmology and the physical properties of the objects involved but also with others for which we expect no cosmological signal. By measuring such observables, we can characterize and correct

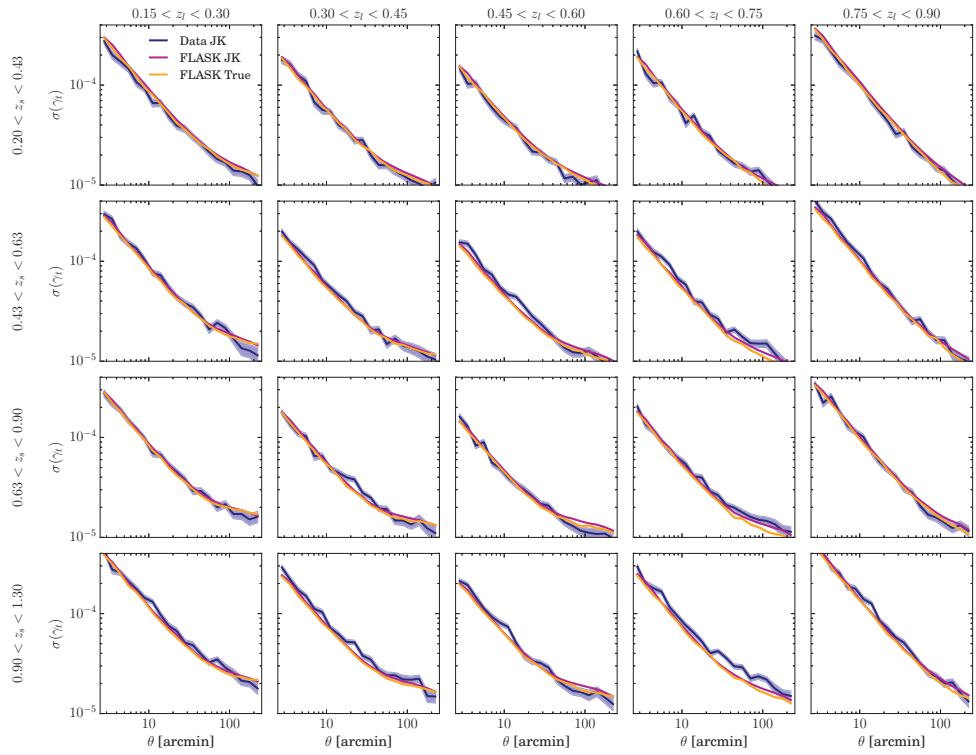

Figure 5.4: Comparison of the diagonal elements of the covariance obtained from the jackknife method on the data (`Data JK`), from the mean of jackknife covariances using 100 FLASK realizations (`FLASK JK`) and from the 1200 lognormal simulations FLASK (`FLASK True`), for all the lens-source combinations.

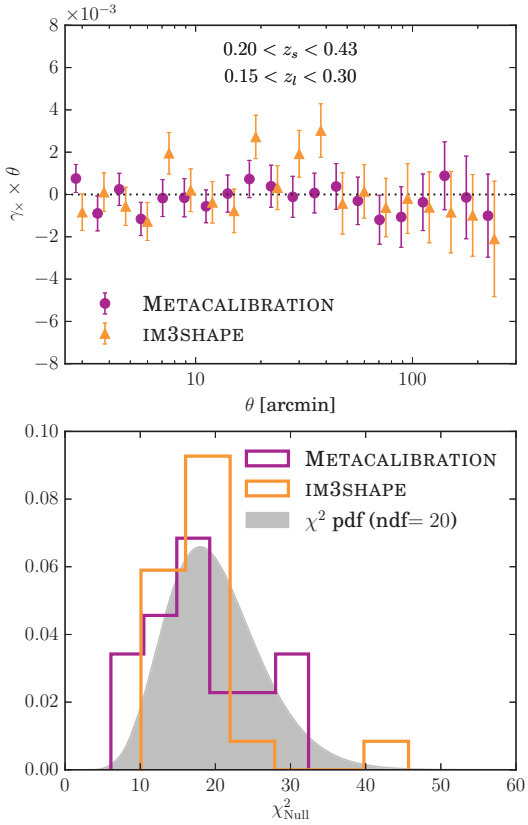

Figure 5.5: (*Top panel*): Cross-component of the galaxy-galaxy lensing signal with random points subtraction for one lens-source redshift bin combination. (*Bottom panel*): The null χ^2 histogram from all 5×4 lens-source redshift bins combinations computed with the jackknife covariance corrected with the Hartlap factor (Hartlap, Simon & Schneider, 2007), compared to the χ^2 distribution with 20 degrees of freedom corresponding to 20 angular bins. We find the cross-component to be consistent with zero.

for systematic effects in the data. In this section, we perform a series of tests that should produce a null signal when applied to true gravitational shear, but whose non-zero measurement, if significant, would be an indication of systematic errors leaking into the galaxy-galaxy lensing observable.

5.5.1 Cross-component

The mean cross-component of the shear $\gamma_\times$, which is rotated 45 degrees with respect to the tangential shear and is defined in Eq. (5.6), should be compatible with zero if the shear is only produced by gravitational lensing, since the tangential shear captures all the galaxy-galaxy lensing signal. Note that the cross-component would also be null in the presence of a systematic error that is invariant under parity.

In the top panel of Fig. 5.5 we show the resulting cross-shear measured around redMaGiC lenses (including random point subtraction) for one lens-source redshift bin combination and for both shear catalogs. In the bottom panel we display the null χ^2 histogram coming from all 5×4 lens-source $\gamma_\times$ measurements, computed using the jackknife covariance for the cross-component, described and validated in Sec. 5.4.3. To compute the null χ^2, i.e. $\chi^2_{\rm null} = \gamma_\times^T\, C^{-1}\, \gamma_\times$, we need an estimate of the inverse of the covariance matrix, but since jackknife covariance matrices contain a non-negligible level of noise, we need to correct for the fact that the inverse of an unbiased but noisy estimate of the covariance matrix is not an unbiased estimator of the inverse of the covariance matrix (Hartlap, Simon & Schneider, 2007). Thus, we apply the Hartlap correcting factor $(N_{\rm JK} - p - 2)/(N_{\rm JK} - 1)$ to the inverse covariance, where $N_{\rm JK}$ is the number of jackknife regions and p the number of angular bins. Our results indicate the cross-component is consistent with zero.

5.5.2 Impact of PSF residuals

The estimation of source galaxy shapes involves modeling them convolved with the PSF pattern, which depends on the atmosphere and the telescope optics and which we characterize using stars in our sample. Next, we test the impact of residuals in the PSF modeling on the galaxy-galaxy lensing estimator, and we compare the size of this error to the actual cosmological signal.

Explicitly, the PSF residuals are the differences between the measured shape of the stars and the PSFEx model (Bertin, 2011; Zuntz et al., 2018) at those same locations. In Fig. 5.6 we show the measured mean of the tangential component of the PSF residuals around redMaGiC galaxies, including the subtraction of the same quantity around random points, in the same manner as for the tangential shear signal. We find it is consistent with zero, and also much smaller than the signal (cf. Figure 5.2).

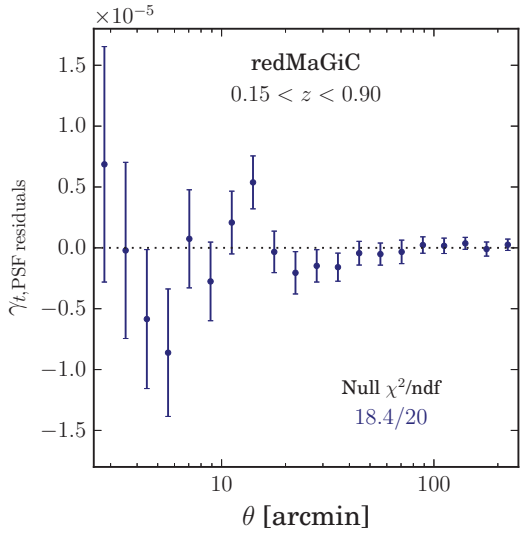

Figure 5.6: PSF residuals for PSFEx model, using a single non-tomographic lens bin, including random-point subtraction. It is consistent with a null measurement and much smaller than the signal.

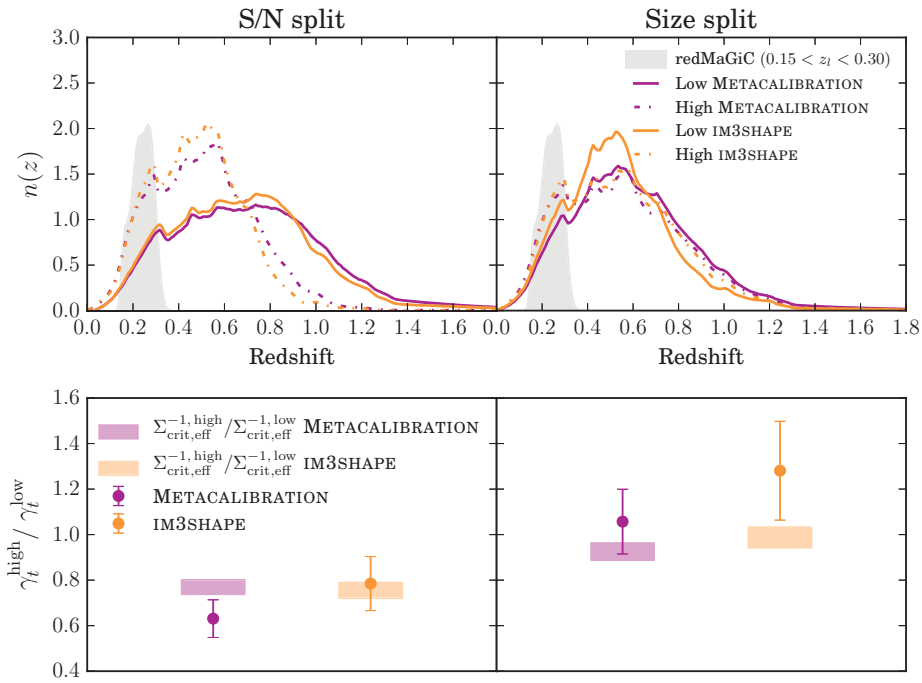

Figure 5.7: S/N (*left*) and size (*right*) splits tests for Metacalibration and im3shape, using scales employed in the cosmology analysis ($> 12\,h^{-1}\mathrm{Mpc}$). (*Top panels*): Redshift distributions of the lens and source samples used for this test. (*Bottom panels*): Comparison between the ratio of $\Sigma^{-1}_{\mathrm{crit,eff}}$ using the above redshift distributions (*boxes*) to the ratio between the amplitudes coming from the fit of the tangential shear measurement for each half to the smooth template from the lognormal simulations (*points*).

5.5.3 Size and S/N splits

Potential biases in shape measurements are likely to be more important for galaxies which are either small or detected at low signal-to-noise (S/N). Even though the shape measurement codes utilized in this work are calibrated in a way such that these effects are taken into account, it is important to test for any residual biases in that calibration. In order to perform such a test, we split the source galaxy samples in halves of either low or high size or S/N, and examine the differences between the galaxy-galaxy lensing measurements using the different halves of the source galaxy samples. For this test, we use the lower redshift lens bin to minimize the overlap in redshift with the source samples. The sources are all combined into a single bin, to maximize the sensitivity to potential differences between the halves.

In order to estimate the size of galaxies, for Metacalibration we use *round* measure of size (`T_r`), and for im3shapewe use the $R_{\rm gpp}/R_{\rm p}$ size parameter, both defined in Jarvis et al. (2016). We estimate the S/N of galaxies using the *round* measure of S/N for Metacalibration, (`s2n_r`), and the `snr` quantity for im3shape, both defined in Jarvis et al. (2016). Splitting the source galaxy samples in halves of low and high galaxy S/N or size, we measure the corresponding galaxy-galaxy lensing signals, and we check their consistency.

Since these quantities can correlate with redshift, differences can arise in the redshift distributions between the halves of S/N and size splits, as seen in the upper panels of Fig. 5.7. When comparing the tangential shear signals of each half of the split, we therefore need to account for the differences in the lensing efficiency given by the two redshift distributions. We do this in the following way. From Eq. (5.3), the ratio between the tangential shear measurements for each half of the split in the absence of systematics effects is

$$\frac{\gamma_t^{l,s_{\rm high}}}{\gamma_t^{l,s_{\rm low}}} = \frac{\Sigma_{\rm crit,eff}^{-1\ l,s_{\rm high}}}{\Sigma_{\rm crit,eff}^{-1\ l,s_{\rm low}}}, \tag{5.17}$$

since $\gamma_t^{l,s_{\rm high}}$ and $\gamma_t^{l,s_{\rm low}}$ share the same lens sample and thus the same $\Delta\Sigma$. $\Sigma_{\rm crit,eff}^{-1}$, defined in Eq. (5.5), is a double integral over the lens and source redshift distributions and the geometrical factor $\Sigma_{\rm crit}^{-1}$, which depends on the distance to the lenses, the sources and the relative distance between them. Then, to check the consistency between the tangential shear measurements for each half of the source split we will compare the ratio between them to the ratio between the corresponding $\Sigma_{\rm crit,eff}^{-1}$'s.

Then, the validity of this test to flag potential biases in shape measurements related to S/N and size is linked to an accurate characterization of the redshift distributions. The ensemble redshift distributions are estimated by stacking the redshift probability density functions of individual galaxies in each split, as given by the BPZ photo-z code. As described in Hoyle et al. (2018) and a series of companion papers (Gatti et al.,

2018; Davis et al., 2017; Cawthon et al., 2018) we do not rely on these estimated redshift distributions to be accurate, but rather calibrate their expectation values using two independent methods: a matched sample with high-precision photometric redshifts from COSMOS, and the clustering of lensing sources with redMaGiC galaxies of well-constrained redshift. These offsets to the BPZ estimate of the ensemble mean redshift, however, could well be different for the two halves of each of the splits.

To estimate these calibration differences between the subsamples, we repeat the COSMOS calibration of the redshift distributions (see Hoyle et al. (2018) for details), splitting the matched COSMOS samples by Metacalibration size and signal-to-noise ratio at the same thresholds as in our data. We find that the shifts required to match the mean redshifts of the subsamples with the mean redshifts of the matched COSMOS galaxies are different by up to $|\Delta(\Delta z)| = 0.035$ for the overall source sample.

In the upper panels of Fig. 5.7, the mean values of the redshift distributions have been corrected using the results found in the analysis described above, and these corrected $n(z)$'s are the ones that have been used in the calculation of $\Sigma^{-1}_{\rm crit,eff}$ in Eq. (5.17). The ratio of $\Sigma^{-1}_{\rm crit,eff}$'s is shown in the lower panels of Fig. 5.7 and its uncertainty comes from the propagation of the error in the mean of the source redshift distributions for each half of the split, i.e. $\sqrt{2}$ times the non-tomographic uncertainty as estimated in Hoyle et al. (2018) using COSMOS.

Regarding the left-hand side of Eq. (5.17), to avoid inducing biases from taking the ratio between two noisy quantities, we fit an amplitude for each half of the split to a smooth tangential shear measurement that we obtain from the mean of tangential shear measurements on 100 independent log-normal simulations. Then, we take the ratio between the amplitudes fitted for each half of the split. We repeat this procedure for each data jackknife resampling, obtaining a ratio for each of those, whose mean and standard deviation are shown in the lower panels of Fig. 5.7 (*points*), compared to the ratio of $\Sigma^{-1}_{\rm crit,eff}$'s (*boxes*).

Given the uncertainties in both the measurements and the photometric redshift distributions presented in Fig. 5.7, we find no significant evidence of a difference in the galaxy-galaxy lensing signal when splitting the Metacalibration or im3shape source samples by size or S/N. Specifically, we find a $1.6\,\sigma$ ($0.24\,\sigma$) difference for the Metacalibration (im3shape) S/N split and a $0.90\,\sigma$ ($1.3\,\sigma$) difference for the Metacalibration (im3shape) size split.

5.5.4 Impact of observing conditions

Time-dependent observing conditions are intrinsic to photometric surveys, and they may impact the derived galaxy catalogs, for instance, introducing galaxy density variations across the survey footprint. In this section we test for potential biases in the galaxy-galaxy lensing measurements due to these differences in observing condi-

tions and their effect in the survey galaxy density. We use projected HEALPix (Gorski et al., 2005) sky maps (with resolution $N_{\rm side} = 4096$) in the r band for the following quantities:

- **AIRMASS:** Mean airmass, computed as the optical path length for light from a celestial object through Earth's atmosphere (in the secant approximation), relative to that at the zenith for the altitude of CTIO.
- **FWHM:** Mean seeing, i.e., full width at half maximum of the flux profile.
- **MAGLIMIT:** Mean magnitude for which galaxies are detected at $S/N = 10$.
- **SKYBRITE:** Mean sky brightness.

More information on these maps can be found in Drlica-Wagner et al. (2018) and Elvin-Poole et al. (2018).

In order to test for potential systematic effects, we split each map into halves of high and low values of a given quantity, and measure the galaxy-galaxy lensing signal in each half. We are using the same configuration as in the S/N and size splits, i.e. the lower redshift lens bin and a single non-tomographic source bin between $0.2 < z_s < 1.3$. In this case, we are splitting both the lens and the source samples, since the split is performed in area.

To check the consistency between the measurements in each half we follow the same approach as for the S/N and size splits, described in detail in the previous section, where we take into account the differences in the redshift distributions of the sources. We find the correlation between observing conditions and redshift to be very mild for the source sample, as can be seen in Fig. 5.8, where the ratios of $\Sigma^{-1}_{\rm crit,eff}$'s are all compatible with unity. For the lens sample this correlation is even smaller, consistent with the lens sample containing brighter and lower-redshift galaxies. The differences on the mean redshift between the lens redshift distributions of the two halves are of the order of 0.001 or smaller for all maps, which is negligible for this test, although we have not performed independent calibration of redshift biases for these split samples.

The results for these area splits are shown in Fig. 5.8 for Metacalibration and im3shape. In most cases, the ratio between the measurements on each half of the splits lie within 1σ of the corresponding ratio of $\Sigma^{-1}_{\rm crit,eff}$'s, and at slightly more than 1σ in the remaining cases. Thus, we do not encounter any significant biases on the galaxy-galaxy lensing signal due to differences in observing conditions.

The effect of the same variable observing conditions in the galaxy clustering measurements using the same DES redMaGiC sample is studied in detail in Elvin-Poole et al. (2018). In that analysis, maps which significantly correlate with galaxy density are first identified, and then a set of weights is computed and applied to the galaxy sample

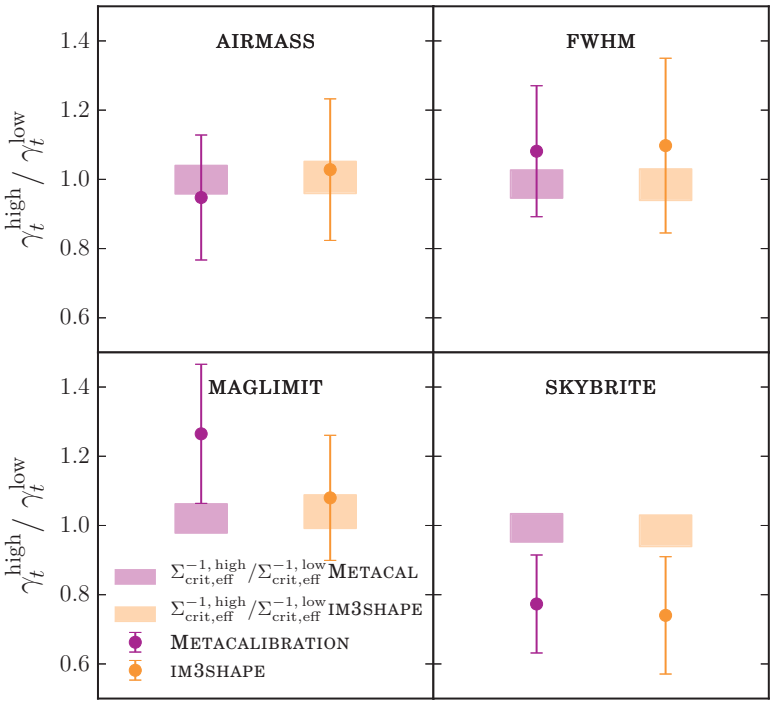

Figure 5.8: Results for the tests involving area splits in halves of different observational systematics maps in the r band, with angular scales used in the cosmology analysis ($12\,h^{-1}\mathrm{Mpc}$). We compare the ratio of $\Sigma_{\rm crit,eff}^{-1}$ (*boxes*) using the redshift distributions for each split to the ratio between the amplitudes coming from the fit of the tangential shear measurement for each half to the smooth template derived from the lognormal simulations (*points*), following the same procedure as for the S/N and size splits, described in Sec. 5.5.3 and shown in Fig. 5.7.

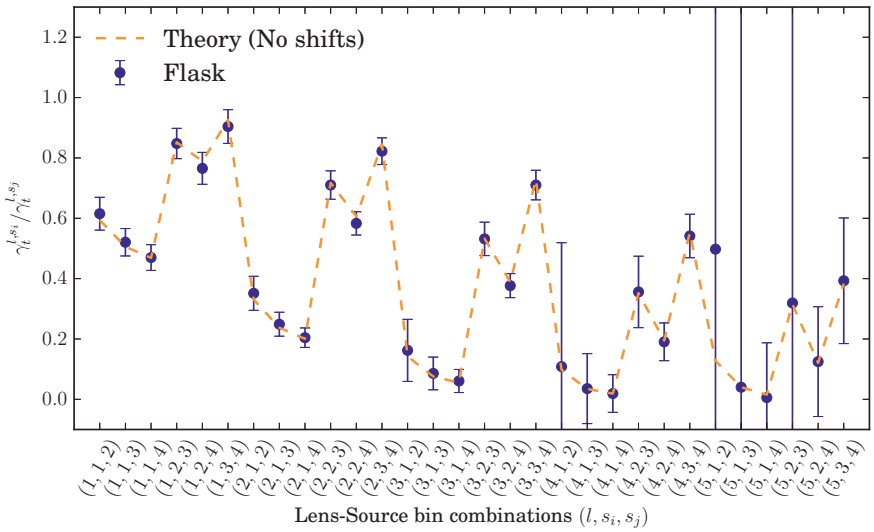

Figure 5.9: Comparison between the mean ratio of tangential shear measurements using 1200 independent log-normal simulations and the ones calculated from theory, for all lens-source bin ratio combinations sharing the same lens bin. The errorbars correspond to the standard deviation of the measurement on individual simulations, thus being representative of the errors that we will obtain from the data.

so that such dependency is removed, following a method similar to that presented in Ross et al. (2012, 2017). The resulting set of weights from that analysis has been also used in this work, for consistency in the combination of two-point correlation functions for the DES Y1 cosmological analysis. Nonetheless, the impact of such a weighting scheme in the galaxy-galaxy lensing observables is found to be insignificant, consistent with the tests presented above in this section and with previous studies (see Kwan et al. 2017).

5.6 Shear-Ratio test

In previous sections we have seen that the variation of the galaxy-galaxy lensing signal with source redshift depends solely on the angular diameter distances relative to foreground and background galaxy populations. Such dependency was initially proposed as a probe for dark energy evolution in Jain & Taylor (2003). The shear-ratio is, however, a weak function of cosmological parameters, and more sensitive to errors in the assignment of source or lens redshifts (Kuijken et al., 2015). Since redshift assignment is a crucial but difficult aspect of robust cosmological estimate for a photometric survey like DES, the shear-ratio test is a valuable cross-check on redshift assignment. In the context of the DES Y1 cosmological analysis, the usage of high-quality photometric redshifts for lens galaxies allows us to put constraints on the mean redshift of source

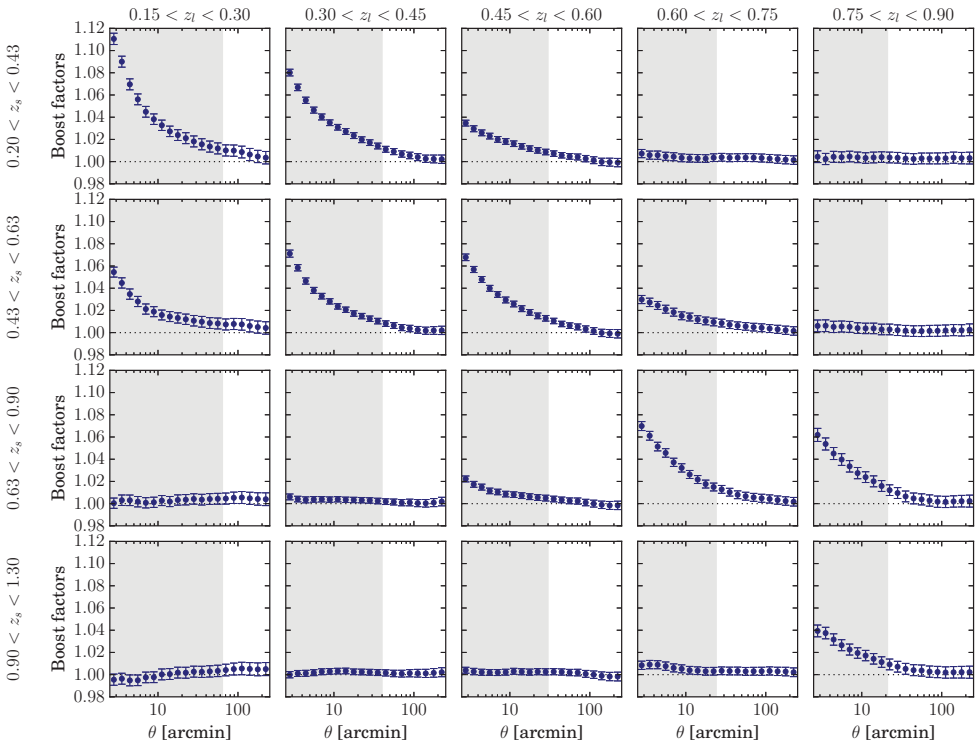

Figure 5.10: Boost factor correction accounting for clustering between lenses and sources in each lens-source bin used in this analysis. Non-shaded scales correspond to scales used in the DES Y1 cosmological analysis, while shaded regions are used for the shear-ratio geometrical test in this Section. Boost factors are unity or percent-level for the former, but can be significantly larger for the latter in some cases, and hence they are applied in our analysis of the shear-ratio test.

galaxy distributions.

In this section we present a general method to constrain potential shifts on redshift distributions using the combination of ratios of galaxy-galaxy lensing measurements. First, we present the details of the implementation, and we test it on lognormal simulations. Then, we use the galaxy-galaxy lensing measurements shown in Fig. 5.2, restricted to angular scales which are not used in the DES Y1 cosmological analysis, to place independent constraints on the mean of the source redshift distributions shown in the lower panel of Fig. 5.1. Finally, we compare our findings with those obtained from a photometric redshift analysis in the COSMOS field and from galaxy angular cross-correlations.

The ratio of two galaxy-galaxy lensing measurements around the same lens bin, hence having equivalent $\Delta\Sigma$, can be derived from Eq. (5.3) and is given by:

$$\frac{\gamma_t^{l,s_i}}{\gamma_t^{l,s_j}} = \frac{\Sigma_{\rm crit,eff}^{-1\ l,s_i}}{\Sigma_{\rm crit,eff}^{-1\ l,s_j}}, \tag{5.18}$$

where $\Sigma_{\rm crit,eff}^{-1}$ is the double integral over lens and source redshift distributions defined in Eq. (5.4). Therefore, for two given γ_t measurements sharing the same lens population but using two different source bins, we can predict their ratio from theory by using the estimated redshift distributions involved. In addition, we can allow for a shift in each of those redshift distributions and use the γ_t measurements to place constraints on them.

In this section we generalize this approach by including all possible combinations of ratios of galaxy-galaxy lensing measurements sharing a given lens bin, and allowing for independent shifts in their redshift distributions. With the purpose of providing constraints on the shifts of redshift distributions which are independent of the measurement involved in the fiducial DES Y1 cosmological analysis, we restrict the galaxy-galaxy lensing measurements used for this shear-ratio test to scales smaller than the ones used by the cosmological analysis but which have still been tested against systematic effects in this work.

In order to estimate the ratio of galaxy-galaxy lensing measurements, which can be noisy and thus bias their ratio, we fit each measurement involved in the ratio, both around the same lens bin, to a power law fit of the highest signal-to-noise γ_t measurement for the same lens bin. That fixes the shape of the galaxy-galaxy lensing signal around that lens galaxy sample. Then, fits to the amplitude of this power law are used to obtain the shear ratio.

5.6.1 Testing the method on simulations

With the purpose of testing our method to estimate ratios of galaxy-galaxy lensing measurements and our ability to recover the expected values from theory, we use the

lognormal simulations described in Sec. 5.3.4, where we know the true lens and source redshift distributions. For that case, we should be able to find good agreement between measurements and theory, without the necessity of allowing for any shifts in the redshift distributions.

Figure 5.9 shows all the possible ratios of two γ_t measurements in the FLASK simulations sharing the same lens bin using the lens-source binning configuration used throughout this chapter (as depicted in Fig. 5.1), with the error bars coming from the variance of the 1200 simulations. It also shows the expected values for the ratios given from theory, using the true corresponding redshift distributions with no shifts applied. The agreement between measurements and theory is excellent, demonstrating that the method described in this section is able to recover the true values of γ_t measurements from theory when the redshift distributions are known.

5.6.2 Application to data

Now we turn to data, and utilize this shear-ratio method to constrain possible biases in the mean of redshift distributions. The lens and source redshift bins considered and their fiducial estimated redshift distributions are depicted in Figure 5.1. The high-precision photometric redshifts of the redMaGiC sample ensure the lens redshift distributions are well known, with potential shifts found to be very small and consistent with zero in Cawthon et al. (2018), and hence we keep them fixed. On the contrary, source galaxies are generally fainter and have a much larger uncertainty in their redshift distributions. Therefore, we allow for an independent shift Δz^i in each of the measured source redshift distributions $n^i_{\rm obs}(z)$, such that

$$n^i_{\rm pred}(z) = n^i_{\rm obs}(z - \Delta z^i), \tag{5.19}$$

to be constrained from the combination of ratios of galaxy-galaxy lensing measurements through their impact in the $\Sigma^{-1}_{\rm crit,eff}$ factors in Eq. (5.18).

When turning to the data case, we also have to consider effects which are not included in the simulations. In particular, next we take into account the effects of potential boost factors and multiplicative shear biases in the measurements.

Boost factors

The calculation of the mean galaxy-galaxy lensing signal in Eq. (5.1) correctly accounts for the fact that some source galaxies are in front of lenses due to overlapping lens and source redshift distributions, but only under the assumption that the galaxies in those distributions are homogeneously distributed across the sky. As galaxies are not homogeneously distributed but they are clustered in space, a number of sources larger than the $n^{\rm obs}(z)$ suggests may be physically associated with lenses. These sources are

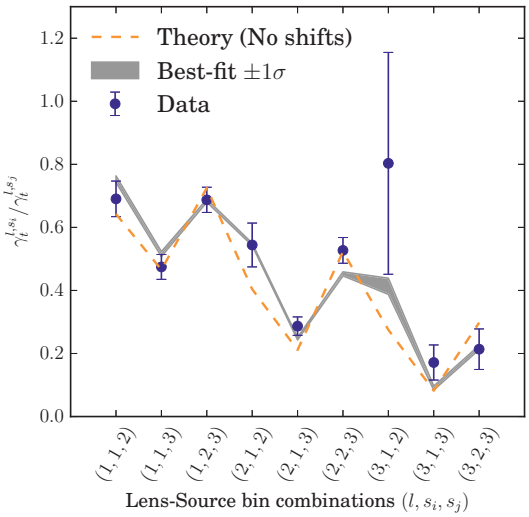

Figure 5.11: Comparison between the ratio of tangential shear measurements on Metacalibration (*blue points*) to the ones calculated from theory, both without applying any shift to the original source $n(z)'s$ (*dashed orange line*) and applying the best-fit shifts with a 1σ uncertainty band (*gray band*).

not lensed, causing a dilution of the lensing signal which can be significant at small scales. In order to estimate the importance of this effect, we compute the excess of sources around lenses compared to random points (Sheldon et al., 2004):

$$B(\theta) = \frac{N_r}{N_l} \frac{\sum_{l,s} w_{l,s}}{\sum_{r,s} w_{r,s}} \tag{5.20}$$

where l, s (r, s) denotes sources around lenses (random points), $w_{l,s}$ ($w_{r,s}$) is the weight for the lens-source (random-source) pair, and the sums are performed over an angular bin θ. Figure 5.10 shows this calculation for every lens-source bin in this analysis. The shaded regions in the plot mark the scales used for the shear-ratio test (unused by the cosmological analysis). The importance of boost factors at small scales can be as large as 10%, while on the large scales used for cosmology it does not depart from unity above the percent level. The data measurements used for the shear-ratio test in this section have been corrected for this effect.

Multiplicative shear biases

Multiplicative shear biases are expected to be present in the galaxy-galaxy lensing signal and need to be taken into account. This potential effect is included as an independent parameter m^i for each source redshift bin, parametrized such that the shear ratios in Eq. (5.18) look like the following:

$$\frac{\gamma_t^{l,s_i}}{\gamma_t^{l,s_j}} = \frac{(1+m_j)\,\Sigma_{\rm crit,eff}^{-1\;l,s_i}}{(1+m^i)\,\Sigma_{\rm crit,eff}^{-1\;l,s_j}}. \tag{5.21}$$

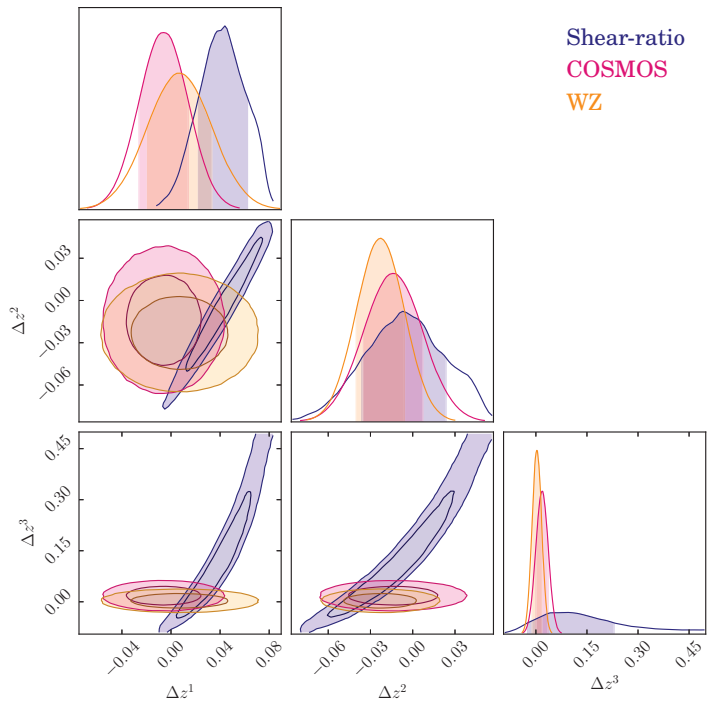

Figure 5.12: Comparison of the constraints obtained on the source redshift distribution shifts using different methods: Shear-ratio test, photo-z studies in the COSMOS field (COSMOS, Hoyle et al. 2018) and cross-correlation redshifts (WZ, Davis et al. 2017; Gatti et al. 2018).

Table 5.1: Priors and posteriors on the mean of source redshift distributions (Δz) and multiplicative shear biases (m) for the first three source bins defined in this work (Fig. 5.1), using the shear-ratio test. Priors are uniform in Δz and Gaussian on m, and posteriors are given as the mean value with 68% constraints.

	Δz Prior	Δz Posterior	m Prior	m Posterior
Source bin 1	Uniform(−0.5,0.5)	$0.046^{+0.017}_{-0.023}$	Gaussian(0.012,0.021)	$0.018^{+0.020}_{-0.021}$
Source bin 2	Uniform(−0.5,0.5)	$-0.005^{+0.028}_{-0.031}$	Gaussian(0.012,0.021)	$-0.012^{+0.017}_{-0.016}$
Source bin 3	Uniform(−0.5,0.5)	$0.10^{+0.13}_{-0.12}$	Gaussian(0.012,0.021)	$0.035^{+0.016}_{-0.019}$

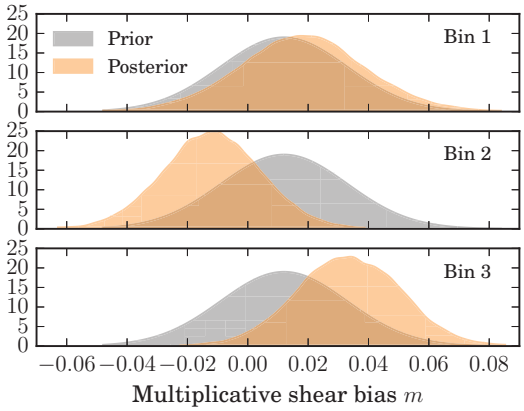

Figure 5.13: Prior and posterior distributions for multiplicative shear biases (m) for the first three source bins defined in this work (Fig. 5.1). The shear-ratio test appears to be informative on the multiplicative shear biases for the second and third source bins, reducing the prior width by as much as 20%, even though posteriors are all consistent with the priors at better than 1-σ level.

Results

In practice, the sensitivity of the shear-ratio geometrical test to shifts in the mean of redshift distributions decreases significantly the higher the distribution is in redshift, due to the relative differences in distance with respect to the lenses and the observer being smaller for that case. For that reason, the sensitivity to shifts in the highest source redshift bin defined in this work is very small, and as there are strong correlations with the other shifts, we left out the fourth source bin. We also leave out the two highest lens redshift bins as the galaxy-galaxy lensing S/N for these cases is very small and they add little information to this test.

In order to find the best-fit shifts for all combinations of fixed-lens γ_t ratios using these redshift bins, we set a Monte-Carlo Markov Chain (MCMC) to let the shifts vary, with a broad flat prior of [-0.5,0.5] for each shift Δz^i. We follow the recommendations in Zuntz et al. (2018) and include a Gaussian prior of $\mu = 0.012$ and $\sigma = 0.021$ on the multiplicative shear biases m^i for each source bin i. As the covariance is estimated from JK resampling, the corresponding Hartlap factor is applied to the covariance. Some recent studies have discussed and presented further corrections to that procedure (Sellentin & Heavens, 2016). Given that in our case the Hartlap factor is $\simeq 0.9$, such corrections would result in a small change to the parameter contours, and have not been

considered in this analysis. However, a more detailed treatment of noisy covariances may need to be considered in forthcoming, more sensitive, DES analyses.

Figure 5.11 shows the equivalent of Fig. 5.9 for the data case, including the theory prediction with no shifts and with best-fit shifts from the MCMC run, and the shear-ratio case in Fig. 5.12 shows the Δz constraints from the MCMC, marginalizing over multiplicative shear biases m, where very clear correlations can be observed between the different shifts. In addition, Table 5.1 presents the derived constraints on Δz and m for the different source bins considered. Even though $\Sigma_{\rm crit}$ depends on cosmology through Ω_m, the results are insensitive to that parameter to the extent that no significant changes on the shifts are observed when marginalizing over it with a broad flat prior of $0.1 < \Omega_m < 0.5$. Also, the boost factor correction from Eq. (5.20) has no significant effect on the derived Δz constraints.

In the past, several studies have proposed shear self-calibration techniques, either from galaxy-galaxy lensing only Bernstein (2006), or using combinations of observables (e. g. Huterer et al. 2006; Bernstein 2009a). Interestingly, the shear-ratio test can also be used as a way to calibrate potential multiplicative shear biases (m) present in the data. Figure 5.13 displays the m priors and posteriors for the three source redshift bins considered, where the posteriors show a reduction of up to 20% in the width of the priors (see also Table 5.1) for the second and third bins, therefore showing potential as a method to internally constrain shear biases in the data.

Caveats and future work

The redshift evolution of the $\Delta\Sigma$ profile of the lens sample within a redshift bin could potentially affect the shear-ratio test and would not be noticeable in the FLASK simulations. This would especially influence the ratios between lens and source bins that are close in redshift. However, the usage of relatively thin lens tomographic bins, of 0.15 in redshift, and the little galaxy bias evolution of the redMaGiC sample for the first three lens bins, as shown in Fig. 5.14 below and Clampitt et al. (2017), suggest that this effect is small compared to our current error bars. On the other hand, mischaracterization of the tails in the fiducial (unshifted) redshift distributions of the source galaxies, especially for those close to the lenses, could also affect the results of the shifts obtained with the shear-ratio test. Studying the impact of such effects in the shear-ratio geometrical test using N-body simulations is beyond the scope of this chapter and it is left for future work.

In addition, intrinsic alignment (IA) between physically associated lens-source galaxy pairs can potentially affect the shear ratio measurement (see, e. g., Sheldon et al. 2004; Blazek et al. 2012). While IA on larger scales is modeled when measuring cosmology or the galaxy bias, we have not included this effect on the small scales used here. The boost factor measurements in Fig. 5.10 yield an estimate of the fraction of physically associ-

ated pairs in all our measurements. As seen in Blazek et al. (2012), for typical lensing sources the impact of IA contamination on the observed lensing signal is smaller than that of the boosts themselves. Since the boost corrections here are small and have a minimal effect on the derived source photo-z shifts, we expect the impact of IA to be highly subdominant. However, it will be beneficial in future work to include the impact of IA when performing shear ratio tests.

Comparison of Δz constraints and conclusions

In Fig. 5.12 we also compare the shear-ratio constraints with those obtained independently from photo-z studies in the COSMOS field (Hoyle et al., 2018) and from galaxy cross-correlations (Davis et al., 2017; Gatti et al., 2018), and we find consistency among the three independent studies, with $\chi^2/\mathrm{dof} = 5.57/6$ for the combination of the three cases. As expected, the constraining power of the shear-ratio test for the shifts on the source distributions decreases rapidly the higher the redshift of the distributions is, so that the 1-D marginalized constraints on the first tomographic bin are competitive with those from the other probes, and for the third tomographic bin they add very little information. However, on the 2-D space, the shear-ratio contours show great potential in breaking degeneracies with other probes. Therefore, the use of this method with forthcoming data sets can have a major impact in determining possible photometric redshift biases, especially from source distributions at low redshift.

The importance of an accurate photometric redshift calibration in DES was already noticed in the analysis of Science Verification data, where it proved to be one of the dominant systematic effects (DES Collaboration, 2015). For this reason, showing the consistency of constraints derived from galaxy-galaxy lensing only to those from more traditional photo-z methods and from galaxy angular cross-correlations represents an important demonstration of the robustness of the companion DES Y1 cosmological analysis.

5.7 redMaGiC galaxy bias

Galaxy-galaxy lensing is sensitive to cosmological parameters and the galaxy bias of the corresponding lens galaxy population, as expressed in Eq. (5.1). Similarly, the galaxy clustering of the same lens population also depends on both cosmology and the galaxy bias, but with a different power of the latter (Elvin-Poole et al., 2018). Therefore, the combination of galaxy clustering and galaxy-galaxy lensing breaks the degeneracy between the galaxy bias and cosmological parameters. This combination is one of the more promising avenues to understand the underlying physical mechanism behind dark energy, and has been used together with cosmic shear measurements to produce cosmological results from DES Y1 (DES Collaboration, 2018b).

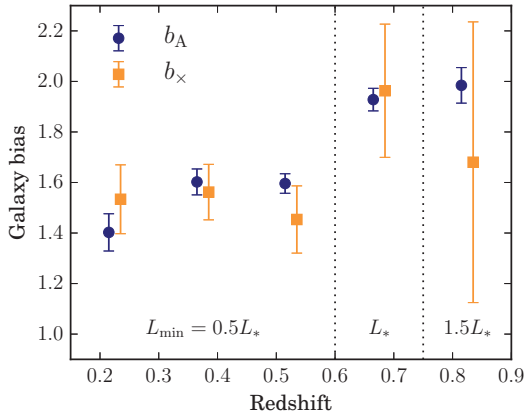

Figure 5.14: Comparison of the galaxy bias results obtained from galaxy clustering measurements (b_A, Elvin-Poole et al. 2018) and from the galaxy-galaxy lensing measurements in this work ($b_\times$), by fixing all cosmological parameters to the 3x2 cosmology best-fit from DES Collaboration (2018b). The vertical dotted lines separate the three redMaGiC samples, which have different luminosity thresholds $L_{\rm min}$, defined in Sec. 5.3.1.

Alternatively, fixing all cosmological parameters, the measurements of galaxy clustering and galaxy-galaxy lensing can provide independent measurements of the galaxy bias of a given lens population. The DES Y1 cosmology analysis relies on the assumption that the linear bias from galaxy clustering and from galaxy-galaxy lensing is the same, which is known to break down on the small-scale regime (Baldauf et al., 2010). To verify this assumption over the scales used in the DES Y1 cosmology analysis, we measure the galaxy bias from each probe separately. In Fig. 5.14 we show the bias constraints from galaxy clustering (or galaxy autocorrelations, b_A) and galaxy-galaxy lensing (or galaxy-shear cross-correlations, $b_\times$) on the five lens redMaGiC tomographic bins defined in this work, fixing all cosmological parameters to the best-fit obtained in the DES Y1 cosmological analysis (DES Collaboration, 2018b). We use comoving angular separations larger than $8h^{-1}$Mpc for galaxy clustering, and larger than $12h^{-1}$Mpc for galaxy-galaxy lensing, which correspond to the scales used in the DES Y1 cosmological analysis. In order to obtain these results, the clustering measurements from Elvin-Poole et al. (2018) and the galaxy-galaxy lensing measurements from this work have been analyzed with the same pipeline used in DES Collaboration (2018b), including the covariance between the two probes and marginalizing over all nuisance parameters like photometric redshift, shear calibration and intrinsic alignments uncertainties. We find the obtained constraints on the galaxy bias from galaxy-galaxy lensing to be in good agreement with those obtained from galaxy clustering.

The results in Fig. 5.14 can also be interpreted by allowing a non-unity cross-correlation parameter between the galaxy and matter distributions. This parameter is usually expressed in terms of the matter and galaxy power spectra, $P_{\delta\delta}$ and P_{gg} respectively, and the galaxy-matter power spectrum $P_{g\delta}$, as

$$r\left(k, \chi(z)\right) = \frac{P_{g\delta}(k, \chi(z))}{\sqrt{P_{\delta\delta}(k, \chi(z))\, P_{gg}(k, \chi(z))}}, \tag{5.22}$$

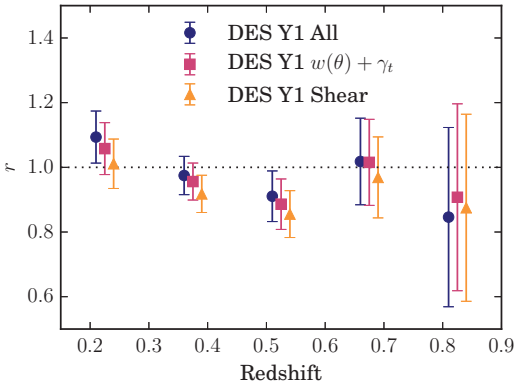

Figure 5.15: Cross-correlation coefficient r between galaxies and dark matter obtained by comparing the galaxy bias from galaxy clustering (b_A) and from galaxy-galaxy lensing only ($b_\times$), fixing all cosmological parameters to three different cosmologies from DES Y1 cosmological results (DES Collaboration, 2018b): (i) 3x2 best-fit (All), (ii) $\omega(\theta)+\gamma_t$ best-fit, and (iii) cosmic shear best-fit.

where we have explicitly included its possible scale and redshift dependence. In the context of this model, the galaxy power spectrum remains unchanged with respect to $r = 1$, $P_{gg} = b^2 P_{\delta\delta}$, but the galaxy-matter power spectrum changes from $P_{g\delta} = bP_{\delta\delta}$ to $P_{g\delta} = b\,r P_{\delta\delta}$. That introduces an r factor in the galaxy-galaxy lensing expression in Eq. (5.1), and hence the two estimates of the galaxy bias in Fig. 5.14 can be transformed to:

$$b = b_A \; ; \; r = b_\times / b_A, \tag{5.23}$$

and this allows us to place constraints on the r parameter using our measurements. If r^i refers to the cross-correlation parameter in lens bin i, the constraints we obtain read: $r^1 = 1.094 \pm 0.080$, $r^2 = 0.975 \pm 0.059$, $r^3 = 0.911 \pm 0.078$, $r^4 = 1.02 \pm 0.13$, $r^5 = 0.85 \pm 0.28$, shown also in Fig. 5.15.

In addition, it is important to note that the specified constraints on the galaxy bias and the cross-correlation coefficient are not independent of the assumed cosmology. The values given above are obtained with the 3x2 best-fit cosmological parameters from the DES Y1 main cosmological analysis (DES Collaboration, 2018b), which favours the cross-correlation coefficient being consistent with one, since the cosmology is determined assuming the galaxy bias for galaxy clustering and for galaxy-galaxy lensing is the same. This is also true for the 2x2 cosmology, from $\omega(\theta) + \gamma_t$. On the contrary, the cosmological parameters obtained only from the cosmic shear analysis are independent of the galaxy bias and the cross-correlation coefficient and therefore provide a way to test the $r = 1$ assumption. In Fig. 5.15, we present the r constraints for each of these three cosmologies, which we find all to be consistent with $r = 1$. The r constraints presented in this section provide further justification for assuming $r = 1$ in the main DES Y1 cosmological analysis.

Previously, different studies had analyzed the consistency between different estimates of the galaxy bias of a given galaxy population. In the context of DES, a number of different analyses using galaxy clustering in Crocce et al. (2016), CMB lensing in Gi-

annantonio et al. (2016), galaxy-galaxy lensing in Prat et al. (2018b), and projected mass maps in Chang et al. (2016) used DES Science Verification (SV) data to obtain constraints on the galaxy bias of the main galaxy population (so-called DES-SV Benchmark sample), finding mild differences in those estimates that were explored as potential differences between clustering and lensing. Outside DES, other studies have also examined potential differences between clustering and lensing. In particular, in Leauthaud et al. (2017) the authors perform a galaxy-galaxy lensing measurement around BOSS CMASS spectroscopic galaxies using data from the CFHTLenS and SDSS Stripe 82 surveys, and find the lensing signal to be lower than that expected from the clustering of lens galaxies and predictions from standard models of the galaxy-halo connection. In this study, as expressed in the r values reported above, and more broadly in the DES Y1 cosmological analysis presented in DES Collaboration (2018b), we find the clustering and lensing signals to be consistent within our uncertainties, though we note that the Leauthaud et al. (2017) analysis was done on significantly smaller scales.

5.8 Conclusions

This chapter is part of the Dark Energy Survey Year 1 (DES Y1) effort to obtain cosmological constraints by combining three different probes, namely galaxy clustering, galaxy-galaxy lensing and cosmic shear. The main goal of this work is to present and characterize one of these two-point correlations functions, the galaxy-galaxy lensing measurement. Besides this principal task, we use source tomography to put constraints on the mean of the source redshift distributions using the geometrical shear-ratio test. Finally, we obtain the galaxy bias from this probe and we compare it to the corresponding result from galaxy clustering.

Our lens sample is composed of redMaGiC galaxies (Rozo et al., 2016), which are photometrically selected luminous red galaxies (LRGs) with high-precision photometric redshifts. This allows us to divide the lens sample into five equally-spaced tomographic bins between 0.15 and 0.9 in redshift. Regarding the source sample, we use two independent shear catalogs, namely Metacalibration and im3shape, which are described in detail in Zuntz et al. (2018). We split the source galaxies into four tomographic bins between 0.2 and 1.3 in redshift using BPZ, a template-based photometric redshift code.

In order to characterize the DES Y1 galaxy-galaxy lensing measurements, we test them for an extensive set of potential systematic effects. First, we show that the cross-component of the shear is compatible with zero, which should be the case if the shear is only produced by gravitational lensing. Second, PSF residuals are considered and found to leave no imprint on the tangential shear measurements. Next, we split the source sample into halves of high and low signal-to-noise or size, observing no signif-

icant differences between the measurements in each half of the split. Finally, we study the impact of the survey observing conditions, i.e. airmass, seeing, magnitude limit and sky brightness, on the galaxy-galaxy lensing signal, finding no significant dependence. To estimate the significance of these tests we use covariance matrices obtained from the jackknife method, which we validate using a suite of log-normal simulations. Overall, we find no significant evidence of systematics contamination of the galaxy-galaxy lensing signal. Besides serving as crucial input and validation for the DES Y1 cosmological analysis, this set of systematics tests will also be useful for potential future work relying on DES Y1 galaxy-galaxy lensing measurements.

In addition to the systematics testing, we apply the shear-ratio test to our source tomographic measurements. Given a fixed lens bin, we make use of the geometrical scaling of the tangential shear for different source redshift bins to constrain the mean of the source tomographic redshift distributions, which is one of the dominant sources of uncertainty in the DES Y1 cosmological analysis. For this test, we restrict the scales to those ignored in the cosmological analysis, so that it is independent of the constraints obtained there. Our results are in agreement with other photo-z studies on the same data sample (Hoyle et al., 2018; Davis et al., 2017; Gatti et al., 2018), thus showing the robustness of the photometric redshifts used in the DES Y1 cosmological analysis. We also find this method to be informative of multiplicative shear biases in the data, hence showing potential as a way of self-calibrating shear biases in future data sets.

Finally, restricting to the scales used in the cosmological analysis, we use the galaxy-galaxy lensing measurements in this work to obtain galaxy bias constraints on the redMaGiC galaxy sample by fixing all the cosmological parameters but leaving free the nuisance parameters as in DES Collaboration (2018b). We compare these constraints from the ones obtained using the corresponding galaxy clustering measurements in the same lens sample in Elvin-Poole et al. (2018) and using the same cosmological model, finding good agreement between them. This agreement can also be understood as a consistency test of the assumption that the galaxy-matter cross-correlation coefficient $r = 1$, made in the cosmology analysis.

Chapter 6

Dark Energy Survey Year 1 Results: Cosmological Constraints from Galaxy Clustering and Weak Lensing

6.1 Introduction

In the chapter above we presented one of the three two-point correlation functions that, along with galaxy clustering and cosmic shear, are used in the DES 3x2pt cosmological analysis of Y1 data. The work from the previous chapter needs to be understood in the broader context in which it is embedded. That is why, in this chapter, we summarize the main results of the DES Y1 cosmological analysis obtained from the combination of galaxy clustering and weak lensing, explaining the motivation behind using this combination and discussing the consistency of the results with those from other cosmological probes.

The discovery of the acceleration of the expansion of the Universe (Riess et al., 1998; Perlmutter et al., 1999) established the cosmological constant (Λ) (Einstein, 1917) + Cold Dark Matter (ΛCDM) model as the standard cosmological paradigm that is able to explain a wide range of events, from the origin and evolution of large-scale structure to the current epoch of accelerated expansion (Lahav & Liddle, 2014; Weinberg et al., 2013). The success of ΛCDM, however, must be counterpoised by its apparent implausibility: three new entities beyond the Standard Model of particle physics — one that drove an early epoch of inflation, another that operates as dark matter, and a third that is driving the current epoch of acceleration — are required, and it is not clear how to connect any of them to the rest of physics (Frieman, Turner & Huterer, 2008). Experiments such as the Dark Energy Survey are devised to test ΛCDM and more generally aim to distinguish the mechanism causing the current epoch of acceleration, which could be the vacuum energy associated with the cosmological constant, another form of dark energy, a modification of General Relativity, or something else more extreme not envisioned

yet.

The spatial distribution of galaxies – the so-called *galaxy clustering*–, and its evolution in time, is sensitive to the physics of the early Universe, as well as to the details of structure evolution in the late Universe, hence providing tests to predictions of ΛCDM. However, the data–model comparison in this case depends on the galaxy bias (Kaiser, 1984), the relation between the galaxy spatial distribution and the theoretically predicted matter distribution. Therefore, in order to break degeneracies with the galaxy bias, it is necessary to include other probes in the analysis, such as weak gravitational lensing, which has become one of the principal probes of cosmology. In particular, *cosmic shear*, the correlation of the observed shapes of pairs of galaxies, sheared by foreground structures provides a direct measurement of the matter distribution, independently from the galaxy bias. On the other hand, further information on the galaxy bias can be obtained from *galaxy–galaxy lensing*, the cross-correlation of lens galaxy positions and source galaxy shapes.

This combination, of galaxy clustering, cosmic shear and galaxy-galaxy lensing, also called 3x2pt since it involves three two-point correlation functions, besides being able to break degeneracies between the galaxy bias and cosmological parameters, has been recognized for more than a decade to contain a tremendous amount of complementary information, and to be remarkably resilient to the presence of nuisance parameters that describe systematic errors and non-cosmological information (Hu & Jain, 2004; Bernstein, 2009b; Joachimi & Bridle, 2010; Nicola, Refregier & Amara, 2016). Such a combination of large-scale structure and weak lensing measurements powerfully constrains structure formation in the late Universe. Then, by comparing the results from this combination to those from the cosmic microwave background (CMB), we can perform a primary test of ΛCDM which is whether measurements of cosmological parameters from late-universe probes are consistent with measurements from the early Universe.

The DES Y1 data set analyzed in this chapter is exactly the same as the one described in the chapter above, therefore we refer the reader to Sec. 5.3 for more details. Summarizing, it covers about $\sim 1500\text{deg}^2$, and provides 650,000 lens galaxies and the shapes of 26 million source galaxies, each of them divided into redshift bins.

In Fig. 6.1 we show a flowchart displaying the relations between the different papers involved in the DES Y1 3x2pt cosmological analysis, where the results from this thesis, published in Prat et al. (2018a), are presenting one of the three two-point correlation function measurements. In this chapter, in Sec. 6.2 we describe each of the three two-point correlation function measurements and corresponding modeling used in the analysis. Then, in Sec. 6.3 we describe the cosmological models and methodology used to infer cosmological parameters. Finally, we present the results in Sec. 6.4 and conclude.

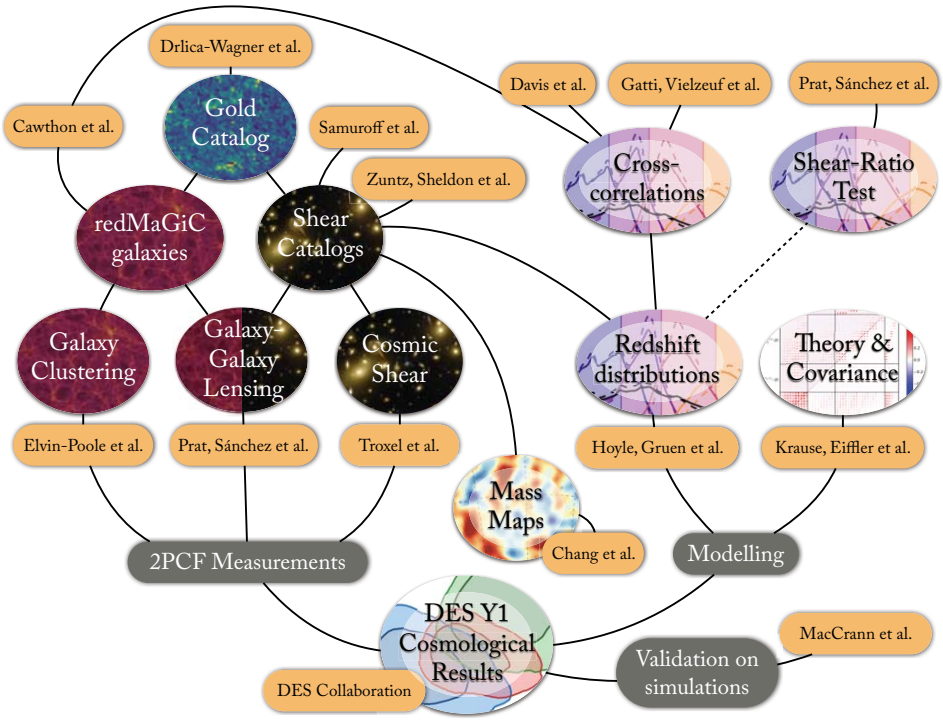

Figure 6.1: Flowchart showing the different parts of the analysis and corresponding papers feeding the DES Y1 3x2pt cosmological analysis.

6.2 Two-point measurements and modeling

In the 3x2pt analysis three two-point correlation function measurements are used: (i) Galaxy clustering, the angular correlation function of the lens galaxies, $w(\theta)$ (ii) Galaxy-galaxy lensing, precisely the correlation of the tangential shear of sources with lens galaxy positions, $\gamma_t(\theta)$ and (iii) Cosmic shear, the correlation functions of different components of the ellipticities of the source galaxies, $\xi_{\pm}(\theta)$. To infer cosmological information from these two-point measurements, we model these functions in terms of the *cosmological parameters*, but also need to add some *nuisance parameters* to account for astrophysical and observational uncertainties. The nuisance parameters we included consider uncertainties in photometric redshifts, shear calibration, the galaxy bias, and the contribution of intrinsic alignment to the shear spectra. All these parameters and corresponding priors are shown in Table. 6.1, together with the cosmological parameters.

Also it is important to note that the measurements are only used on scales where it has been verified that the model is good enough to describe the data. For galaxy clustering and galaxy-galaxy lensing the limiting factor is the galaxy bias modeling, which restricts the analysis for scales above 8 Mpc/h for galaxy clustering and for 12 Mpc/h for the tangential shear, where the difference is arising from the fact that γ_t is non-local as opposed to $w(\theta)$. For cosmic shear, the limiting factor are baryonic effects, impacting $\xi_{+/-}$ at small scales. Especifically, all data points having a fractional contribution from baryonic interactions exceeding 2% are removed from the analysis, with scale cuts ranging between $\sim 3-8$ arcmin for ξ_+ and between $\sim 40-100$ arcmin for ξ_-, which is more affected. Below, we describe how we measure and model each of the two-point functions.

6.2.1 Galaxy Clustering: $w(\theta)$

For imaging galaxy surveys such as DES, the angular clustering of galaxies is the simplest measurement we can perform, which is defined as the overabundance of pairs at angular separation θ above that expected in a random distribution. It is sensitive to how inhomogeneous the distribution of matter in the Universe is, modulo the galaxy bias. The main difficulty of this measurement is that there are other effects besides the intrinsic clustering of galaxies that can also cause spacial correlations between galaxies. For instance, variations in the depth of the survey or other observing quantities across the sky can produce "fake" correlations which need to be accounted for. Other effects such as star contamination in the sample can introduce biases in the measurement. For the DES Y1 3x2pt analysis, a thorough study and correction of these effects is performed in Elvin-Poole et al. (2018).

We model the projected (angular) density contrast of galaxies in redshift bin i by

Table 6.1: Parameters and priors used in the 3x2pt analysis modeling. *Flat* denotes a flat prior in the range given while *Gauss*(μ, σ) is a Gaussian prior with mean μ and width σ. The Δz^i priors listed are for Metacalibration galaxies and BPZ photo-z estimates (see Hoyle et al. (2018) for other combinations). The parameter w is fixed to -1 in the ΛCDM runs.

Parameter	Prior
Cosmology	
Ω_m	flat (0.1, 0.9)
A_s	flat $(5 \times 10^{-10}, 5 \times 10^{-9})$
n_s	flat (0.87, 1.07)
Ω_b	flat (0.03, 0.07)
h	flat (0.55, 0.91)
$\Omega_\nu h^2$	flat(5×10^{-4},10^{-2})
w	flat (-2,-0.33)
Lens Galaxy Bias	
$b_i (i = 1, 5)$	flat (0.8, 3.0)
Intrinsic Alignment	
$A_{\rm IA}(z) = A_{\rm IA}[(1+z)/1.62]^{\eta_{\rm IA}}$	
$A_{\rm IA}$	flat $(-5, 5)$
$\eta_{\rm IA}$	flat $(-5, 5)$
Lens photo-z shift (red sequence)	
$\Delta z^1_{\rm l}$	Gauss $(0.008, 0.007)$
$\Delta z^2_{\rm l}$	Gauss $(-0.005, 0.007)$
$\Delta z^3_{\rm l}$	Gauss $(0.006, 0.006)$
$\Delta z^4_{\rm l}$	Gauss $(0.000, 0.010)$
$\Delta z^5_{\rm l}$	Gauss $(0.000, 0.010)$
Source photo-z shift	
$\Delta z^1_{\rm s}$	Gauss $(-0.001, 0.016)$
$\Delta z^2_{\rm s}$	Gauss $(-0.019, 0.013)$
$\Delta z^3_{\rm s}$	Gauss $(+0.009, 0.011)$
$\Delta z^4_{\rm s}$	Gauss $(-0.018, 0.022)$
Shear calibration	
$m^i_{\rm Metacalibration} (i = 1, 4)$	Gauss $(0.012, 0.023)$
$m^i_{\rm im3shape} (i = 1, 4)$	Gauss $(0.0, 0.035)$

$\delta^i_{\rm g}$, the convergence field of source tomography bin j as κ^j, the redshift distribution of the redMaGiC/source galaxy sample in tomography bin i as $n^i_{{\rm g}/\kappa}(z)$, and the angular number densities of galaxies in this redshift bin as

$$\bar{n}^i_{{\rm g}/\kappa} = \int dz\, n^i_{{\rm g}/\kappa}(z)\,. \tag{6.1}$$

The radial weight function for clustering in terms of the comoving radial distance χ is

$$q^i_{\delta_{\rm g}}(k,\chi) = b^i\,(k, z(\chi))\,\frac{n^i_{\rm g}(z(\chi))}{\bar{n}^i_{\rm g}}\frac{dz}{d\chi}\,, \tag{6.2}$$

where $b^i(k, z(\chi))$ is the galaxy bias of the redMaGiC galaxies in tomographic bin i, and the lensing efficiency

$$q^i_\kappa(\chi) = \frac{3H_0^2\Omega_m}{2{\rm c}^2}\frac{\chi}{a(\chi)}\int_\chi^{\chi_{\rm h}} {\rm d}\chi' \frac{n^i_\kappa(z(\chi'))dz/d\chi'}{\bar{n}^i_\kappa}\frac{\chi'-\chi}{\chi'}\,, \tag{6.3}$$

where H_0 is the Hubble constant, c the speed of light, and a the scale factor. Under the *hybrid* Limber approximation[1], the angular correlation function for galaxy clustering can be written as

$$\begin{aligned} w^i(\theta) = \int \frac{d\ell\,\ell}{2\pi} J_0(\ell\theta) \int d\chi\, \frac{q^i_{\delta_{\rm g}}\left(\frac{\ell+1/2}{\chi},\chi\right) q^j_{\delta_{\rm g}}\left(\frac{\ell+1/2}{\chi},\chi\right)}{\chi^2} \\ \times P_{\rm NL}\left(\frac{\ell+1/2}{\chi}, z(\chi)\right) \end{aligned} \tag{6.4}$$

where $P_{\rm NL}(k,z)$ is the non-linear matter power spectrum at wave vector k and redshift z.

6.2.2 Galaxy–galaxy lensing: $\gamma_t(\theta)$

We will not get into many details about this probe since it was already extensively described in the previous chapters. In Fig. 5.2 we showed the measurements of galaxy–galaxy lensing in all pairs of lens-source tomographic bins, including the model prediction for our best-fit parameters. The plots include bin pairs for which the lenses are nominally behind the sources, which are expected to have no gravitational lensing signal. However, they can still be useful in constraining the intrinsic alignment param-

[1] Standard Limber approximation uses $k = \ell/\chi$, while an extended version of this approximation uses $k = (\ell+1/2)/\chi$, both in the prefactor and power-spectrum argument. This extended version is actually a worse approximation than standard Limber, since the approximated prefactor converges only with $\mathcal{O}(\ell)$. Better is a hybrid version, with ℓ in the prefactor, but $\ell + 1/2$ in integral.

eters in our model (see, e.g., Troxel & Ishak (2014)). In the previous chapter we carried out a number of null tests to ensure the robustness of these measurements, none of which showed evidence for significant systematic uncertainties besides the ones characterized by the nuisance parameters in this analysis. Here, we write the modeling of the tangential shear specifically for the cosmological analysis:

$$\gamma_{\rm t}^{ij}(\theta) = (1+m^j)\int \frac{d\ell\,\ell}{2\pi}\,J_2(\ell\theta)\int d\chi \frac{q^i_{\delta_{\rm g}}\left(\frac{\ell+1/2}{\chi},\chi\right)q^j_\kappa(\chi)}{\chi^2} \times P_{\rm NL}\left(\frac{\ell+1/2}{\chi}, z(\chi)\right) \tag{6.5}$$

where m^j is the multiplicative shear bias, and J_2 is the 2nd-order Bessel function.

6.2.3 Cosmic shear: $\xi_\pm(\theta)$

For galaxy shapes correlations, a pair of two-point functions are used to capture the relevant information: $\xi_+(\theta)$ and $\xi_-(\theta)$ are the sum and difference of the products of the tangential and cross components of the shear, measured with respect to the line connecting each galaxy pair. For more details, see Troxel et al. (2018). The cosmic shear signal is independent of galaxy bias but shares the same general form as the other sets of two-point functions. The theoretical predictions for these shear-shear two-point functions are

$$\xi^{ij}_{+/-}(\theta) = (1+m^i)(1+m^j)\int \frac{d\ell\,\ell}{2\pi}\,J_{0/4}(\ell\theta) \times \int d\chi \frac{q^i_\kappa(\chi)q^j_\kappa(\chi)}{\chi^2} P_{\rm NL}\left(\frac{\ell+1/2}{\chi}, z(\chi)\right) \tag{6.6}$$

where the efficiency functions are defined above, and J_0 and J_4 are the Bessel functions for ξ_+ and ξ_-.

6.3 Inferring cosmological parameters

We use these measurements from the DES Y1 data to estimate cosmological parameters in the framework of two cosmological models: ΛCDM and wCDM, both already discussed in Chapter 1. In summary, ΛCDM contains three energy densities in units of the critical density: the matter, baryon, and massive neutrino energy densities, Ω_m, Ω_b, and Ω_ν. Note that in Eq. (1.26) from Sec. 1.5 baryons were included in the form of matter, and neutrinos in the form of radiation, but the same equations apply. The density

parameter of neutrinos is defined as

$$\Omega_\nu h^2 = \frac{\sum m_\nu}{93\text{eV}} \tag{6.7}$$

for neutrinos of mass in the range 5×10^{-4} eV to 1 MeV, where the sum is over all families with mass in that range (Patrignani et al., 2016). The energy density in massive neutrinos is a free parameter here although it is often fixed in cosmological analyses to either zero or to a value corresponding to the minimum allowed neutrino mass of 0.06 eV from oscillation experiments (Patrignani et al., 2016). The mass is split equally among the three eigenstates, hence assuming a degenerate mass hierarchy for the neutrinos. Note that even if neutrinos account for a very small fraction of the total energy density, they can have an observable effect on the formation of structure, as neutrino free-streaming damps the growth of perturbations.

Apart from the energy densities, ΛCDM has three more free parameters: the Hubble parameter today, H_0, and the amplitude and spectral index of the primordial scalar density perturbations, A_s and n_s, defined in Eq. (1.48). Since this model is based on inflation, which predicts a flat universe, we fix Ω_k here and assume $\Omega_\Lambda = 1 - \Omega_m$. In a subsequent DES study (DES Collaboration et al., 2018) some extended models including curvature as a free parameter were considered, but the constraining power resulted poor without combining with external data. Moreover, it is common to replace A_s with the RMS amplitude of mass fluctuations on 8 h^{-1} Mpc scale in linear theory, σ_8, which can be derived from the other parameters, and which we defined in Eq. (1.47). However, σ_8 and Ω_m are usually very correlated in posteriors coming from weak lensing studies. Therefore, it is useful to define another parameter removing this correlation:

$$S_8 \equiv \sigma_8 \left(\frac{\Omega_m}{0.3}\right)^{0.5}. \tag{6.8}$$

The other model considered in this work is wCDM, which allows for dark energy to evolve with time. Within the wCDM model, the dark energy equation of state parameter w is taken as an additional free parameter instead of being fixed at $w = -1$ as in ΛCDM. wCDM thus contains 7 cosmological parameters, while ΛCDM has 6 of them. In a subsequent study presented in DES Collaboration et al. (2018) extended models in which w is allowed to vary in time are also considered.

In addition to the cosmological parameters, both models include 20 nuisance parameters, which are are the nine shift redshift parameters, Δz^i, for the source and lens redshift distributions in each bin, the five redMaGiC galaxy bias parameters, b^i, the four multiplicative shear biases, m^i, and two parameters, $A_{\rm IA}$ and $\eta_{\rm IA}$ that parametrize the intrinsic alignment model.

6.3.1 Likelihood analysis

The basic function used to infer cosmological parameters from a set of measurements, in this case the two-point correlation functions, is the *likelihood*, which is the probability that a given experiment would get the data it did given a theory. Generally, from a statistical point of view, the observations are a random sample from an unknown population, and the goal of a statistical analysis is to inference the population that is most likely to have generated the sample, specifically the probability distribution corresponding to the population. For instance, in cosmology, and specifically here, the two-point correlation functions measured from the data are one sample of all possible two-point correlation functions that could be measured from all realizations of the density field (see discussion in Sec. 1.7.2). Assuming the two-point correlation functions D_i are multivariate random variables, we can use a Gaussian likelihood to infer the cosmological parameters. Then, we can determine the parameters $\vec{p}$ of the theory along with errors, which we will call posterior "contours", by sampling the likelihood in the many-dimensional parameter space:

$$\ln \mathcal{L}(\vec{p}) = -\frac{1}{2} \sum_{ij} \left[D_i - T_i(\vec{p})\right] {C^{-1}}_{ij} \left[D_j - T_j(\vec{p})\right], \tag{6.9}$$

where $\vec{p}$ include both the cosmological and nuisance parameters and $T_i(\vec{p})$ are the theoretical predictions as given in Eqs. 6.4, 6.5 and 6.6. To form the posterior, we multiply the likelihood by the priors, $\mathcal{P}(\vec{p})$ specified in Table 6.1.

Assuming D_i are drawn from a Gaussian distribution is very common (there is no realistic alternative nowadays) but it does not necessarily mean it is correct. Density fluctuations at low redshift, after undergoing gravitational evolution for the past 13 billion years, have become non-Gaussian, and therefore it could be that two-point correlation functions obtained from an underlying non-Gaussian filed would actually not follow a Gaussian distribution. In that case, using a Gaussian likelihood would be a source of systematic error and could bias the posteriors. Studies such as Sellentin & Heavens (2018) suggest this is still a subdominant effect but might need consideration in future analyses.

Also, the covariance matrix C enters the likelihood function, since each of the measurements might be correlated with all the others, including between angular and redshift bins. The DES Y1 3x2pt data vector contains 457 points and hence the covariance is a symmetric 457×457 matrix. The covariance matrix is obtained using `CosmoLike` (Krause & Eifler, 2017), which computes the relevant four-point functions in the halo model, as described in Krause et al. (2017). Parallel pipelines, `CosmoSIS`[2] (Zuntz et al., 2015b) and `CosmoLike`, are used to compute the theoretical predictions and to

[2] `https://bitbucket.org/joezuntz/cosmosis/`

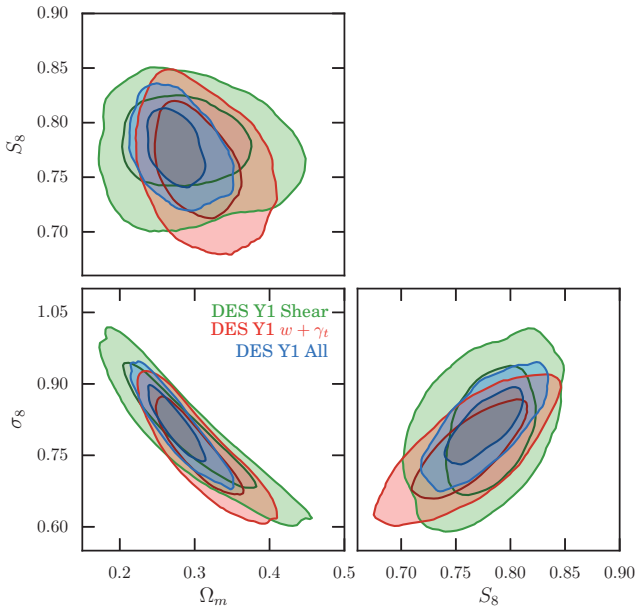

Figure 6.2: ΛCDM constraints from DES Y1 on Ω_m, σ_8, and S_8 from cosmic shear (green), redMaGiC galaxy clustering plus galaxy–galaxy lensing (red), and their combination (blue). Here, and in all such 2D plots below, the two sets of contours depict the 68% and 95% confidence levels.

generate the Monte Carlo Markov Chain (MCMC) samples that map out the posterior space leading to parameter constraints.

Also, and end-to-end analysis was also performed on two different cosmological N-body simulations, Buzzard (Busha et al., 2013) and MICE (Fosalba et al., 2015) where all the steps of the analysis were applied, checking that the true cosmological parameters could be recovered (MacCrann et al., 2018). Finally, a blinding procedure was carefully followed throughout all the analysis to avoid confirmation biases.

6.4 DES Y1 3x2pt Cosmological Results and Conclusions

We first consider the ΛCDM model with six cosmological parameters. The 3x2pt combination is most sensitive to two cosmological parameters, Ω_m and S_8, and hence here we focus on constraints on these parameters. In Fig. 6.2 we show the constraints on Ω_m and S_8, and also on the more correlated parameter σ_8. The results are displayed for the whole 3x2pt analysis, but also for two subsets of the data, one with galaxy clustering and galaxy-galaxy lensing only, which is already sufficient to break degeneracies with the galaxy bias, and the other for cosmic shear only, to demonstrate they are consistent before they are combined. The combined results lead to the following constraints

$$\begin{aligned} \Omega_m &= 0.267^{+0.030}_{-0.017} \\ S_8 &= 0.773^{+0.026}_{-0.020} \\ \sigma_8 &= 0.817^{+0.045}_{-0.056}. \end{aligned} \tag{6.10}$$

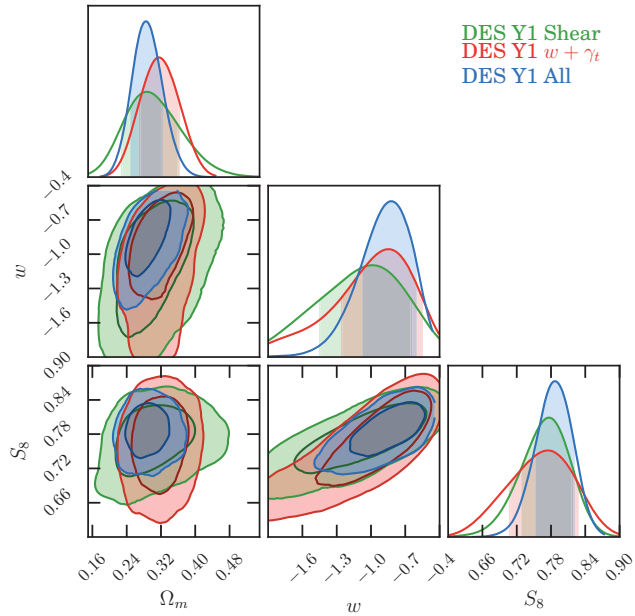

Figure 6.3: Constraints on the three cosmological parameters σ_8, Ω_m, and w in wCDM from DES Y1. The constraints from cosmic shear only (green); $w(\theta) + \gamma_t(\theta)$ (red); and all three two-point functions (blue) are shown. Here and below, outlying panels show the marginalized 1D posteriors and the corresponding 68% confidence regions.

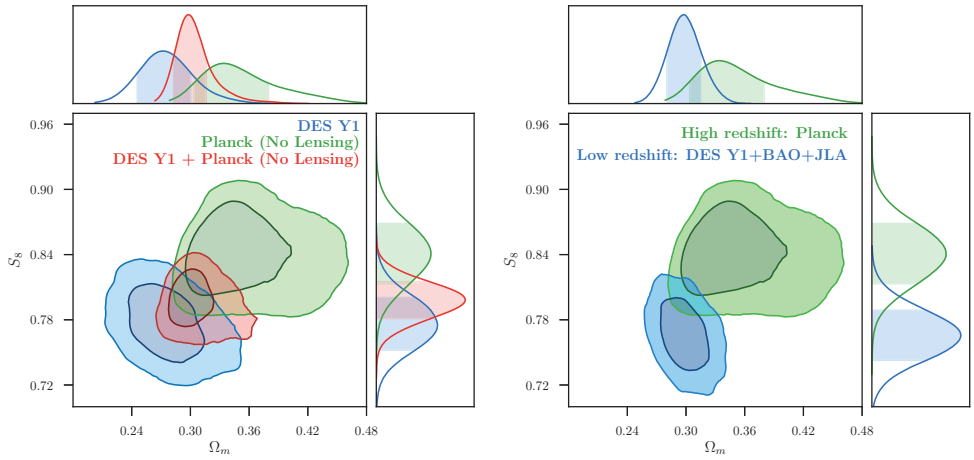

Figure 6.4: **Left:** ΛCDM constraints from the three combined probes in DES Y1 (blue), Planck with no lensing (green), and their combination (red). **Right:** ΛCDM constraints from high redshift (Planck, without lensing) and multiple low redshift experiments: DES Y1, Baryon Acoustic Oscillations (BAO) and Type Ia Supernovae (JLA).

For wCDM, results are shown in Fig. 6.3 for Ω_m, S_8, and w. Again, the constraints from cosmic shear and from galaxy–galaxy lensing + galaxy clustering are depicted, showing they agree with one another before they are combined. w is found to be consistent with -1, thus being compatible with dark energy being a cosmological constant.

Finally, the results from the DES Y1 3x2pt analysis are compared with findings from other experiments. On the left side of Fig. 6.4, we compare them with *Planck* results coming from the Cosmic Microwave Background. Note the *Planck* contours are obtained after marginalizing over the neutrino energy density parameter, in the same way as the DES contours are. The CMB measures the state of the Universe when it was 380,000 years old, while DES measures the matter distribution in the Universe roughly ten billion years later. Then, comparing these results is a very important test for the current standard cosmological model. Moreover, to perform a more stringent test, we combined results from different low-redshift experiments besides DES, such as Baryon Acoustic Oscillations (BAO) and Type Ia Supernovae, and compared their combination with the CMB *Planck* results, shown on the right side of Fig. 6.4. On the displayed $\Omega_m - \sigma_8$ 2D plane, a mild tension is apparent both when comparing DES alone with *Planck* and when low redshift probes are combined. This tension is however diluted when the whole 26 parameter space is considered. Future analysis including larger data sets for DES and other galaxy surveys will shed light on this mild tension and will provide more decisive tests of ΛCDM.

Concluding, we have presented cosmological results from a combined analysis of galaxy clustering and weak gravitational lensing, using photometric data from the first year of observations of the Dark Energy Survey. These combined probes demonstrate that galaxy surveys have now achieved comparable constraining power to that of the cosmic microwave background in the Ω_m–S_8 plane, starting a new era in cosmology, and have been able to test the ΛCDM and wCDMmodels. The results at this level of accuracy are not conclusive, but pave the path for upcoming cosmological analysis with larger data sets. The next round of cosmological analyses of DES data will include data from the first three years of the survey (DES Y3), which cover more than three times as much area to greater depth than Y1, and will incorporate constraints from clusters, supernovae, and cross-correlation with CMB lensing, providing more insight on dark energy and cosmic acceleration.

Part IV

Cosmological Constraints from Lensing Ratios

In this part we present a measurement of lensing ratios using galaxy position and lensing data from the Dark Energy Survey, and CMB lensing data from the South Pole Telescope and Planck. We use the ratio measurements to generate cosmological constraints, focusing on the curvature parameter. We demonstrate that photometrically selected galaxies can be used to measure lensing ratios, and argue that future lensing ratio measurements with data from a combination of LSST and Stage-4 CMB experiments can be used to place interesting cosmological constraints, even after marginalizing over systematic uncertainties.

Chapter 7

Cosmological lensing ratios with DES Y1, SPT and *Planck*

7.1 Introduction

As photons from a distant light source traverse the Universe, their paths are perturbed by the gravitational influence of large scale structure. Since galaxies trace this structure, the projected galaxy density on the sky, δ_g, is correlated with the strength of gravitational lensing, as quantified via the convergence, κ. Two-point correlation functions between δ_g and κ are sensitive to the cosmological growth of structure and to the geometry of the Universe (e.g. Bianchini et al., 2015; Giannantonio et al., 2016; Prat et al., 2018a). We refer to the galaxies used to compute δ_g as *tracer* galaxies since we use them as tracers of the large scale structure.

Extracting useful cosmological information from tracer-lensing correlations is complicated by the need to model the relationship between the galaxy density field and the underlying matter field, i.e. galaxy bias (Benson et al., 2000). Furthermore, at small angular separations, lensing-galaxy two-point functions become sensitive to the small scale matter power spectrum, which is difficult to model due to e.g. nonlinearities and baryonic effects (van Daalen et al., 2011; Takahashi et al., 2012). For these reasons, many recent analyses (e.g. DES Collaboration, 2018b) have restricted the usage of galaxy-lensing correlations to the regime where a simple linear bias model can be assumed and baryonic effects on the matter power spectrum can be neglected. While this approach has the advantage of decreasing the complexity of the required modeling, it comes at the cost of increased statistical uncertainty.

Several authors (e.g. Jain & Taylor, 2003; Bernstein, 2006; Hu, Holz & Vale, 2007; Das & Spergel, 2009) have pointed out that if one considers suitably defined *ratios* between lensing-galaxy two-point functions, the dependence of these ratios on the galaxy-matter power spectrum cancels, but the ratio is still sensitive to the angular diameter distances to the tracer galaxies and to the sources of light used to measure lensing. This

sensitivity can be used to constrain cosmology via the distance-redshift relation. The cancellation of the galaxy-matter power spectrum is valid when two conditions are met: (1) the ratio is between two two-point functions that involve the same set of tracer galaxies, but sources at two different redshifts, and (2) the tracer galaxies are narrowly distributed in redshift.

In principle, any two sources of light could be used to compute a lensing ratio. However, as pointed out by Hu, Holz & Vale (2007) and Das & Spergel (2009), lensing ratios that involve galaxy light as one of the source planes and CMB light as the other are especially interesting cosmological probes. There are two reasons for this. First, the CMB provides a very long redshift lever arm, which increases the sensitivity of the ratios to cosmological parameters. Second, the redshift of the CMB is known very precisely and is not subject to e.g. photometric redshift uncertainty. In contrast, lensing ratios involving only galaxy lensing are more sensitive to photometric redshift and shear calibration errors, and less sensitive to cosmology because both source planes are then at low redshift. Indeed, the recent galaxy-galaxy lensing analysis of Prat et al. (2018a) used lensing ratios to place constraints on the photometric redshifts of source galaxies, and demonstrated their ability to inform shear calibration priors as well. On the other hand, Kitching et al. (2015) used lensing ratio measurements involving only galaxy lensing with galaxy clusters as lenses to measure the distance-redshift relation, and infer cosmological parameters in combination with other probes.

In this work, we present measurements of lensing ratios involving galaxy lensing and CMB lensing using data from the Dark Energy Survey (DES), the South Pole Telescope (SPT) and *Planck*. The DES data is used to construct samples of tracer galaxies and to generate weak lensing convergence maps. The SPT and *Planck* data are used to construct CMB lensing convergence maps. We measure angular correlations between the tracer galaxy samples and the convergence maps, and use these measurements to constrain lensing ratios for multiple source and tracer galaxy redshift bins. The measured ratios are then used to constrain cosmology, focusing on the curvature parameter, Ω_k.

For current data, with measurement uncertainty on the lensing ratios of roughly 10%, the cosmological constraints obtained from the ratio measurements are fairly weak. We therefore also explore the potential of future data to constrain cosmology using lensing ratios. In particular, we consider how the presence of systematic errors in estimated redshifts and shears can degrade the cosmological constraints from lensing ratio measurements. As part of this analysis, we consider how future lensing ratio constraints can potentially be improved by using photometrically identified tracer galaxies rather the spectroscopically identified galaxies, sacrificing some redshift precision for increased number density and increased overlap on the sky with planned CMB experiments.

An analysis of lensing ratios formed with galaxy lensing and CMB lensing measure-

ments was recently presented by Miyatake et al. (2017). In addition to using different, more constraining data, the present work differs from that of Miyatake et al. (2017) in two important respects. For the first time, we use a set of tracer galaxies obtained from a photometric survey. This is possible because of the redMaGiC algorithm (Rozo et al., 2016), which produces a selection of galaxies with tightly constrained photometric redshifts, whose error distributions are very well understood. Second, we perform a complete cosmological analysis to obtain parameter constraints from the lensing ratios.

Our measurements of the correlations between tracer galaxies and both galaxy and CMB lensing are similar to those of Baxter et al. (2016). However, in that work, the measured correlation functions were fit directly, rather than being used to compute lensing ratios. The complications of galaxy bias and baryonic effects at small scales were circumvented by introducing additional freedom into the model for the small-scale galaxy-matter power spectrum. The main advantage of the present work over Baxter et al. (2016) is the reduced complexity of the modeling and the fact that the constraints obtained here are purely geometrical in nature. Similarly, forthcoming analyses from DES and SPT will perform a joint analysis of cross-correlations between DES data products and CMB lensing maps produced from a combination of SPT and *Planck* data (see Baxter et al. 2019 for an overview of the analysis and methodology and Abbott et al. 2018a for the results). While such joint two-point analyses can place tight cosmological constraints, they are limited by our ability to model the data across a wide range of angular scales.

This paper is organized as follows. In Sec. 7.2 we introduce the basic formalism for describing the lensing ratios; in Sec. 7.3 we describe the data sets used in this work; in Sec. 7.4 we describe the process of extracting constraints on the lensing ratios from the data; in Sec. 7.5 we extend our modeling to include important systematic effects, and describe tests of the model's robustness; the results of our analysis of the data are presented in Sec. 7.6; we make forecasts for future experiments in Sec. 7.7, with emphasis on the impact of systematic errors in measurement of source galaxy redshifts; we conclude in Sec. 7.8.

7.2 Formalism

In this section we present the theory relevant to computing the lensing ratios of two point correlation functions between some set of tracer galaxies and gravitational lensing convergence, which can be reconstructed using either galaxy shear measurements at redshift of $z \sim 1$ or using the CMB at redshift of $z \sim 1100$. The lensing convergence, κ, in the direction $\hat{\theta}$ is given by

$$\kappa(\hat{\theta}) = \frac{3}{2}\Omega_{\rm m} H_0^2 \int d\chi \, d_A^2(\chi) \frac{q_s(\chi)}{a(\chi)} \delta(\hat{\theta}, \chi), \tag{7.1}$$

where $\Omega_{\rm m}$ is the matter density parameter today, H_0 is the Hubble constant today, χ is comoving distance, $d_A(\chi)$ is the angular diameter distance to χ, $a(\chi)$ is the scale factor, and $\delta(\hat{\theta}, \chi)$ is the overdensity at a particular point along the line of sight. We have defined the lensing weight function

$$q_s(\chi) = \frac{1}{d_A(\chi)} \int_{\chi}^{\infty} d\chi' W_s(\chi') \frac{d_A(\chi, \chi')}{d_A(\chi')}, \tag{7.2}$$

where $W_s(\chi)$ is the normalized distribution of source light as a function of redshift and we use the notation $d_A(\chi, \chi')$ to represent the angular diameter distance between comoving distance χ and χ'. For the CMB source plane, the source distribution can be approximated as a Dirac δ function centered at the comoving distance to the surface of last scattering, χ^*. In this case, the lensing weight function becomes

$$q_{\rm CMB}(\chi) = \frac{d_A(\chi, \chi^*)}{d_A(\chi^*)\, d_A(\chi)}. \tag{7.3}$$

We are interested in correlations between κ and the projected density of the tracer galaxies on the sky, $\delta_g(\hat{\theta})$. For tracer galaxies whose normalized redshift distribution is described by $W_l(\chi)$, the projected density on the sky can be written as

$$\delta_g(\hat{\theta}) = \int d\chi W_l(\chi)\, \delta_g^{3D}(\hat{\theta}, \chi), \tag{7.4}$$

where $\delta_g^{3D}(\hat{\theta}, \chi)$ is the 3D galaxy overdensity.

We write the two-point angular correlation between tracer galaxies and the lensing convergence as $w^{i\kappa}(\theta)$, where i labels the redshift bin of the lenses and κ can represent either the galaxy lensing map (κ_s^j for the lensing map derived from the jth galaxy source bin) or the CMB lensing map ($\kappa_{\rm CMB}$). It is also useful to define the harmonic space cross-spectrum between the galaxy density and lensing fields, which we write as $C^{i\kappa}(\ell)$. Using the Limber and flat sky approximations, we have

$$C^{i\kappa}(\ell) = \frac{3}{2}\Omega_{\rm m} H_0^2 \int d\chi W_l(\chi) \frac{q(\chi)}{a(\chi)} b\left(\frac{\ell}{d_A(\chi)}, \chi\right) P_{\rm NL}\left(\frac{\ell}{d_A(\chi)}, \chi\right), \tag{7.5}$$

where $q(\chi)$ is the lensing weight function corresponding to κ. We have written the galaxy-matter power spectrum as a bias factor, $b(k, \chi)$, multiplied by the non-linear matter power spectrum, $P_{\rm NL}(k, \chi)$. We can now convert the harmonic space cross-correlation to the angular two-point function:

$$w^{i\kappa}(\theta) = \sum \frac{2\ell + 1}{4\pi} F(\ell) P_\ell(\cos(\theta)) C^{i\kappa}(\ell), \tag{7.6}$$

where P_ℓ is the ℓth order Legendre polynomial and $F(\ell)$ describes additional filtering that is applied to the κ maps.

As described in Baxter et al. (2019), modes below $\ell < 30$ and above $\ell \gtrsim 3000$ in the CMB κ maps generated by Omori et al. (2017) can be very noisy, or potentially biased. We therefore filter the CMB maps to remove these modes. Since we are interested in ratios between correlations with $\kappa_{\rm CMB}$ and with κ_s, we apply the same filter to κ_s as we use for $\kappa_{\rm CMB}$; this ensures that the expectation of the ratio of the correlation functions remains a constant function of angular scale. Following Baxter et al. (2019), we adopt the filter function

$$F(\ell) = \exp(-\ell(\ell+1)/\ell^2_{\rm beam})\Theta(\ell - 30)\Theta(3000 - \ell), \tag{7.7}$$

where $\ell_{\rm beam} \equiv \sqrt{16 \ln 2}/\theta_{\rm FWHM} \approx 2120$ and $\Theta(\ell)$ is a step function. The use of the Gaussian smoothing reduces ringing as a result of the low-pass filtering.

In the limit that the tracer galaxies are narrowly distributed in redshift, the $W(\chi)$ factor in Eq. (7.5) can be replaced by $W(\chi) = \delta(\chi - \chi_l)$, where χ_l is the comoving distance to the tracer galaxies. After transforming to an integral over redshift, the ratio of the galaxy-CMB lensing cross-correlation to the galaxy-galaxy lensing cross-correlation can then be expressed as

$$r^{ij} = \frac{w^{i\,\kappa_{\rm CMB}}(\theta)}{w^{i\kappa^j_s}(\theta)} = \frac{d_A(z^i_l, z^*)}{d_A(z^*)\int_{z^i_l}^{\infty} dz\, n^j_s(z) \frac{d_A(z^i_l, z)}{d_A(z)}}, \tag{7.8}$$

where $n^j_s(z)$ is the normalized redshift distribution of the source galaxies and z^i_l is the redshift of the tracer galaxies in the ith bin. Eq. 7.8 depends only on the redshift to the tracer galaxies, the source galaxies, and the surface of last scattering. Therefore, the lensing ratios depend only on the distance-redshift relation in this limit. This is the main selling point of lensing ratios as cosmological observables: they contain information about the expansion history of the Universe, but do not require modeling galaxy bias or the matter power spectrum to extract this information. Bernstein (2006) has also pointed out that similar cosmographic measurements using a combination of gravitational lensing and observations of the transverse baryon acoustic oscillation feature can constrain curvature without assuming anything about the dynamics or content of the Universe. This is in contrast to other cosmological observables — including the angular scale of the CMB power spectrum and measurements of the distances and redshifts of supernovae — for which the dynamics must be specified in order to translate constraints on the distance-redshift relation to a constraint on curvature. In this work, however, we will specify the dynamics by considering models with dark energy parameterized by an equation of state w.

In the analysis presented here, the tracer galaxies have a non-zero extent in red-

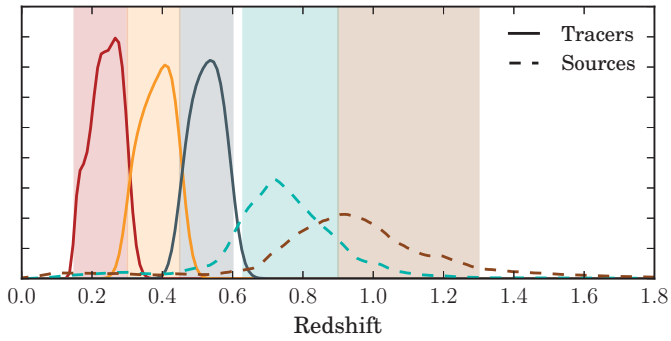

Figure 7.1: The estimated redshift distributions of the tracer and source galaxies for the different bins used in this analysis. Shaded bands represent the selection functions for the bins; galaxies are placed into bins according to the mean of their redshift probability distribution functions.

shift, so the δ-function approximation made above is questionable. However, we will show in Sec. 7.5.3 that the width of the tracergalaxy redshift distribution is sufficiently narrow, and the error bars on the ratio measurements are sufficiently large, that the redshift distribution of the tracer galaxies can be approximated as infinitely narrow. Additionally, the above model description assumes that all redshift and shear measurements are performed without biases. In Sec. 7.5 we will extend the model to include parameterizations for systematic errors in the measurements.

7.3 Data

In this work, we measure correlations between the tracer galaxies and lensing convergence maps generated from both the CMB and source galaxies. We use data from the first year observations of DES (Flaugher et al., 2015; DES Collaboration, 2016; Drlica-Wagner et al., 2018) for both the tracer galaxy sample and the galaxy lensing convergence maps (Chang et al., 2018). For the CMB convergence map, we use the map described in Omori et al. (2017), which used a combination of CMB data from SPT and *Planck*. Below we describe in more detail the tracer galaxies and the convergence maps used in this work.

7.3.1 Tracer galaxies

For the foreground tracer galaxies, we use a sample of galaxies referred to as "redMaGiC." This sample is the same galaxy sample used in the DES Y1 cosmological analysis (DES Collaboration, 2018b). redMaGiC galaxies are luminous red galaxies selected based on goodness of fit to a red sequence template, as described in Rozo et al. (2016).

The main advantage of the redMaGiC galaxy sample is that it is constructed to have very small photo-z uncertainties. In particular, the DES Y1 redMaGiC photo-zs have a scatter of $\sigma_z = 0.0166(1+z)$. The tracer redshift distributions shown in Fig. 7.1 are computed from the sum of Gaussians with $\sigma = \sigma_z$, centered on the redshift estimates computed by redMaGiC for each galaxy. For a more detailed description of the tracer galaxy sample, see Elvin-Poole et al. (2018) and Prat et al. (2018a).

We divide the tracer galaxies into three redshift bins between redshift 0.15 and 0.6, using the same z-binning as in the DES Y1 cosmology analysis (DES Collaboration, 2018b). The redshift distributions for these bins are estimated as the sum of the individual redshift probability distribution functions (PDF) for each redMaGiC galaxy, and are shown in Fig. 7.1. Galaxies were divided into bins based on the mean of the redshift PDF estimate for each galaxy. In this work we do not use the two higher redshift bins used by DES Collaboration (2018b) in order to minimize the overlap between tracers and sources. The uncertainty on the mean redshift for each of the redshift bins was studied in Cawthon et al. (2018), finding photometric redshift biases of $|\Delta z| < 0.01$.

7.3.2 Galaxy lensing convergence maps

We use the $\sim$ 1300 sq. deg. weak lensing convergence maps described in Chang et al. (2018). These maps were generated from the DES Y1 Metacalibration shear catalog (Zuntz et al., 2018), using the same sample that was used to obtain the DES Y1 3x2pt cosmology results (DES Collaboration, 2018b). Metacalibration is a recently developed method to calibrate galaxy shear measurements from the data itself, measuring the response of a shear estimator to an artificially applied shear, without relying on calibration from simulations (Sheldon & Huff, 2017; Huff & Mandelbaum, 2017). More details about the source sample and how the response corrections have been applied to the maps can be found in Troxel et al. (2018) and in Chang et al. (2018).

The galaxy convergence maps of Chang et al. (2018) were constructed using an implementation of the Kaiser-Squires method (Kaiser & Squires, 1993; Schneider, 1996) on a sphere (Heavens, 2003; Castro, Heavens & Kitching, 2005; Heavens, Kitching & Taylor, 2006; Leistedt et al., 2017; Wallis et al., 2017), which converts the shear, γ, into the convergence κ. The galaxy κ maps used here were generated on `HEALpix` maps with `nside` $= 2048$, as opposed to the maps described in Chang et al. (2018), which have `nside` $= 1024$. To match filtering applied to the CMB lensing maps described below, the galaxy κ maps were smoothed with a 5.4 arcmin (FWHM) Gaussian, and were filtered to remove modes with $l < l_{\rm min} = 30$ and $l > l_{\rm max} = 3000$.

We use the two higher redshift ($0.63 < z < 0.9$ and $0.9 < z < 1.3$) mass maps constructed in Chang et al. (2018) for this work. The redshift distributions of the source galaxies used to construct these maps are shown in Fig. 7.1, which have been obtained stacking a random sample from the redshift probability distribution of each galaxy. The

source galaxy samples that were used to construct these two maps correspond to the two high-redshift source bins used in the DES Y1 cosmological analysis, and hence they have been studied extensively for both their photo-z characteristics, (Hoyle et al., 2018; Gatti et al., 2018; Davis et al., 2017; Prat et al., 2018a) and their shear measurement biases (Zuntz et al., 2018; Samuroff et al., 2018). Briefly, their photometric redshift distributions have been estimated using the BPZ code (Benitez, 2000), and calibrated using COSMOS galaxies and galaxy clustering cross-correlations with the redMaGiC sample. This allows us to use the results of these studies as priors in our model-fitting, which is essential for extracting cosmological information from the lensing ratios.

7.3.3 CMB lensing map

The CMB lensing map used in this analysis is presented in Omori et al. (2017), and we refer readers to that work for more details. Briefly, Omori et al. (2017) combined 150 GHz maps from SPT and 143 GHz maps from *Planck* using inverse variance weighting to generate a combined CMB temperature map. A quadratic lensing estimator (Hu & Okamoto, 2002b) was then applied to the combined CMB temperature map to estimate $\kappa_{\rm CMB}$. Bright point sources detected in the flux density range $50 < F_{150} < 500$ mJy and $F_{150} > 500$ mJy in the 150 GHz band were masked with apertures of radius 6' and 9', respectively, prior to reconstruction. Modes in the $\kappa_{\rm CMB}$ maps with $\ell < 30$ and $\ell > 3000$ were removed to reduce the impact of mean-field calibration and to suppress potential biases due to foregrounds, and a 5.4 arcmin Gaussian smoothing was applied, consistently with the galaxy κ maps.

We note that using the joint SPT+*Planck* map from Omori et al. (2017) significantly improves the total signal-to-noise of the tracer-CMB lensing correlation measurements relative to using a CMB lensing map derived from *Planck* alone, and it also improves the results we would obtain with SPT alone.

7.4 Measurements of the lensing ratios

In this section we describe the procedure for obtaining constraints on lensing ratios from the combination of DES, SPT and *Planck* data. We begin by describing the procedure used to measure the galaxy-lensing correlation functions and their corresponding covariance matrix. Next, we describe corrections for possible tSZ contamination of the CMB lensing maps. Finally, we describe our fitting procedure for using the measured correlation functions to constrain the amplitudes of the lensing ratios.

7.4.1 Measuring the tracer-lensing two-point functions

We measure the angular two-point correlation function between the pixelized lensing convergence maps κ and the galaxy distribution δ_g by summing over tracer–convergence pixel pairs g, separated by angle θ. We subtract the corresponding correlation with a sample of random points in place of the tracer galaxies, where the sum is over random–convergence pairs r separated by θ. The final estimator is

$$w^{i\kappa}(\theta) = \frac{\sum_g \omega_g \kappa_g}{\sum_g \omega_g}(\theta) - \frac{\sum_r \omega_r \kappa_r}{\sum_r \omega_r}(\theta), \tag{7.9}$$

where ω_g and ω_r are the weights associated respectively with each tracer galaxy and random point. This estimator is analogous to that used in tangential shear measurements in galaxy-galaxy lensing (see e. g. Prat et al. 2018a). For the random points we set $\omega_r = 1$, and for the galaxies this weight was computed in Elvin-Poole et al. (2018) to reduce the correlation with observational systematics. For the fiducial measurements in this work, we grouped the tracer-convergence pairs in five log-spaced angular separation bins between 2.5 and 100 arcmin. We use `TreeCorr` [1] (Jarvis, Bernstein & Jain, 2004) to measure all two-point correlation functions in this work. The measured correlation functions are shown in Fig. 7.3.

7.4.2 Covariance matrix of the two-point functions

We estimate the covariance matrix between the measurements using the jackknife method. In this approach, the survey area is divided into $N_{\rm JK}$ regions ('jackknife patches'), and the correlation function measurements are repeated once with each jackknife patch removed for the tracer sample, while we keep the convergence map untouched. The estimate of the covariance of measurements is then

$$C^{\rm JK}_{i\kappa\theta,i'\kappa'\theta'} = \frac{N_{\rm JK}-1}{N_{\rm JK}} \sum_{n=1}^{N_{\rm JK}} \left(w_n^{i\kappa}(\theta) - \overline{w^{i\kappa}}(\theta) \right) \left(w_n^{i'\kappa'}(\theta') - \overline{w^{i'\kappa'}}(\theta') \right), \tag{7.10}$$

where i denotes the tracer galaxy bin, κ denotes the convergence map, n denotes the jackknife patch being removed, and $\overline{w^{i\kappa}}(\theta)$ is the mean across the $N_{\rm JK}$ resamplings. The jackknife provides a *data*-based estimate of the covariance. It is well motivated here since our analysis focuses on the small scales of the tracer-lensing correlations (down to 2.5') which are difficult to model theoretically. Although the jackknife cannot capture super sample covariance (Takada & Hu, 2013) since by definition no samples are available outside the survey, this contribution to the covariance is expected to be negligible over the scales considered (i.e. below 100'). Moreover, at small scales, jack-

[1] `https://github.com/rmjarvis/TreeCorr`

knife estimates have been extensively validated; see e.g. Prat et al. (2018a) and Omori et al. (2018b).

The jackknife regions are obtained using the `kmeans` algorithm[2] run on a homogeneous random point catalog with the same survey geometry. We choose $N_{\rm JK} = 500$, which corresponds to jackknife regions whose typical size matches the maximum scale used in this work, of 100 arcmin.

7.4.3 Correcting the two-point functions for thermal Sunyaev-Zel'dovich contamination

A study of the systematics affecting the $w^{i\kappa_{\rm CMB}}$ measurements using the DES redMaGiC galaxies and the Omori et al. (2017) CMB lensing map was performed in Baxter et al. (2019). In that work, the presence of the thermal Sunyaev-Zel'dovich (tSZ) effect in the CMB lensing map from Omori et al. (2017) was identified as a potentially significant source of contamination. To reduce this contamination, Baxter et al. (2019) took the conservative approach of excluding the small angular scales from the analysis that were estimated to be most contaminated.

Here, we take a more aggressive approach by explicitly modeling the tSZ contamination in our analysis. We use the model of tSZ contamination from Baxter et al. (2019) for this purpose (see their Eq. 22). The Baxter et al. (2019) model was derived in the following manner. First, the tSZ signal over the SPT patch was estimated using catalogs of galaxy clusters detected by DES, SPT and *Planck*. The tSZ signal for each cluster was estimated using a β-model (Cavaliere & Fusco-Femiano, 1976) fit to the observed cluster tSZ profile (for SPT-detected clusters) or by adopting a model profile given an estimate of the cluster mass (for DES and *Planck* detected clusters). The resulting tSZ map was then processed through the κ estimation pipeline of Omori et al. (2017) to calculate spatially varying tSZ contamination in the $\kappa_{\rm CMB}$ maps. Finally, the contaminant maps were correlated with the DES redMaGic catalogs to estimate the bias in $w^{i\kappa_{\rm CMB}}(\theta)$ due to tSZ contamination. Fitting functions for the measured biases are provided in Baxter et al. (2019), and we adopt those fitting functions here.

We test the sensitivity of our results to the model for tSZ contamination in Sec. 7.5.3. Note that in this analysis, we make the same masking choices as in Baxter et al. (2019) so that the tSZ model derived therein is appropriate; this includes masking the most massive galaxy clusters across the SPT field. Note that in Baxter et al. (2019) the effects of such masking on the correlation functions was found to be negligible relative to the statistical uncertainties.

[2] `https://github.com/esheldon/kmeans_radec`

7.4.4 Extracting constraints on the lensing ratios

Given the measurements of the tracer-lensing correlation functions, we wish to extract constraints on the ratios of these correlations. Simply taking the ratios of the correlation function measurements is not optimal when the two measurements have non-zero uncertainties and can lead to biased results. Instead, we take the approach described below to measure the ratios.

We model the correlation functions as

$$w^{i\kappa_{\rm s}^j}(\theta_a) = \beta_{ij}\alpha_{ia} \tag{7.11}$$

$$w^{i\kappa_{\rm CMB}}(\theta_a) = \beta_{i\rm CMB}\alpha_{ia} f_i^{\rm tSZ}(\theta_a) \tag{7.12}$$

where α_{ia}, β_{ij} and $\beta_{i\rm CMB}$ are free parameters. Here, $f_i^{tSZ}(\theta)$ is the tSZ bias model for each tracer bin i described in Sec. 7.4.3. Without loss of generality, we set $\beta_{i0} = 1$. In effect, the α_{ia} control the *shape* of the correlation function between the ith tracer redshift bin and each of the convergence maps.

On the other hand, the β_{ij} and $\beta_{i\rm CMB}$ (which we can group as $\beta_{i\kappa}$), control the *amplitudes* of the correlation functions of different convergence maps with the tracer galaxies in redshift bin i; we will use the βs to extract constraints on the lensing ratios.

Given our model for the measured correlation functions, we define a Gaussian likelihood for the measurements, $\{w^{i\kappa}(\theta)\}$, where κ can either be $\kappa_{\rm CMB}$ or the galaxy mass map in redshift bin j, κ_s^j:

$$\ln\mathcal{L}(\{\, w^{i\kappa}(\theta)\,\}|\{\alpha_i(\theta),\beta_{i\kappa}\}) = -\frac{1}{2}\sum_{i\kappa\theta\, i'\kappa'\theta'}\left(w^{i\kappa}(\theta) - \hat{w}^{i\kappa}(\theta)\right) \times \left[\mathbf{C}^{-1}\right]_{i\kappa\theta,i'\kappa'\theta'}\left(w^{i\kappa'}(\theta') - \hat{w}^{i\kappa'}(\theta')\right). \tag{7.13}$$

In the equation above $\hat{w}$ represents the correlation function model from Eq. 7.11 and Eq. 7.12, and $\mathbf{C}$ is the covariance matrix of the observations, as estimated with the jackknife method described in Sec. 7.4.1. We apply the so-called Hartlap factor (Hartlap, Simon & Schneider, 2007) to the inverted covariance to account for the noise in the jackknife covariance matrix estimate. We assume flat priors on the α and β, so the posterior on these parameters is simply proportional to the likelihood. We sample from the model posterior using a Monte Carlo Markov Chain (MCMC) method implemented in the code `emcee` (Foreman-Mackey et al., 2013).

Ultimately, we are not interested in the α or β themselves, but rather the ratios of the correlation function measurements for pairs that use the same tracer galaxy bin. We can obtain the posterior on the ratios by computing these ratios at each point in the

Markov chains for the β's. At each point in the chains, we compute

$$r_{ij} = \frac{\beta_{i\,\mathrm{CMB}}}{\beta_{ij}}. \tag{7.14}$$

The distribution of r_{ij} then provides the posterior of the ratios, without loss of information. By choosing to keep the (noisier) galaxy-CMB lensing two-point functions in the numerator of the ratio, we reduce the possibility of divergences in the ratios of the βs (which can occur if the posterior on a β has support at $\beta = 0$). Hereafter, we use the term *lensing ratio* to refer to this definition of such ratios.

7.5 Modeling the lensing ratios

Above we have developed a model for the correlation functions that allows us to extract constraints on the lensing ratios in Eq. 7.14. We now describe our parameterized model for the measured lensing ratios, including prescriptions for various systematic uncertainties, in order to extract constraints on cosmology.

7.5.1 Modeling photometric redshift and shear calibration bias

As noted above, we assume that all of the tracer galaxies are located at a single redshift, z_l. We obtain z_l from the mean of the redshift distributions of the redMaGiC galaxies shown in Fig. 7.1. For the source galaxies, we use the full $n_s(z)$ when computing the model for the ratios.

Following Krause et al. (2017), we parameterize redshift uncertainties in the estimated tracer and source galaxy redshift distributions with the bias parameters, Δz_l and Δz_s, respectively. This means that in Eq. (7.8) we make the replacements

$$n_s^j(z) \to n_s^j(z - \Delta z_s^j) \tag{7.15}$$

and

$$z_l^i \to z_l^i + \Delta z_l^i, \tag{7.16}$$

where Δz_s^j and Δz_l^i are treated as free parameters (with priors) for each source and tracer galaxy redshift bin, respectively.

We parameterize shear calibration bias with the parameter m such that the observed shear is related to the true shear via $\gamma_{\mathrm{obs}} = (1 + m)\,\gamma_{\mathrm{true}}$. This means that we make the replacement

$$r_{ij} \to \frac{r_{ij}}{1 + m_j}, \tag{7.17}$$

where m_j is a free parameter for each source galaxy redshift bin.

7.5.2 Complete model for the lensing ratio

Following from Eq. (7.8) and including the above prescriptions for systematic uncertainties, our complete model for r_{ij} is:

$$\hat{r}_{ij}\left(\vec{\theta}_{\rm cosmo}, \vec{\theta}_{\rm sys}\right) = \frac{(1+m_j)\, d_A\left(z_l^i + \Delta z_l^i, z^*\right)}{d_A(z^*) \int_{z_l^i+\Delta z_l^i}^{\infty} dz\, n_s^j(z - \Delta z_s^j) \frac{d_A(z_l^i+\Delta z_l^i, z)}{d_A(z)}}, \tag{7.18}$$

where $\vec{\theta}_{\rm cosmo}$ is the set of cosmological parameters and $\vec{\theta}_{\rm sys}$ is the vector of systematics parameters. We use `Astropy` for computing cosmological distances (Astropy Collaboration et al., 2018).

The posterior on the parameters given the set of measured ratios, $\{r\}$, is given by

$$P(\vec{\theta}_{\rm cosmo}, \vec{\theta}_{\rm sys}|\{r\}) = P(\{r\}|\{\hat{r}(\vec{\theta}_{\rm cosmo}, \vec{\theta}_{\rm sys})\}) P_{\rm prior}(\vec{\theta}_{\rm cosmo}) P_{\rm prior}(\vec{\theta}_{\rm sys}), \tag{7.19}$$

where $P_{\rm prior}(\vec{\theta}_{\rm cosmo})$ is the prior on the cosmological parameters, and $P_{\rm prior}(\vec{\theta}_{\rm sys})$ is the prior on the systematics parameters. For the likelihood $P(\{r\}|\{\hat{r}\})$ we adopt a multivariate Gaussian approximation to the posterior from Sec. 7.4.4:

$$\ln P(\{r\}|\{\hat{r}\}) = -\frac{1}{2}(r-\hat{r})\, \mathbf{C}_r^{-1} (r-\hat{r})^T. \tag{7.20}$$

We compute the covariance matrix of the ratio estimates, $\mathbf{C}_r$, from the Markov chains for the ratios described in Sec. 7.4.4. We discuss the accuracy of the Gaussian approximation to the true posterior in Appendix D.

7.5.3 Model Validation

Narrow tracer bin approximation

A fundamental assumption of our analysis is that in our modeling, we can approximate the tracer galaxy redshift distribution with a δ function centered at the mean of full redshift distribution. Only in the δ function limit does the cancellation of the galaxy-matter power spectrum occur. However, as described in Sec. 7.3.1, the tracer galaxies used in this work are not all at the same redshift, but they are distributed over a relatively narrow redshift interval. Furthermore, as seen in Fig. 7.1, there is some overlap in the redshift distributions of the third tracer bin, and first source bin. This overlap, which is not included in our modeling, will reduce the lensing signal (since sources at lower redshift than the tracers will not be lensed).

To test the impact of the narrow tracer bin approximation on our analysis, we generate simulated correlation function measurements using Eq. (7.6). To do this, we assume a linear bias model with $b = (1.45, 1.55, 1.65)$ for each of the tracer galaxy

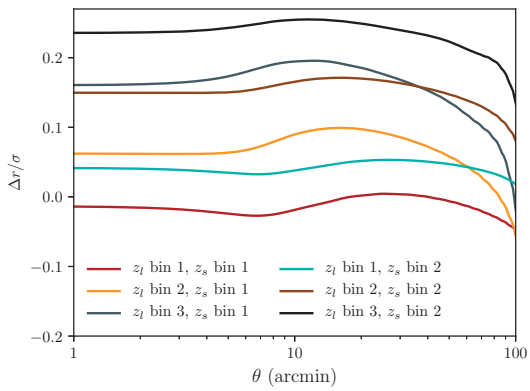

Figure 7.2: Test of the narrow tracer bin approximation used in this analysis. We compute the error in the ratio, $\Delta r(\theta)$, incurred by assuming the tracer galaxies are distributed in infinitely narrow redshift bins. This quantity is plotted relative to the statistical errors in the ratio measurements, σ, which is the uncertainty from all angular bins combined. At most, the error incurred by assuming narrow tracer bins is $\sim 25\%$ of the statistical error on the ratio, and we therefore ignore it in this analysis.

redshift bins, following the analysis of DES Collaboration (2018b). Thus, for this test, we are assuming that the galaxy bias is independent of scale and of redshift within each tracer bin. The angular dependence of the ratio can then be computed from the simulated data vectors and compared to the approximate value of the ratio computed assuming infinitely narrow tracer redshift bins; we denote the difference between the true ratio and the approximated ratio as Δr.

We plot the angular dependence of Δr relative to the error bars on the ratio measurements in Fig. 7.2. We see that for all tracer-source bin combinations, the error induced by the narrow tracer bin approximation is small compared to the error bars on the ratio. Note that the decline in $\Delta r/\sigma$ close to 100 arcmin is due to the high-pass filtering that is applied to the lensing convergence maps.

Lensing dilution and galaxy lensing boost factors

When there is overlap in redshift between the source and the tracer galaxies two different effects occur. The first one is already mentioned in the section above, which is the dilution of the lensing signal when source galaxies are in front or at the same redshfit of tracer galaxies. In our analysis we make use of the narrow tracer bin approximation and therefore some of this dilution is not naturally accounted for in the theory prediction. Thus, to test for the impact of this effect, we have removed the bin combination which shows the largest overlap in redshift, which is the third tracer bin and first source bin combination (as seen in Fig. 7.1), and found that removing it has negligible impact on the inferred cosmological parameters.

The second effect results from the tracer and source galaxies being physically correlated, since they both trace the large scale structure. This changes the galaxy lensing signal since it will change the true $n(z)$ on the sky in a way that is not captured by the full survey $n(z)$. Generally, this effect reduces the lensing signal since source galaxies

behind the tracer galaxies will be on average closer to the tracer galaxies than what it is predicted by the full survey $n(z)$. To take into account this effect in the modelling we would need to measure the redshift distributions of the galaxies included in each of the angular bins. Alternatively, one can correct for this effect using the so-called boost factors. This correction is scale dependent and is bigger at small scales, where the clustering is also larger. Using the same data as employed here, Prat et al. (2018a) estimated the magnitude of this effect (i.e. the boost factor) by measuring the excess of sources around tracers compared to random points, as a function of scale, for every tracer-source bin combination (cf. their Figure 10). For the tracer-source binning configurations and for the choice of scales used in this analysis, the results in Prat et al. (2018a) demonstrate that the boost factors are 1% or less over all angular scales, allowing us to safely ignore this effect in our analysis. This makes sense, because we have attempted to use only tracer and source galaxy combinations that are well separated in redshift, so as to make the narrow tracer bin approximation more accurate.

Intrinsic alignments

Another systematic effect related to the overlap in redshift between the tracer and source galaxies is the intrinsic alignments (IA) of the shapes and orientations of source galaxies resulting from gravitational tidal fields during galaxy formation and evolution. IA can generate correlations between the source ellipticity and the lens position if the two galaxies are physically close.

In Eq. (7.8) we have assumed that there is no contribution from IA in the cross-correlation measurements with the galaxy convergence maps. IA are detected in the multiprobe correlation function analysis of DES Collaboration (2018b). However, since here we analyze only those tracer and source redshift bin combinations that are widely separated in redshift, we expect the contribution from IA to be minimal for our analysis. Moreover, Blazek et al. (2012) found that when boost factors are not significant, IA can be ignored as well.

tSZ validation

Our model of tSZ contamination of the measured two-point functions relies on estimating the tSZ signal for galaxy clusters across the SPT field. To estimate possible systematic errors in our anlaysis associated with these modeling estimates, we recompute the bias corrections by modifying the assumed masses of the DES-detected clusters used when generating the contaminant maps. The DES clusters dominate our estimate of the tSZ bias because the more massive SPT-detected clusters are masked. The difference between the estimated biases for the fiducial and perturbed models should therefore provide a reasonable estimate of our modeling uncertainty. We generate two

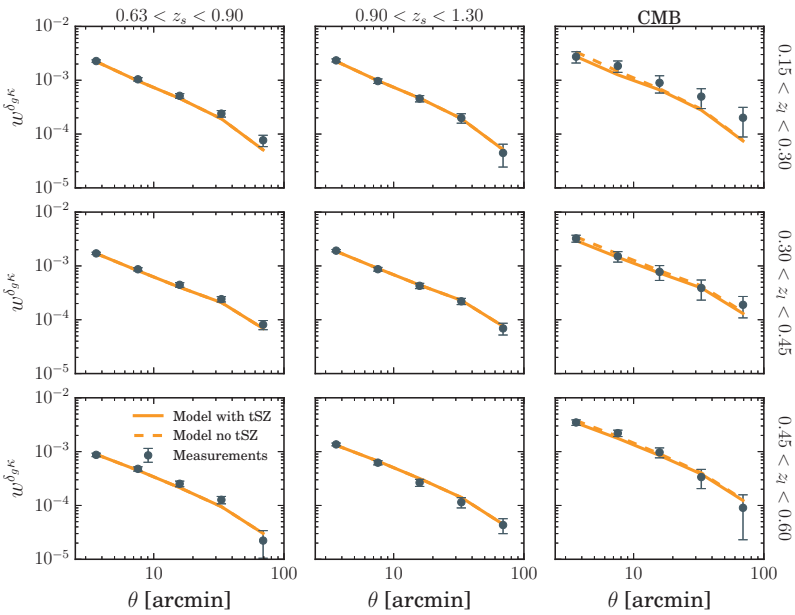

Figure 7.3: Tracer-lensing correlation function measurements, together with the best fit ratio model described in Sec. 7.4.4. The model for the galaxy-CMB lensing correlations has been corrected for the tSZ-induced bias as explained in Sec. 7.4.3. We also show the uncorrected model in dashed lines for comparison.

perturbed models by increasing and decreasing the amplitude of the assumed mass-richness relationship. The fiducial mass-richness model is based on the weak lensing calibration of Melchior et al. (2017); the perturbed models adjust the amplitude of the normalization by $\pm 1\sigma$, where σ represents the statistical uncertainty on the amplitude from the Melchior et al. (2017) analysis. Note that the updated weak lensing calibration of DES redMaPPer clusters by McClintock et al. (2019) is consistent with that of Melchior et al. (2017), albeit with smaller error bars; using the 1σ error from Melchior et al. (2017) is therefore a conservative choice. We show the result of analyzing the data using our fiducial tSZ bias model and the two perturbed models in Sec. 7.6. Note that simply varying the amplitude of the assumed mass-richness relation does not necessarily capture all of the uncertainty in the tSZ bias model. However, since the tSZ amplitude scales strongly with mass, we expect the mass uncertainty to capture a dominant part of the total tSZ bias uncertainty.

7.6 Results

We now present the constraints obtained on the lensing ratios and cosmological parameters from our analysis of data from DES, SPT and *Planck*. We note that in order to avoid confirmation bias, our analysis was blinded during testing by replacing the true

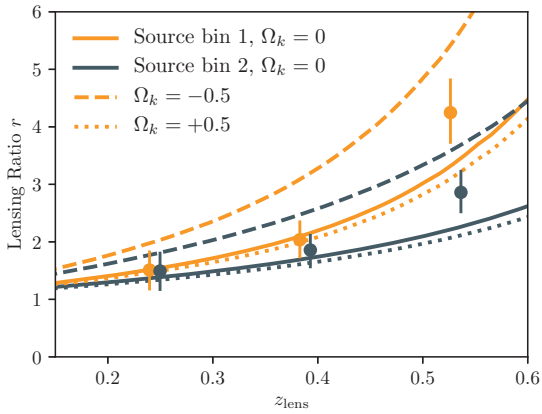

Figure 7.4: Measurements of the lensing ratios (points with error bars) as a function of lens redshift for two different source galaxy redshift bins (orange and gray curves). The corresponding redshift distributions for these bins are shown in Fig. 7.1. Also shown are theoretical predictions (curves) for ΛCDM models with $\Omega_{\rm m} = 0.3$, but with different values of Ω_k. Solid curves correspond to $\Omega_k = 0$, while the dashed and dotted curves change Ω_k to -0.5 and 0.5, respectively. Relative to the concordance flat ΛCDM model, the ratio measurements prefer an amplitude of $A = 1.1 \pm 0.1$, indicating consistency with this model. While the highest redshift data points appear in some tension with the $\Omega_k = 0.0$ model, these points are covariant; the χ^2 per degree of freedom relative to that model is $8.5/5$, corresponding to a probability to exceed of $\mathrm{p.t.e} = 0.13$.

measurements with simulated data vectors. The real data was used only after we were confident that the analysis pipelines were working correctly and the model had been validated.

7.6.1 Correlation function and ratio constraints

The measurements of the two-point correlation functions between galaxies and (galaxy and CMB) lensing are shown as a function of angular scale in Fig. 7.3 (*points*), together with the best-fit ratio model described in Sec. 7.4.4 (*lines*). For the cross-correlations with the $\kappa_{\rm CMB}$ map, we show both the model corrected by the tSZ effect (*solid*), as described in Sec. 7.4.3, and the uncorrected model (*dashed*) for comparison.

The corresponding constraints on the lensing ratios are shown in Fig. 7.4 as a function of the mean lens redshift. The full posteriors on the lensing ratios are shown in Fig. D.1. In total, we constrain six lensing ratios at the 13-23% level. The highest signal-to-noise ratio constraints are those corresponding to the highest lens redshift bin.

We first fit the measured ratios using a fiducial cosmological model. We compute the expectation value of the ratios using the best-fit cosmology from the `TT,TE,EE+lowP + lensing+ext` analysis in Ade et al. (2016). We call these values $r_{\rm Planck}$ and fit the measured ratios with a model of the form $\hat{r} = A r_{\rm Planck}$, where A is a free parameter.

We find $A = 1.1 \pm 0.1$. This measurement demonstrates that the ratio measurements are consistent with the fiducial cosmology within the statistical error bars, and are measured a combined precision of roughly 10%. For comparison, the measurement of lensing ratios presented in Miyatake et al. (2017) using CMASS galaxies as tracers, galaxy shapes from CFHTLenS and *Planck* data, reports a 17% uncertainty on a joint measurement of the ratio, obtained from combining results from three tracer galaxy redshift bins and a single source galaxy bin. The χ^2 per degree of freedom for the measurements relative to the $r_{\rm Planck}$ model is $8.5/5$, corresponding to a probability to exceed of 0.13. This indicates a reasonable fit to the *Planck* model. Note that the ratio measurements for different source bins but the same tracer galaxy bin are highly covariant, as can be seen in Fig. D.1.

7.6.2 Cosmological constraints

We now use the ratio measurements presented above to constrain cosmological parameters. As an illustration of the cosmological sensitivity of the ratios, Fig. 7.4 shows the theoretical predictions for two cosmological ΛCDM models with different values of Ω_k, with $\Omega_{\rm m}$ fixed to 0.3. Throughout this analysis, we fix the redshift of the surface of last scattering to $z^* = 1090$. From this figure, we see that negative values of Ω_k have a significantly greater impact on the lensing ratios than positive values. This is due to the fact that the angular diameter distance to the surface of the last scattering changes more with curvature for negative Ω_k than for positive Ω_k.

To obtain cosmological constraints we use the methodology described in Sec. 7.5.2. We consider curved ΛCDM models where we vary the cosmological parameters Ω_k and $\Omega_{\rm m}$ and the systematics parameters described in Sec. 7.5.1. We use the priors on the multiplicative shear bias derived in Zuntz et al. (2018) and the redshift bias parameters from Hoyle et al. (2018); Davis et al. (2017); Gatti et al. (2018).

Fig. 7.5 shows the resultant marginalized posterior density (colored region) as a function $\Omega_{\rm m}$ and Ω_k. We find that the data strongly rule out low values of $\Omega_{\rm m}$ and very negative values of Ω_k. However, at each $\Omega_{\rm m}$, we obtain only a lower limit on Ω_k. Consequently, we focus on how the data constrain Ω_k. We derive limits on Ω_k in the following way. For each value of $\Omega_{\rm m}$, we determine the value of Ω_k such that the marginalized posterior on Ω_k is lower than the peak of the posterior by a factor of $1/e^2$. For a Gaussian distribution, this would correspond to the 2σ lower limit. This limit is shown in Fig. 7.5 as the solid red line. Consistent with the marginalized posterior, we rule out very negative Ω_k, with the limit tightening for lower values of $\Omega_{\rm m}$.

As seen in Fig. 7.5, the data somewhat prefer models with negative curvature over models with $\Omega_k = 0$. This preference is driven by the high redshift data points seen in Fig. 7.4. However, this preference is not statistically significant. For $\Omega_k \gtrsim -0.1$, the posterior on Ω_k is quite flat for all Ω_m. This is consistent with the finding noted above

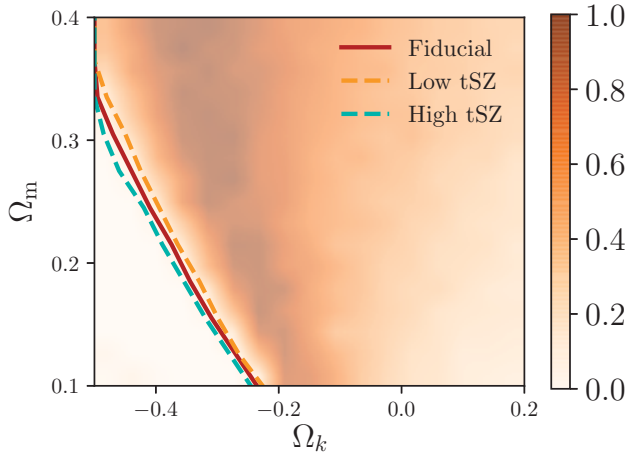

Figure 7.5: The constraints on $\Omega_{\rm m}$ and Ω_k resulting from analysis of the measured lensing ratios. The background color shows the marginalized posterior density for these two parameters. The data strongly rule out regions of parameter space with low $\Omega_{\rm m}$ and very negative Ω_k. At each $\Omega_{\rm m}$, we identify a lower limit on Ω_k by identifying the value of Ω_k for which the marginalized posterior falls by $1/e^2$ relative to the maximum, which for a Gaussian distribution would correspond to the 2σ lower limit. This limit is illustrated with the red solid curve. We also show (dashed curves) the changes to these limits when using two variations on the fiducial tSZ model, as described in Sec. 7.4.3.

that the amplitude of the lensing ratios is consistent (to 1σ) with the prediction from flat ΛCDM, which has $\Omega_k = 0$.

Fig. 7.5 also shows the impact of using the high and low-amplitude tSZ models (see discussion in Sec. 7.5.3) on the cosmological constraints with the green and orange dashed curves, respectively. The uncertainty on the tSZ amplitude contributes a non-negligible amount of systematic uncertainty to our analysis, but it is subdominant to the statistical uncertainty.

We have tested that the constraints obtained by varying only the cosmological parameters, and not marginalizing over the shear and photometric redshifts systematics parameters are essentially identical to those obtained when the systematics parameters are varied. Therefore, we conclude that at the current level of statistical uncertainty on the lensing ratios, the impact of systematics errors in photometric redshifts and shear calibration are not significant. Note that the systematics parameters Δz_s^i, Δz_l^i, and m_i are strongly prior dominated.

7.7 Forecasts

Upcoming data from DES, SPT and future surveys have the potential to significantly reduce the statistical uncertainty on measurements of lensing ratios. Das & Spergel (2009) calculated the uncertainty on lensing ratios that could be obtained with the combination of a lens galaxy sample from a futuristic spectroscopic survey, a LSST-like galaxy weak lensing survey, and a CMB lensing map from a CMBPOL-like survey. They found that a roughly 1% constraint on the lensing ratio could be obtained with this combination of experiments, and that such a constraint could contribute useful cosmological information that is complementary to e.g. *Planck* and future measurements of the baryon acoustic oscillation (BAO) feature in the galaxy distribution.

Here, we extend the analysis of Das & Spergel (2009) to account for the effects of systematic errors in the redshift and shear measurements. We also update the forecasts given current expectations for future survey designs. Finally, we show how using a lens galaxy population identified with photometric data from LSST can be used to decrease the error bars on the ratio measurements. For this analysis, we consider curved wCDM cosmological models, parameterized by $\Omega_{\rm m}$, Ω_k and w, the equation of state parameter of dark energy.

As discussed in Sec. 7.5, there are several potential sources of systematic error that could affect measurement of lensing ratios beyond errors in the source redshift distributions and shear calibration errors. In particular, tSZ bias in the $\kappa_{\rm CMB}$ maps is a potentially significant concern. Here, we ignore bias due to tSZ contamination of the $\kappa_{\rm CMB}$ map under the assumption that future experiments will use lensing estimators based on CMB polarization data (which is much less severely impacted by tSZ), or that they will use some multi-frequency cleaning strategy, such as that discussed in Madhavacheril & Hill (2018).

7.7.1 Calculation of projected uncertainty

To estimate the error on the lensing ratios with future data we use a methodology similar to Das & Spergel (2009). We define

$$Z_\ell = C_\ell^{\kappa_{\rm CMB}\delta_g} - r\, C_\ell^{\kappa_s\delta_g}, \tag{7.21}$$

and a corresponding χ^2 via

$$\chi^2(r) = \sum_l \frac{Z_l^2}{\sigma^2(Z_l)}, \tag{7.22}$$

where $\sigma^2(Z_l)$ is the variance of Z_l. The uncertainty on the ratio, $\sigma(r)$, can then be calculated as

$$\frac{1}{\sigma^2(r)} = \frac{1}{2}\frac{\partial^2\chi^2(r)}{\partial r^2}. \tag{7.23}$$

To compute Z_l, we must extend the formalism of Das & Spergel (2009) to include partial overlap between surveys. Given a fiducial value of the ratio, r_0, the variance of Z_l can be computed using the expressions in White, Song & Percival (2009). We find

$$\begin{aligned}\sigma^2\left(Z_\ell\right) =& \frac{1}{(2\ell+1)}\left[\frac{1}{f_{\rm sky}^{\kappa_{\rm CMB}\delta_g}}\left(\tilde{C}_\ell^{\kappa_{\rm CMB}\kappa_{\rm CMB}}\tilde{C}_\ell^{\delta_g\delta_g} + \left(C_\ell^{\kappa_{\rm CMB}\delta_g}\right)^2\right)\right. \\ &+ \frac{r_0^2}{f_{\rm sky}^{\kappa_s\delta_g}}\left(\tilde{C}_\ell^{\kappa_s\kappa_s}\tilde{C}_\ell^{\delta_g\delta_g} + \left(C_\ell^{\kappa_s\delta_g}\right)^2\right) \\ &\left.- 2r_0\frac{f_{\rm sky}^{\kappa_{\rm CMB}\kappa_s\delta_g}}{f_{\rm sky}^{\kappa_{\rm CMB}\delta_g} f_{\rm sky}^{\kappa_s\delta_g}}\left(C_\ell^{\kappa_{\rm CMB}\kappa_s}\tilde{C}_\ell^{\delta_g\delta_g} + C_\ell^{\kappa_{\rm CMB}\delta_g}C_\ell^{\kappa_s\delta_g}\right)\right],\end{aligned} \tag{7.24}$$

where

$$\tilde{C}_\ell^{XX} = C_\ell^{XX} + N_\ell^{XX}, \tag{7.25}$$

and N_ℓ is the corresponding noise power spectrum. The Poisson noise for the tracer sample is $N_\ell^{\delta_g\delta_g} = 1/n_g$, where n_g is the number density of tracer galaxies per steradian. We compute $N_\ell^{\kappa_s\kappa_s}$ as

$$N_\ell^{\kappa_s\kappa_s} = \frac{\sigma_\epsilon^2}{n_{\rm s}}, \tag{7.26}$$

where σ_ϵ is the standard deviation of the weighted galaxy shapes and $n_{\rm s}$ is the number density of the source galaxies per steradian used to produce the lensing maps. We adopt $\sigma_\epsilon = 0.26$ below. The various noise curves used in the forecasts are shown for the different surveys in Fig. 7.6.

The $f_{\rm sky}$ factors in Eq. (7.24) approximately take into account the fact that the variance of the C_ℓ measurements is increased for partial sky coverage. We define $f_{\rm sky}^{\kappa_{\rm CMB}\delta_g}$ and $f_{\rm sky}^{\kappa_s\delta_g}$ as the sky fractions over which $C_\ell^{\kappa_{\rm CMB}\delta_g}$ and $C_\ell^{\kappa_s\delta_g}$ are measured, respectively, and $f_{\rm sky}^{\kappa_{\rm CMB}\kappa_s\delta_g}$ is the sky fraction over which the δ_g, $\kappa_{\rm CMB}$ and κ_s measurements all overlap. In the case that there is no overlap between all three measurements, $C_\ell^{\kappa_{\rm CMB}\delta_g}$ and $C_\ell^{\kappa_s\delta_g}$ are uncorrelated and the variance of Z_l is given by the sum of the variances of the two terms in Eq. (7.21). In the case where there is overlap between the lens galaxies, source galaxies, and CMB lensing measurements, some reduction of variance can be obtained via sample variance cancellation.

Finally, $\sigma(r)$ is calculated by substituting Eqs. (7.22) and (7.24) into Eq. (7.23). For the purposes of these forecasts, we adopt the best-fit ΛCDM cosmological model from

Surveys	Lens z range	$N_{\rm lens\ bins}$	Source z range	$N_{\rm source\ bins}$	$\sigma_{r,\rm stat}$ [min, max]
DES Y1 + SPT-SZ (current measurements)	$0.15 < z_l < 0.6$	3	$0.6 < z_s < 1.3$	2	[0.13, 0.23]
DES Y5 + SPT-SZ	$0.15 < z_l < 0.6$	3	$0.6 < z_s < 1.3$	2	[0.098, 0.15]
DES Y5 + CMB-S3	$0.15 < z_l < 0.6$	3	$0.6 < z_s < 1.3$	2	[0.042, 0.060]
DESI + LSST + CMB-S4	$0.2 < z_l < 0.4$ (BGS) $0.8 < z_l < 1.0$ (ELG)	4 2	$1.0 < z_s < 1.6$	1	[0.018, 0.019] (BGS) [0.040, 0.054] (ELG)
LSST + CMB-S4	$0.2 < z_l < 0.7$	10	$1.0 < z_s < 1.6$	1	[0.013,0.015]

Table 7.1: Forecasts for precision of ratio measurements for the future experiment configurations described in Sec. 7.7.2, except for the first row, which corresponds to the measurements presented in this paper in Fig. 7.4. Last column represents the minimum and maximum statistical errors on the ratios over all tracer and source galaxy bin combinations.

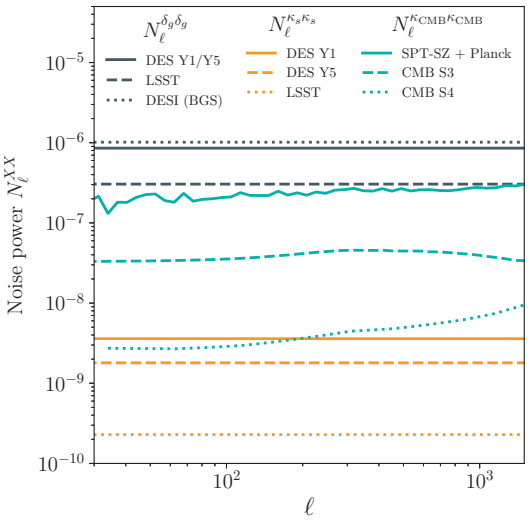

Figure 7.6: Noise power spectra for the experimental configurations described in Sec. 7.7.2. The noise power for $C_\ell^{\delta_g\delta_g}$ (gray curves) is inversely proportional to the lens galaxy density; the noise power for $C_\ell^{\kappa_s\kappa_s}$ (orange curves) is inversely proportional to source galaxy denisty. Noise power in the CMB lensing maps (blue curves) is dependent on the details of the experimental configurations of the CMB telescope. For SPT-SZ we use the measured CMB lensing noise power, while for CMB-S3 and S4, we use forecasts.

the analysis of `TT,TE,EE+lowP+lensing+ext` datasets in Ade et al. (2016).

7.7.2 FUTURE EXPERIMENT CONFIGURATION

We consider several future experimental configurations using both current and future surveys, which are also summarized in Table 7.1:

- **DES Y5 + SPT-SZ**: this represents what can be achieved with full-survey DES data and current SPT-SZ data. We assume an overlapping area of 2500 sq. deg. (i.e. the full area of the SPT-SZ survey). For the tracer and source galaxies, we adopt the current redshift bins and the same number densities for the tracer galaxies; we assume an increased source density of a factor of two with respect to the Y1 density, due to the higher depth of Y5 data. The assumed CMB noise power, $N_\ell^{\kappa_{\rm CMB}\kappa_{\rm CMB}}$, is taken from Omori et al. (2017). Finally we assume that

tSZ bias can be mitigated using multi-frequency information, allowing us to exploit all angular scales.

- **DES Y5 + Stage 3 CMB**: this represents what can be achieved with full-survey DES data and a near-term, Stage 3 CMB experiment (CMB-S3). Stage 3 CMB experiments include SPT-3G (Benson et al., 2014) and Advanced ACTPol (Henderson et al., 2016). We assume an overlapping area of 5000 sq. deg. and use the CMB-S3 noise curve from Abazajian et al. (2016). We adopt the same tracer and source galaxy bins as the current analysis, with a source density of twice the Y1 density.

- **DESI + LSST + Stage 4 CMB**: this represents one possible use of future survey data to constrain lensing ratios. We assume that the tracer galaxies are spectroscopically identified using the Dark Energy Spectroscopic Instrument (DESI Collaboration et al., 2016), allowing us to ignore redshift errors for this sample. The tracer galaxies are assumed to be drawn from two DESI populations: a set of low-z galaxies from the Bright Galaxy (BGS) sample and a set of high-z galaxies from the Emission Line Galaxy (ELG) sample. The BGS tracer galaxies are divided into four redshift bins between $z = 0.2$ and $z = 0.4$, and the tracer galaxy bias is assumed to be $1.34/D(z)$, where $D(z)$ is the linear growth factor, normalized to $D(z = 0) = 1$; the ELG galaxies are divided into two redshift bins between $z = 0.8$ and $z = 1.0$, and are assumed to have a bias of $0.84/D(z)$ (DESI Collaboration et al., 2016). The tracer galaxy density for the BGS redshift bins (width of $\Delta z = 0.05$) is assumed to be 75 per sq. deg. and 150 per sq. deg for the ELG redshift bins (width of $\Delta z = 0.1$). We assume that LSST (LSST Dark Energy Science Collaboration, 2012) is used to measure shapes of source galaxies, with a source density of 25 galaxies per sq. arcmin and redshift range from $z = 1.0$ to $z = 1.6$.

  The CMB lensing map is assumed to come from a Stage 4 (CMB-S4) like experiment (Abazajian et al., 2016); we adopt the minimum variance CMB lensing noise curve from Schaan et al. (2017). Finally, we assume overlapping area between DESI and CMB-S4 of 16500 sq. deg., overlap between DESI and LSST of 3000 sq. deg., and overlap between all three surveys of 3000 sq. deg.

- **LSST + CMB-S4**: another possible use of future survey data for measuring lensing ratios is to define a tracer galaxy sample using photometric data from LSST. As we have shown above, algorithms like redMaGiC can be used to define galaxy populations that are sufficiently narrowly distributed in redshift for the purposes of measuring lensing ratios. We assume that the LSST tracer galaxy sample is divided into 10 bins between $z = 0.2$ and $z = 0.7$, with number density of 100 galaxies per square degree for each bin. Such densities are comparable to what

is currently achieved with DES redMaGiC. We make the same source galaxy and CMB lensing assumptions as above.

In addition to the survey assumptions described above, we must adopt some prescription for the expected systematic errors on shear calibration and photometric redshift determination. We assume that the multiplicative shear bias from LSST can be calibrated to $\sigma(m) = 0.001$, which is the requirement set in LSST Science Collaboration et al. (2009) and also of the order of what is expected from Schaan et al. (2017). When using DESI to create the tracer galaxy sample, we ignore redshift errors in the analysis; for LSST we assume that with a redMaGic-like algorithm, the tracer galaxy redshifts can be calibrated to $\sigma(\Delta z_l) = 0.005$. We assume that the source photo-zs measured by LSST can be calibrated to the level of $\sigma(\Delta z_s) = 0.01$ (LSST Science Collaboration et al., 2009).

Note that in the forecasts below, we ignore the issue of the finite width of the tracer galaxy redshift bins. For the survey assumptions defined above, we have tested that the errors on the ratios induced by the narrow lens approximation are significantly below the statistical uncertainties on the ratios. Furthermore, given the small assumed redshift errors of the lens galaxies, we could in principle divide the tracer galaxies into more redshift bins and the narrow lens approximation would improve. We find, however, that doing so does not appreciably change our results.

7.7.3 Future constraints on lensing ratios

There are three sources of statistical noise in the measurements of the lensing ratios: noise in the measurement of galaxy density, noise in the galaxy lensing maps, and noise in the CMB lensing maps. For current data, all of these components make significant contributions to the total uncertainty on the ratios, although noise in the CMB lensing map and galaxy density dominate. For instance, increasing the number density of tracers by a factor of two would decrease the uncertainty on the ratios by roughly 15%. Significant improvement could also be obtained by reducing the noise in the κ maps, especially $\kappa_{\rm CMB}$. Halving the noise in the CMB κ maps would decrease the ratio uncertainty by 25%, while the same improvement in the galaxy κ maps would reduce the ratio uncertainty by 5%. Finally, doubling the area of the surveys would reduce by 40% the uncertainty on the ratios. The future survey configurations described in Sec. 7.7.2 make improvements to the lensing ratio constraints in all of these ways.

The projected cosmological constraints on $\Omega_{\rm m}$, Ω_k and w obtained from the forecasted lensing ratio constraints for DESI, LSST and CMB S4 are shown in Fig. 7.7, assuming the tomographic ratio measurements are independent. This is a reasonable assumption because for these configurations there is only one source bin (see Table. 7.1) and the covariance between measurements using different tracer bins is small, as shown

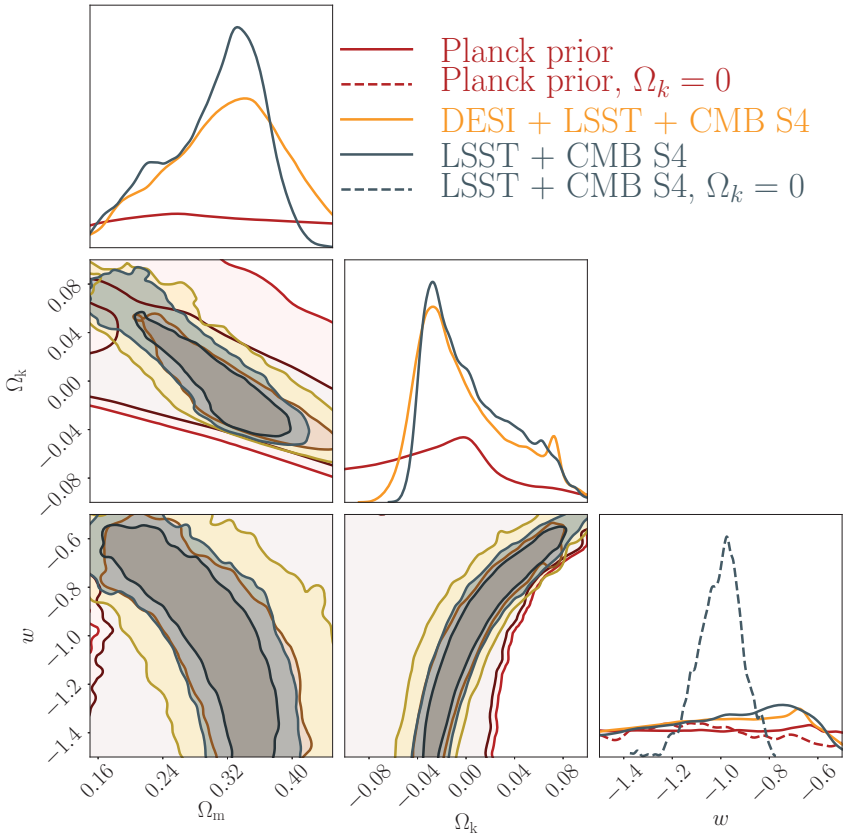

Figure 7.7: Projected cosmological constraints from lensing ratios when using LSST + DESI + CMB-S4 vs. LSST + CMB-S4, using the geometrical *Planck* prior, which is also shown in the figure. We have marginalized over parameters describing systematic uncertainties in lens and source galaxy redshifts, and systematic errors in source galaxy shears. We also marginalize over h and Ω_b as these appear in the geometrical *Planck* prior (see text). The constraints that can be obtained using a photometrically identified tracer galaxy population (LSST+CMB-S4) are tighter than those that can be obtained from a spectroscopically identified tracer galaxy population (DESI+LSST+CMB-S4). Apparently, the increased number density of the tracer galaxies with the photometric survey outweighs the increased redshift uncertainties.

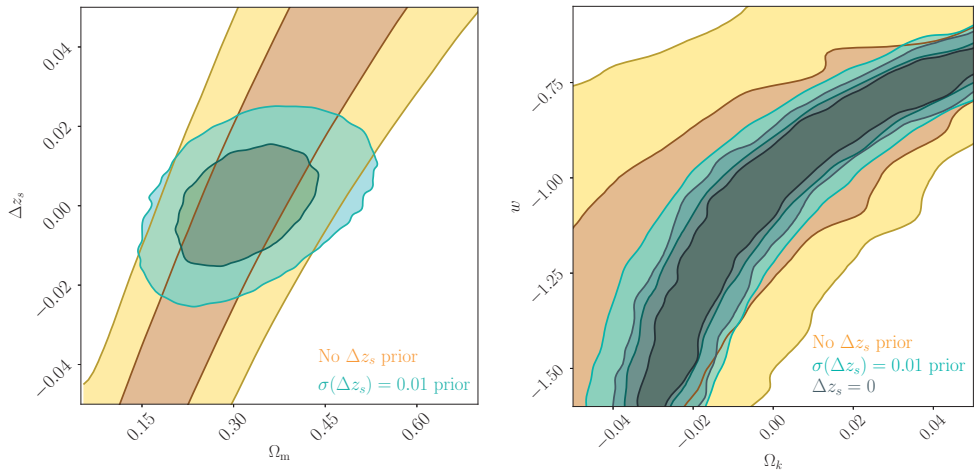

Figure 7.8: (a) Degeneracy between Ω_m and source redshift bias, Δz_s, for the case of one lens and source redshift bin when the lensing ratio is measured to 1% precision. Since there is only one ratio measurement, the constraint on $\Omega_{\rm m}$ is completely degenerate with the redshift bias. (b) Projected constraints on Ω_k and w for different priors on the redshift bias parameter, Δz_s. We have assumed the projected constraints for LSST+CMB S4 in this figure. Uncertainty on Δz_s significantly degrades the cosmological constraints. For the projected level of constraints, $\sigma(\Delta z_s) = 0.01$, the degradation is small, but non-zero.

in Fig. D.1. When generating this figure, we have adopted priors from the *Planck* measurement of the CMB power spectrum in Ade et al. (2016). Since the lensing ratio measurements are purely geometrical in nature, we choose to use only geometric information from the CMB power spectrum. For this purpose, we use the geometric CMB prior defined in Aubourg et al. (2015). Since most of the information in this prior comes from the first few peaks of the CMB temperature power spectrum, constructing this prior from the *Planck* constraints is a reasonable approximation for future surveys. Since the CMB prior depends on h and $\Omega_{\rm b}$, we have marginalized over these quantities in generating Fig. 7.7. Additionally, in Fig. 7.7 we have marginalized over the systematics parameters Δz_l, Δz_s and m for each redshift bin, imposing the priors described in Sec. 7.7.2.

Fig. 7.7 makes it clear that the lensing ratios contribute information beyond that contained in the geometrical CMB prior. Because of the "geometrical degeneracy" in the CMB power spectrum (Efstathiou & Bond, 1999), the CMB constraints on $\Omega_{\rm m}$, Ω_k and w are quite weak when all three parameters are varied simultaneously (the red contours). However, future lensing ratio constraints help to break these degeneracies. The combination of the lensing ratio and geometric CMB prior is particularly powerful in the space of Ω_k and w. The main impact of the lensing ratio constraints is to remove regions of parameter space with negative Ω_k and with small w in absolute value, leading

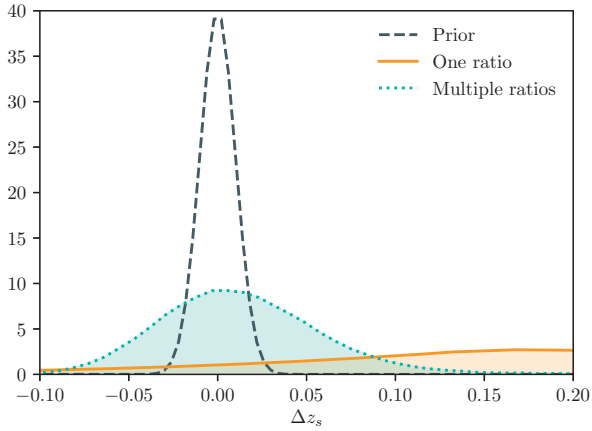

Figure 7.9: Posteriors on the source redshift bias parameter, Δz_s, when using only one lens bin and source bin (one ratio) vs using three lens and one source bins (three ratios). Using multiple lens redshift bins allows one to obtain some self-calibration of the photo-z bias. However, the level of self-calibration achieved is not as tight as expected priors, $\sigma(\Delta z_s) = 0.01$.

to a tight degeneracy between Ω_k and w. This degeneracy can be broken using e.g. information from BAO (Das & Spergel, 2009). Alternatively, if flatness is assumed (i.e. $\Omega_k = 0$), the resultant constraint is $w = -1.0 \pm 0.1$ (grey dashed curve in lower right panel).

Additionally, from Fig. 7.7 it can be seen that the cosmological constraints obtained from using LSST redMaGiC-like galaxies as the tracers are tighter than what is obtained by using DESI galaxies as the tracers. This is one of the main findings of our analysis: because of the tight photometric redshift errors that can be obtained with a redMaGiC-like algorithm, lensing ratios can be measured to high precision using a combination of photometric galaxy measurement and CMB lensing. A spectroscopic lens galaxy catalog is not necessary for the purposes of measuring lensing ratios. For fixed $w = -1$, the constraint obtained on Ω_k for the case of DESI tracers is $\sigma(\Omega_k) = 0.014$; for the case of LSST tracers, it is $\sigma(\Omega_k) = 0.009$. Similarly, for fixed $\Omega_k = 0$, the constraint obtained on w for the case of DESI tracers is $\sigma(w) = 0.15$; for the case of LSST tracers, it is $\sigma(w) = 0.09$.

7.7.4 Impact of systematic errors on lensing ratios

We now investigate in more detail the impact of systematic errors on future ratio measurements. For illustrative purposes, we first consider the case of a ratio measurement using a single lens and source galaxy bin, for which we adopt a 1% error typical of the LSST + CMB-S4 forecasts. In this case, since there is only a single ratio mea-

surement, systematic errors on shear calibration and photometric redshift bias will be completely degenerate with the cosmological constraints. This degeneracy is illustrated for the case of $\Omega_{\rm m}$ in Fig. 7.8a. Without a prior on Δz_s, $\Omega_{\rm m}$ cannot be constrained at all (orange contour). Given the projected prior on Δz_s of 0.01, we can obtain a constraint on $\Omega_{\rm m}$ (light green contour). However, in this case the cosmological constraint will be strongly determined by the accuracy of our prior on Δz_s and the constraining power on $\Omega_{\rm m}$ will be reduced by photo-z uncertainties.

In Fig. 7.8b we show the impact of source redshift errors in the $w - \Omega_k$ plane when more cosmological parameters are added into the model, and also when multiple ratios coming from different lens and source bin combinations are used. For this figure, lensing ratio constraints are taken from LSST + CMB-S4 forecasts, which match the ones from Fig. 7.7 for the contours marginalizing over Δz_s with the fiducial prior (light blue). In this figure, we also show the results of marginalizing over Δz_s with a wide, flat prior (orange), and fixing $\Delta z_s = 0$ (grey). Degeneracy between the cosmological parameters and Δz_s can have a large impact, as evidenced by the change in constraints in going from $\Delta z_s = 0$ to marginalizing over Δz_s with the wide, flat prior. However, with the assumed Δz_s priors of 0.01 we find that the effect of source redshift uncertainty on the lensing ratios constraints is fairly small, but also not negligible.

If multiple lens redshift bins are used to measure multiple lensing ratios, the degeneracy between Δz_s and the cosmological parameters can be broken somewhat. To illustrate this point, Fig. 7.9 shows the posteriors on Δz_s when using a single ratio or multiple ratio measurements. With only a single ratio measurement (orange curve), the ratio is highly degenerate with the systematic uncertainty on the redshift bias parameter, Δz_s, so the posterior on Δz_s is very broad. Using multiple ratios allows for some self-calibration of the photo-z bias (blue curve); in this case, the ratio measurements alone are being used to calibrate Δz_s. However, we see that the level of self-calibration of Δz_s remains weaker than the prior (black dashed curve) and, therefore, not using any Δz_s prior in the cosmology analysis would result in some degradation of the cosmology constraints. Note that the preference for large Δz_s exhibited in Fig. 7.9 for the case of a single ratio measurement is due to the projection of the higher-dimensional parameter space to the one-dimensional constraints on Δz_s.

We have also investigated the impact of shear calibration uncertainty on the constraints, as parameterized via m. Since Δz_s and m both affect all ratio measurements for a single source galaxy bin, their impacts on the lensing ratios are largely degenerate. Consequently, even for multiple lens redshift bins, when both Δz_s and m are left completely free, no useful level of self-calibration can be achieved, and the cosmological constraints are significantly degraded. However, for the projected priors on m of $\sigma(m) = 0.001$, the impact of marginalizing over m on the cosmological constraints is negligible, given the projected statistical error bars on the ratios. Note that the cosmological constraints presented in Fig. 7.7 include marginalization over m with the

fiducial $\sigma(m) = 0.001$ prior.

7.8 Conclusions

Using a combination of galaxy position measurements and galaxy lensing maps from DES, and CMB lensing measurements from SPT and *Planck*, we have measured several cosmological lensing ratios. These ratios have the attractive feature that they can be modeled using only geometrical information (i.e. distances as a function of redshift), and do not depend on the galaxy-matter power spectrum. Although lensing ratios use the CMB as a source plane, they are completely independent of the physics of baryon acoustic oscillations in the primordial plasma, making them a useful cross-check of geometrical constraints from the CMB and the BAO feature in the galaxy distribution. Similarly, lensing ratios provide a test of cosmological distances that is completely independent of constraints from supernovae.

Enabled by the well-understood photometric redshifts of the redMaGic galaxies, we have for the first time measured lensing ratios without the use of spectroscopic galaxy samples. Each lensing ratio is constrained to 13 to 23% precision, and the combined constraint from all ratios is roughly 10%. Using these measurements, we place constraints on curved ΛCDM cosmological models, finding consistency with the concordance cosmological model. Our most interesting cosmological constraint is on Ω_k and is shown in Fig. 7.5.

We have also predicted the constraining power on lensing ratios of future experiments. While previous forecasts have focused on spectroscopic identification of tracer galaxies, we argue that photometrically identified galaxies can be used, provided their redshifts can be constrained with redMaGiC-like accuracy. Given this observation, we argue that the combination of data from LSST and CMB-S4 experiments will provide tight constraints on lensing ratios, achieving roughly 1.5% precision for tracers distributed over $z \in [0.2, 0.7]$. Additionally, we showed that systematic uncertainty in the redshift estimates for the source galaxies significantly degrades the cosmological constraints from lensing ratios. However, given the expected priors on the source galaxy redshift biases, the degradation from the source redshift uncertainty will be smaller than the statistical uncertainties. Moreover, we have found that using multiple lens and source bins allows for some self-calibration of the photometric redshifts, but not to the level of the expected priors. We have ignored the complication that photometric redshift errors may not be adequately parameterized by a single shift parameters as in Eq. (7.16). Exploring the consequences of more generic redshift bias models is one avenue for future work. We have also found that multiplicative shear biases will not be a limiting factor for lensing ratios given the expected priors on these parameters.

When combined with geometrical constraints from the CMB, the lensing ratios ex-

plored in this work offer the possibility of deriving purely geometric constraints on the curvature of the Universe and the equation of state parameter of dark energy. Analyses with future data sets will be able to significantly improve on current lensing ratio measurements, as seen in Table 7.1 and Fig. 7.7. While such future constraints would be interesting in their own right, their geometric nature also means that comparisons to cosmological probes that use growth and power spectrum information are particularly interesting. Modified gravity, for instance, is expected to lead to differences in cosmological models inferred from geometry and growth measurements (e.g. Ruiz & Huterer, 2015). Exploring these possibilities with lensing ratios is another exciting avenue for future work.

Part of the appeal of lensing ratios is their simplicity: they do not require complicated modeling of the two-point functions that they depend on. Unfortunately, this simplicity comes at the cost of reduced sensitivity to cosmological parameters. While lensing ratios have already been used to provide competitive constraints on systematics parameters (e.g. Prat et al., 2018a), competitive cosmological constraints with lensing ratios have yet to be demonstrated. Still, the geometric nature of the constraints, the fact that they are independent of the physics of BAO, and the fact that their sensitivity spans a wide range of redshifts make lensing ratios worth exploring with future data. Furthermore, assuming cosmologists continue to measure two-point functions between galaxy density and gravitational lensing, lensing ratio constraints on cosmology come essentially for free.

Summary and conclusions

In this thesis we have studied cosmology and the galaxy-matter connection with weak gravitational lensing using data from the Dark Energy Survey (DES), the South Pole Telescope (SPT) and Planck. In particular, we have used cross-correlations between a background source of light, such as distant galaxies or the Cosmic Microwave Background (CMB), and galaxy positions in the foreground, tracing the Large-Scale Structure producing the lensing. On one hand, these weak lensing cross-correlations are sensitive to the history of growth of structure and to the geometry of the Universe, allowing us to constrain cosmological parameters in combination with other probes. On the other hand, they are also sensitive to the relation between the baryonic matter forming galaxies and the underlying (mostly) dark matter field, a relation that is encapsulated in the so-called galaxy bias.

In Part II of this thesis, we have used tangential shear measurements to constrain the galaxy bias. The tangential shear is one of the main observables of galaxy-galaxy lensing, which aims to detect the effect some foreground galaxies (lenses) have on the shapes that we see of some other background galaxies (sources) due to the foreground galaxy masses, dominated by their dark matter halos. In this thesis, we have measured the tangential shear of background galaxies around lens galaxies contained in a magnitude limited sample, using the DES Science Verification data set. Then, fixing cosmology, we have been able to put constraints on the galaxy bias of the lens sample, and have compared our results with galaxy bias measurements on the same sample obtained from other probes, such as galaxy clustering from Crocce et al. (2016) and CMB lensing from Giannantonio et al. (2016), finding some mild tension which could be due to the combination of various reasons, discussed in detail in Chapter 4.

The main work of this thesis is presented in Part III, where in Chapter 6 we show the results from the DES Y1 cosmological analysis coming from the combination of galaxy clustering and weak lensing, the so-called 3x2pt, since it involves three two-point correlation function measurements: (i) cosmic shear, (ii) galaxy-galaxy lensing and (iii) galaxy clustering. This combination, besides being able to break degeneracies between the galaxy bias and cosmological parameters, has been recognized for more than a decade to contain a tremendous amount of complementary information, and to

be remarkably resilient to the presence of nuisance parameters that describe systematic errors and non-cosmological information. For the first time, the precision of the DES Y1 cosmological constraints rivals that from the *Planck* cosmic microwave background measurements, allowing a comparison of structure in the very early and late Universe on equal terms, testing the ΛCDM model. Under the DES Y1 tension metrics framework, DES cosmology results from 3x2pt are found compatible with *Planck* results and therefore combined, deriving very tight constraints on cosmological parameters. This thesis has contributed to this highly collaborative effort providing the measurement and careful systematics treatment of one of the three probes involved in the analysis, the galaxy-galaxy lensing part, which is presented in Chapter 5. In that chapter we also constrain the galaxy bias and test the linear bias assumption used in the whole 3x2pt analysis, by comparing the galaxy bias results obtained from galaxy clustering measurements with the ones obtained using galaxy-galaxy lensing, finding agreement.

Moreover, in Chapter 5 and still in the context of the DES Y1 3x2pt analysis, we perform the so-called shear-ratio test, which uses the geometrical information of the tangential shear measurements to put constraints on the redshift distributions of the source sample. In order to place these constraints we use the fact that the scaling of the tangential shear for different source redshift bins sharing the same lens sample depends only on the angular diameter distances relative to the foreground and background samples, in the limit where the lens galaxies are narrowly distributed in redshift. Such dependency was initially proposed as a probe for dark energy evolution, but we found the shear-ratio to have negligible cosmological dependency and that instead it is much more sensitive to uncertainties in the redshift distributions. We find agreement between the results obtained using the shear-ratio method developed in this thesis and the results from other methods, including calibration from the high-quality photometric redshifts of the multi-band COSMOS survey and angular cross-correlation redshifts.

Finally, in Part IV, we present cosmological constraints obtained just from geometrical information, taking appropriately defined ratios of CMB lensing and galaxy-galaxy lensing measurements using DES Y1, South Pole Telescope (SPT) and Planck data. Such lensing ratios depend only on the angular diameter distances to the tracer objects and to the gravitational lensing source planes, similarly to the shear-ratio test. However, including the much longer distance to the CMB shell makes this measurement sensitive to cosmological parameters. Because of their simple cosmological dependence, such ratios can exploit available signal down to small angular scales, even where directly modeling the correlation functions is difficult and is usually left out of conventional cosmological analyses. Also, we found that future lensing ratio measurements with data from a combination of LSST and Stage-4 CMB experiments can be used to place interesting cosmological constraints, even after considering the systematic uncertainties associated with photometric redshift and galaxy shear estimation.

Appendix A

$\Delta\Sigma$ AND γ_t

When we measure the mean tangential alignment of background galaxies around lenses, we need to make a choice as to how we weight each of the lens-source pairs. In this appendix, we discuss the implications of using either a uniform weight for all source-lens pairs in a given combination of source and lens redshift bins, or a weight that takes into account the photometric redshift estimate of the source to yield a minimum variance estimate of the surface mass density contrast of the lens.

In the first case, and without a shape noise weighting of sources, our measurement γ_t is simply the arithmetic mean of the tangential components of ellipticities of sources i:

$$\gamma_t = N^{-1} \sum_{i=1}^{N} e_{t,i} \ . \tag{A.1}$$

In the second case, we weight each lens-source pair by a weight $w_{\mathrm{e},i}$,

$$\gamma_t = \frac{\sum_{i=1}^{N} w_{\mathrm{e},i} e_{t,i}}{\sum_{i=1}^{N} w_{\mathrm{e},i}} \ . \tag{A.2}$$

For optimal signal-to-noise ratio and uniform shape noise of our sample of source galaxies, $w_{\mathrm{e},i}$ should be chosen to be proportional to the amplitude of the signal in each lens-source pair, i.e.

$$w_{\mathrm{e},i} \propto \frac{D_\mathrm{l} D_\mathrm{ls}}{D_\mathrm{s}} \ . \tag{A.3}$$

We note that, for a given cosmology, the mean shears of both Eq. (A.1) and Eq. (A.2) can be converted to an estimate of surface mass density $\Delta\Sigma$, by multiplying with the (weighted) estimate of $\Sigma_\mathrm{crit}^{-1}$, as in Eq. (5.3). In the case of Eq. (A.2) with the weights equal to the expectation value of Eq. (A.3), this is identical to the common $\Delta\Sigma$ estimator of Sheldon et al. (2004).

The unweighted mean of Eq. (A.1) has the considerable advantage that nuisance pa-

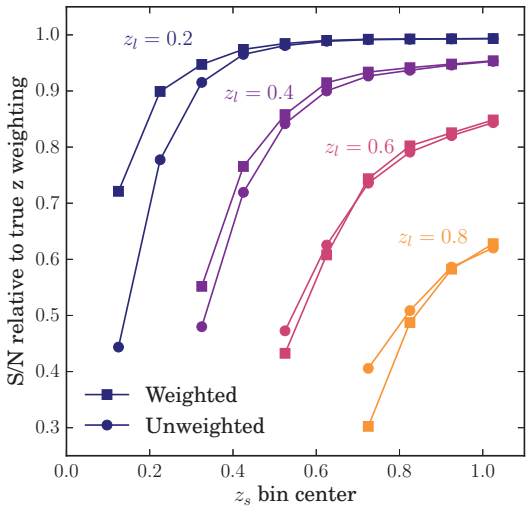

Figure A.1: Relative signal-to-noise ratio of lensing signal recovered when weighting sources uniformly (commonly called γ_t, circles) and with "$\Delta\Sigma$ weighting" according to a DES-like photometric redshift point estimate (squares) with $\sigma_p = -0.1\,(1+z) + 0.12\,(1+z)^2$ scatter around the true redshift (Hoyle et al., 2018). The point estimate is used to select source bins of width $\Delta z = 0.25$.

rameters describing the systematic uncertainty of shear and redshift estimates of the source redshift bins are identical to the ones determined for a cosmic shear analysis using the same samples (Troxel et al., 2018; Hoyle et al., 2018; Zuntz et al., 2018). This is of particular importance when joining cosmic shear and galaxy-galaxy lensing measurements into one combined probe (DES Collaboration, 2018b). The question at hand therefore is whether the increase in signal-to-noise ratio (S/N) due to the optimal weighting of Eq. (A.2) would warrant the added complication.

We make a simple estimate of the loss in S/N incurred by uniform weighting of sources. To this end, we simulate a source sample with overall Gaussian distribution of true redshifts z_t with a mean $\langle z_t \rangle = 0.6$ and width $\sigma_t = 0.3$. We split sources into redshift bins of width $\Delta z_p = 0.25$ by a point estimate z_p of their redshift. For a given source redshift bin centered on z_m, we emulate the latter by adding a Gaussian scatter of $\sigma_p = -0.1\,(1+z) + 0.12\,(1+z)^2$ to z_t, which is a realistic scatter for DES-Y1 photo-z's (Hoyle et al., 2018).

Figure A.1 compares the recovered S/N of the galaxy-galaxy lensing signal to that of weighting each source by the optimal weight using its true redshift for two cases: (1) uniform weighting of all sources in a redshift bin (circles) and (2) weighting each source by Eq. (A.3) evaluated at the source redshift point estimate (squares). Except in the case of source redshift bins overlapping the lens redshift, uniform weighting does not considerably lower the S/N of the measured galaxy-galaxy lensing signal. The photo-z resolution results in a bigger gain when using optimal weighting compared to uniform weighting. For instance, for $z_l = 0.4$ and $z_s = 0.425$, the gain of using photo-z optimal weighting is 6.4% for the fiducial photo-z scatter while it goes up to 25% if we improve the resolution by a factor of two. In a case with less overlap between the lens

and source redshift distributions the improvement is reduced, as expected. For example, for $z_l = 0.4$ and $z_s = 0.625$, the gain of using photo-z optimal weighting is 1.6% for the fiducial photo-z scatter while it is 2.1% for a photo-z resolution that is twice as good. Therefore, we conclude that, even though optimal weighting can be important, for the photo-z precision and the source binning used in this work, photo-z-dependent weighting of sources does not significantly improve the constraining power, and decide to use uniformly weighted tangential shears in this analysis.

Appendix B

Effect of random point subtraction in the tangential shear measurement

Our estimator of galaxy-galaxy lensing in Eq. (5.8) includes subtracting the measurement around random points that trace the same survey geometry. This measurement, using a set of random points with 10 times as many points as lens galaxies, is shown in Fig. B.1. Even though this is a correction included in the measurement, it is nonetheless useful to confirm that it is small at all scales used in the analysis. The measurement tests the importance of systematic shear which is especially problematic at the survey boundary, and allows us to compare the magnitude of the systematic shear with the magnitude of the signal around actual lens galaxies. We find the tangential shear around random points to be a small correction, consistent with the null hypothesis, as it is seen in the top left panel of Fig. B.2.

Even though the random point subtraction is a mild correction to the signal, it has an important effect on the covariance matrix. Subtracting the measurement around random points removes a term in the covariance due to performing the measurement using the over-density field instead of the density field, as it was studied in detail in Singh et al. (2016). As seen in Fig. B.2, we observe this effect on scales larger than 20 arcmin., where the covariance is no longer dominated by shape noise. When subtracting the measurement around random points, we detect both a significant decrease on the uncertainty of the tangential shear (top right panel) and a reduction of the correlation between angular bins (lower panels).

Finally, another argument that strongly favours applying the random points subtraction is the following. In Sec. 5.4.3 we validated the jackknife method using log-normal simulations, showing that the uncertainties on the tangential shear are compatible when using the jackknife method and when using the true variance from 1200 independent FLASK simulations (Fig. 5.4). We have performed this comparison both with and without the random point subtraction, finding that there is only agreement between the different methods when the tangential shear around random points is re-

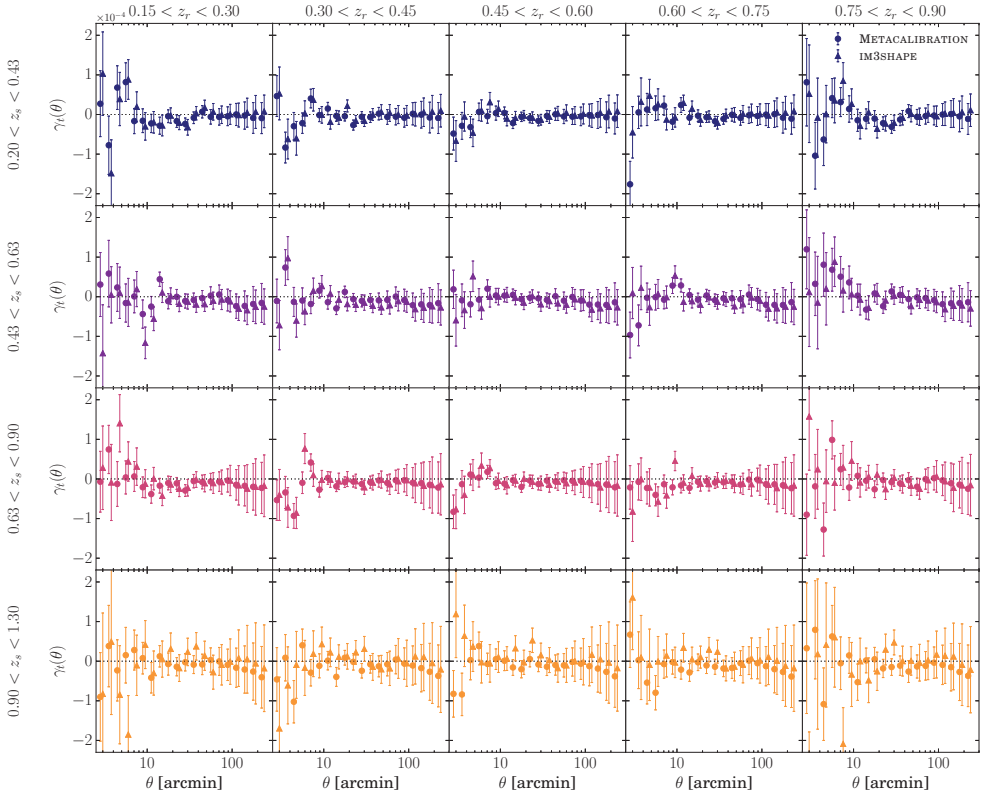

Figure B.1: Tangential shear around random points for Metacalibration and im3shape.

moved from the signal.

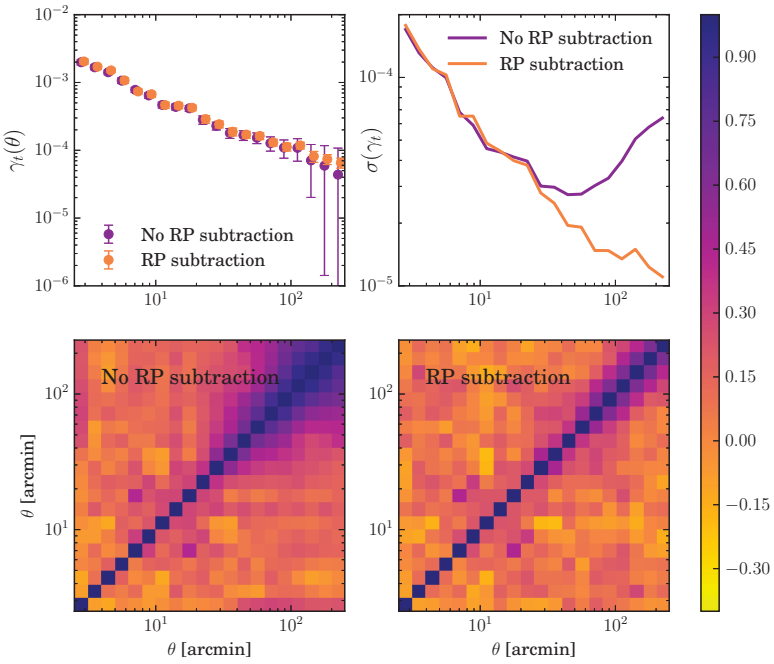

Figure B.2: We show the impact the random point subtraction has on the tangential shear measurement and its corresponding jackknife covariance matrix for an example redshift bin ($0.3 < z_l < 0.45$ and $0.63 < z_s < 0.90$ for METACALIBRATION).

Appendix C

Metacalibration responses scale dependence

As explained in Sec. 5.4.1, when applying the Metacalibration responses we approximate them as being scale independent. In this appendix we test the validity of this approximation by measuring the scale dependence of the responses for all the tomographic lens-source bin combinations.

In Fig. C.1 we display the Metacalibration responses for all the lens-source redshift bins combinations averaged in 20 log-spaced angular bins using the `NK` `TreeCorr` correlation function. Comparing to the mean of the responses over the ensemble in each source redshift bin, we find the variation with θ to be very small compared to the size of our measurement uncertainties and thus decide to use a constant value for simplicity. Future analyses using Metacalibration on larger data samples with smaller uncertainties may need to include the scale-dependent responses in their measurements.

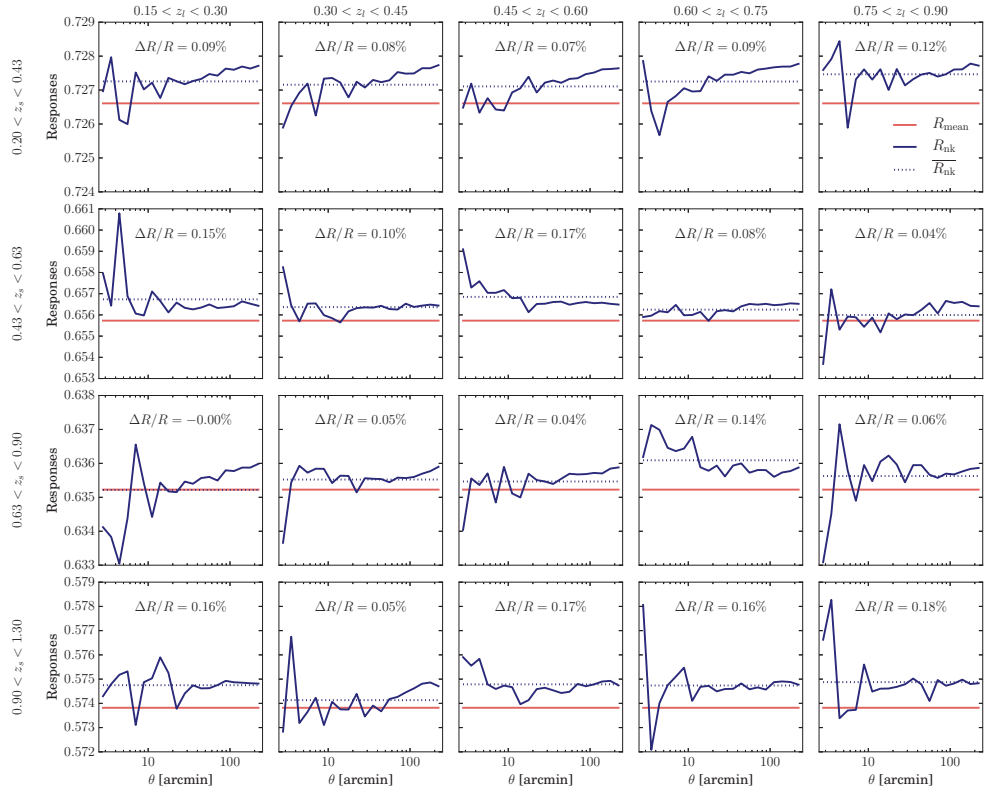

Figure C.1: METACALIBRATION responses scale dependence and mean values. We compare the responses averaged in 20 log-spaced angular bins between 2.5 and 250 arcmin in each lens-source redshift bin combination ($R_{\rm nk}$) to the average of the responses in each source redshift bin ($R_{\rm mean}$). The maximum difference between them is at the 0.2% level.

Appendix D

Test of Gaussian approximation to ratio posteriors

In Fig. D.1 we show the posteriors on the lensing ratios obtained from the fitting procedure to the two-point correlation functions using an MCMC, described in detail in Sec. 7.4.4. These posteriors serve as the likelihood to then measure the cosmological parameters running a second MCMC, as can be seen in Eq. (7.19). In our analysis, for simplicity, we assume this likelihood is a multivariate Gaussian with a covariance coming from the fitting procedure of Sec. 7.4.4. We test this assumption in Fig. D.1, where we compare the measured lensing ratio posteriors with contours drawn from a multivariate Gaussian centered at the same value, and using the measured covariance, finding that they are indeed very similar.

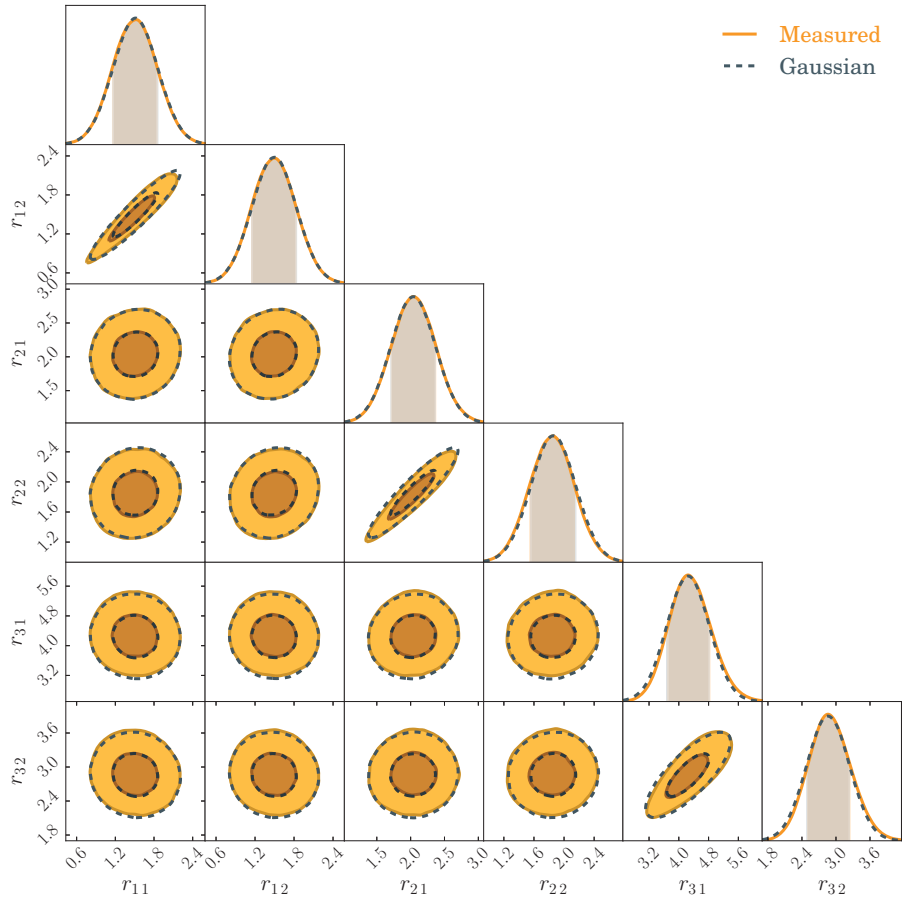

Figure D.1: Measured posteriors on the lensing ratios compared to a multivariate Gaussian drawn from the measured covariance between the ratios centered in the same value. r_{ij} is the ratio between the measurements in the CMB lensing map and the lens bin i and the convergence map in source bin j and same lens bin, as defined in Eq. (7.14).

Bibliography

Abazajian K. N. et al., 2016, ArXiv e-prints

Abbott T. M. C. et al., 2018a, ArXiv e-prints

Abbott T. M. C. et al., 2018b, The Astrophysical Journal Supplement Series, 239, 18

Ade P. A. R., et al., 2014, Astron. Astrophys., 571, A16

Ade P. A. R., et al., 2016, Astron. Astrophys., 594, A13

Amara A., et al., 2012, Mon. Not. R. Astron. Soc., 424, 553

Astropy Collaboration et al., 2018, AJ, 156, 123

Aubourg É. et al., 2015, Phys. Rev. D, 92, 123516

Baldauf T., Smith R. E., Seljak U., Mandelbaum R., 2010, Phys. Rev. D, 81, 063531

Bardeen J. M., Bond J. R., Kaiser N., Szalay A. S., 1986, Astrophys. J., 304, 15

Bartelmann M., Maturi M., 2017, Scholarpedia, 12, 32440

Bartelmann M., Schneider P., 2001, Phys. Rep., 340, 291

Baxter E., et al., 2016, Mon. Not. R. Astron. Soc., 461, 4099

Baxter E. J. et al., 2019, Phys. Rev. D, 99, 023508

Becker M. R., et al., 2016, Phys. Rev. D, 94, 022002

Benitez N., 2000, Astrophys. J., 536, 571

Bennett C. L. et al., 2013, ApJS, 208, 20

Benson A. J., Cole S., Frenk C. S., Baugh C. M., Lacey C. G., 2000, MNRAS, 311, 793

Benson B. A. et al., 2014, in SPIE, Vol. 9153, Millimeter, Submillimeter, and Far-Infrared Detectors and Instrumentation for Astronomy VII, p. 91531P

Berlind A. A., Weinberg D. H., 2002, Astrophys. J., 575, 587

Bernstein G., 2006, ApJ, 637, 598

Bernstein G. M., 2009a, Astrophys. J., 695, 652

Bernstein G. M., 2009b, Astrophys. J., 695, 652

Bertin E., 2011, Evans I. N., Accomazzi A., Mink D. J., Rots A. H., eds, Astron. Soc. Pacific Conf. Astron. Data Anal. Softw. Syst. XX., 442, 435

Bertin E., Arnouts S., 1996, Astron. Astrophys. Suppl. Ser., 117, 393

Bianchini F. et al., 2015, ApJ, 802, 64

Blazek J., Mandelbaum R., Seljak U., Nakajima R., 2012, JCAP, 5, 041

Blazek J., Vlah Z., Seljak U., 2015, J. Cosmol. Astropart. Phys., 2015, 015

Bonnett C., 2015, Mon. Not. R. Astron. Soc., 449, 1043

Bonnett C., et al., 2016, Phys. Rev. D, 94, 042005

Brainerd T. G., Blandford R. D., Smail I., 1996, Astrophys. J., 466, 623

Bridle S., King L., 2007, New J. Phys., 9, 444

Brown M. L., Taylor A. N., Hambly N. C., Dye S., 2002, Mon. Not. R. Astron. Soc., 333, 501

Busha M. T., Wechsler R. H., Becker M. R., Erickson B., Evrard A. E., 2013, in American Astronomical Society Meeting Abstracts, Vol. 221, American Astronomical Society Meeting Abstracts #221, p. 341.07

Cacciato M., van den Bosch F. C., More S., Li R., Mo H. J., Yang X., 2009, Mon. Not. R. Astron. Soc., 394, 929

Cacciato M., van den Bosch F. C., More S., Mo H., Yang X., 2013, Mon. Not. R. Astron. Soc., 430, 767

Carrasco Kind M., Brunner R. J., 2013, Mon. Not. R. Astron. Soc., 432, 1483

Carretero J., Castander F. J., Gaztanaga E., Crocce M., Fosalba P., 2014, Mon. Not. R. Astron. Soc., 447, 646

Castro P. G., Heavens A. F., Kitching T. D., 2005, Phys. Rev. D, 72, 023516

Catelan P., Kamionkowski M., Blandford R. D., 2001, Mon. Not. R. Astron. Soc., 320, L7

Cavaliere A., Fusco-Femiano R., 1976, A&A, 49, 137

Cawthon R. et al., 2018, MNRAS, 481, 2427

Chang C. et al., 2018, MNRAS, 475, 3165

Chang C., et al., 2016, Mon. Not. R. Astron. Soc., 459, 3203

Clampitt J., et al., 2017, Mon. Not. R. Astron. Soc., 465, 4204

Coe D., Benítez N., Sánchez S. F., Jee M., Bouwens R., Ford H., 2006, Astron. J., 132, 926

Coles P., Jones B., 1991, Mon. Not. R. Astron. Soc., 248, 1

Colless M. et al., 2001, MNRAS, 328, 1039

Cooper M. C. et al., 2012, Mon. Not. R. Astron. Soc., 419, 3018

Cooray A., Sheth R., 2002, Phys. Rep., 372, 1

Coupon J. et al., 2012, Astron. Astrophys., 542, A5

Crocce M., Castander F. J., Gaztañaga E., Fosalba P., Carretero J., 2015, Mon. Not. R. Astron. Soc., 453, 1513

Crocce M., et al., 2016, Mon. Not. R. Astron. Soc., 455, 4301

Das S., Spergel D. N., 2009, Phys. Rev. D, 79, 043509

Davis C. et al., 2017, ArXiv e-prints

de Jong J. T. A., Verdoes Kleijn G. A., Kuijken K. H., Valentijn E. A., 2013, Exp. Astron., 35, 25

Dekel A., Lahav O., 1999, Astrophys. J., 520, 24

Dell'Antonio I. P., Tyson J. A., 1996, Astrophys. J., 473, L17

DeRose J., et al., 2017, in prep

DES Collaboration, 2015, Phys. Rev. D, 94, 022001

DES Collaboration, 2016, Mon. Not. R. Astron. Soc., 460, 1270

DES Collaboration, 2018a, arXiv e-prints

DES Collaboration, 2018b, Phys. Rev. D, 98, 043526

DES Collaboration et al., 2018, arXiv e-prints, arXiv:1810.02499

Desai S., et al., 2012, Astrophys. J., 757, 83

DESI Collaboration et al., 2016, ArXiv e-prints

Dodelson S., 2003, Modern Cosmology

Dodelson S., 2017, Gravitational lensing

Drlica-Wagner A. et al., 2018, ApJS, 235, 33

Efstathiou G., Bond J. R., 1999, MNRAS, 304, 75

Einstein A., 1917, Sitzungsber. Preuss. Akad. Wiss. Berlin (Math. Phys.), 1917, 142

Elvin-Poole J., et al., 2018, Phys. Rev. D, 98, 042006

Erben T., et al., 2013, Mon. Not. R. Astron. Soc., 433, 2545

Fixsen D. J., 2009, ApJ, 707, 916

Flaugher B., et al., 2015, Astron. J., 150, 150

Foreman-Mackey D., Hogg D. W., Lang D., Goodman J., 2013, PASP, 125, 306

Fosalba P., Crocce M., Gaztanaga E., Castander F. J., 2015, Mon. Not. R. Astron. Soc., 448, 2987

Fosalba P., Gaztañaga E., Castander F. J., Crocce M., 2015, MNRAS, 447, 1319

Fosalba P., Gaztanaga E., Castander F. J., Crocce M., 2015, Mon. Not. R. Astron. Soc., 447, 1319

Frieman J., Turner M., Huterer D., 2008, Ann. Rev. Astron. Astrophys., 46, 385

Fry J. N., Gaztanaga E., 1993, Astrophys. J., 413, 447

Gatti M. et al., 2018, MNRAS, 477, 1664

Gaztañaga E., Eriksen M., Crocce M., Castander F. J., Fosalba P., Marti P., Miquel R., Cabré A., 2012, Mon. Not. R. Astron. Soc., 422, 2904

Giannantonio T. et al., 2016, MNRAS, 456, 3213

Gillis B. R. et al., 2013, Mon. Not. R. Astron. Soc., 431, 1439

Gorski K. M., Hivon E., Banday A. J., Wandelt B. D., Hansen F. K., Reinecke M., Bartelmann M., 2005, Astrophys. J., 622, 759

Graff P., Feroz F., Hobson M. P., Lasenby A., 2014, Mon. Not. R. Astron. Soc., 441, 1741

Harrison E. R., 1970, Phys. Rev. D, 1, 2726

Hartlap J., Simon P., Schneider P., 2007, Astron. Astrophys., 464, 399

Heavens A., 2003, MNRAS, 343, 1327

Heavens A. F., Kitching T. D., Taylor A. N., 2006, MNRAS, 373, 105

Henderson S. W. et al., 2016, Journal of Low Temperature Physics, 184, 772

Heymans C. et al., 2013, Mon. Not. R. Astron. Soc., 432, 2433

Heymans C., et al., 2012, Mon. Not. R. Astron. Soc., 427, 146

Hilbert S., Hartlap J., Schneider P., 2011, Astron. Astrophys., 536, A85

Hirata C. M., Mandelbaum R., Ishak M., Seljak U., Nichol R., Pimbblet K. A., Ross N. P., Wake D., 2007, Mon. Not. R. Astron. Soc., 381, 1197

Hirata C. M., Seljak U., 2004, Phys. Rev. D, 70, 063526

Hoecker A., et al., 2007

Hoekstra H., van Waerbeke L., Gladders M. D., Mellier Y., Yee H. K. C., 2002, Astrophys. J., 577, 604

Honscheid K., DePoy D. L., et al., 2008, arXiv e-prints, arXiv:0810.3600

Hoyle B. et al., 2018, MNRAS, 478, 592

Hu W., Holz D. E., Vale C., 2007, Phys. Rev. D, 76, 127301

Hu W., Jain B., 2004, Phys. Rev., D70, 043009

Hu W., Okamoto T., 2002a, ApJ, 574, 566

Hu W., Okamoto T., 2002b, ApJ, 574, 566

Huchra J., Davis M., Latham D., Tonry J., 1983, ApJS, 52, 89

Hudson M. J., et al., 2015, Mon. Not. R. Astron. Soc., 447, 298

Huff E., Mandelbaum R., 2017, ArXiv e-prints

Huterer D., Takada M., Bernstein G., Jain B., 2006, Mon. Not. R. Astron. Soc., 366, 101

Jain B., Taylor A., 2003, Phys. Rev. Lett., 91, 141302

Jain B., Taylor A., 2003, Physical Review Letters, 91, 141302

Jarvis M., Bernstein G., Jain B., 2004, Mon. Not. R. Astron. Soc., 352, 338

Jarvis M., et al., 2016, Mon. Not. R. Astron. Soc., 460, 2245

Jeong D., Komatsu E., Jain B., 2009, Phys. Rev. D, 80, 123527

Joachimi B., Bridle S. L., 2010, Astron. Astrophys., 523, A1

Joudaki S., et al., 2017, arXiv e-prints

Joudaki S., et al., 2018, Mon. Not. Roy. Astron. Soc., 474, 4894

Jullo E. et al., 2012, Astrophys. J., 750, 37

Kacprzak T., Zuntz J., Rowe B., Bridle S., Refregier A., Amara A., Voigt L., Hirsch M., 2012, Mon. Not. R. Astron. Soc., 427, 2711

Kacprzak T., et al., 2016, Mon. Not. R. Astron. Soc., stw2070

Kaiser N., 1984, Astrophys. J., 284, L9

Kaiser N., Squires G., 1993, Astrophys. J., 404, 441

Kaufman G.M, 1967, Cent. Oper. Res. Econom. Cathol. Univ. Louvain, Heverlee, Belgium, Rep. No. 6710

Kayo I., Taruya A., Suto Y., 2001, Astrophys. J., 561, 22

Kitching T. D. et al., 2015, ArXiv e-prints

Koekemoer A. M. et al., 2007, Astrophys. J. Suppl. Ser., 172, 196

Krause E., Eifler T., 2017, Mon. Not. Roy. Astron. Soc., 470, 2100

Krause E. et al., 2017, ArXiv e-prints

Kuijken K., et al., 2015, Mon. Not. R. Astron. Soc., 454, 3500

Kwan J., et al., 2017, Mon. Not. R. Astron. Soc., 464, 4045

Lahav O., Liddle A. R., 2014

Lahav O., Suto Y., 2004, Living Rev. Relativ., 7, 8

Le Fèvre O., et al., 2005, Astron. Astrophys., 439, 845

Leauthaud A., et al., 2012, Astrophys. J., 744, 159

Leauthaud A., et al., 2017, Mon. Not. R. Astron. Soc., 467, 3024

Lee J., Pen U.-L., 2000, Astrophys. J., 532, L5

Leistedt B., McEwen J. D., Büttner M., Peiris H. V., 2017, MNRAS, 466, 3728

Leistedt B., et al., 2016, Astrophys. J. Suppl. Ser., 226, 24

Lilly S. J., et al., 2007, Astrophys. J. Suppl. Ser., 172, 70

LSST Dark Energy Science Collaboration, 2012, ArXiv e-prints

LSST Science Collaboration et al., 2009, ArXiv e-prints

MacCrann N. et al., 2018, MNRAS, 480, 4614

Madhavacheril M. S., Hill J. C., 2018, Phys. Rev. D, 98, 023534

Mandelbaum R. et al., 2005, Mon. Not. R. Astron. Soc., 361, 1287

Mandelbaum R., Seljak U., Baldauf T., Smith R. E., 2010, Mon. Not. R. Astron. Soc., 405, 2078

Mandelbaum R., Seljak U., Kauffmann G., Hirata C. M., Brinkmann J., 2006, Mon. Not. R. Astron. Soc., 368, 715

Mandelbaum R., Slosar A., Baldauf T., Seljak U., Hirata C. M., Nakajima R., Reyes R., Smith R. E., 2013, Mon. Not. R. Astron. Soc., 432, 1544

Mandelbaum R., et al., 2011, Mon. Not. R. Astron. Soc., 410, 844

Marian L., Smith R. E., Angulo R. E., 2015, Mon. Not. R. Astron. Soc., 451, 1418

Mather J. C. et al., 1994, ApJ, 420, 439

McClintock T. et al., 2019, MNRAS, 482, 1352

McDonald P., 2006, Phys. Rev. D, 74, 103512

Melchior P. et al., 2017, MNRAS, 469, 4899

Miller L., Kitching T. D., Heymans C., Heavens A. F., Van Waerbeke L., 2007, Mon. Not. R. Astron. Soc., 382, 315

Miyatake H., Madhavacheril M. S., Sehgal N., Slosar A., Spergel D. N., Sherwin B., van Engelen A., 2017, Physical Review Letters, 118, 161301

Mo H. J., White S. D. M., 1996, MNRAS, 282, 347

More S., Miyatake H., Mandelbaum R., Takada M., Spergel D. N., Brownstein J. R., Schneider D. P., 2015, Astrophys. J., 806, 2

Nakajima R., Mandelbaum R., Seljak U., Cohn J. D., Reyes R., Cool R., 2012, MNRAS, 420, 3240

Navarro J. F., Frenk C. S., White S. D. M., 1997, Astrophys. J., 490, 493

Nicola A., Refregier A., Amara A., 2016, Phys. Rev., D94, 083517

Norberg P., Baugh C. M., Gaztañaga E., Croton D. J., 2009, Mon. Not. R. Astron. Soc., 396, 19

Omori Y. et al., 2018a, arXiv e-prints

Omori Y. et al., 2017, Astrophys. J., 849, 124

Omori Y. et al., 2018b, ArXiv e-prints

Park Y., et al., 2016, Phys. Rev. D, 94, 063533

Patrignani C., et al., 2016, Chin. Phys., C40, 100001

Peebles P., 1980, The large-scale structure of the universe. Princeton University Press

Pen U., 1998, Astrophys. J., 504, 601

Penzias A. A., Wilson R. W., 1965, ApJ, 142, 419

Perlmutter S., et al., 1999, Astrophys. J., 517, 565

Planck Collaboration, 2018, arXiv e-prints

Prat J. et al., 2019, MNRAS, 487, 1363

Prat J. et al., 2018a, Phys. Rev. D, 98, 042005

Prat J., et al., 2018b, Mon. Not. R. Astron. Soc., 473, 1667

Press W. H., Schechter P., 1974, ApJ, 187, 425

Pujol A. et al., 2016, Mon. Not. R. Astron. Soc., 462, 35

Refregier A., Kacprzak T., Amara A., Bridle S., Rowe B., 2012, Mon. Not. R. Astron. Soc., 425, 1951

Riess A. G., et al., 1998, AJ, 116, 1009

Ross A. J., et al., 2012, Mon. Not. R. Astron. Soc., 424, 564

Ross A. J., et al., 2017, Mon. Not. R. Astron. Soc., 464, 1168

Rozo E., et al., 2016, Mon. Not. R. Astron. Soc., 461, 1431

Ruiz E. J., Huterer D., 2015, Phys. Rev. D, 91, 063009

Rykoff E. S. et al., 2014, Astrophys. J., 785, 104

Rykoff E. S., et al., 2016, Astrophys. J. Suppl. Ser., 224, 1

Sadeh I., Abdalla F. B., Lahav O., 2015, arXiv:1507.00490

Samuroff S. et al., 2018, MNRAS, 475, 4524

Sánchez C., et al., 2014, Mon. Not. R. Astron. Soc., 445, 1482

Sánchez C., et al., 2017, Mon. Not. R. Astron. Soc., 465, 746

Schaan E., Krause E., Eifler T., Doré O., Miyatake H., Rhodes J., Spergel D. N., 2017, Phys. Rev. D, 95, 123512

Schneider P., 1996, Mon. Not. R. Astron. Soc., 283, 837

Schneider P., Kochaneck C., Wambsganss J., 2006, Gravitational Lensing: Strong, Weak and Micro. Springer

Sellentin E., Heavens A. F., 2016, Mon. Not. R. Astron. Soc., 456, L132

Sellentin E., Heavens A. F., 2018, MNRAS, 473, 2355

Sheldon E. S., 2014, Mon. Not. R. Astron. Soc. Lett., 444, L25

Sheldon E. S., Huff E. M., 2017, Astrophys. J., 841, 24

Sheldon E. S. et al., 2004, Astron. J., 127, 2544

Shirasaki M., Takada M., Miyatake H., Takahashi R., Hamana T., Nishimichi T., Murata R., 2016, arxiv:1607.08679

Sifon C. et al., 2015, Mon. Not. R. Astron. Soc., 454, 3938

Simon P., Hetterscheidt M., Schirmer M., Erben T., Schneider P., Wolf C., Meisenheimer K., 2007, Astron. Astrophys., 461, 861

Singh S., Mandelbaum R., Seljak U., Slosar A., Gonzalez J. V., 2016, arXiv:1611.00752

Smith K. M., Zahn O., Doré O., 2007, Phys. Rev. D, 76, 043510

Smith R. E. et al., 2003, Mon. Not. R. Astron. Soc., 341, 1311

Smoot G. F. et al., 1992, ApJL, 396, L1

Suchyta E., et al., 2016, Mon. Not. R. Astron. Soc., 457, 786

Takada M., Hu W., 2013, Phys. Rev. D, 87, 123504

Takahashi R., Sato M., Nishimichi T., Taruya A., Oguri M., 2012, Astrophys. J., 761, 152

Takahashi R., Sato M., Nishimichi T., Taruya A., Oguri M., 2012, ApJ, 761, 152

Troxel M., Ishak M., 2015, Phys. Rep., 558, 1

Troxel M. A., Ishak M., 2014, Phys. Rept., 558, 1

Troxel M. A. et al., 2018, Phys. Rev. D, 98, 043528

Tyson J. A., Valdes F., Jarvis J. F., Mills, Jr. A. P., 1984, ApJL, 281, L59

van Daalen M. P., Schaye J., Booth C. M., Dalla Vecchia C., 2011, MNRAS, 415, 3649

van Uitert E., et al., 2016, Mon. Not. R. Astron. Soc., 459, 3251

van Uitert E., et al., 2017a, arXiv e-prints

van Uitert E., et al., 2017b

Velander M., et al., 2014, Mon. Not. R. Astron. Soc., 437, 2111

Viola M., et al., 2015, Mon. Not. R. Astron. Soc., 452, 3529

Wallis C. G. R., McEwen J. D., Kitching T. D., Leistedt B., Plouviez A., 2017, ArXiv e-prints

Weinberg D. H., Dave R., Katz N., Hernquist L., 2004, Astrophys. J., 601, 1

Weinberg D. H., Mortonson M. J., Eisenstein D. J., Hirata C., Riess A. G., Rozo E., 2013, Phys. Rept., 530, 87

White M., Song Y.-S., Percival W. J., 2009, MNRAS, 397, 1348

Xavier H. S., Abdalla F. B., Joachimi B., 2016, Mon. Not. R. Astron. Soc., 459, 3693

Zeldovich Y. B., 1972, MNRAS, 160, 1P

Zuntz J., Kacprzak T., Voigt L., Hirsch M., Rowe B., Bridle S., 2013, Mon. Not. R. Astron. Soc., 434, 1604

Zuntz J. et al., 2015a, Astron. Comput., 12, 45

Zuntz J. et al., 2015b, Astron. Comput., 12, 45

Zuntz J. et al., 2018, MNRAS, 481, 1149